รายงานวิจัยฉบับสมบูรณ์

โครงการ วัสดุผสมชนิดใหม่ของคอปเปอร์อินเดียมซัลไฟด์และโลหะวาเนเดตโครงสร้างนาโนสามมิติที่มีประสิทธิภาพสูงในการเร่งปฏิกิริยาด้วยแสงและเคมีไฟฟ้าเชิงแสง

โดย ผู้ช่วยศาสตราจารย์ ดร.สุลาวัลย์ ขาวผ่อง

มีนาคม 2562

สัญญาเลขที่ **MRG6080270**

รายงานวิจัยฉบับสมบูรณ์

โครงการ วัสดุผสมชนิดใหม่ของคอปเปอร์อินเดียมซัลไฟด์และโลหะวา เนเดตโครงสร้างนาโนสามมิติที่มีประสิทธิภาพสูง ในการเร่งปฏิกิริยาด้วยแสงและเคมีไฟฟ้าเชิงแสง

ผศ.ดร.สุลาวัลย์ ขาวผ่อง

ภาควิชาเคมี คณะวิทยาศาสตร์
มหาวิทยาลัยเชียงใหม่

สนับสนุนโดย
สำนักงานกองทุนสนับสนุนการวิจัย และมหาวิทยาลัยเชียงใหม่

Contents

Page

Figure contents

Page

Table contents

Page

Abstract

Project Code : MRG6080270

Project Title : Novel three–dimensional (3D) nanostructured $CuInS_2$/metal vanadate composites with highly efficient photocatalytic and photoelectrochemical activities

Investigator : Asst. Prof. Dr. Sulawan Kaowphong
Faculty of Science, Chiang Mai University

E–mail Address : sulawank@gmail.com, sulawan.k@cmu.ac.th

ระยะเวลาโครงการ : 3 April 2017 – 2 April 2019

Novel $CuInS_2$/m–$BiVO_4$ composites with different mass ratios ($CuInS_2$ to m–$BiVO_4$ = 1:3, 1:1, and 3:1) were synthesized by cyclic microwave irradiation, followed by thermal treatment process. Potential photocatalytic applications of the samples for photodegradation of organic compounds (methylene blue, rhodamine B, methyl orange) under visible light irradiation were investigated. The $CuInS_2$/m–$BiVO_4$ photocatalyst with mass ratio of 1:3 exhibited better photocatalytic degradation of methylene blue than those of either pure $CuInS_2$ or m–$BiVO_4$. The PEC properties of the $CuInS_2$/m–$BiVO_4$ photoelectrode, evaluated by linear sweep voltammetry measurement, revealed that the composite photoelectrode exhibited higher current density and the onset potential in comparison with the m–$BiVO_4$ photoelectrode. The enhanced photocatalytic and PEC performance of the $CuInS_2$/m–$BiVO_4$ was ascribed not only that the $CuInS_2$/m–$BiVO_4$ extended the light absorption in visible light region but also that the formation of a heterojunction structure, which promoted photogenerated electrons and holes as well as facilitated effective charge separation and transportation between the $CuInS_2$ and m–$BiVO_4$ contact interface.

Novel $FeVO_4/Bi_7O_9I_3$ nanocomposites with different weight percentages (3, 6.25, 12.5, and 25%wt) of $FeVO_4$ were reported. The $FeVO_4$ and $Bi_7O_9I_3$ contents played an important role in the photocatalytic activity of the nanocomposite. The 6.25%wt-$FeVO_4/Bi_7O_9I_3$ photocatalyst exhibited excellent photocatalytic efficiency for the degradation of different organic dyes under visible light irradiation. In addition, it was effective in the reuse, and exhibited good stability after three times of usage. The $O_2^{\bullet-}$ and h^+ were found to contribute as the main active species in the trapping experiments for the decomposition of RhB under visible–light irradiation. The photocurrent response of the 6.25%wt-$FeVO_4/Bi_7O_9I_3$ photoanode was ca. 3.7 times higher than that of the pure $Bi_7O_9I_3$. The improved photogenerated charge separation in the $FeVO_4/Bi_7O_9I_3$ nanocomposite was mainly responsible for the enhanced photocatalytic activity, which was supported by photoluminescence spectra. Owing to notable enhancements in the photocatalytic dye degradation and the photoelectrochemical property of the $FeVO_4/Bi_7O_9I_3$ heterojunction, it is potentially applicable to the field of environmental remediation as well as solar water splitting.

Keywords : $FeVO_4/Bi_7O_9I_3$, $CuInS_2$/m–$BiVO_4$, Photocatalyst, Photoelectrochemical, Photodegradation, Composite, Heterojunction

บทคัดย่อ

รหัสโครงการ : MRG6080270

ชื่อโครงการ : วัสดุผสมชนิดใหม่ของคอปเปอร์อินเดียมซัลไฟด์และโลหะวาเนเดตโครงสร้างนาโนสามมิติที่มีประสิทธิภาพสูงในการเร่งปฏิกิริยาด้วยแสงและเคมีไฟฟ้าเชิงแสง

ชื่อนักวิจัย : ผู้ช่วยศาสตราจารย์ ดร. สุลาวัลย์ ขาวผ่อง
คณะวิทยาศาสตร์ มหาวิทยาลัยเชียงใหม่

E-mail Address : sulawank@gmail.com and sulawan.k@cmu.ac.th

ระยะเวลาโครงการ : 3 เมษายน 2560 – 2 เมษายน 2562

วัสดุคอมโพสิตของคอปเปอร์อินเดียมซัลไฟด์/โมโนคลินิกบิสมัทวานาเดตชนิดใหม่ ($CuInS_2$/m–$BiVO_4$) ที่มีอัตราส่วนโดยมวลต่างกัน ($CuInS_2$ ต่อ m–$BiVO_4$ เท่ากับ 1:3 1:1 และ 3:1) ถูกสังเคราะห์ด้วยวิธีแผ่รังสีไมโครเวฟแบบรอบตามด้วยกระบวนการปรับปรุงด้วยความร้อน และทดสอบความเป็นไปได้ในการประยุกต์ใช้เร่งปฏิกิริยาด้วยแสงของสารตัวอย่างเพื่อการย่อยสลายทางแสงของสารประกอบอินทรีย์ (เมทิลลีนบลู โรดามีน บี เมทิลออเรนจ์) ภายใต้การฉายแสงที่มองเห็นได้ พบว่าตัวเร่งปฏิกิริยาด้วยแสง $CuInS_2$/m–$BiVO_4$ ที่มีอัตราส่วนโดยมวลเท่ากับ 1:3 สามารถย่อยสลายเมทิลลีนบลูด้วยการเร่งปฏิกิริยาด้วยแสงได้มากกว่า $CuInS_2$ หรือ m–$BiVO_4$ คุณสมบัติไฟฟ้าเคมีทางแสงของ $CuInS_2$/m–$BiVO_4$ ขั้วรับแสง ที่วัดค่าได้โดยโวแทมเมทรีแบบเพิ่มศักย์กับวงจรในอัตราเร็วคงที่ แสดงให้เห็นว่าขั้วรับแสงวัสดุคอมโพสิตมีความหนาแน่นของกระแส และค่าความต่างศักย์ที่มีการเปลี่ยนแปลงกระแสอย่างชัดเจนสูงขึ้นเมื่อเปรียบเทียบกับ ขั้วรับแสง m–$BiVO_4$ ซึ่งการเพิ่มขึ้นของการเร่งปฏิกิริยาด้วยแสงและคุณสมบัติไฟฟ้าเคมีทางแสงของ $CuInS_2$/m–$BiVO_4$ สามารถอธิบายได้ว่า $CuInS_2$/m–$BiVO_4$ ไม่เพียงแค่เพิ่มการดูดกลืนแสงในช่วงแสงที่มองเห็นได้ แต่การเกิดโครงสร้างรอยต่อเฮทเทอโรยังช่วยส่งเสริมการเกิดอิเล็กตรอนและโฮลที่ถูกกระตุ้นด้วยโฟตอน

เช่นเดียวกันยังช่วยส่งเสริมประสิทธิภาพการแยกและเคลื่อนย้ายของประจุระหว่างผิวที่อยู่ติดกันของ $CuInS_2$ และ m–$BiVO_4$ อีกด้วย

วัสดุนาโนคอมโพสิตของเฟอริกวานาเดต/บิสมัทออกซีไอโอไดด์ชนิดใหม่ ($FeVO_4/Bi_7O_9I_3$) ที่มีร้อยละโดยน้ำหนักแตกต่างกัน (3 6.25 12.5 และ 25%wt) ของ $FeVO_4$ ถูกรายงาน ซึ่งปริมาณของ $FeVO_4$ และ $Bi_7O_9I_3$ มีความสำคัญในกระบวนการเร่งปฏิกิริยาด้วยแสงของวัสดุนาโนคอมโพสิต โดยตัวเร่งปฏิกิริยาด้วยแสง $FeVO_4/Bi_7O_9I_3$ ที่มีร้อยละโดยน้ำหนักเท่ากับ 6.25 มีประสิทธิภาพในการเร่งปฏิกิริยาด้วยแสงที่ยอดเยี่ยมสำหรับการย่อยสลายของสีย้อมอินทรีย์ที่แตกต่างกันภายใต้การฉายแสงที่มองเห็นได้ นอกจากนี้ยังมีประสิทธิภาพในการนำกลับมาใช้ใหม่และแสดงความเสถียรภาพที่ดีหลังการใช้งานซ้ำสามครั้ง โดยจากการทดลองการตรวจจับอนุพันธ์ที่ว่องไวในการเกิดปฏิกิริยาพบว่า $O_2^{\bullet-}$ และ h^+ เป็นอนุพันธ์หลักและมีส่วนในการช่วยสลายตัวของโรดามีน บี ภายใต้การฉายแสงที่มองเห็นได้ การตอบสนองการสร้างกระแสไฟฟ้าภายใต้การฉายแสงของขั้วแอโนดรับแสง $FeVO_4/Bi_7O_9I_3$ ที่มีร้อยละโดยน้ำหนักเท่ากับ 6.25 มีค่าสูงกว่า $Bi_7O_9I_3$ ถึง 3.7 เท่า การเพิ่มขึ้นของกระบวนการการเร่งปฏิกิริยาด้วยแสงนี้เป็นผลจากการแยกกันของประจุที่ถูกกระตุ้นด้วยโฟตอนที่เพิ่มขึ้นในวัสดุนาโนคอมโพสิต $FeVO_4/Bi_7O_9I_3$ ซึ่งมียืนยันจากโฟโตลูมิเนสเซนต์สเปกตรัม เนื่องจากการเพิ่มคุณภาพที่โดดเด่นในการย่อยสลายสีย้อมด้วยการเร่งปฏิกิริยาด้วยแสงและคุณสมบัติไฟฟ้าเคมีทางแสงของ $FeVO_4/Bi_7O_9I_3$ อาจประยุกต์ใช้ในการฟื้นฟูสิ่งแวดล้อมและการแยกน้ำด้วยพลังงานแสงอาทิตย์ได้

Keywords : $FeVO_4/Bi_7O_9I_3$, $CuInS_2$/m–$BiVO_4$, ตัวเร่งปฏิกิริยา, เคมีไฟฟ้าเชิงแสง, การย่อยสลายเชิงแสง คอมโพสิท, รอยต่อเฮทเทอโร

Chapter 1 Introduction

1.1 Introduction

With the overpopulation in the world, enormous of pollutants have been released into the environment [1]. Wastewater from the textile and dyeing industry are among the significant sources of organic pollutants, affecting the aquatic living lives in water, human beings, and ecosystems [2]. Semiconductor photocatalysis is considered as a potential technology to treat these problems, especially for the disposing of organic dyes [2]. TiO_2 and ZnO are the most widely used as photocatalytic semiconducting materials for water purification. However, they possess wide band gap energy so that limit the practical applications. They can only active with the UV light which occupies only about 5% of solar energy. Therefore, it is important to explore a suitable photocatalytic material that can harvest visible light, which is the major constituent of the solar spectrum (46%) [2–6]. Monoclinic $BiVO_4$ (m–$BiVO_4$) with a narrow band gap energy of 2.4 eV is found to be a promising candidate photocatalyst for visible–light–driven photocatalytic environmental remediation [7] and solar H_2 and O_2 production [8] due to its surface adsorption capacity and long–term stability against photocorrosion [7–9]. Moreover, iodide–deficient bismuth oxyiodide ($Bi_7O_9I_3$) has attracted considerable interest in recent years as it has exhibited excellent visible–light photocatalytic activity for degradation of organic compounds such as colorless bisphenol–A, phenol, and rhodamine B under visible–light irradiation [10–12]. Nevertheless, the photocatalytic efficiency of these single materials remains far from suitable for practical applications because the quantum yield of $Bi_7O_9I_3$ and m–$BiVO_4$ is rather poor due to the rapid recombination of photogenerated electron–hole pairs and slow rate of photogenerated charge transfer [13–19]. The fabrication of heterojunction photocatalysts by coupling of two semiconductors with matching band potentials has been a promising approach that can effectively separate and transfer the photogenerated electrons and holes, thus resulting in improved photocatalytic performance [13,20–22].

$CuInS_2$ has been increasingly considered as a photocatalyst owing to its large absorption coefficient over a wide spectral range and excellent optoelectrical properties [23–25]. It has been reported that coupling $CuInS_2$ with other wider band gap photocatalysts highly improved the photocatalytic degradation of organic dyes [26–28] and photoelectrochemical (PEC) conversion efficiency [29,30] compared to individual photocatalyst. For example, the $ZnO/CuInS_2$ and $CuInS_2/TiO_2$ heterojunctions shown to be beneficial to the photodegradations of organic dyes in aqueous solution such as rhodamine B [26], crystal violet [27], and methyl orange [28]. The $ZnO/CuInS_2$ [29] and $CuInS_2/TiO_2$ electrodes [30] also exhibited significantly enhanced PEC activity under visible light irradiation compared to pure ZnO or TiO_2 electrodes. In addition, the $CuInS_2/TiO_2$ also served as an effective photocatalyst for H_2 generation with stable activities under long periods of light irradiation [31]. Higher photocatalytic H_2 evolution rate of the $CuInS_2/TiO_2$ composite comparing with pure TiO_2 and pure $CuInS_2$ materials caused by the improved charge transfer efficiency and reduced recombination rate of photogenerated electrons and holes.

Apart from the narrow band gap $CuInS_2$ photocatalyst, nanocrystalline $FeVO_4$ with a band gap energy of 2.0 eV is a highly stable and preferred catalyst for photocatalytic degradation of organic pollutants under a natural solar light irradiation [32,33] and a catalytic oxidation [34]. It can be used as a potential visible-light photocatalyst through a combination with other semiconductors to form heterojunctions such as $BiVO_4/FeVO_4$ [35] and $Bi_2O_3/FeVO_4$ [36]. These heterojunctions can facilitate an efficient charge separation and suppress the recombination of photogenerated electron–hole pairs, thereby leading to enhanced photocatalytic performance. Additionally, the enhancement of the photocatalytic performance can be triggered by an increase in the visible-light absorption ability, which enables the heterojunctions to absorb more visible light and produce more electron–hole pairs [19,35,36]. Hence, coupling m-$BiVO_4$ with $CuInS_2$ and coupling $Bi_7O_9I_3$ with $FeVO_4$ containing matched band potentials to form $CuInS_2$/m-$BiVO_4$ and $FeVO_4/Bi_7O_9I_3$ heterojunctions, respectively, is a promising way to enhance their photocatalytic performance.

1.2 Research objective

1.2.1 To synthesize $CuInS_2$ $BiVO_4$, $FeVO_4$, and $Bi_7O_9I_3$ nanostructures by a cyclic microwave irradiation method

1.2.2 To synthesize the novel $CuInS_2$/m–$BiVO_4$ and $FeVO_4$/$Bi_7O_9I_3$ composites

1.2.3 To investigate physicochemical, optical, and electrical properties of the synthesized materials

1.2.4 To utilize the novel composites for the photocatalytic and photoelectrochemical applications

Chapter 2 Theoretical Background

2.1 Principles of photocatalysis

"Photocatalysis" means the acceleration of a photoreaction in the presence of catalyst and light source such as sunlight. Photocatalyst is a compound that accelerate the rate of photoreaction by interaction with the substrate or media in its ground or excited state to generate other active species, for example, hydroxyl radical (OH•) **[1]**.

2.1.1 The components in photocatalytic process

a. Semiconductor catalyst

When semiconductors are irradiated by photo–energy equal to or greater than the band gap energy of the semiconductor photocatalyst, electron from the valence band (VB) will be excited to the conduction band (CB). This generates electrons in the conduction band and leaves generated holes in the valence band. The occurred electrons and generated holes are usually called photo–generated electron–hole pairs

b. Energy source (light)

In the photocatalytic process, energy from light source has to be higher or equal to energy band gap (E_g) as shown in the equation below.

$$E = h\nu = \frac{hc}{\lambda}$$

When E = Quantum Energy (Joules, J)

h = Planck's Constant = 6.625×10^{-34} Js

ν = Frequency of radiated light (Hertz, Hz, s^{-1})

λ = Wavelength (nm)

c = speed of light = 2.997×10^{8} (m/s)

From this equation, the energy is higher when the wavelength is lower as in Figure 2.1.

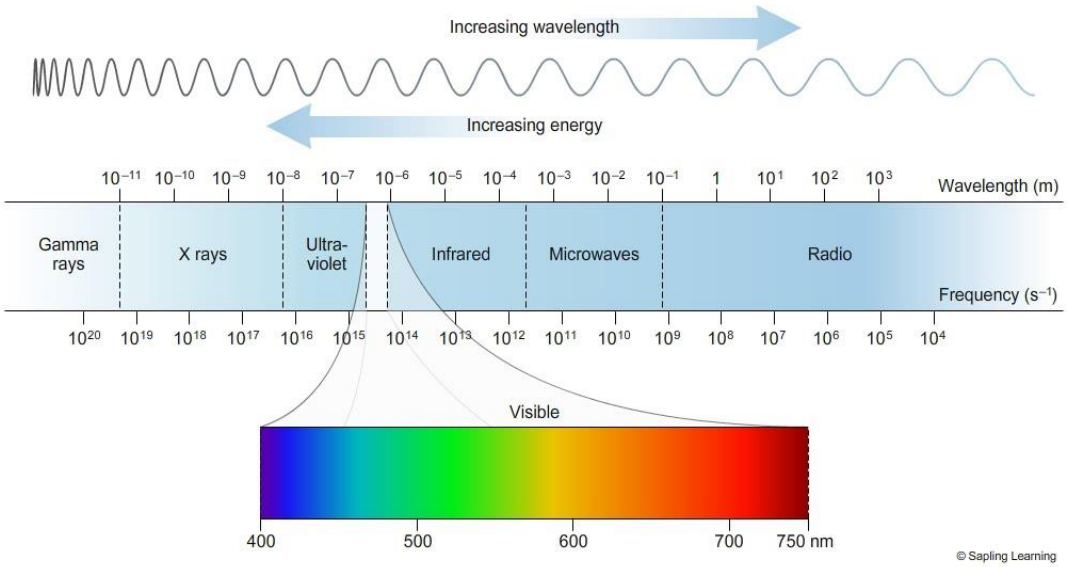

Figure 2.1 Electromagnetic spectrum [37]

2.1.2 Types of photocatalysis

a. Homogeneous photocatalysis

In homogeneous photocatalytic reaction, the reactants and catalyst are in the same phase, usually in liquid phase. For example, the degradation of 2,4–dinitroluene using UV/H_2O_2.

b. Heterogeneous photocatalysis

This process consists of a catalyst in a different phase from the reactants. For example, the degradation of 2–chlorophenol using UV/TiO_2. Generally, semiconductors such as metal oxides and metal sulfides are one of the outstanding candidates due to their characteristic properties. These semiconductors have appropriate band gap that reduce electron–hole recombination possibility and the generated hole and electron can react with oxidants or reactants to generate active species such as hydroxyl radicals.

2.1.3 Mechanism of photocatalytic reaction

There are three simple steps in photocatalytic reaction:

1. Photoexcitation of charge carrier
2. Charge carrier separation and diffusion to surface
3. Oxidation and reduction at the surface

In semiconductor photocatalysis, the photocatalytic process occurs when the semiconductors are irradiated equal or higher than their band gap energy and followed by the generation of excited electrons from valence band (VB) to conduction band (CB) (e_{CB}^-) which leaves generated holes in valence band (h_{VB}^+) (eq.1). The e_{CB}^- and h_{VB}^+ are strong reducing and oxidizing agents. Thus, the h_{VB}^+ reacts to organic molecules such as dyes and then produces small molecules (CO_2 and H_2O) as final products (eq. 2). Moreover, this active species (h_{VB}^+) can also react with water molecules, hydroxy anion or even organic compounds to generate another active species which is hydroxyl radical (OH •) (eq. 3,4). This generated OH • can non–selectively react with other electron–rich organic molecules and convert to CO_2 and water (eq. 5). In addition, e_{CB}^- can also generate superoxide radical (O_2•) by reacting with presence absorbed oxygen molecules on the catalyst surface (eq. 6). After that, this O_2• can combine with proton and lead to the formation of peroxy radical (•OOH) (eq. 7). Further reaction between peroxy radical and e_{CB}^- in the presence of proton can produce hydrogen peroxide (H_2O_2) (eq. 8). This generated hydrogen peroxide can react with e_{CB}^- and lead to the formation of another hydroxy radical and hydroxy anion (eq. 9). Generated hydroxy anion can further react with h_{VB}^+ to produce hydroxyl radical and the reactive species will degrade organic molecules as write in eq. 5. The photocatalytic mechanism is shown in Figure 2.2.

$$\text{Semiconductors} + h\nu \longrightarrow e_{CB}^- + h_{VB}^+ \quad \text{(eq. 1)}$$

$$h_{VB}^+ + R \longrightarrow [\text{intermediates}] \longrightarrow CO_2 + H_2O \quad \text{(eq. 2)}$$

$$OH^- + h_{VB}^+ \longrightarrow {}^{\bullet}OH \quad \text{(eq. 3)}$$

$$H_2O + h_{VB}^+ \longrightarrow {}^{\bullet}OH + H^+ \quad \text{(eq. 4)}$$

$${}^{\bullet}OH + R \longrightarrow [\text{intermediates}] \longrightarrow CO_2 + H_2O \quad \text{(eq. 5)}$$

$$e_{CB}^- + O_2 \longrightarrow O_2^{\bullet -} \quad \text{(eq. 6)}$$

$${}^{\bullet}OOH + e_{CB}^- + h_{VB}^+ \longrightarrow H_2O_2 \quad \text{(eq. 7)}$$

$$H_2O_2 + e_{CB}^- \longrightarrow {}^{\bullet}OH + OH^- \quad \text{(eq. 8)}$$

$OH^- + h_{VB}^+ \longrightarrow \cdot OH$ (eq. 9)

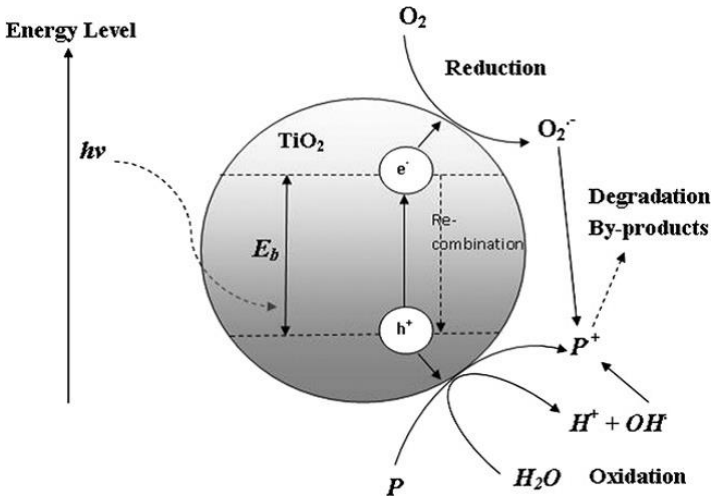

Figure 2.2 Mechanism of electron–hole pair formation in TiO_2 particles. [3]

Nevertheless, the major factor affecting the efficient of photocatalysts is the probability of electron–hole recombination that can simultaneous occur when electron–hole pairs are generated as shown in Figure 2.3. This recombination process can reduce and inhibit photocatalytic process. Thus, the charge carrier recombination must be inhibited to improve photocatalytic performance. The valence band and conduction band are usually related to defects in the crystal. Therefore, generally, perfect crystals can reduce the recombination rate. Moreover, larger surface area of particles can also enhance photocatalytic performance due to better absorbing of organic molecules with increasing surface area of catalysts.

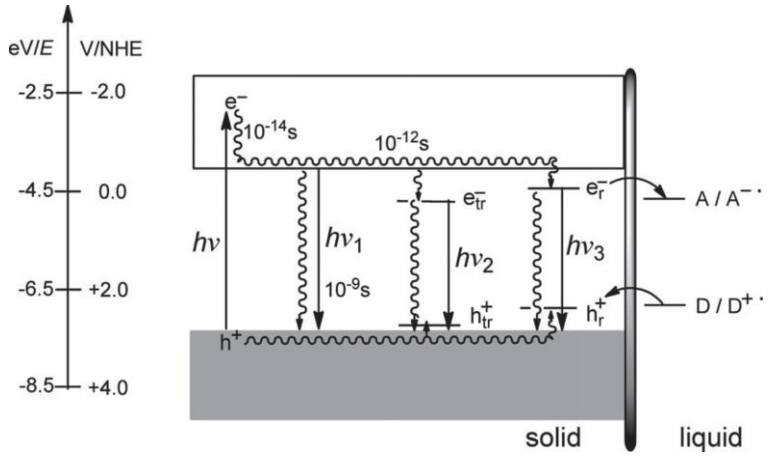

Figure 2.3 Mechanism of electron–hole pair recombination between semiconductor and liquid media. [3]

2.2 Dyes

Dyes are soluble coloured organic compounds that are usually applied to textiles from a solution in water. Dyes are coloured because they absorb some wavelength of light. Dye can be classified into 9 types, according to their solubility and chemical properties. [38–41]

1. Acid dyes: water–soluble anion dyes that used on fibrers such as silk or nylon
2. Basic dyes: water–soluble cation dyes that usually used on acrylic fibers
3. Direct or substantive dyes: dyes that normally occurs in neutral and used on cotton or leather
4. Mordant dyes: dyes that require a mordant and the most important mordant dyes are chrome dyes which used for wool
5. Vat dyes: water–insoluble dyes that need to be reduced to produce water–soluble dyes
6. Reactive dyes: use its chromophore to attract to a substituent which can directly react with substrate
7. Disperse dyes: water–insoluble dyes that mainly suspend in a dispersing agent and used on polyester
8. Azoic dyes: insoluble azo dye which produced onto fiber or cotton but this dye' type is unique due to its toxicity.
9. Sulfur dyes: inexpensive dyes that apply on cotton especially result in dark colors, for example, Sulfur Black 1.

In addition, dyes can be divided into 12 groups, according to their chromophores as followed; Acridine dyes, Anthraquinone dyes, Arylmethane dyes, Azo dyes, Diazonium dyes, Nitro dyes, Nitroso dyes, Phthalocyanine dyes, Quinone–imine dyes, Thiazole dyes, Safranin dyes, Xanthene dyes. There are a lot of publications have reported the use of photocatalysts for dyes degradation under UV or visible light. The estimation of the number of publications are shown in Table 2.1. The most studied dyes are the thiazine dyes (the majority is methylene blue) and the second are xanthenes dyes (the majority is rhodamine B). However, the most used and globally produced dyes is azo dyes.

The utilizations of dyes for studying photocatalytic process are the ability to use UV–Vis spectroscopy to observe decolorization of dyes, a non–expensive and easy techniques and easy to measure the kinetic of photocatalytic degradation. However, there are still some disadvantages, for example, the presence of other species such as intermediate products or even aggregated dyes on the catalyst surface.

Table 2.1 An estimated number of the publication on the photocatalytic dyes degradation under UV or visible light irradiation.[39]

Class	UV	Visible
Anthraquinones	238	390
Azo dyes	1285	2006
Natural dyes	187	303
Thiazines	7496	13471
Triarylmethanes	1439	2758
Xanthenes	5625	12244
Others	303	557

In 2015, K. M. Reza, *et. al.* [40] reported that there are some parameters affecting the photocatalytic degradation of dyes by using TiO_2 as a photocatalyst. It was shown that the higher concentration of oxidants, for example, O_3 or H_2O_2 increases the formation rate of hydroxyl radical by (1) the reduction process with conduction band of photocatalyst or (2) self–decomposition. The higher concentration of hydroxyl radicals accelerates photocatalytic degradation of dyes by reducing electron–hole recombination rate. However, H_2O_2 can react with the catalyst surface and decrease its photocatalytic efficiency. The second parameter is pH of solution [42]. The varied pH values affect total charge of dyes and make a lower or higher absorption between dyes and catalyst surface. Third, the effect of dyes concentration, as the concentration of dye increases, dyes molecules are adsorbed on the catalyst surface and dramatically lowering amount of light that absorbed by catalyst particles. Thus, the amount of generated hydroxyl radical is reduced and the degradation rate is consequently decreased. The forth factor is the concentration of photocatalyst. In 1991, T. Y. Wei and C. C. Wan [43] reported that the amount of catalyst has an impact on the photodegradation rate. The result showed that the rate of decolonization rapidly increases when the concentration of catalyst increases and then decrease to a constant value when the amount of catalyst further increases. Thus, the optimum amount of catalyst needs to be added. The last factor is intensity and wavelength of light [44]. This factor affects the rate of photodegradation of dyes. As the light intensity increases, the reaction rate increases and reaches the maximum. However, as the light intensity still increases, the number of activation sites on catalyst surface remain constant. So, the reaction rate remains constant even the light intensity still increases. Moreover, the higher light intensity can effectively enhance electron–hole formation; hence, electron–hole recombination rate is negligible.

Usually, methylene blue (MB), an indicator dye, has been chosen as a model to study photocatalytic process of synthesized photocatalysts. Methylene blue (or methylthioninium chloride) is belongs to a group of thiazide dye with the molecular formula $C_{16}H_{18}N_3SCl$ and its chemical structure is shown in Figure 2.4. Methylene blue can be detected by simple UV–Vis spectroscopy due to its aromatic system which is a chromophore. Peaks absorption are observed at around 609 and 668 nm. The first

absorption band is corresponding to **π**–**π*** transition of benzene ring while the second is corresponding to n–**π*** transitions which moving according to the pH of solution (n is the free doublet on the nitrogen atom of C=N bond and free doublet of S atom on S=C bond).

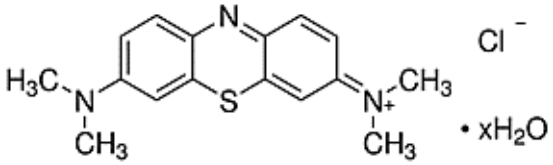

Figure 2.4 Chemical structure of methylene blue [45]

2.3 Microwave irradiation method

To study why microwave radiation can be used as heating source, it is necessary to understand the mechanism of microwave heating first. Microwave can be divided into an electric field which perpendicular to a magnetic field and these components are responsible for the dielectric heating via two major mechanisms.

1) Dipolar polarization or diploe rotation mechanism [46]

This mechanism (Figure 2.5) occurs when electric field interacted with substrates. The substrates, which can generate heat, must have a dipole moment, for example, water molecule. This dipole moment is very sensitive to an applied electric field and will align itself by rotation. The rotational motion is resulted in energy transfer to other molecules. So, any molecules with a dipole moment will encounter with this mechanism to generate heat.

In gases, molecules are freely packed, so the alignment is very rapid. In contrast, liquid molecules are tighter packed and the rotation is prohibited by the presence of other molecules. However, the ability of alignment of liquid molecules are varied by frequency of microwave source and its viscosity. In microwave radiation, the applied frequency is low so that the dipole molecules can respond to applied electric field and therefore rotate. However, the microwave frequency is not high enough to make molecules precisely rotate follow applied electric field. Thereby, phase difference will occur and resulted

in friction and collision which lost a generated energy and rise dielectric heating. For example, dixoane, low dipole moment molecule, cannot be heated by microwave radiation while water molecule, large dipole moment molecule, can be rapidly heated. So, that's why gases molecules cannot be heated by microwave because the distance between adjacent molecule is very long and the molecules are able to perfectly follow the electric field, so no phase difference occurs.

Figure 2.5 Dipolar molecules which align itself with an applied electric field [46].

2) Ionic conduction mechanism [46]

The second mechanism (Figure 2.6) is the resulted of free ions or charged particles in the heated substance. The electric field will generate a motion of ionic or charged particles that orient themselves to the applied electric filed. Thus, collision occurs and converting from kinetic energy to heat. This mechanism is much stronger than the dipole mechanism regarding to the heat–generating capacity.

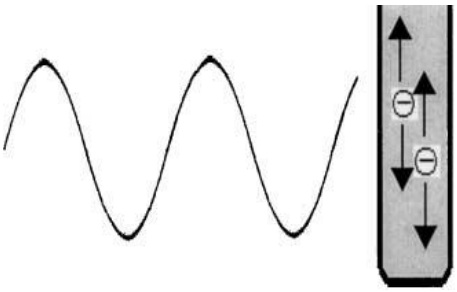

Figure 2.6 Charged particles in a heated substance following the applied electric field [46].

2.3.1 Solvents used in microwave synthesis [46]

Many factors affect the polarity and absorbing characteristics of solvent, for example, the dielectric constant, dipole moment, dielectric loss, tangent delta, and dielectric relaxation time.

1) The dielectric constant (**ε'**)

The dielectric constant (**ε'**) or relative permittivity of a solvent is or relative permittivity of a solvent is store electric charges. It is the ratio between electric capacity of solvent filled capacitor and evacuated capacitor. This factor depends on temperature and radiated frequency.

$$\varepsilon' = \frac{\boldsymbol{C_{filled}}}{\boldsymbol{C_{evacuated}}}$$

2) The dipole moment

The dipole moment is the mathematically calculated by the following equation below.

$$T = pE \text{ or } \mu = Qr$$

where T = torque

p = dipole moment

E = field strength

μ = dipole moment

Q = charge

r = distance between charges

According to this equation, molecules with high dipole moment also have high dielectric constant. Because, the polarization depends on dipole rotation.

3) Tangent delta (**δ**)

The tangent delta or loss tangent is the ability of a substance to convert electromagnetic wave into heat. In addition, the tangent delta is described as an efficiency of the sample that convert microwave power into heat and determined as shown in the equation below.

$$\boldsymbol{\delta = \frac{\varepsilon''}{\varepsilon'}}$$

where δ = Tangent delta

ε' = Dielectric constant

ε'' = Dielectric loss or complexed permittivity

Dielectric loss is an amount of transferred input energy to the sample. Thus, the solvent that has high dielectric loss can generate a large amount of heat. Dielectric constant is an ability to store electrical charges of particular solvent and affected by temperature and microwave frequency.

4) Dielectric relaxation time

Relaxation time is the needed time to transfer an input microwave energy into thermal energy. In conclusion, solvent with high dielectric constant and tangent delta will be resulted in the high final temperature. For example, acetone and ethanol with a comparable dielectric constant and tangent delta are heated at the same environment and the resulted final temperature of ethanol is higher than acetone as shown in Figure 2.7.

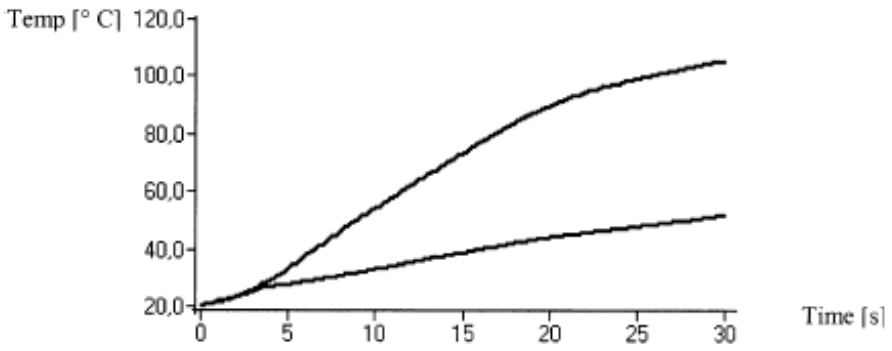

Figure 2.7 The temperature of ethanol and acetone. The upper curve is ethanol and the lower curve is acetone. [46]

Table 2.2 Dielectric constant and tangent delta for some solvents (values determined at 2.45 GHz and room temperature) [46].

Solvent	Dielectric constant (ε')	Tangent delta (tan δ)
Propylene glycol	32.0	
Poly(ethylene glycol) 300	16.0	
Benzene	2.3	
Carbon tetrachloride	2.2	
Chloroform	4.7	
Hexane	1.9	0.20
Acetic acid	6.1	0.091
Ethyl acetate	6.2	0.174
THF	7.6	0.059
Methylene chloride	9.1	0.047
Acetone	20.6	0.042
Ethanol	24.6	0.054
Methanol	32.7	0.941
Water	80.4	0.123
Ethylene glycol	37.0	1.350
2–propanol	18.3	0.799

2.3.2 Superheating effect [46]

The dielectric constant and dielectric lose are relevant and dependent on relaxation time (τ). The relaxation time defines as the time it takes for one molecule to return to 36.8% of its original situation when the electric field is switched off. Thus, the ability of solvent to convert microwave energy into heat is not only depend on microwave frequency but also on the temperature. Thereby, solvent

with a relaxation time >65 ps will have a lose tangent that increases with temperature and consequently increase the heating rate due to the limitation of the formation of 'boiling nuclei'.

2.3.4 Comparison of microwave heating with conventional heating and the reason why microwave irradiation can enhance the rate of reaction [47,48]

Microwave can accelerate chemical reaction by giving rapidly transferred electromagnetic energy in 10^{-9} sec with each irradiated cycle whereas the kinetic molecular relaxation will take only 10^{-5} sec. Thus, energy transfer is faster than the molecular relaxation. Additionally, the lifetime of activated complexes is only 10^{-13} sec. However, there are some resonance-able compounds which have a longer lifetime than 10^{-9} seconds and resulted in polar species even ionic character which enhance microwave energy transfer.

The rate of reaction can be described by an Arrhenius rate equation.

$$K = Ae^{-\Delta E_a/RT}$$

Where K = rate constant

T = absolute temperature (Kelvin, K)

A = pre-exponential factor, a molecular mobility

E_a = activation energy of the reaction (Joules, J)

R = gas constant

Microwave energy will affect reaction temperature. An increasing of temperature will consequently increase rate constant and reaction rate which is the result of higher collision probability. To sum up, traditional heating is using external heating source and the generated heat pass through the wall of vessel. In contrast, microwave radiation can heat the substrate from inside by interacting with present dipole or charged molecules or ions and do not depend on thermal conductivity of the vessel as shown in Figure 2.8.

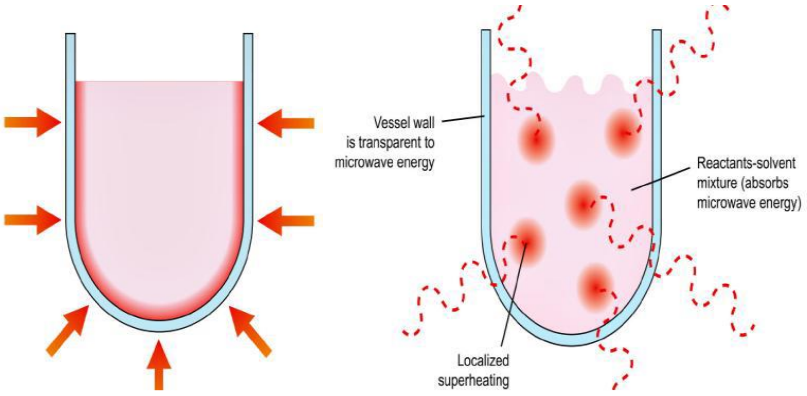

Figure 2.8 Sample heating; tradition heating (left) and microwave heating (right). [49]

Advantages:	Uniform heating occurs throughout the material
	Process speed is increased
	High efficiency of heating
	Reduction in unwanted side reaction
	Purity in final product
	Improve reproducibility
	Environmental heat loss can be avoided
Disadvantages:	Heat force control is difficult.
	Closed container is difficult because it could burst
	In-situ monitoring
	Expensive setup

2.4 Composite photocatalysts

For photocatalysts, the structure designation extremely affects photocatalytic performance including electronic structure, surface structure and crystal structure. There are many strategies to improve light absorption ability such as metal-doping or even doping with ions. However, this method can also reduce oxidation and reduction potential and lead to the higher probability of electron-hole

recombination [50]. The photocatalytic activity of semiconductor photocatalysts could be also distinctively mediated by three structural parameters; size, morphology and defect. However, there are practically difficult due to the unclear formation mechanism and correlation between morphology/structure and the corresponding photocatalytic properties [51]. Therefore, formation of semiconductor heterostructure could be a promising approach to enhance the photo–generated charges separation efficiency and the photocatalytic performance. The formation of heterostructure (or composite) has a separation efficiency and migration ability of photo–generated charge carriers which can prevent photo–generated charges recombination process. Consequently, charge recombination is decreased and charge carriers have a longer lifetime–resulting in higher photocatalytic efficiency.

The composite fabrication can be divided into three types according to band position of two semiconductors as shown in Figure 2.9 [13]

1) Type I heterojunction

In type I heterojunction, the valence band (VB) of semiconductor 1 is higher than VB of semiconductor 2 while the conduction band (CB) of semiconductor 1 is lower than CB of semiconductor 2.

2) Type II heterojunction

Type II heterojunction provides the optimum band position between two semiconductors which VB and CB of semiconductor 1 are higher or lower than semiconductor 2. This arrangement provides the transferring of photogenerated–electrons and generated–holes between two different semiconductors and inhibits electron–hole recombination by the separation of electrons and holes.

3) Type III heterojunction

In type III heterojunction, charge carries act as the same manner as in type II heterojunction and the difference between these two types is the band position in Type III heterojunction are even more set off. This arrangement called broken–gap situations.

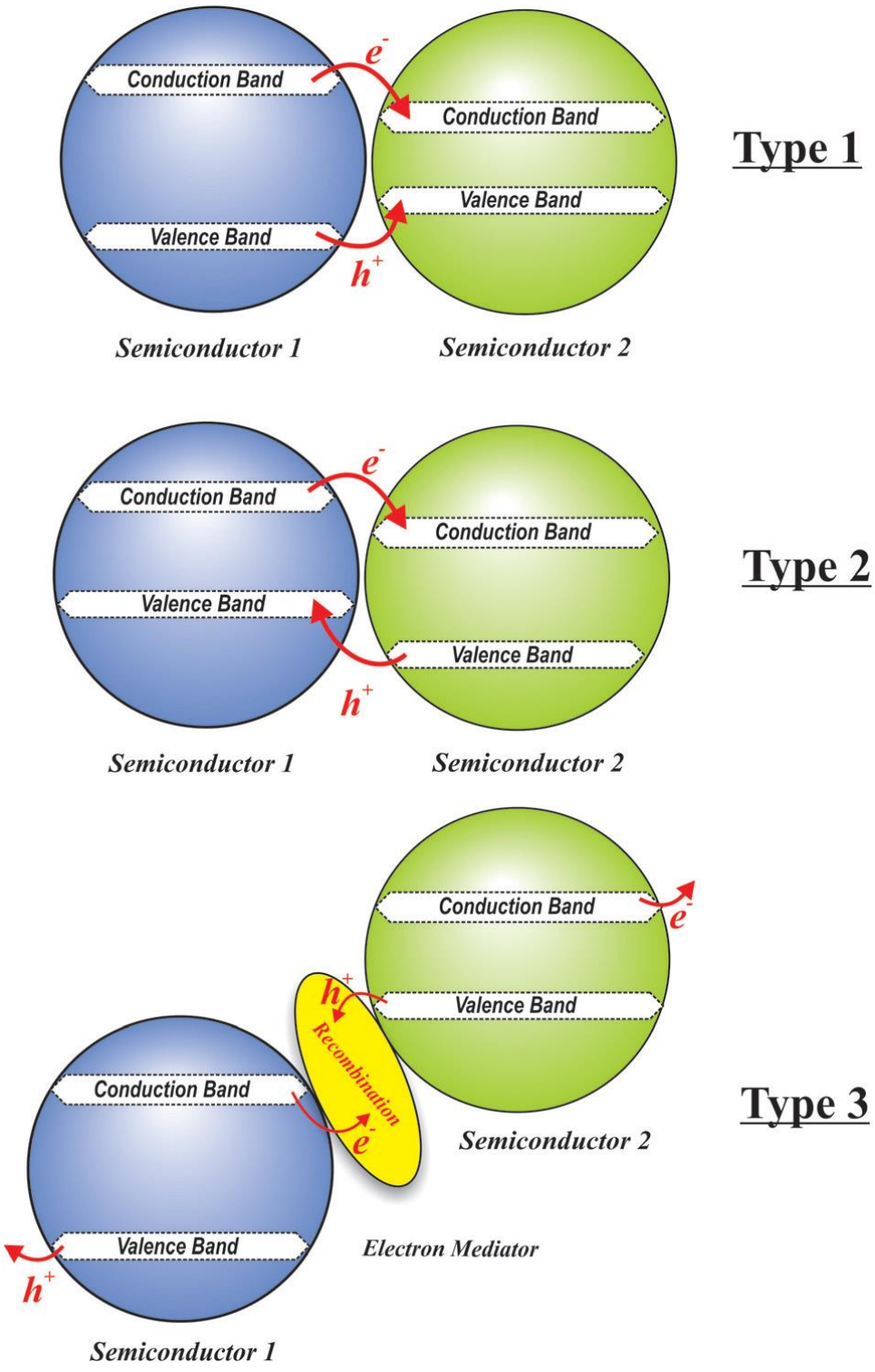

Figure 2.9 Schematic diagrams of type I, II and III heterojunctions [52].

Chapter 3 Synthesis and Characterization of $CuInS_2$

Recently, hollow nano/microstructure materials have attracted extensive attention because of their unique structures that enable useful physical properties, such as large specific surface area, low density, and good surface permeability [53,54]. Studies have demonstrated that their large surface areas are favorable for improving photocatalytic efficiency [55,56], performance of gas sensors [57], and dye loading capacity of dye–sensitized solar cells [58]. The cavities inside hollow microspheres are also useful in drug delivery and chemical storage applications [59,60]. In addition, the multiple reflection and scattering of light within their structures enhance the solar energy conversion efficiency of solar cells, due to the longer optical path length and greater light absorption than other morphologies [58,61,62].

$CuInS_2$ powder has been considered as an attractive semiconductor photocatalyst for H_2 evolution reaction [23,63], organic dye degradation [64], and nitrate ions removal [24,25]. Moreover, $CuInS_2$ is an efficient light–absorbing material for application in solar cells due to its direct band gap of 1.5 eV that matches the solar spectrum with a large absorption coefficient [65,66]. $CuInS_2$ hollow nano/microspheres have been synthesized through sacrificial templates, such as Cu_2O nanospheres [67], cubic Cu_2O crystals [68], $Cu(OH)_2$ films [69], and CuS hollow microspheres [70], but these require multistep synthetic procedures and expensive materials. Although a previous study used a solvothermal method to synthesize $CuInS_2$ hollow microspheres without using any templates [71], it required complicated equipment and considerable time. In addition, these studies did not report on the potential use of hollow nano/microspheres for solar energy conversion applications. Microwave heating has been used for the synthesis of nanocrystalline materials with various morphologies and sizes [48,72]. It is a low–cost, energy–saving, and highly efficient method for fabricating nanomaterials with high purity, small particle sizes, and narrow size distribution. The microwave radiation interacts with polar molecules and conducting ions to provide rapid volumetric heating and results in a shorter reaction time and faster

reaction rate comparing to conventional heating methods [48]. Our previous study [73] successfully synthesized $CuInS_2$ nanoparticles via cyclic microwave irradiation method using thioacetamide as a sulfur source. The $CuInS_2$ nanoparticles in microclusters were purified at 450 W and 600 W of the microwave powers. Although, the broken $CuInS_2$ hollow microsphere was found at 180 W, the CuS was still co–existed and morphological inhomogeneity was obtained.

In this Chapter, $CuInS_2$ powder was synthesized by a microwave irradiation method. Effects of solvent, sulfur source, and microwave power on characteristics of the synthesized $CuInS_2$ were investigated.

3.1 Effect of solvents

Different polyol solvents have different physical and chemical properties which differentially affect the microwave synthesis of nanomaterials. This study synthesized $CuInS_2$ nanoparticles by a cyclic microwave irradiation method using three different polyol solvents – ethylene glycol (EG), glycerol (Gly), and propylene glycol (PG) – to investigate their effects on the characteristics of the synthesized powders. The characteristics of the synthesized powders were examined by XRD and FESEM techniques. In addition, the reducing capability of each solvent was determined by FTIR technique.

3.1.1 Experimental procedure

In a typical procedure, $CuCl_2 \cdot 2H_2O$ (2 mmol), $InCl_3 \cdot 4H_2O$ (2 mmol), and CH_3CSNH_3 (4 mmol) were separately dissolved in 10.0 mL of the polyol solvent. The solutions were mixed together for 30 min, and then the mixed solution was irradiated using 2.45 GHz microwave radiation at 600 W for 75 cycles. For each cycle, the microwave power was turned on for 30 s of every 60 s (50% power). The resulting powder was collected and washed with deionized water and then ethanol. Finally, the powder was dried at 80 °C overnight and then characterized using XRD, FTIR, and FESEM techniques.

The purity, crystallinity, and crystal structure of the synthesized powders were characterized by XRD (Rigaku MiniFlex II) with a Cu$K\alpha$ radiation (1.5406 Å). Vibration modes of the powders were investigated by FTIR (Bruker TENSOR27) using the KBr pellet technique. Particle size and morphology of the powders were determined by FESEM (JEOL JSM-6335F), operated at 15 kV of accelerating voltage.

3.1.2 Physicochemical characterization

The XRD spectra of the powders synthesized using different solvents are shown in

Table 3.1(a). In all powders, the diffraction peaks at 2θ of 27.86°, 32.24°, 46.32°, and 54.87° were indexed to the (112), (004), (204), and (312) planes of a tetragonal $CuInS_2$ structure (JCPDS no. 032-0339). However, in the XRD spectrum of the powder synthesized using PG, the diffraction peaks of a hexagonal CuS structure (JCPDS no. 06-0464) were also found, implying that pure $CuInS_2$ did not completely form at the given microwave heating power. In addition, the intensity of the diffraction peaks of the $CuInS_2$ powder synthesized using EG were higher than those synthesized using Gly and PG, suggesting higher crystallinity. These results could be explained by the reaction temperature of the solvents. The ability of a conductive media to convert electromagnetic energy into heat at a given frequency and microwave power is determined by the dielectric loss tangent (tan δ = δ"/ δ'), where δ" is the dielectric loss and δ' is the dielectric constant . A solvent with high tan δ more effectively convert microwave energy to thermal energy; as a result, high reaction temperature can be achieved. The tan δ of the solvents used in this research are shown in

Table 3.1. In Figure 3.1(b), the measured reaction temperatures of EG, Gly and PG irradiated at 600 W were 190 °C, 186 °C, and 157 °C, respectively. The higher crystallinity of the $CuInS_2$ powder synthesized using EG could be due to the higher reaction temperature of the solution, relating to its

higher tan δ [48]. On the other hand, the lowest tan δ of PG corresponded to the lowest reaction temperature of the solution. This could be the reason that the CuS phase still remained in the $CuInS_2$ powder synthesized using PG at given microwave power. This result was consistent with the previous study reporting the remaining of CuS when the temperature was lower than 160 °C [71].

Table 3.1 Some properties of the solvents used [48,74,75].

Solvents	Ethylene glycol	Glycerol	Propylene glycol
Structure	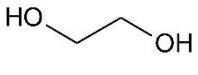	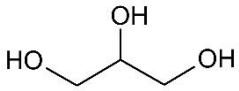	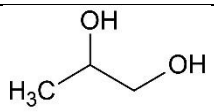
Boiling point (°C)	197	290	187
Dielectric loss tangent (at 2.45 GHz)	1.35 (at 20 °C)	0.54 (at 20 °C)	~0.23 (at 25 °C)
Viscosity (mPa•s at 25 °C)	16.2	934	11.3

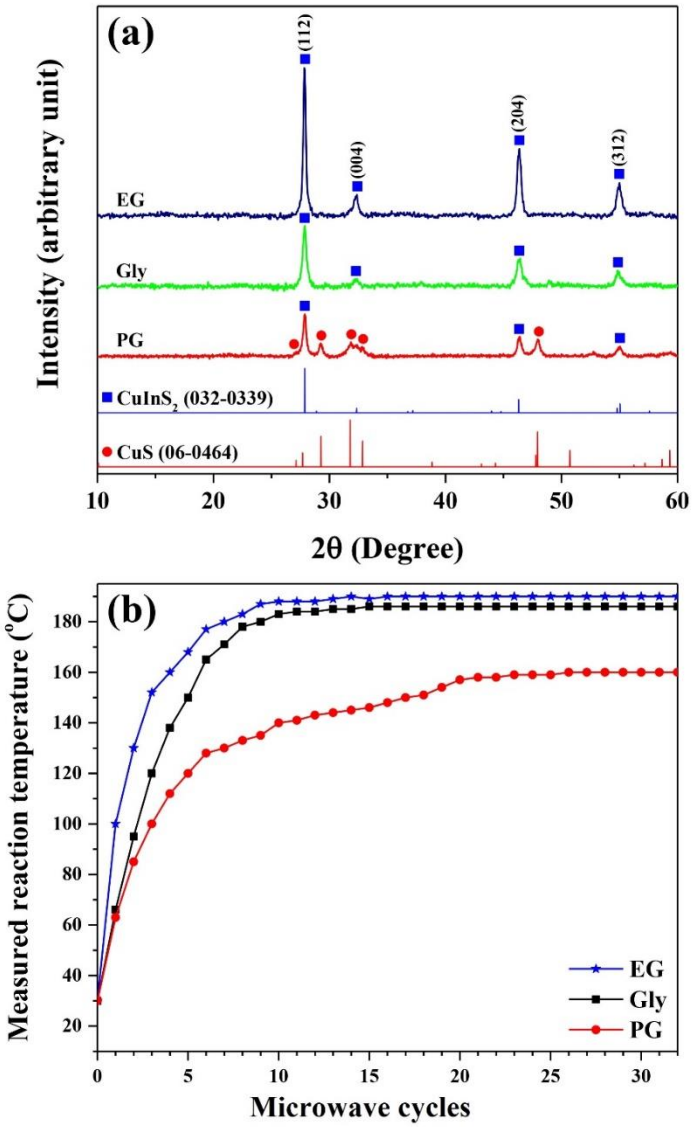

Figure 3.1 *(a)* XRD pattern of the powders synthesized using different solvents and *(b)* measured reaction temperatures of the different solvents irradiated at 600 W with the prolonged reaction time.

The formation of $CuInS_2$ nanostructures was related to the reduction of Cu^{2+} to Cu^{+} in solvent under microwave radiation [73]. After the reduction, the H_2S released from CH_3CSNH_3 reacted with Cu^{+} and In^{3+} to yield $CuInS_2$. Since each polyol solvent possesses different oxidation potentials, a solvent with stronger reducing capability is a more effective reducing agent. During the synthesis process, the

hydroxyl groups in polyol solvent can be oxidized by the metallic precursor. To investigate the reducing capability of the polyol solvents, pure solvents, residual solvents after the synthesis, and pure solvents irradiated at 600 W for 75 cycles were further analyzed by FTIR (Figure 3.2). Vibration peaks of the pure solvents (EG, Gly and PG) exhibited at 3384—3385 cm^{-1}, 2933—2946 cm^{-1}, 2879—2883 cm^{-1}, 1652—1654 cm^{-1}, 1414—1457 cm^{-1}, and 1079—1110 cm^{-1} are attributed to O—H stretching, C—H asymmetric stretching, C—H symmetric stretching, O—H bending, C—H bending, and C—O stretching, respectively.

The FTIR spectrum of the residual EG after the synthesis showed a strong vibration peak of C=O stretching at 1758 cm^{-1}, contributed to the ketone carbonyl group of diacetyl [76]. In addition, the O—H stretching band of the hydroxyl group was disappeared, implying that EG was completely oxidized to diacetyl during the microwave reaction. The FTIR spectrum of the residual Gly showed a weak vibration peak of C=O stretching at 1725 cm^{-1}, contributed to the aldehyde group of glyceraldehyde or ketone carbonyl group of dihydroxyacetone, and the remaining of the O—H stretching band could be the hydroxyl groups of the oxidation products [77]. Generally, PG can also reduce the metallic precursor resulting in acetone, propanal, and allyl alcohol [78]. But, these product compounds can evaporate and/or decompose during the microwave synthesis, due to their relatively low boiling points (56 °C, 48 °C, and 97 °C for acetone, propanal, and allyl alcohol, respectively). For this reason, the vibration peaks of the C=O stretching of these products were not observed in the FTIR spectrum of the residual PG. However, the remaining of O—H stretching band implied that PG was not completely reduced Cu^{2+} ions during the microwave synthesis in according to the XRD result (Figure 3.1(a). It is noted that the FTIR spectra of the EG, Gly, and PG irradiated at 600 W for 75 cycles (Figure 3.2) were the same as the respective pure solvents, confirming that the microwave irradiation did not decompose the pure solvents. These results suggested that microwave radiation enhanced the reducing capability of EG and Gly. As a result, the CuS was not found in the $CuInS_2$ powders synthesized using EG and Gly as revealed in their XRD spectra (Figure 3.1(a)). Based on the XRD and the FTIR results, EG was the most favorable

solvent for the microwave synthesis where the $CuInS_2$ powder synthesized using EG had the highest crystallinity.

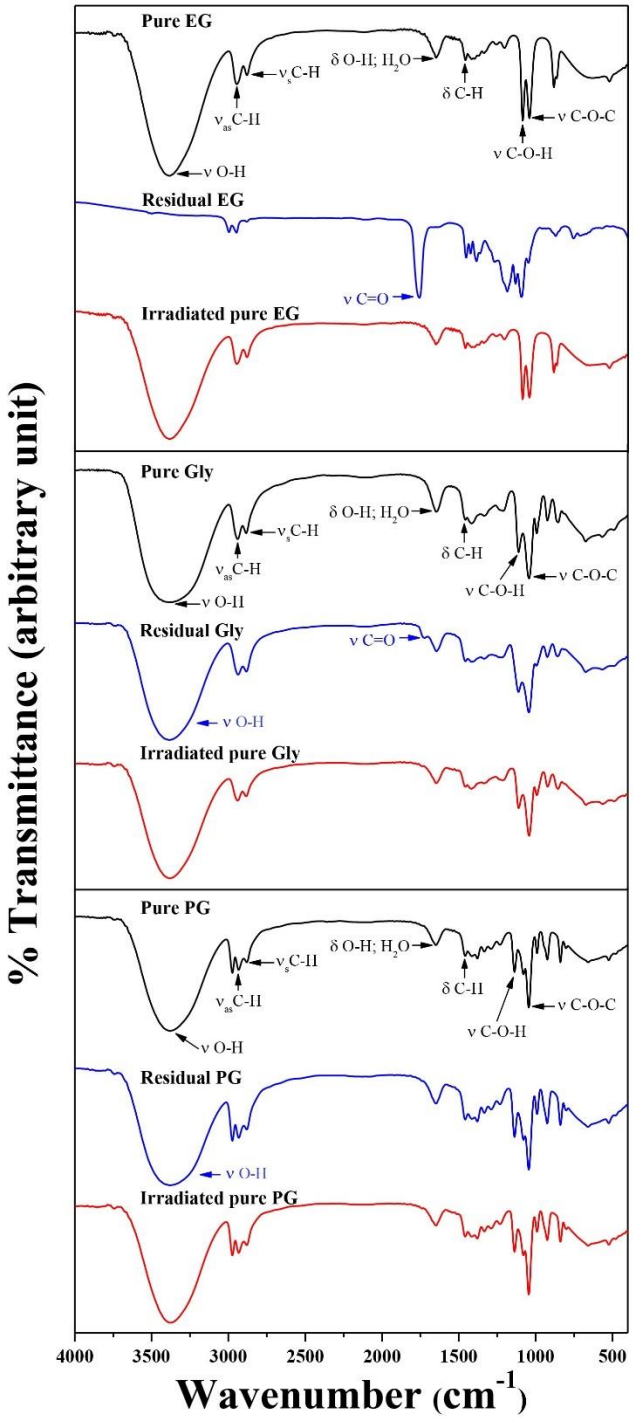

Figure 3.2 FTIR spectra of pure solvents, residual solvents after the synthesis process and pure solvents irradiated at 600 W for 75 cycles.

FESEM images (Figure 3.3) of the $CuInS_2$ powders synthesized using EG and Gly were composed of $CuInS_2$ nanoparticles with diameters in the range of 20—100 nm. The nanoparticles synthesized using Gly were smaller than those synthesized using EG. This difference could be due to the different solvent viscosities (Table 3.1). The viscosity of Gly is significantly higher than EG; the solubility and diffusion rate of ions in the Gly solution is, therefore, lower. This suppresses crystalline growth, resulting in the smaller size of the synthesized $CuInS_2$ nanoparticles. The optical properties of the $CuInS_2$ powders synthesized using EG and Gly were investigated by UV–Vis diffuse reflectance spectrum (Figure 3.4). The spectrum exhibited light absorption in the visible light region, extending into the near–infrared region. The $CuInS_2$ nanoparticles synthesized using Gly exhibited stronger absorption compared to those synthesized using EG. The $CuInS_2$ nanoparticles with smaller in size have a greater ability to reflect and scatter light. Thus, we obtained different results of light absorption ability.

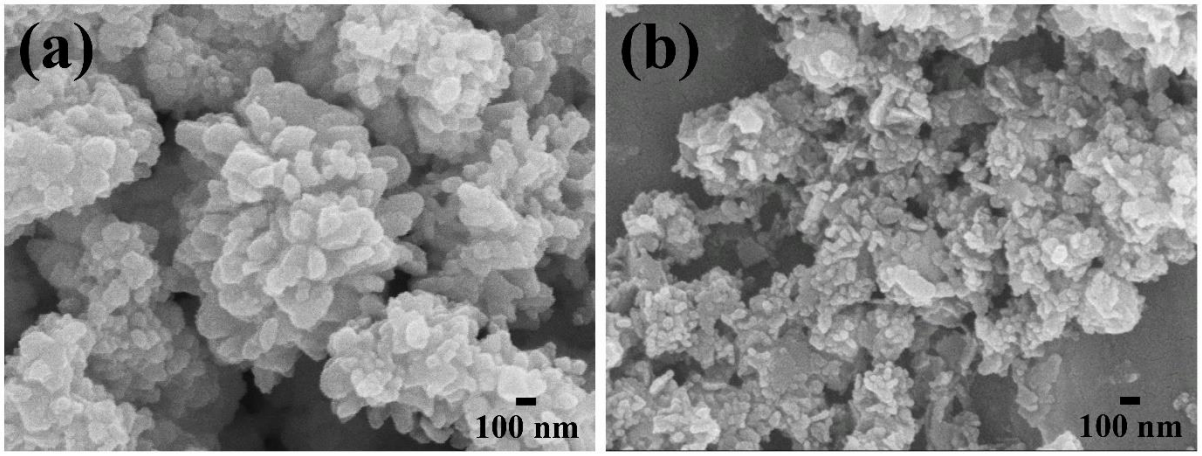

Figure 3.3 FESEM images of the $CuInS_2$ nanoparticles synthesized using *(a)* EG and *(b)* Gly.

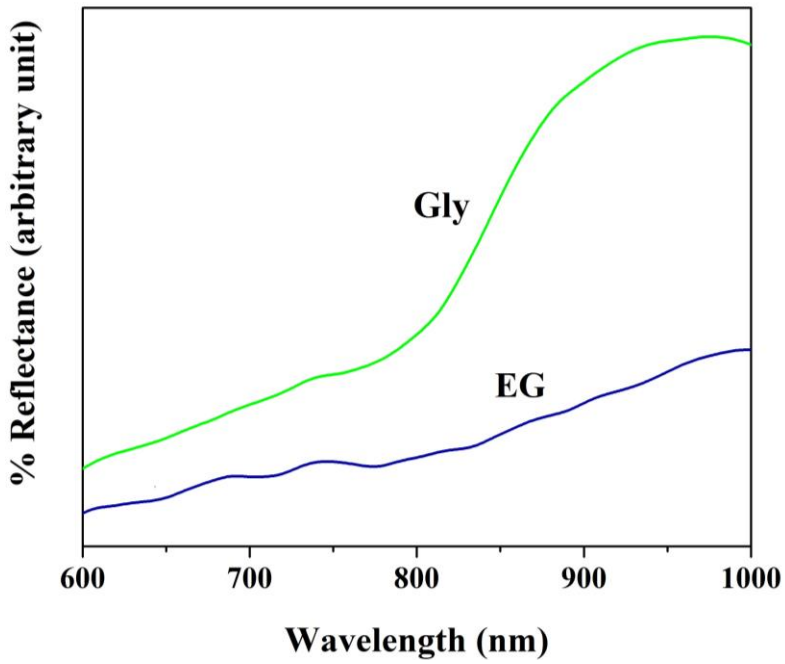

Figure 3.4 UV–Vis diffuse reflectance spectrum of the $CuInS_2$ nanoparticles.

3.2 Effect of sulfur source

In this study, the uniform $CuInS_2$ hollow sub–microspheres were synthesized by a cyclic microwave radiation method without using any templates or surfactants. L–cysteine, an inexpensive, simple, and environmentally friendly thiol–containing amino acid, was chosen as a sulfur source. It has a strong affinity to metal ions, forming metal–ligand complexes that can serve as a precursor for the preparation of inorganic materials [79]. Ethylene glycol was used as a solvent due to its high boiling point and high dipole moment, which was suitable for microwave heating synthesis [80]. In addition, microwave irradiation enhances the reducing power of ethylene glycol. We then investigated the effect of different microwave powers on the purity, particle size, and morphology of the synthesized $CuInS_2$ powders. We also conducted time–dependent experiment to study possible formation mechanisms of the $CuInS_2$ hollow and solid sub–microspheres. Finally, photoconductivities and optical properties of the $CuInS_2$ hollow and solid sub–microspheres were compared and discussed in this research.

3.2.1 Experimental procedure

$CuCl_2 \cdot 2H_2O$ (2 mmol) (BDH Chemicals, Ltd.; 98%), $InCl_3 \cdot 4H_2O$ (2 mmol) (Sigma–Aldrich, Co.; 99.9%), and $C_3H_7NO_2S$ (4 mmol) (Sigma–Aldrich, Co.; 97.0%) were separately dissolved in 10.0 mL of ethylene glycol. The solutions were mixed together at room temperature for 30 min. Subsequently, the mixed solution was irradiated using 2.45 GHz microwave radiation at different microwave powers (180–600 W) for 75 cycles. Each cycle was 30 second on for every 60–second interval. Black powder was collected and washed with deionized water and ethanol, respectively. Finally, the powder was dried overnight at 80 °C for further characterization using different techniques.

Purity, structure, and crystallinity of the powders were characterized by X–ray diffraction spectroscopy (XRD, Rigaku Miniflex II) with CuKα radiation (λ=1.5406 Å). Particle size and morphology of the powders were determined by a transmission electron microscope (TEM, JEOL JEM–2010) operating at 200 kV. UV–Vis diffuse reflectance spectra were recorded by a UV–Vis–NIR spectrophotometer (UV–3101PC, Shimadzu), equipped with an ISR–3100 integrating sphere attachment. Twenty–five mg of each sample was well mixed with 0.5 g of $BaSO_4$ and spread onto the sampling plate prior to the measurement.

Simple photovoltaic devices were fabricated as follows: 0.05 g of $CuInS_2$ powder was dispersed in the mixture of 5 mL of ethanol, 0.05 mL of terpineol, and 0.05 mL of Triton X–100. Then, the $CuInS_2$ slurry was coated on a fluorine doped tin oxide (FTO)–coated glass substrate using a spin coater at 500 rpm for 30 s. The substrate was heated at 250 °C for 30 min to eliminate the remaining organic compounds. Finally, the substrate was coated by radio frequency (RF) sputtering of the Au electrode. Current–voltage curves of the devices were measured by a Keithley 2611A source meter under illumination using a solar simulator (AM1.5, 100 mW/cm^2). Light flux density was calibrated with a second class pyranometer (Hukseflux, LP02).

3.2.2 Physicochemical characterization

The XRD patterns of the powders synthesized using different microwave powers are shown in Figure 3.5. All of the diffraction peaks were well matched to the JCPDS database no. 032-0339, which corresponded to a tetragonal $CuInS_2$ structure. No diffraction peaks from possible impurities, such as CuS, Cu_2S, and In_2S_3, were detected, indicating the purity of the synthesized $CuInS_2$ powders. Using L-cysteine as a sulfur source, a complete formation of $CuInS_2$ was attained at a lower microwave power, and the crystallite size of the $CuInS_2$ nanoparticles was relatively larger than that of our previous study [26], indicating that the difference in sulfur sources affected the purity and the size of the $CuInS_2$ crystals. XRD patterns of the powders, synthesized at 180 W for 75 cycles using different sulfur sources, are shown in Figure 3.6. XRD diffraction angle, FWHM, and the estimated crystallite size of the $CuInS_2$ powders synthesized using different sulfur sources are summarized in Table 3.2. Using L-cysteine, the width of the diffraction peak was relatively narrower, revealing that the crystallite size of the $CuInS_2$ crystals was larger than that of those synthesized using thioacetamide. These results could be explained by the rate of the sulfur released during the synthesis process. During the synthesis process using L-cysteine, a transparent solution was obtained after the reactants were mixed, suggesting that L-cysteine coordinated with the metal ions in the reaction system to form complexes [81,82]. After heating, the complexes decomposed and slowly released S^{2-} to generate $CuInS_2$ nuclei. The slow formation rate of $CuInS_2$ led to the powder with higher purity as well as better growth of the $CuInS_2$ nanocrystals. As a result, pure $CuInS_2$ nanocrystals with larger crystallite size were obtained. The formation mechanism of the $CuInS_2$ prepared using L-cysteine was further discussed with the results from time-dependent experiment.

Upon the use of thioacetamide as a sulfur source, a dark-brown solution formed immediately when the reactants were mixed together. This suggested that thioacetamide was easily hydrolyzed resulting in the rapidly generated H_2S. Then, H_2S molecules reacted directly with Cu^{2+} ions to form CuS particles quickly, which were subsequently reduced to Cu^+ by ethylene glycol. Finally, Cu^+ reacted with In^{3+} and H_2S to form $CuInS_2$ nanoparticles [73]. The CuS could not be completely reduced to Cu^+ at the

given microwave power. Thus, the CuS phase still remained in the $CuInS_2$ sample. In addition, the fast formation rate resulted in a large number of the $CuInS_2$ nanocrystals with relatively small crystallite size mixed with the CuS particles.

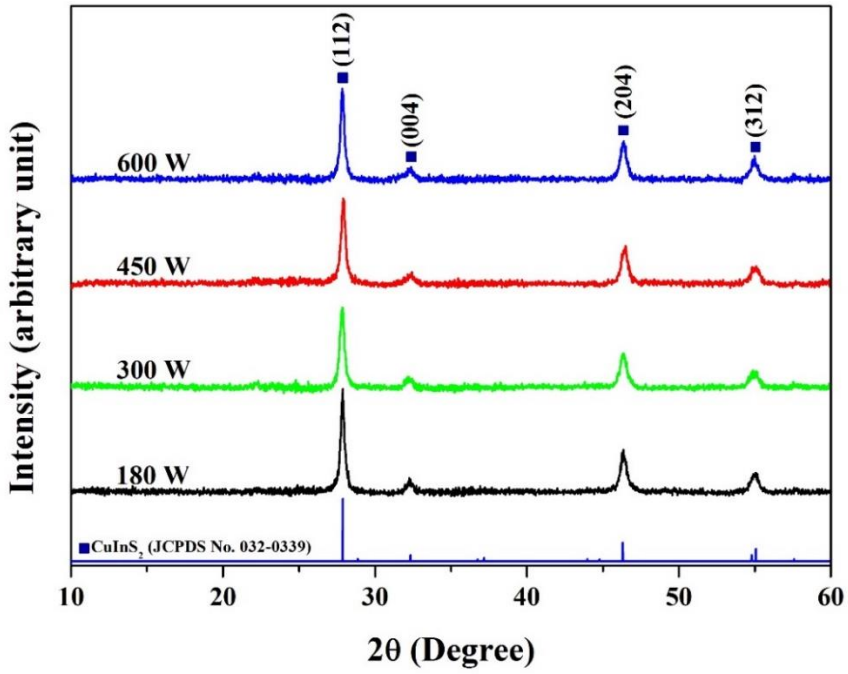

Figure 3.5 XRD pattern of the $CuInS_2$ powders synthesized using different microwave powers.

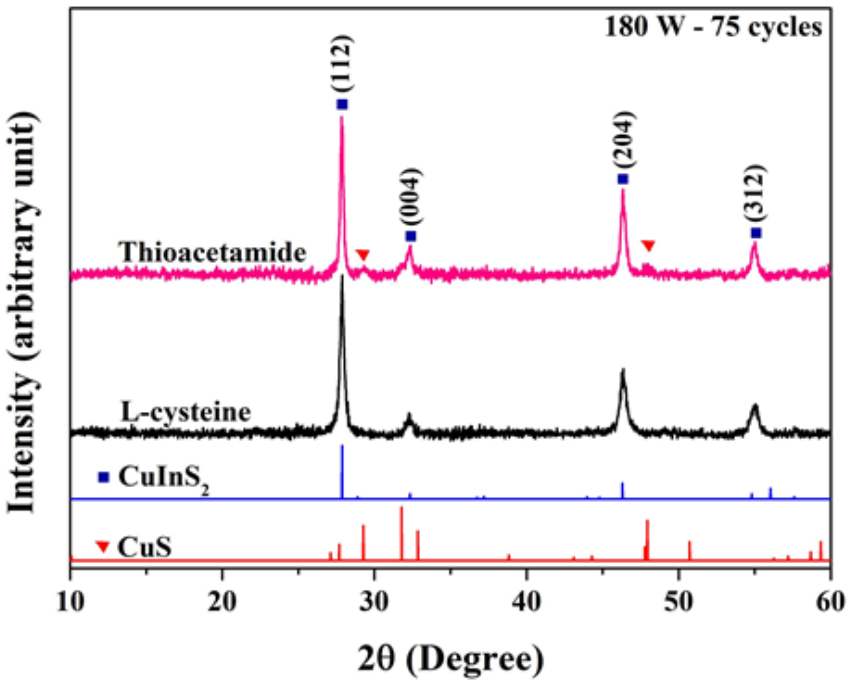

Figure 3.6 XRD pattern of the powders synthesized at 180 W for 75 processing cycles using different sulfur sources.

Table 3.2 XRD diffraction angle, full-width-at-half-maximum (FWHM), and the estimated crystallite size (D) of the $CuInS_2$ powders synthesized using different sulfur sources. The crystallite size was estimated from FWHM of the (112) diffraction peak using the Scherrer equation. Using L-cysteine, the width of the diffraction peak was narrower confirming that the crystallite size of the $CuInS_2$ crystals was larger than those synthesized using thioacetamide.

Sulfur source	2θ, deg	FWHM, deg	*D*(112) / nm
L-cysteine	27.86	0.1771	81
Thioacetamide	27.86	0.2480	58

The TEM images of the $CuInS_2$ powders synthesized using different microwave powers are shown in Figure 3.7. The powder synthesized at 180 W composed of microspheres with a diameter of about 250 nm. The dark center of the sub–microspheres suggested that the $CuInS_2$ powder was solid sub–microspheres (Figure 3.7(a)). Increasing the microwave power to 300 W (Figure 3.7(b)) and 450 W (Figure 3.7(c)) transformed some of the solid sub–microspheres to hollow sub–microspheres with a diameter of about 200 nm and wall thicknesses in the range of 80–100 nm. At 600 W, hollow sub–microspheres with a diameter of about 300 nm and wall thicknesses in the range of 40–60 nm were clearly observed (Figure 3.7(d) and 3.7(e)). All of the hollow sub–microspheres had a uniform morphology. All of the corresponding SAED patterns showed bright $CuInS_2$ concentric rings corresponding to the (112), (004), (204), and (312) diffraction planes. These results confirmed that all of the $CuInS_2$ powders were crystallized with a tetragonal structure in accordance with the above XRD analysis. High resolution TEM (HRTEM) image of the hollow sub–microspheres (Figure 3.7(f)) indicated that the $CuInS_2$ hollow sub–microspheres was an apparent crystalline structure. The crystal lattice fringe of the 0.32 nm planar spaces corresponded well with the (004) plane of tetragonal $CuInS_2$.

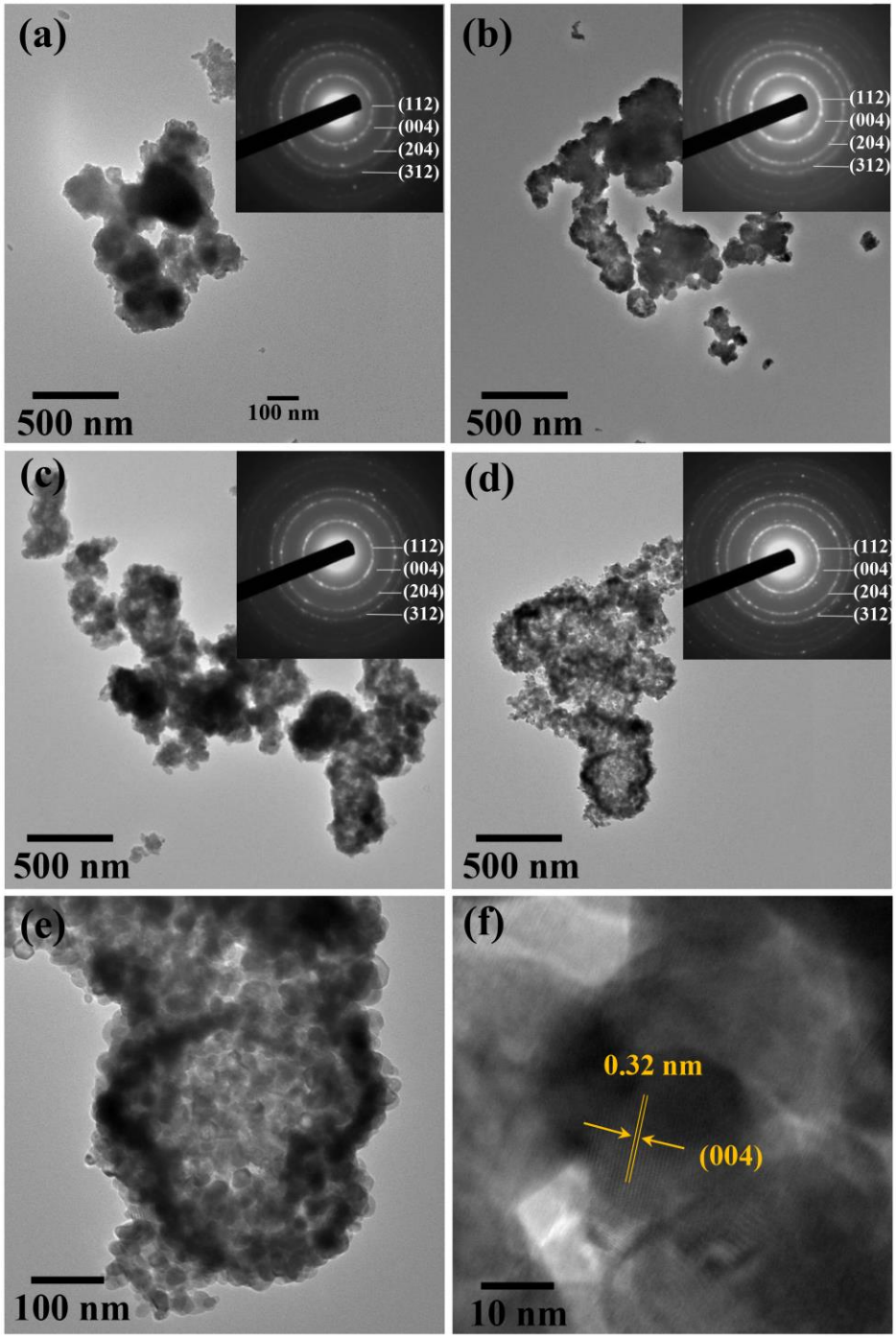

Figure 3.7 TEM images and SAED patterns of the $CuInS_2$ powders synthesized using *(a)* 180 W, *(b)* 300 W, *(c)* 450 W and *(d)* 600 W. *(e)* Higher magnified TEM and *(f)* high resolution TEM images of the $CuInS_2$ powders synthesized using 600 W for 75 processing cycles.

To investigate the formation mechanisms of the $CuInS_2$ solid and hollow sub-microspheres, the powders were synthesized at 180 W and 600 W with different processing cycles. Then, XRD and TEM analyses were performed on these synthesized powders. It should be noted that this time-dependent study was performed by irradiating each of the solutions with different processing cycles. For example, one solution was prepared for 15 cycles and another solution was for 30 cycles. The XRD patterns of the powders synthesized at 180 W with different processing cycles are shown in Figure 3.8(a). All of the XRD spectra showed that the synthesized powders contained a tetragonal $CuInS_2$ phase mixed with a hexagonal CuS phase. The XRD patterns of the powders synthesized at 600 W with different processing cycles are shown in Figure 3.8(b). The XRD spectrum of the powder synthesized at 600 W for 6 cycles can be indexed to a hexagonal CuS structure. At 15, 30, and 60 cycles, the additional diffraction peaks at 2θ of 27.76°, 32.35°, 46.39°, and 54.92° indexed to the (112), (004), (204), and (312) planes of the tetragonal $CuInS_2$ structure, respectively, indicating the existence of the $CuInS_2$ phase. When the irradiation times were lengthened, the diffraction peak intensities of the $CuInS_2$ phase gradually stronger, while those of the CuS phase decreased, demonstrating the increased purity and crystallinity of the $CuInS_2$ powders.

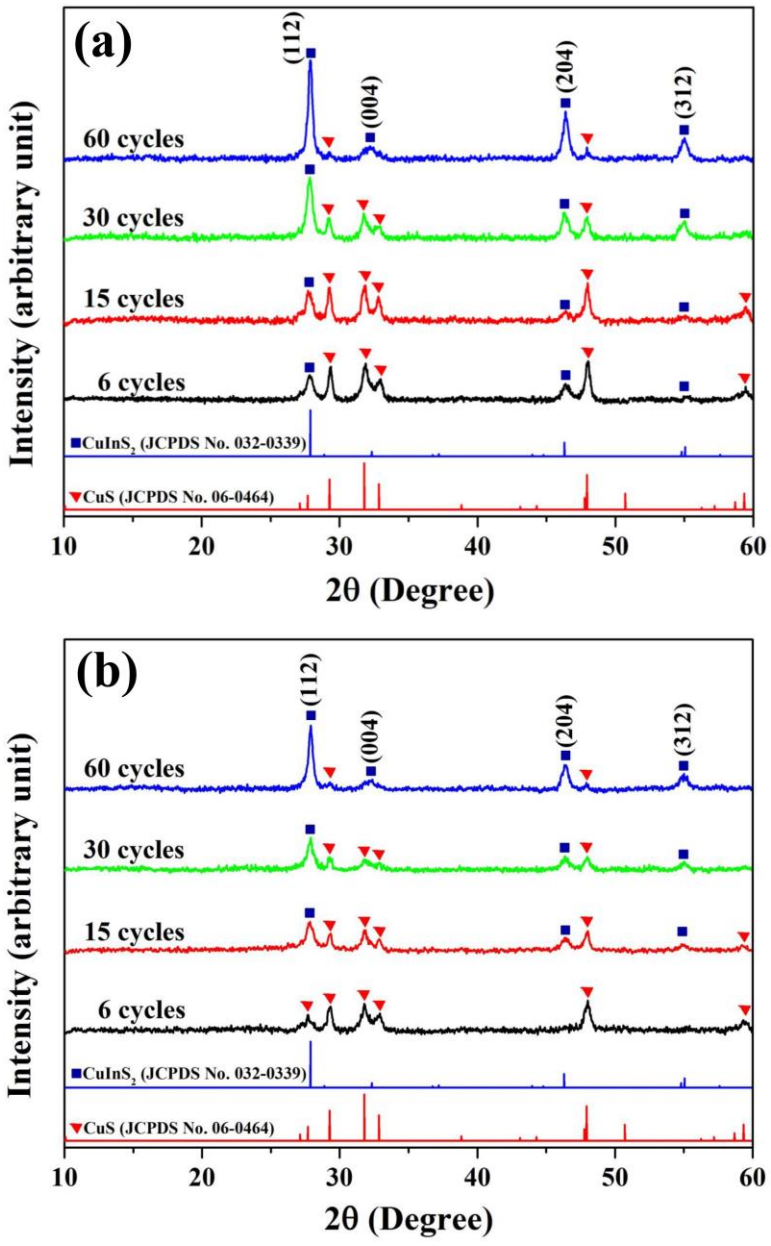

Figure 3.8 XRD patterns of the $CuInS_2$ powders synthesized using *(a)* 180 W and *(b)* 600 W with different processing cycles.

The TEM images and SAED patterns of the powders synthesized at 600 W with different processing cycles are shown in Figure 3.9. At 6 cycles, the powder composed of agglomerated nanoparticles with diameters in the range of 50–100 nm (Figure 3.9(a) and 3.9(e)). The corresponding

SAED pattern (Figure 3.9(i)) showed concentric rings corresponding to the (100), (102), (103), (006), (110), and (116) diffraction planes of the hexagonal CuS structure. When the irradiation times were prolonged to 15 cycles (Figure 3.9(b) and 3.9(f)), and 30 cycles (Figure 3.9(c) and 3.9(g)), the nanoparticles were transformed into microspheres with 200−400 nm diameter composed of several nanoflakes. The corresponding SAED patterns (Figure 3.9(j) and 3.9(k)) showed bright concentric rings of the hexagonal CuS and tetragonal $CuInS_2$ structures, which were consistent with the JCPDS databases. At 60 cycles, the nanoflake–assembled sub–microspheres transformed into sub–microspheres made up of nanoparticles (Figure 3.9(d) and 3.9(h)). The diffraction planes of CuS were still observed in the corresponding SAED pattern (Figure 3.9(l)). Notably, the bright concentric rings of $CuInS_2$ became sharpened when the processing time was increased to 75 cycles, as shown in Figure 3.7(d), implying that the recrystallization process was simultaneously proceeding. TEM images and SAED patterns of the powders synthesized at 180 W with 6 and 30 cycles are shown in Figure 3.10. At 6 cycles, the powder appeared to contain spherical nanoparticles with diameters in a range of 20–30 nm (Figure 3.10(a) and 3.10(c)). The corresponding SAED pattern (Figure 3.10(e)) showed concentric rings of the hexagonal CuS and tetragonal $CuInS_2$ structures. At 30 cycles, the spherical nanoparticles tended to form agglomerates (Figure 3.10(b) and 3.10(d)) with the corresponding SAED pattern (Figure 3.10(f)) showed concentric rings of the hexagonal CuS and tetragonal $CuInS_2$ structures.

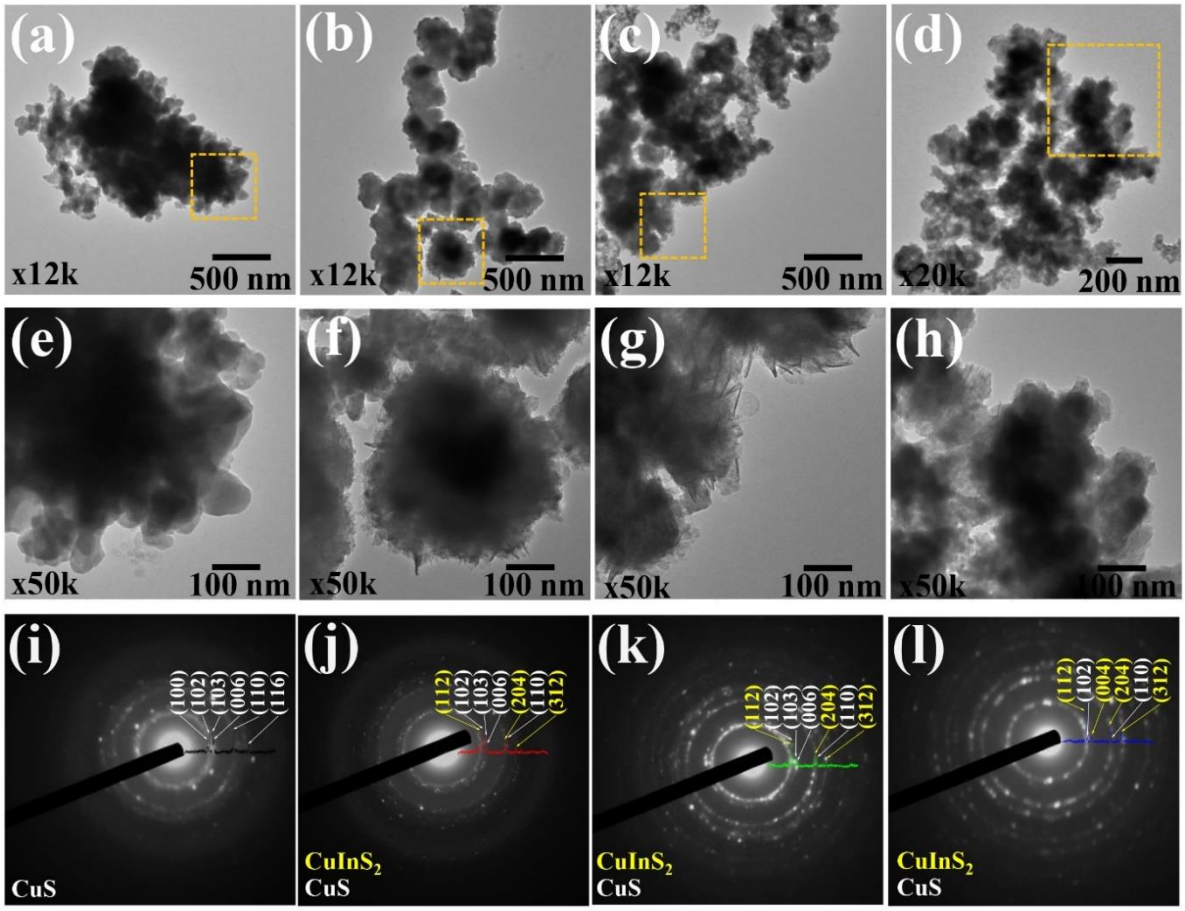

Figure 3.9*(a–d)* TEM images, *(e–h)* high magnification TEM images, and *(i–l)* SAED patterns of the powders synthesized at 600 W for 6, 15, 30, and 60 cycles, respectively.

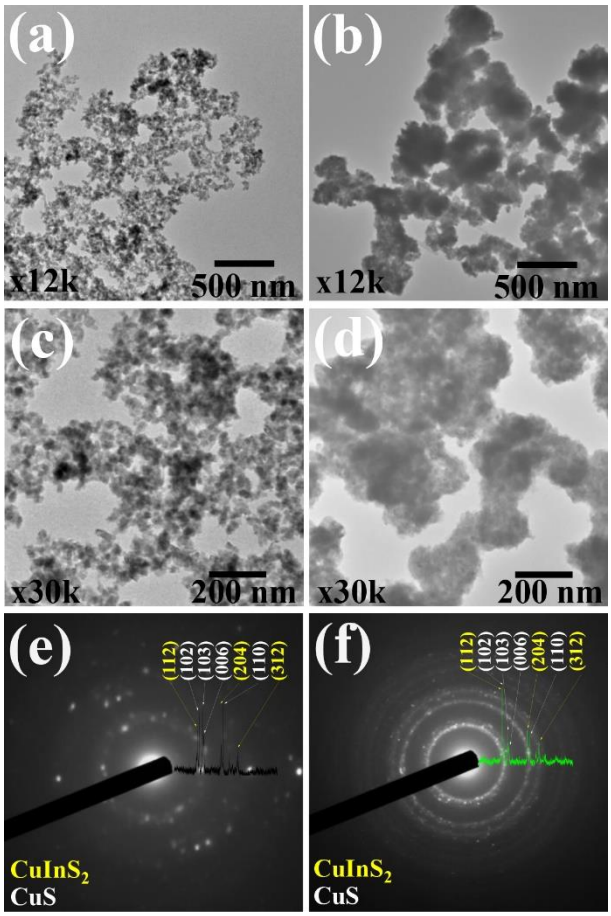

Figure 3.10*(a–b)* TEM images, *(c–d)* high magnification TEM images, and *(e–f)* SAED patterns of the powders synthesized at 180 W for 6 and 30 cycles, respectively.

Based on the time–dependent study, the formation mechanisms of the $CuInS_2$ hollow and solid sub–microspheres were discussed. During the experiment, when $CuCl_2$, $InCl_3$, and L–cysteine were mixed in ethylene glycol, a transparent solution was obtained after the reactants were mixed, suggesting that the Cu^{2+} and In^{3+} ions coordinated with L–cysteine to form Cu(L–cysteine)$_n^{2+}$ and In(L–cysteine)$_n^{3+}$ complexes through thiol chains [81,82], due to the strong nucleophilicity of the thiol group of L–cysteine. Under heating, the coordination bond between the thiol group and Cu^{2+} weakened the S–H bond in the L–cysteine. Then, the C–S bond in the Cu(L–cysteine)$_n^{2+}$ complex was gradually broken. The released S^{2-} combined with Cu^{2+} to form tiny CuS particles. Notably, unstable In_2S_3 was not found

according to the hard soft acid base (HSAB) concept; which has been used in chemistry to predict the stability of various compounds. Using 600 W of the microwave power, the reaction rate rose rapidly during the microwave heating process. As a result, the CuS nanoparticles quickly aggregated together to form CuS sub–microspheres to minimize their surface energy and the total energy of the system. This led to the formation of poorly crystallized CuS nanoparticles that were comprised of a primary core of CuS sub–microspheres. Then, well–crystallized CuS nanoflakes formed on the surface of the primary CuS sub–microspheres due to the intrinsic anisotropic characteristics of the hexagonal CuS structure [83,84]. When the number of processing cycles increased, the reaction temperature increased and the CuS nanoflakes coated on the surface of the primary CuS sub–microspheres were then reduced to Cu_2S by ethylene glycol. The produced Cu_2S subsequently reacted with In^{3+} and S^{2-} ions in the solution to form $CuInS_2$ nanoparticles covering the surface of the primary CuS sub–microspheres. Simultaneously, the primary CuS core dissolved, producing a cavity inside the sub–microspheres. The dissolved CuS was also reduced to Cu_2S by ethylene glycol, and then reacted with In^{3+} and S^{2-} to form $CuInS_2$ nuclei. Finally, the secondary $CuInS_2$ nuclei crystallized and grew on the external surface of the sub–microspheres, consistent with the previous study [71]. Using a lower microwave power of 180 W, the reaction proceeded more slowly. Consequently, formation of the $CuInS_2$ nanoparticles was slower than that of the reaction at 600 W of microwave power. The $CuInS_2$ nanoparticles were gradually agglomerated to reduce their surface energy. When the reaction temperature was increased by extending the irradiation time, the agglomerated nanoparticles became more compact to form the solid sub–microspheres.

3.2.3 Solar cell evaluation

In order to investigate the potential use of the synthesized $CuInS_2$ powders as an active layer in solar cell applications, the photoconductivity of the $CuInS_2$ photoelectrode was studied. Current–voltage (I–V) curves of the $CuInS_2$ thin films were measured under illumination using a solar simulator (AM1.5, 100 mW/cm^2). Figure 3.11 shows the current–voltage curves of the fabricated devices operated in the dark (black line) and under illumination (red line). The current linearly increased with the applied voltage, implying the ohmic nature of the contacts. At all bias voltages, the conductivity of the device under illumination was higher than that under dark condition because electrons in valence band of $CuInS_2$ were excited to conduction band under illumination [85]. The current difference between the dark and illuminated (ΔI) conditions of the $CuInS_2$ films at a given bias voltage were measured to determine their photoconductivities. At a bias voltage of 0.4 V, the photoconductivities of the devices fabricated using the $CuInS_2$ powders synthesized at 180, 300, 450, and 600 W were 0.37, 0.63, 1.10, and 1.98 mA, respectively. The device fabricated using the $CuInS_2$ hollow sub–microspheres exhibited the improved photoconductivity with lower resistance, suggesting that the $CuInS_2$ hollow sub–microspheres were favorable to increase current carrier concentration and to improve electron transport [85–88].

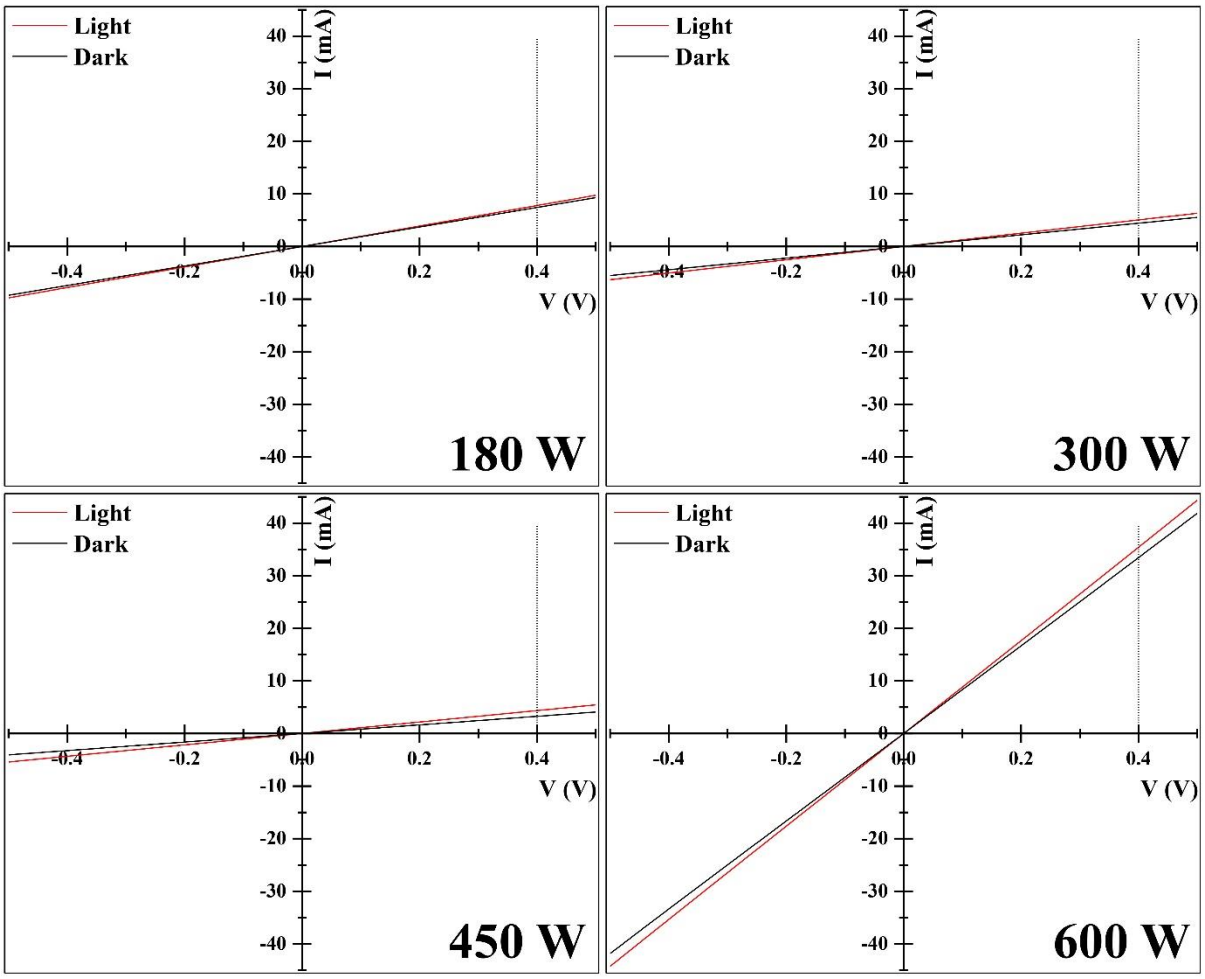

Figure 3.11 Current–voltage curves of the $CuInS_2$ powders synthesized at different microwave powers operated in the dark *(*black line*)* and under illumination *(*red line*).*

To confirm the enhancement of photoconductivity of the $CuInS_2$ hollow sub–microspheres, optical properties of the $CuInS_2$ powders synthesized at 180 W and 600 W of microwave powers were investigated by analyzing UV–Vis diffuse reflectance spectra (Figure 3.12). The reflectance spectra were converted into an absorption coefficient *F(R),* according to the Kubelka–Munk equation: $F(R) = (1-R)^2/2R$, where R is the proportion of light reflected. The Kubelka–Munk (K–M) absorption spectra (Figure 3.12(a)) exhibited light absorption in the region of visible light, extending into the near–infrared region. Among the most basic requirements for a high performance in solar cell, it can be seen that the $CuInS_2$ powder

synthesized at 600 W showed a stronger absorption intensity [86]. This feature might be caused by the unique $CuInS_2$ hollow structure, which enhanced the ability of the light reflecting and scattering in their structure. This promotes current carrier concentration and electron transport and, hence, leads to the improved photoconductivity [85,86]. In addition, the apparent crystalline structure, as revealed by the HRTEM (Figure 3.7(f)) analysis, improved the conversion efficiency, resulting in the enhancement of photoconductivity [87]. The band gap energy of the $CuInS_2$ powders were estimated by a plot of $(F(R).h\nu)^2$ versus $h\nu$, and by extrapolating the linear portion of the curve to intersect the $h\nu$ axis (Figure 3.12(b)). The estimated band gap energy was 1.48 eV, which was close to the values observed in other studies [70,71]. Together, these results indicated that the $CuInS_2$ hollow microspheres could become highly useful in solar–light driven applications.

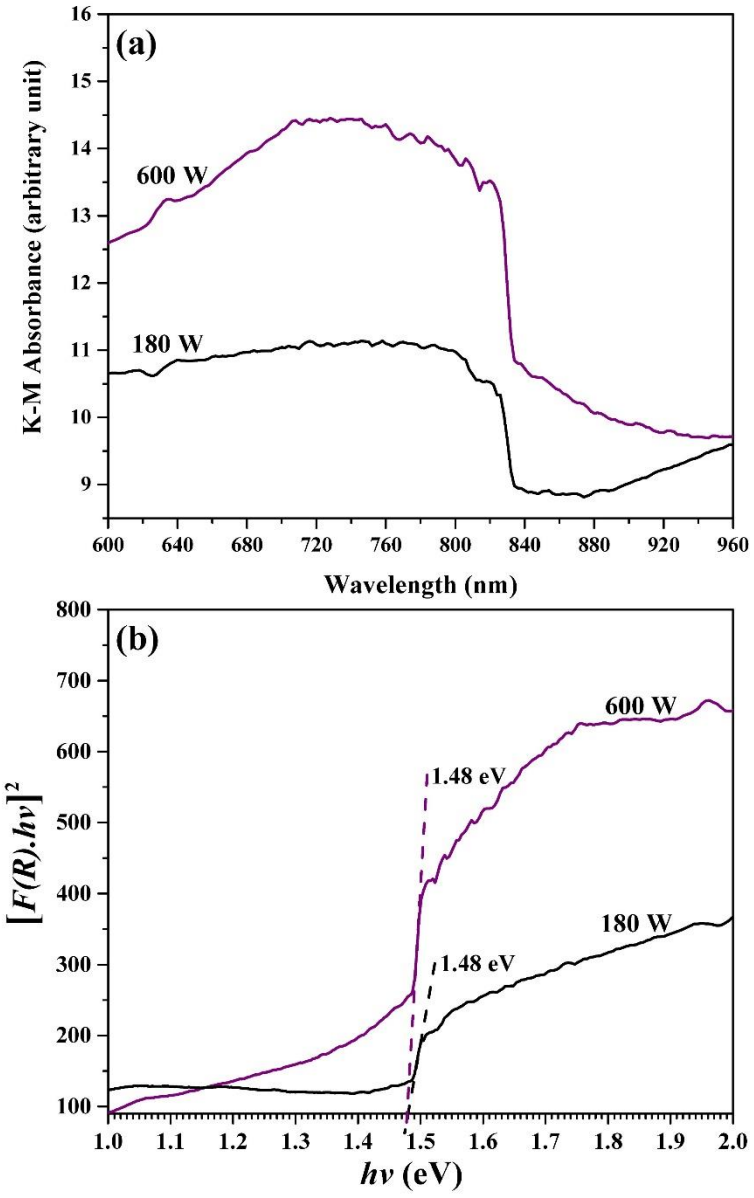

Figure 3.12*(a)* UV–Vis diffuse reflectance spectra of the $CuInS_2$ powders synthesized using different microwave powers. *(b)* Plot of $(F(R)h\nu)^2$ versus $h\nu$ for estimating the band gap energy.

Chapter 4 Synthesis, Characterization and Photocatalytic activity of $BiVO_4$

We have synthesized $BiVO_4$ photocatalysts with monoclinic and tetragonal (t–$BiVO_4$ and m–$BiVO_4$) structures using a cyclic microwave irradiation method at low microwave heating power. The photocatalytic activities of monoclinic and tetragonal of $BiVO_4$ were compared on the decomposition of 10 ppm methylene blue (MB) under visible light irradiation.

4.1 Experimental procedure

$Bi(NO_3)_3 \cdot 5H_2O$ (6.25 mmol) and NH_4VO_3 (6.25 mmol) were separately dissolved in 25.0 mL of ethylene glycol. The solutions were mixed together for 30 min. Then, the mixed solution was irradiated using 2.45 GHz microwave radiation operated at 300 W for 75 cycles. Each cycle was 30 s on for every 90–s interval. After that, the obtained powder was filtered, washed with deionized water, and dried in oven at 70 °C for 24 h. Finally, the as–prepared powder was calcined at 600 °C for 6 h.

Photocatalytic degradation experiment: The catalyst (100 mg) was dispersed in aqueous solution of methylene blue (200 mL, 10 mgL^{-1}). Before irradiation, the suspension was magnetically stirred in dark for 30 min to establish the adsorption/desorption equilibrium on the surface of catalyst. Then, the suspension was irradiated under the 50 W of LED lamp for 360 mins. At every 30 min of irradiation, a 5 mL of suspension was taken from the reaction solution and determined by a UV–Vis spectrophotometer at 664 nm. Methylene blue photolysis (without catalyst) was also performed under the same experimental conditions. The decolorization efficiency (% DE) was calculated using the following equation;

$$\%\ \mathrm{DE} = \frac{C_0 - C}{C_0}\ x\ 100$$

where C_0 and C are the concentrations of methylene blue before and after the light irradiation, respectively.

4.2 Physicochemical characterization

The XRD patterns of t–$BiVO_4$ and m–$BiVO_4$ powders shown in Figure 4.1 and 4.2, respectively, revealed that the crystal structures of $BiVO_4$ particles were tetragonal (Figure 4.1) and monoclinic phase (Figure 4.2). The diffraction peaks of t–$BiVO_4$ powders was corresponded to JCPDS No. 014–0133. In XRD pattern of m–$BiVO_4$ without calcination, no diffraction peak can be observed, indicating that m–$BiVO_4$ has not yet formed. After calcination at 600 °C, pure m–$BiVO_4$ was obtained which corresponds to JCPDs No. 014–0688. The sharp and narrow diffraction signals of t–$BiVO_4$ and m–$BiVO_4$ after calcination indicated high crystallinity. These results suggesting that the synthetic method developed in this study provided a simple, and rapid process for producing highly crystalline $BiVO_4$.

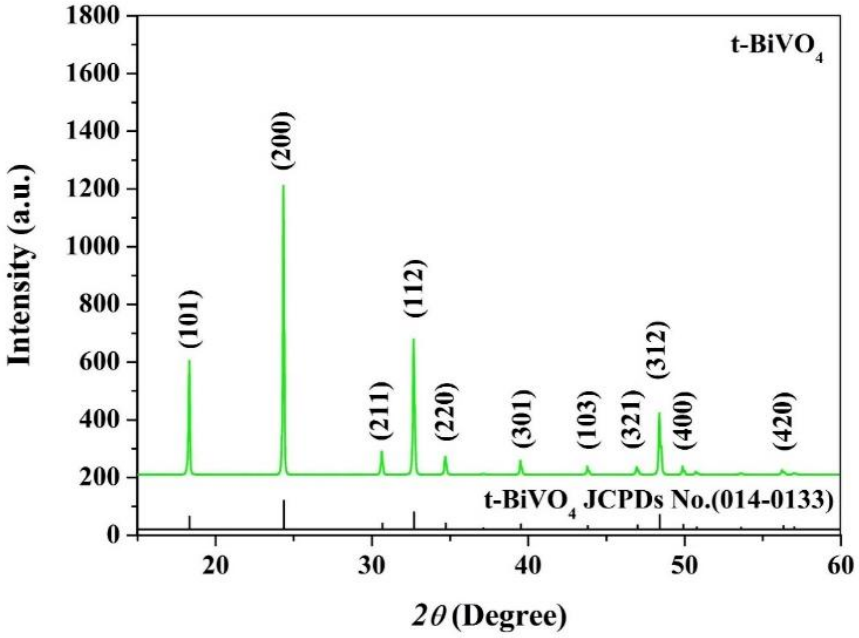

Figure 4.1 XRD patterns of t–$BiVO_4$ powders.

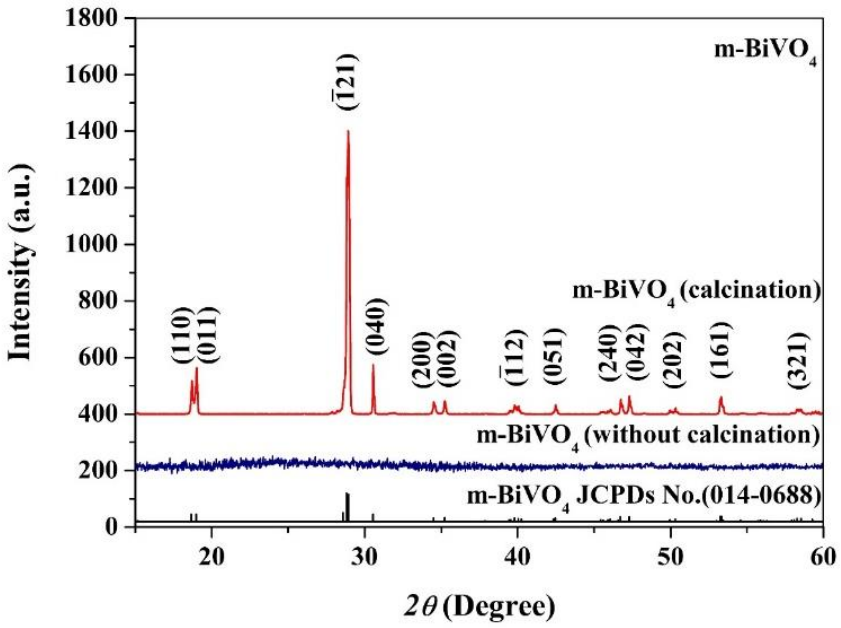

Figure 4.2 XRD patterns of m–$BiVO_4$ powders with calcination and without calcination.

The FTIR spectrum of m–$BiVO_4$ powders with calcination and without calcination shown in Figure 4.3. The FTIR spectrum of m–$BiVO_4$ without calcination showed that O–H stretching, O–H bending C–H bending and V–O stretching signals was detected at 3456, 1622,1384 and 810 cm^{-1}, respectively. In addition, no peak shift or splitting was observed in FTIR spectrum of m–$BiVO_4$ without calcination, confirming that no Bi–EG complex was formed, suggesting that the EG molecules were physically adsorbed on the particle's surface as neutral species. The adsorbed EG molecules may be resulted in the amorphous–liked XRD pattern of the m–$BiVO_4$ without calcination. After calcination, the absorption peaks of O–H stretching, O–H bending, and C–H bending were disappeared suggesting that the EG was removed from the m–$BiVO_4$ powder.

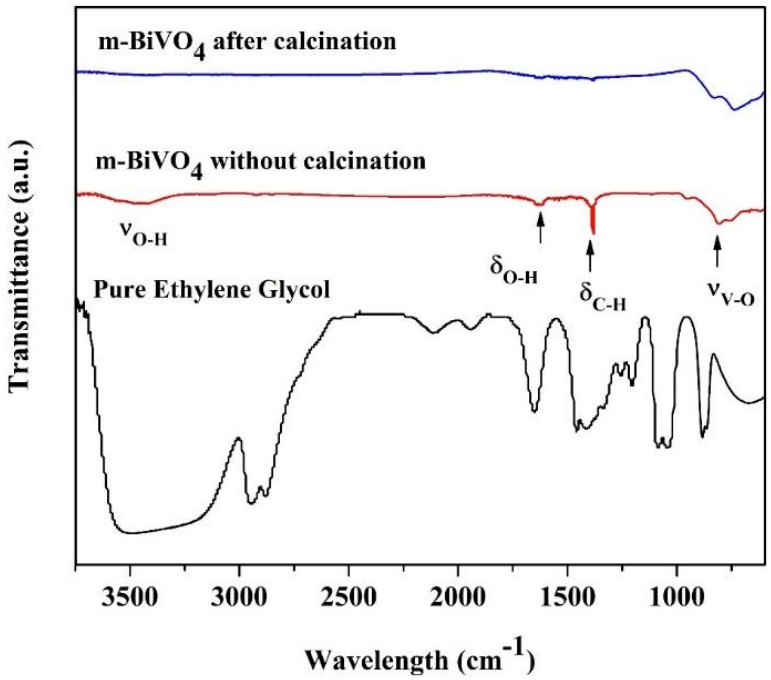

Figure 4.3 FTIR spectrum of m–$BiVO_4$ powders with calcination and without calcination.

The FESEM images of the t–$BiVO_4$ and m–$BiVO_4$ powders are shown in Figure 4.4(a) and 4.4(b), respectively. In Figure 4.4(a), the SEM image reveals that the t–$BiVO_4$ microsphere was composed of irregular particles (about 240 nm). The obtained microspheres had an averaged diameter of 4 μm with the rough surfaces. In contrast, the morphology of m–$BiVO_4$ powders was aggregated spherical with a particle size of about 760 nm as shown in Figure 4.4(b). This aggregated morphology was caused by the calcination process. The TEM image and HRTEM of t–$BiVO_4$ powders are show in Figure 4.4(c) and 4.4(d). The t–$BiVO_4$ powders are composed of cluster size of 4 μm, which corresponded to the FESEM images of the t–$BiVO_4$ (Figure 4.4(a)). The HRTEM in Figure 4.4(d) shows crystal lattice fringes of 0.24 nm which corresponds to the (202) plane of t–$BiVO_4$. On the other hand, the TEM image and HRTEM of m–$BiVO_4$ powders are show in Figure 4.4(e) and 4.4(f). The HRTEM in Figure 4.4(f) shows crystal lattice fringes of 0.58 nm which corresponds to the (020) plane of m–$BiVO_4$.

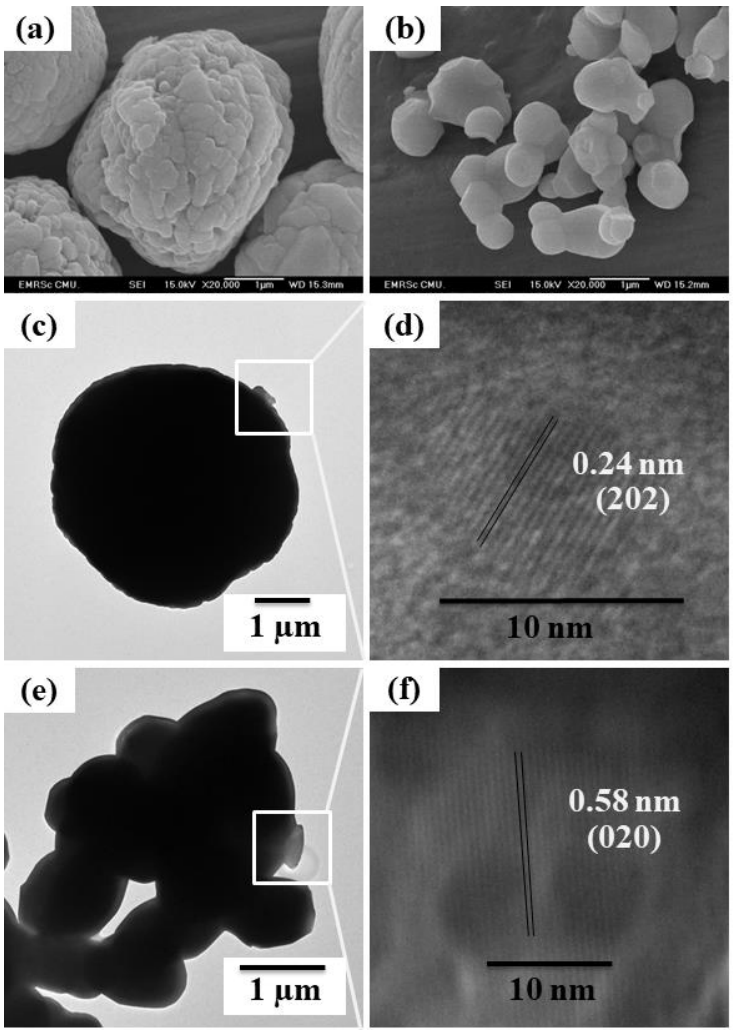

Figure 4.4 *(*a, b*)* FESEM, *(*c, e*)* TEM, and *(*d, f*)* HRTEM images of the t–$BiVO_4$ and m–$BiVO_4$ powders, respectively

Figure 4.5 showed Tauc plot of t–$BiVO_4$ and m–$BiVO_4$ powders. The band gap energy of them can be calculated form Kubelka–munk function and Tauc plot. The data were plotted as the function $F(R) = (1 - R_\infty)^2/(2R_\infty)$ [89], where R is diffuse reflectance. The absorption edge and the photon energy are related by the equation $(\alpha hv)^n = A(hv - E_g)$, where h is Planck's constant, ν is frequency, α is absorption coefficient, E_g is band gap size, A is proportioanality constant and n is nature of transition: 2 for direct allowed and 1/2 for indirect allowed. The band gap sizes can be extracted via

Tauc plots of $(\alpha hv)^n$ versus hv. However, α is proportional to $F(R)$. The band gap energy of t–$BiVO_4$ and m–$BiVO_4$ powders are direct band gap [90], n is 2. The Tauc equation can be plotted of $[F(R)hv]^2$ versus hv The band gap energy can be obtained from the X–axis intersection. The band gap energy of t–$BiVO_4$ and m–$BiVO_4$ powders were measured as 2.33 and 2.12 eV, respectively. In addition, the different structures of t–$BiVO_4$ and m–$BiVO_4$ could affect to their band gap energy.

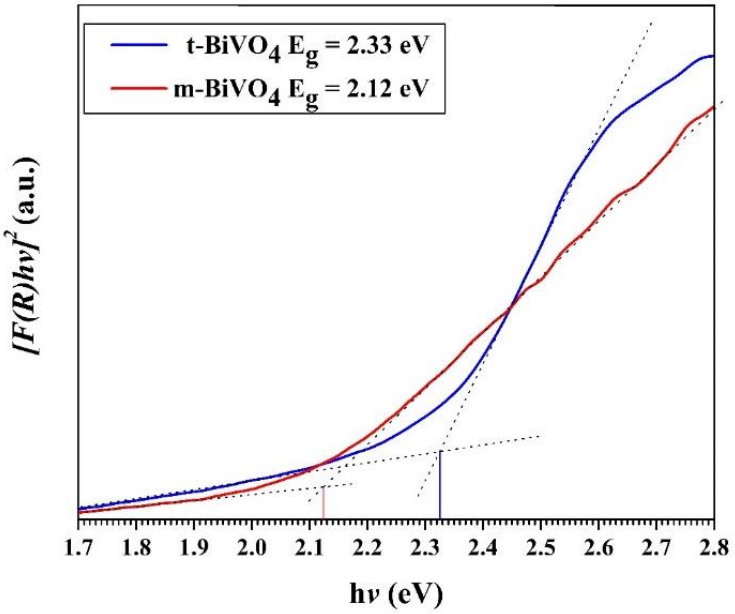

Figure 4.5 Tauc plot of the t–$BiVO_4$ and m–$BiVO_4$ powders with the calculated band gap energies.

4.3 Photocatalytic activity tests

The photocatalytic activity of the t–$BiVO_4$ and m–$BiVO_4$ was evaluated by the photodegradation of methylene blue in aqueous solution under visible light irradiation. The visible light was generated by 50W LED lamp within 360 min. Figure 4.6 shows %decolorization versus visible light irradiation time of the t–$BiVO_4$ and m–$BiVO_4$ for the degradation of methylene blue in aqueous solution. In absence of any photocatalyst (blank experiment), the concentration of MB remains unchanged indicating the stability of methylene blue under visible light and the photolysis could be ignored. In the presence of t–$BiVO_4$, only 42.9% of methylene blue was degraded after irradiation for 360 min, while the m–$BiVO_4$ exhibited a higher photocatalytic dye degradation with %decolorization of 60.57% after the same irradiation time.

The pseudo–first order rate constant (k) of the t–$BiVO_4$ and m–$BiVO_4$ were calculated to be 1.7 x 10^{-3} min^{-1} and 2.5 x 10^{-3} min^{-1}, respectively. The m–$BiVO_4$ exhibited 1.47 times higher calculated pseudo–first order rate constant (k) than t–$BiVO_4$. The higher photocatalytic activity of m–$BiVO_4$ could be ascribed to two reasons, optical band gap and particle size. The UV–Vis DRS results (Figure 4.5) show that the t–$BiVO_4$ had a wider band gap energy than m–$BiVO_4$. The narrower band gap of the m–$BiVO_4$ could lower the energy required for the electron–hole transition between the valence and conduction band. In addition, other factors such as highly crystalline structures and high specific surface area of the photocatalysts could also attribute to its high photocatalytic activity. In addition, SEM images (Figure 4.4(a–b)) show that the particle size of m–$BiVO_4$ was smaller than t–$BiVO_4$, consequently, the active surface area of m–$BiVO_4$ was larger than t–$BiVO_4$.

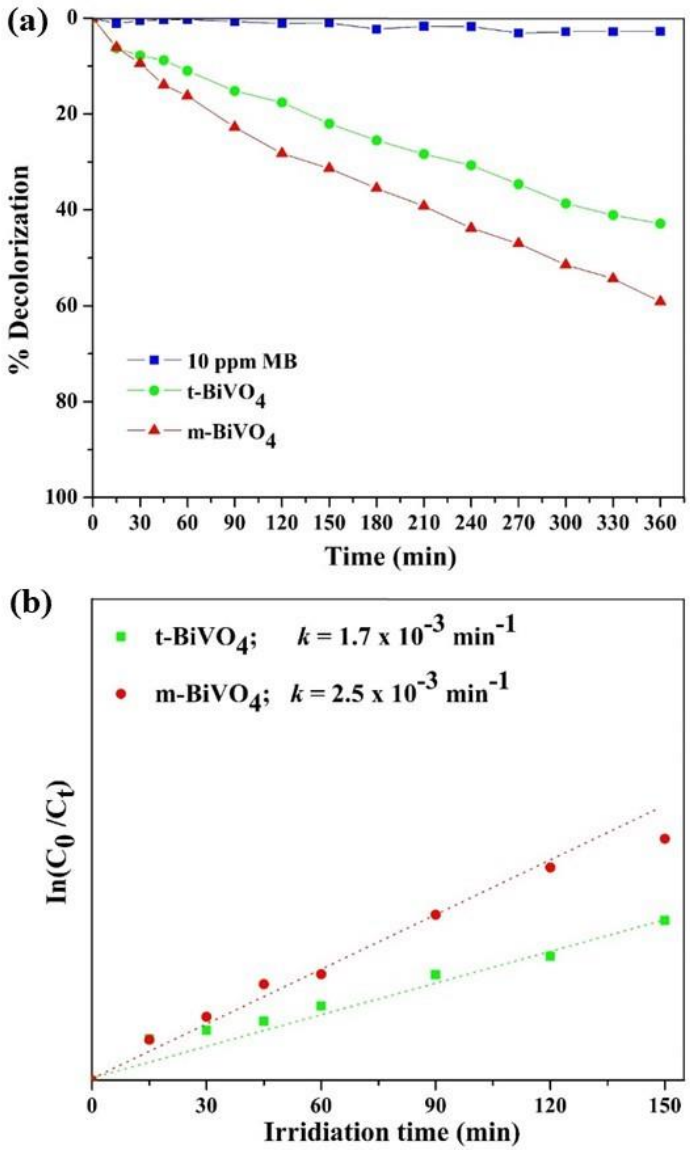

Figure 4.6 (a) Photocatalytic activities of t–$BiVO_4$ and m–$BiVO_4$ for the degradation of 10 ppm methylene solution blue under visible light and (b) the calculated pseudo–first order kinetic rate plotted as a function of $\ln(C_0/C)$ vs. time.

Chapter 5 Synthesis, Characterization and Photocatalytic activity of $CuInS_2$/m–$BiVO_4$

We fabricated $CuInS_2$/m–$BiVO_4$ composites with different mass ratios ($CuInS_2$ to m–$BiVO_4$ = 1:3, 1:1, and 3:1) by a cyclic microwave radiation, followed by a thermal treatment process. Photocatalytic activity of the photocatalysts was evaluated by degrading methylene blue, methyl orange, and rhodamine B (model of organic pollutants) under visible light irradiation. In addition, a potential use of the $CuInS_2$/m–$BiVO_4$ as a photoelectrode in PEC cell was investigated. A possible photocatalytic mechanism of the $CuInS_2$/m–$BiVO_4$ composite for the photodegradation of dye was also proposed.

5.1 Experimental procedure

$CuCl_2 \cdot 2H_2O$ (2 mmol), $InCl_3 \cdot 4H_2O$ (2 mmol), and thioacetamide (4 mmol) were separately dissolved in 10.0 mL of deionized water and mixed together for 30 min. Then, the mixed solution was irradiated using 2.45 GHz microwave radiation operated at 600 W for 75 cycles. Each cycle was 30 s on for every 90–s interval. After that, the obtained powder was filtered, washed with deionized water, and dried in oven at 70 °C for 24 h.

$Bi(NO_3)_3 \cdot 5H_2O$ (6.25 mmol) and NH_4VO_3 (6.25 mmol) were separately dissolved in 25.0 mL of ethylene glycol and mixed together for 30 min. Then, the experimental procedure was similar to that of $CuCl_2 \cdot 2H_2O$, except that the microwave power was operated at 300 W for 75 cycles and the as–prepared powder was calcined at 600 °C for 6 h.

Synthesis of $CuInS_2$/m–$BiVO_4$ composite: $CuInS_2$/m–$BiVO_4$ composites with different mass ratios ($CuInS_2$ to m–$BiVO_4$ = 1:3, 1:1, and 3:1) were prepared by thermal treatment process [26,27]. The m–$BiVO_4$ powder was first dispersed in 10.00 mL of chloroform. Then, the required amount of the $CuInS_2$ powder was mixed with the m–$BiVO_4$ suspension and stirred at room temperature until the solvent was completely volatilized. Finally, the $CuInS_2$/m–$BiVO_4$ composite was dried at 70 °C for 24 h, and subsequently heated at 200 °C for 15 min.

Purity, structure, and crystallinity of the samples were characterized by X-ray diffraction spectroscopy (XRD, Rigaku Miniflex II) with a CuK_{α} radiation (λ=1.5406 Å). Morphology and particle size of the samples were examined by a field emission scanning electron microscopy (FESEM, JEOL JSM-6335F) with energy dispersive X-ray spectrometry (EDX), and transmission electron microscopy (TEM, JEOL JEM-2010). Optical properties were also studied by UV-vis diffuse reflectance spectroscopy (UV-vis DRS, UV-1800 Shimadzu), equipped with a specular reflectance attachment. Photoluminescence spectra were examined by a photoluminescence spectrometer (PL, Avantes AvaSpec-2048TEC-USB2) with an excitation wavelength of 345 nm. Zeta potential of the composite was also performed on Zetasizer (Malvern Nano ZS).

The photocatalyst (100 mg) was dispersed in an aqueous solution of dye (methylene blue, MB or rhodamine B, RhB or methyl orange, MO; 200 mL of 10 mgL^{-1}). Before irradiation, the suspension was magnetically stirred in dark for 30 min to establish the adsorption/desorption equilibrium on the surface of the photocatalyst. Then, the suspension was irradiated with a visible light for 360 min using a 50 W light-emitting-diode (LED) lamp as a visible light source. At irradiation intervals, 5 mL of the suspension was sampled from the reaction and determined by a UV-vis spectrophotometer at 664 nm, 554 nm, and 464 nm for MB, RhB, and MO, respectively. The decolorization efficiency (%DE) was calculated using the following equation;

$$\% \text{ DE} = \frac{C_0 - C}{C_0} \times 100$$

where C_0 and C are the concentrations of the dye when an adsorption/desorption equilibrium was achieved and after the light irradiation, respectively.

PEC properties of the $CuInS_2$/m-$BiVO_4$ composite with mass ratio of 1:3 in comparison with pure m-$BiVO_4$ were investigated by linear sweep voltammetry (LSV). The PEC measurement was conducted on an electrochemical analyzer (Autolab, μAUTOLABIII), equipped with a conventional three-electrode system, which sample film as a working electrode, Pt sheet as a counter electrode, and Ag/AgCl (3.0 M KCl) as a reference electrode. 0.5 M Na_2SO_4 (pH ~ 6.0) was used as an electrolyte solution. Film

working electrode was prepared by a doctor's blading method as follows: 50.0 mg of photocatalyst was dispersed in a mixture of 5 mL of ethanol, 0.05 mL of terpineol, and 0.05 mL of Triton X–100. Then, the slurry was coated on a fluorine–doped tin oxide (FTO)–coated glass substrate with a fixed area of 1 x 1 cm^2. After that, the coated substrate was heated at 250 °C for 45 min to eliminate remaining organic compounds. The 50 W of LED lamp was used as a light source. The LSV was measured at a potential scan rate of 50 mVs^{-1} and the applied voltage potential was varied from –0.4 to 1.4 V under the dark and light irradiation. Potentials were reported versus Ag/AgCl and reversible hydrogen electrode (RHE). The Ag/AgCl scale was converted to the RHE scale via the Nernst relation; V_{RHE} (volt) = $V_{Ag/AgCl}$ + (0.0591 x pH) + 0.210 V, where V_{RHE} is the converted potential vs. RHE, $V_{Ag/AgCl}$ is the measured potential vs. the Ag/AgCl reference electrode.

5.2 Physicochemical characterization

XRD patterns of the m–$BiVO_4$, $CuInS_2$, and $CuInS_2$/m–$BiVO_4$ powders are shown in Figure 5.1. For m–$BiVO_4$, the diffraction peaks matched to the JCPDS No. 014–0688, which were well indexed as a monoclinic $BiVO_4$ structure. For $CuInS_2$, the diffraction peaks were found to match with the JCPDS No. 032–0339, which corresponded to a tetragonal $CuInS_2$ structure. No additional diffraction peaks from any other impurities were observed in the XRD patterns of the m–$BiVO_4$ and $CuInS_2$, suggesting a high purity of the synthesized powders. Strong and narrow diffraction peaks of the m–$BiVO_4$ were found, indicating high crystallinity and large crystallite size. The XRD pattern of the $CuInS_2$/m–$BiVO_4$ composites with different mass ratios showed the characteristic diffraction peaks from both m–$BiVO_4$ and $CuInS_2$ crystals. The diffraction peaks positions of the m–$BiVO_4$ did not shift, implying that the $CuInS_2$ was merely deposited on the surface of the m–$BiVO_4$ instead of merging into the crystal lattice.

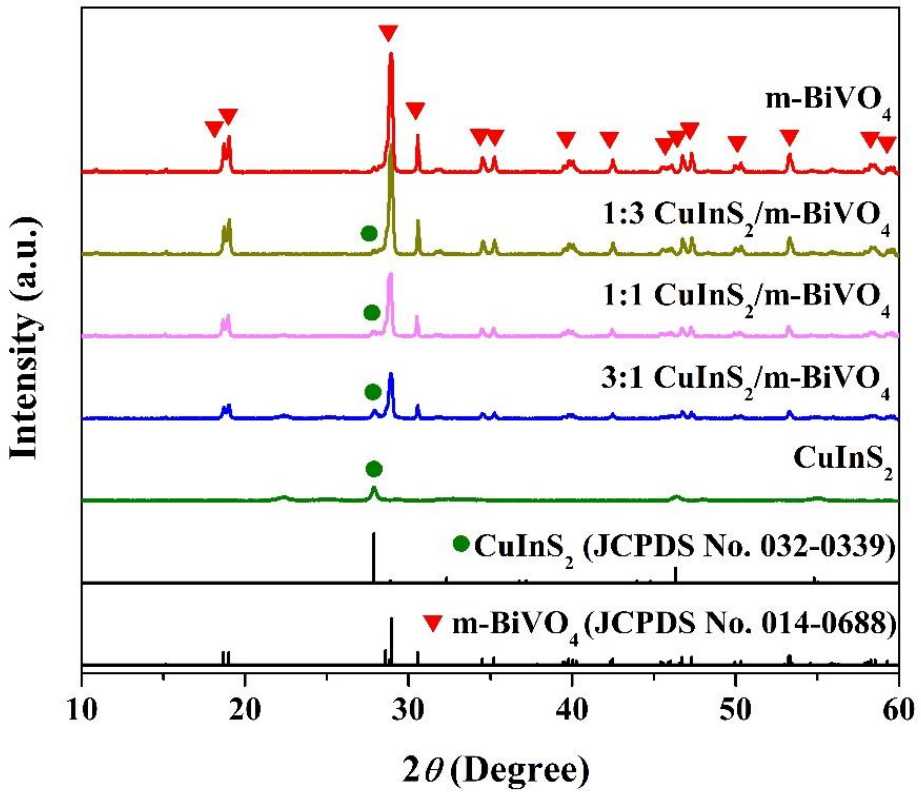

Figure 5.1 XRD patterns of the $CuInS_2$, m–$BiVO_4$, and $CuInS_2$/m–$BiVO_4$ powders.

TEM and high resolution TEM (HRTEM) images of the m–$BiVO_4$ and the $CuInS_2$ powders are shown in Figure 5.2(a)–(d). The m–$BiVO_4$ powder (Figure 5.2(a)) composed of aggregated spherical particles with diameter of about 1.1 μm. The aggregation of the m–$BiVO_4$ could be caused by the calcination process. The corresponding HRTEM image (Figure 5.2(c)) showed the crystal lattice fringe of 0.583 nm planar space which corresponded with the (020) plane of monoclinic $BiVO_4$. The $CuInS_2$ powder (Figure 5.2(b)) composed of spherical nanoparticles with diameter in the range of 10–20 nm. The corresponding HRTEM image (Figure 5.2(d)) showed the crystal lattice fringe of 0.165 nm which corresponded with the (116) plane of tetragonal $CuInS_2$. The HRTEM images (Figure 5.2(c) and 5.2(d)) indicated that the m–$BiVO_4$ and $CuInS_2$ particles had good crystallinity. The TEM images of the $CuInS_2$/m–$BiVO_4$ composites with different mass ratios (Figure 5.2(f)–(h)) clearly showed that the $CuInS_2$

nanoparticles deposited on the surface of the m–$BiVO_4$ particles. By increasing the amount of the $CuInS_2$ in the composite samples, more $CuInS_2$ nanoparticles were observed on the surface of the m–$BiVO_4$ particles. This corresponded to the XRD result (Figure 5.1) that the diffraction peak of the $CuInS_2$ located at 2θ of 27.96° became more intensified. EDX spectrum of the $CuInS_2$/m–$BiVO_4$ composite with mass ratio of 1:3 (Figure 5.2(e)) showed the characteristic peaks of Cu, In, S, Bi, V, and O elements, confirming the existence of both $CuInS_2$ and m–$BiVO_4$ in the composite.

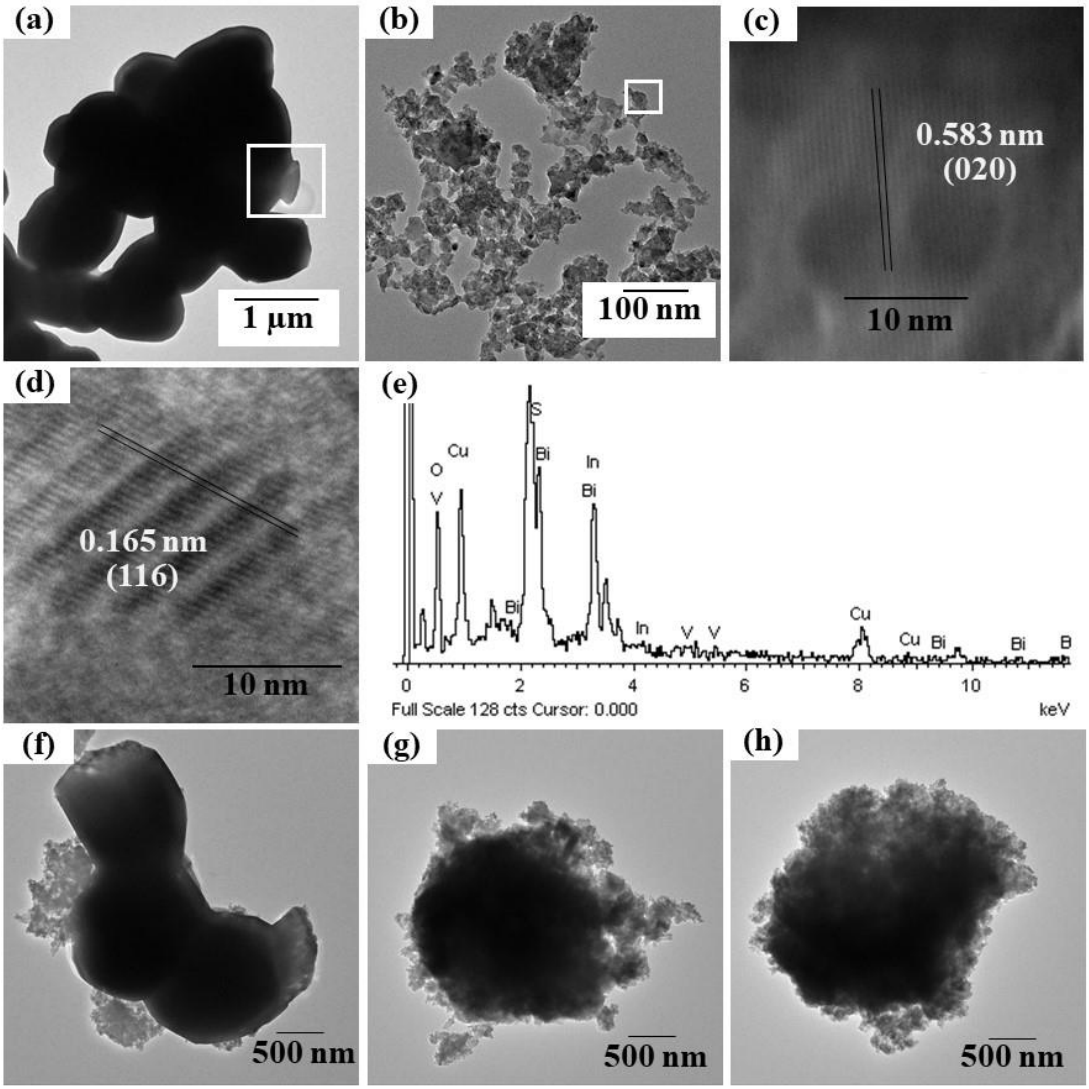

Figure 5.2 *(*a, b*)* TEM and *(*c, d*)* HRTEM images of the m–$BiVO_4$ and the $CuInS_2$ powders, respectively, (e) EDX spectrum of the $CuInS_2$/m–$BiVO_4$ composite with mass ratio of 1:3, and (f–h) TEM images of the $CuInS_2$/m–$BiVO_4$ composites with mass ratios of 1:3, 1:1 and 3:1, respectively.

Figure 5.3 shows UV–vis diffuse reflectance (UV–vis DRS) spectra of the m–$BiVO_4$, $CuInS_2$, and $CuInS_2$/m–$BiVO_4$ composite with mass ratio of 1:3. The reflectance spectra were converted to an absorption coefficient F(R), according to the Kubelka–Munk (K–M) equation: $F(R) = (1-R)^2/2R$, where R is the proportion of light reflected. The K–M absorption spectrum of the pure m–$BiVO_4$ (Figure 5.3(a)) exhibited light absorption in the region of visible light, while the spectrum of the pure $CuInS_2$ (Figure 5.3(b)) exhibited the absorption peak in the visible light and near–infrared regions. In Figure 5.3(c), the absorption edge of the $CuInS_2$/m–$BiVO_4$ composite extended into larger range of visible light region compared to the pure m–$BiVO_4$, suggesting that the visible light absorption of the m–$BiVO_4$ was improved after coupling with the $CuInS_2$. Band gap energy (E_g) was determined from the equation: $E_g = 1241/\lambda_{absorbance}$, where λ is the wavelength (nm). The absorption band edges of the m–$BiVO_4$, $CuInS_2$, and $CuInS_2$/m–$BiVO_4$ powders were 550, 835, and 600 nm, which corresponded to the band gap energies of 2.21, 1.49, and 2.07 eV, respectively. These results suggested that the $CuInS_2$/m–$BiVO_4$ composite efficiently utilized solar light and produced more photogenerated electrons and holes. The PL spectrum of the $CuInS_2$/m–$BiVO_4$ composite with mass ratio of 1:3 was analyzed in comparison with the pure m–$BiVO_4$ to evaluate the recombination rate of the photogenerated electron–hole pairs in the composite. The emission intensity of the PL spectrum (Figure 5.3(d)) of the $CuInS_2$/m–$BiVO_4$ composite was lower than that of the pure m–$BiVO_4$, indicating lower recombination rate of photogenerated electron–hole pairs in the composite, which is beneficial to improve the photocatalytic activity of the photocatalyst [91].

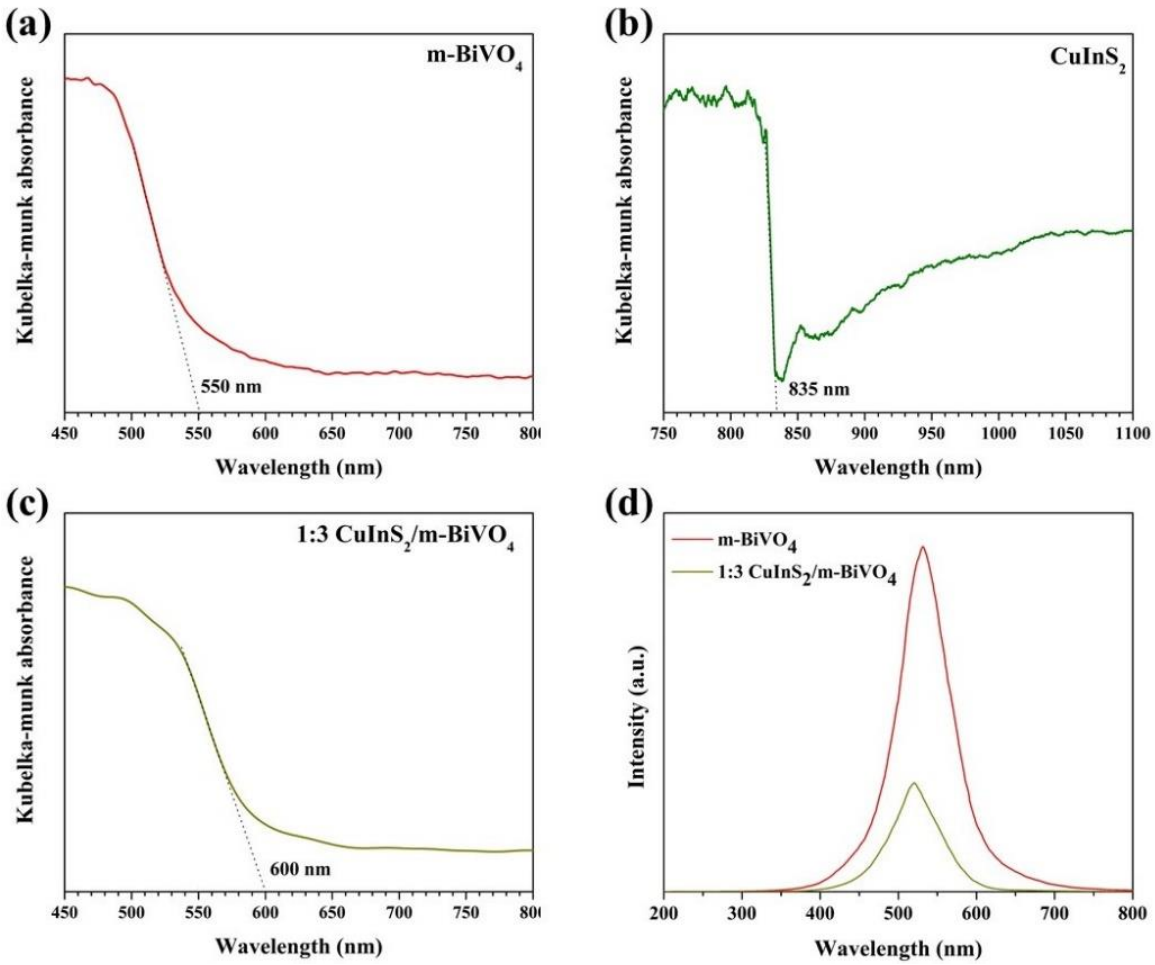

Figure 5.3 UV–vis DRS spectra of the (a) m–$BiVO_4$, (b) $CuInS_2$, and (c) $CuInS_2$/m–$BiVO_4$ and (d) PL spectrum of the $CuInS_2$/m–$BiVO_4$ composite in comparison with the pure m–$BiVO_4$.

5.3 Photocatalytic activity tests

Photocatalytic activities of the m–$BiVO_4$, $CuInS_2$, and $CuInS_2$/m–$BiVO_4$ photocatalysts were investigated by photodegradation of MB aqueous solution under visible light irradiation. Figure 5.4(a) presents %DE of MB irradiated using the LED lamp. The photolysis of MB was also carried out at the same condition but without any photocatalyst. After irradiating for 360 min, only 2.80% of MB was removed, suggesting that decomposition of MB by photolysis mechanism could be neglected. The m–$BiVO_4$ and $CuInS_2$ decolorized MB with an efficiency of 58.03% and 14.79%, respectively. Introducing

the $CuInS_2$ into the m–$BiVO_4$ with mass ratios of 1:3, 1:1, and 3:1 provided photocatalytic degradation with %DE of 90.21%, 72.08%, and 29.23%, respectively. It was found that the $CuInS_2$/m–$BiVO_4$ with mass ratio of 1:3 showed the highest %DE. Notably, using the $CuInS_2$/m–$BiVO_4$ with mass ratio of 3:1 as photocatalyst, the photocatalytic degradation was lower than the pure m–$BiVO_4$. This could be because the excess less–active $CuInS_2$ covering on the surface of the m–$BiVO_4$ particles shielded the surface of the more active m–$BiVO_4$ particles from the irradiated light as presented in Figure 5.2(h).

To further investigate the degradation kinetics of MB by the photocatalysts, pseudo–first–order kinetic equation; $\ln(C_0/C) = kt$, was applied to fit experimental data, where k is the rate constant and t is the irradiation time. The plots of $\ln(C_0/C)$ vs. t illustrated that the photocatalytic degradation of MB fitted well by pseudo–first–order kinetic as shown in Figure 5.4(b). The k value of the $CuInS_2$/m–$BiVO_4$ photocatalyst with mass ratio of 1:3 was calculated to be 6.2×10^{-3} min^{-1}, which was 15.5 and 2.7 times greater than that of the pure $CuInS_2$ (0.40×10^{-3} min^{-1}) and m–$BiVO_4$ (2.3×10^{-3} min^{-1}), respectively. The photocatalytic RhB and MO degradation of the $CuInS_2$/m–$BiVO_4$ photocatalyst with mass ratio of 1:3 under visible light was further evaluated and compared, and the results are shown in Figure 5.4(c). The experimental results showed that 46.07% of RhB and 33.63% of MO were degraded after 360 min visible light irradiation with the k value of 1.6×10^{-3} min^{-1} and 1.1×10^{-3} min^{-1}, respectively. The $CuInS_2$/m–$BiVO_4$ composite photocatalyst exhibited higher photocatalytic activity towards MB than RhB and MO, respectively, because the negative charges on the surface of the composite (Figure 5.5) preferentially adsorbed cationic dye molecules (MB and RhB) rather than anionic dye molecules (MO). The UV–Vis absorption spectra of the MB and RhB solution during the photodegradation reactions by the $CuInS_2$/m–$BiVO_4$ photocatalyst at different time intervals shown in Figure 5.6 demonstrated a gradual depletion of the absorbance value without the shift of the MB and RhB absorption peaks. These results indicated that the decomposition of MB and RhB molecules did not occur by the de–methylated MB or de–ethylated RhB reactions, respectively, but instead by the cleavage of the aromatic chromophore rings [2,92]. For this reason, under the same photocatalytic

reaction pathway, lower the activity of RhB than that of MB could be attributed to the more complicated and larger structure of the RhB molecule.

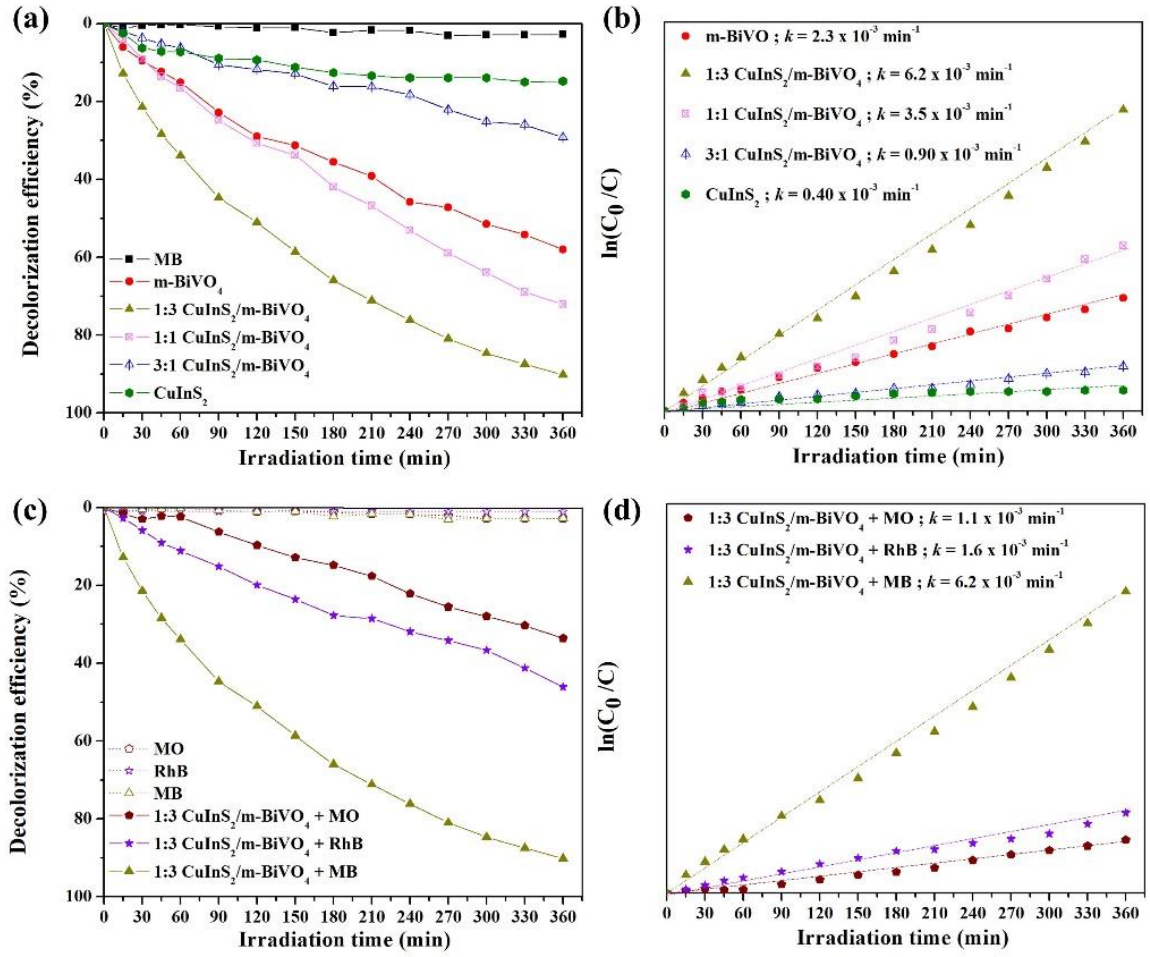

Figure 5.4 *(a)* Decolorization efficiency (%) of MB irradiated under visible light irradiation, *(b)* photocatalytic reaction kinetics of the degradation of MB. (c) and (d) a comparison of the $CuInS_2$/m–$BiVO_4$ with mass ratio of 1:3 on the photodegradation of MB, MO, and RhB aqueous solution under visible light irradiation.

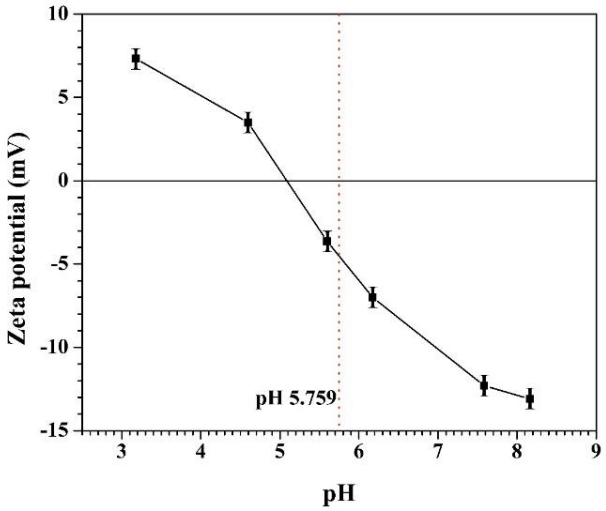

Figure 5.5 Point of zero charge determination of $CuInS_2$/m–$BiVO_4$ composite with mass ratio of 1:3.

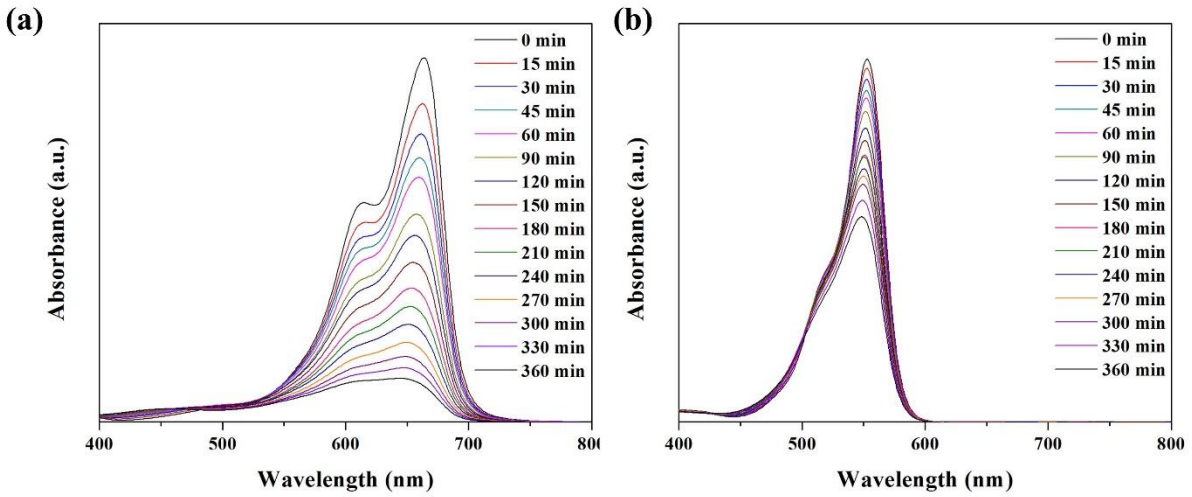

Figure 5.6 UV–Vis absorption spectra of (a) MB and (b) RhB solutions during photodegradation by the $CuInS_2$/m–$BiVO_4$ photocatalyst at different time intervals.

5.4 Photoelectrochemical measurements

Figure 5.7(a) presents linear sweep voltammetry (LSV) curves recorded from the m–$BiVO_4$ and $CuInS_2$/m–$BiVO_4$ photoelectrodes under the dark and visible light conditions. Under the dark condition, almost no photocurrent responses were observed for the m–$BiVO_4$ and $CuInS_2$/m–$BiVO_4$ photoelectrodes. Under the visible light irradiation, current density of the m–$BiVO_4$ photoelectrode was

0.0069 $mAcm^{-2}$ at an applied potential of 1.23 V (*vs.* RHE) while the $CuInS_2$/m–$BiVO_4$ photoelectrode exhibited current density of 0.030 $mAcm^{-2}$ at the same applied potential, which was 4.6 times higher than that of the pure m–$BiVO_4$. It should be noted that the current density of the $CuInS_2$/m–$BiVO_4$ was found to be lower than that of the m–$BiVO_4$ photoelectrode reported in the previously literature [17] since the power of the LED light source used in this study was lower (50W). The enhanced current density could be because photogenerated electron−hole pairs were separated at the contact interface of the $CuInS_2$/m–$BiVO_4$ heterojunction, so that the recombination rate of photogenerated electron–hole pairs was reduced [93–95]. In addition, a negative shift of the onset potential of the $CuInS_2$/m–$BiVO_4$ photoelectrode (the inset of Figure 5.7(a)) illustrated that the photogenerated charge transfer was more efficient [93,96,97]. To further explore the charge transfer resistance and the separation of photogenerated charge carrier at solid/electrolyte interfaces in the photocatalyst, Nyquist plots from the electrochemical impedance spectra (EIS) of the m–$BiVO_4$ and $CuInS_2$/m–$BiVO_4$ were performed (Figure 5.7(b)). In the EIS Nyquist plot, a smaller radius of impedance semicircle suggests an efficient charge transfer at an electrode–electrolyte interface with a lower charge transfer resistance [98]. The smaller arc radius on the Nyquist plot of the $CuInS_2$/m–$BiVO_4$, compared to that of the pure m–$BiVO_4$, indicating a fast electron–transfer process with a smaller electron transfer resistance at the surface of the photoelectrode. These PEC results demonstrated the potential use of the $CuInS_2$/m–$BiVO_4$ as a photoelectrode for PEC cell.

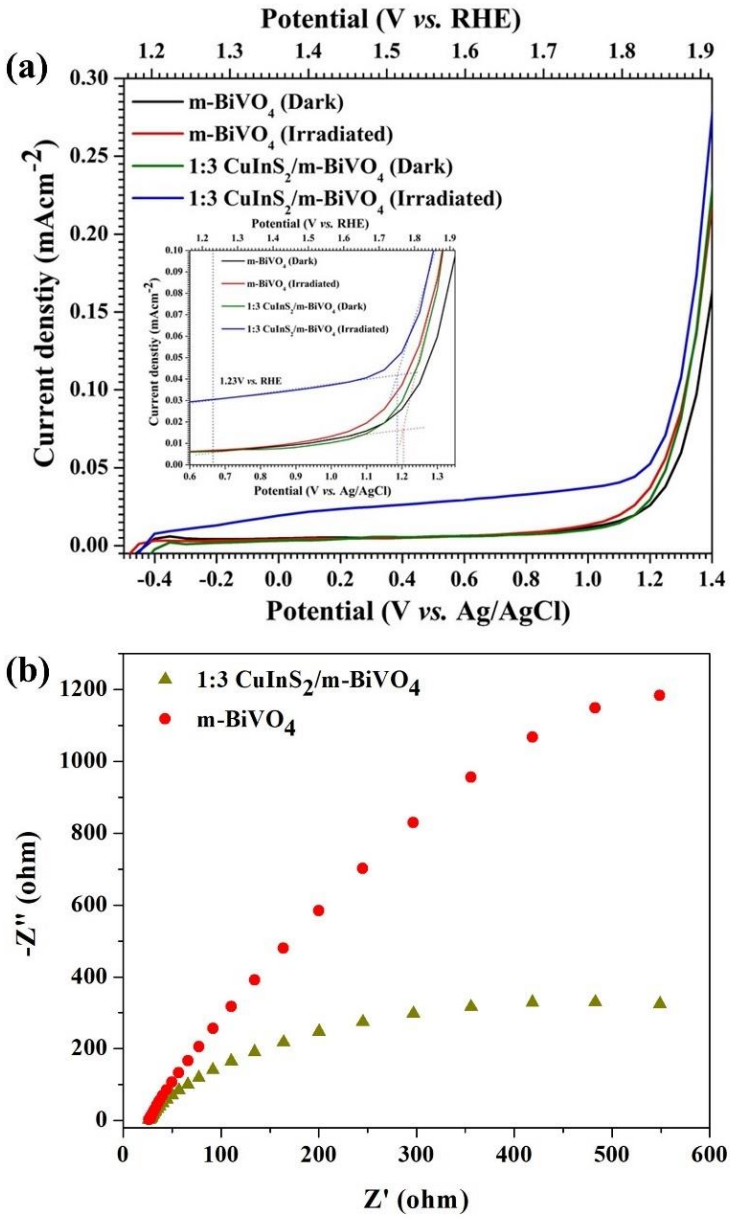

Figure 5.7 (a) Linear sweep voltammograms and (b) electrochemical impedance spectra of the m–$BiVO_4$ and $CuInS_2$/m–$BiVO_4$ composite with mass ratio of 1:3 under the dark and light irradiation. Inset of (a): a magnified view in the range of 0.60 – 1.35 V (vs. Ag/AgCl).

To determine the possible photogenerated charge transfer between the m–$BiVO_4$ and $CuInS_2$, the band positions of the m–$BiVO_4$ and $CuInS_2$ photocatalysts were calculated by the following equations

[99]: $E_{CB} = X - E_e - 0.5E_g$ and $E_{VB} = E_{CB} + E_g$, where E_{CB} is the conduction band potential, E_{VB} is the valence band potential, X is the electronegativity of the semiconductor (6.04 eV for m–$BiVO_4$ [100] and 4.81 for $CuInS_2$ [101]), E_e is the energy of free electrons on the hydrogen scale (4.50 eV), E_g is the band gap energy of the material. According to the E_g values (2.21 eV for m–$BiVO_4$ and 1.49 eV for $CuInS_2$) calculated from the UV–vis DRS analysis (Figure 5.3), the E_{CB} of m–$BiVO_4$ and $CuInS_2$ were calculated to be 0.44 and –0.44 eV, and the E_{VB} of m–$BiVO_4$ and $CuInS_2$ were 2.65 and 1.05 eV, respectively. Due to the suitable band gap energies and band positions of the m–$BiVO_4$ and $CuInS_2$, type II heterojunction was formed. A schematic diagram of the photogenerated charge transfer process in the $CuInS_2$/m–$BiVO_4$ photocatalyst was illustrated in Figure 5.8. Under the irradiation of visible light, the m–$BiVO_4$ and $CuInS_2$ were excited and then generated electron–hole pairs. Since the CB edge potential of m–$BiVO_4$ (0.44 eV *vs.* NHE) was more positive than that of $CuInS_2$ (–0.44 eV *vs.* NHE), the photogenerated electrons easily transferred from CB of $CuInS_2$ to CB of m–$BiVO_4$. Meanwhile, photogenerated holes simultaneously transferred from VB of m–$BiVO_4$ to VB of $CuInS_2$ due to the less positive VB edge potential of $CuInS_2$ (1.05 eV *vs.* NHE) than that of m–$BiVO_4$ (2.65 eV *vs.* NHE). The photogenerated electrons at CB of m–$BiVO_4$ could react with O_2 to generate H_2O_2, since CB of m–$BiVO_4$ (0.44 eV) was less positive than the standard reduction potential of O_2/H_2O_2 (0.68 eV *vs.* NHE [102]), Then, the generated H_2O_2 molecules could react with the electrons to produce •OH radicals. Meanwhile, the holes at VB of $CuInS_2$ could not be oxidized by H_2O or OH^- to yield •OH radicals, since VB potential of $CuInS_2$ (1.05 eV) was less positive than standard reduction potentials of •OH/H_2O (2.72 eV vs. NHE) and •OH/OH^- (2.38 eV *vs.* NHE) [103]. Therefore, the accumulated holes at VB of $CuInS_2$ directly reacted with the dye molecule to yield final degradation products.

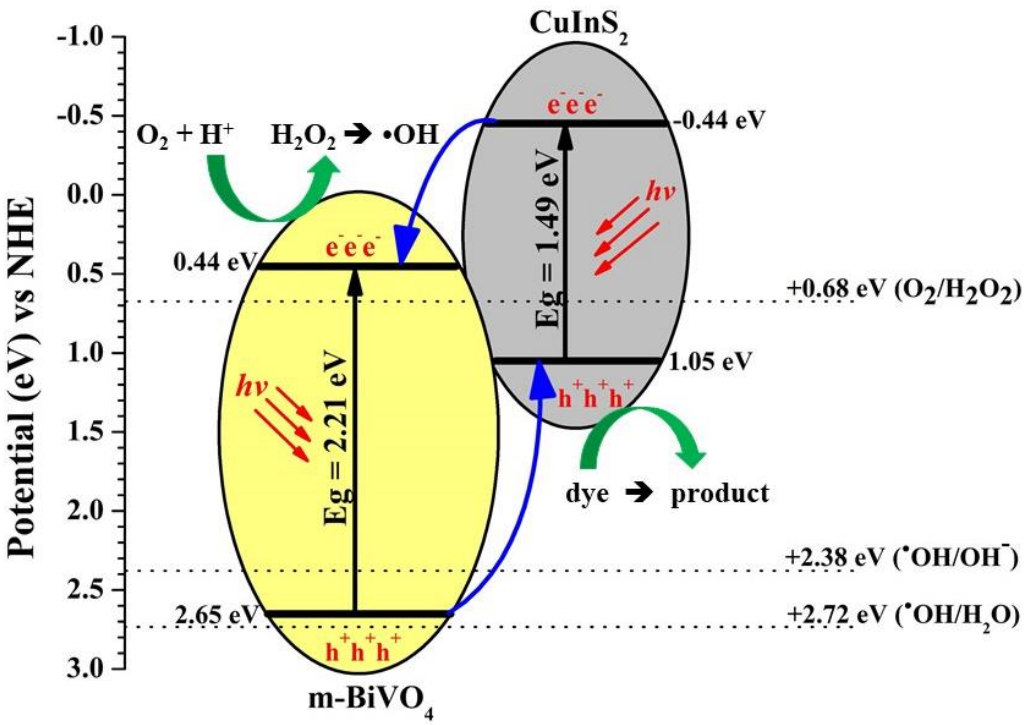

Figure 5.8 Schematic diagram of the photogenerated charge transfer process in the $CuInS_2$/m–$BiVO_4$ composite.

Chapter 6 Synthesis, Characterization and Photocatalytic activity of $FeVO_4/Bi_7O_9I_3$

In this Chapter, synthesis, photocatalytic dye degradation, and photoelectrochemical activity of a novel $FeVO_4/Bi_7O_9I_3$ nanocomposite was reported. The $FeVO_4$ and the $Bi_7O_9I_3$ powders were prepared separately using a cyclic microwave irradiation method, which was a simple, rapid, economical, and environmentally friendly technique. The two components were then mixed together to form a heterojunction via a wet impregnation method. Photocatalytic degradation of methylene blue, rhodamine B, and methyl orange by the $FeVO_4/Bi_7O_9I_3$ nanocomposite was examined. Potential use of the $FeVO_4/Bi_7O_9I_3$ nanocomposite as a photoanode for photoelectrochemical (PEC) water oxidation was also investigated. A possible photocatalytic mechanism of the $FeVO_4/Bi_7O_9I_3$ heterojunction was proposed based on the optical characterization, energy band positions, and active species trapping experiments.

6.1 Experimental procedure

The $Bi_7O_9I_3$ photocatalyst was synthesized by a facile microwave irradiation method. Firstly, $Bi(NO_3)_3{\cdot}5H_2O$ (1 mmol) and KI (1 mmol) were separately dissolved in 20.0 mL of ethylene glycol. Then, the solutions were mixed together for 30 min. After that, the mixed solution was then irradiated using 2.45 GHz microwave radiation operated at 600 W for 60 cycles. Each irradiation cycle lasted 30 s with a 90–s interval. The orange–yellow powder obtained was filtered, washed with deionized water, and dried overnight in an oven at 70°C.

To synthesize $FeVO_4$, $Fe(NO_3)_3{\cdot}9H_2O$ (2 mmol) and NH_4VO_3 (2 mmol) were separately dissolved in 20.0 mL of deionized water. The solutions were mixed together for 30 min. Then, the pH of the mixed solution was adjusted to 4 by slowly adding 2.0 M of NH_4OH solution. Subsequently, the solution was irradiated using 2.45 GHz microwave radiation operated at 600 W for 30 cycles. Each cycle was lasted 30 s with a 90–s interval. The brown powder obtained was then filtered, washed with deionized

water, and dried overnight in an oven at 70°C. Finally, the powder was calcined in air at 600°C for 5 h to yield $FeVO_4$ powder.

The preparation of $FeVO_4/Bi_7O_9I_3$ composites were proceeded by wet–impregnation method. First, the $Bi_7O_9I_3$ powder was sonochemically dispersed in 50.0 mL of methanol for 30 min. The required amount of the $FeVO_4$ powder was then mixed with the $Bi_7O_9I_3$ suspension and stirred at room temperature until methanol was completely volatized. Finally, the $FeVO_4/Bi_7O_9I_3$ powder was dried at 70°C for 24 h and subsequently heated at 200°C for 30 min. The amounts of $FeVO_4$ in the $FeVO_4/Bi_7O_9I_3$ nanocomposites were 3%, 6.25%, 12.5%, and 25% by weight, and the resulted $FeVO_4/Bi_7O_9I_3$ nanocomposites were denoted as x%wt–$FeVO_4/Bi_7O_9I_3$, where x = 3, 6.25, 12.5, and 25. Mole ratios between $FeVO_4$ and $Bi_7O_9I_3$ in the nanocomposites were presented in Table 6.1.The $FeVO_4/Bi_7O_9I_3$ powder were also synthesized by a physical grinding for comparison.

Purity, structure, and crystallinity of the powders were characterized by X–ray diffraction spectroscopy (XRD, Rigaku Miniflex II) with CuK_α radiation (λ = 1.5406 Å). Morphology and particle size of the powders were examined by field emission scanning electron microscopy (FESEM, JEOL JSM–6335F) and transmission electron microscopy (TEM, JEOL JEM–2010) with energy dispersive X–ray (EDX) spectrometry. Optical properties were also studied by UV–vis diffuse reflectance spectroscopy (UV–vis DRS, UV–1800 Shimadzu) using an instrument equipped with a specular reflectance attachment. Elemental composition and chemical state were measured by X–ray photoelectron spectroscopy (XPS, AXIS Ultra DLD, Kratos Analytical Ltd.) using an Al K_α X–ray source at 1.4 keV radiation. Binding energy of adventitious carbon (C 1s) peak at 284.6 eV was used for energy referencing. Photoluminescence spectra were recorded by a photoluminescence spectrometer (PL, Avantes AvaSpec–2048TEC–USB2) with an excitation wavelength of 345 nm.

Table 6.1 Weights (mg) and contents (mmol) of the $FeVO_4$ and $Bi_7O_9I_3$, and mole ratios of $FeVO_4$ (or $Bi_7O_9I_3$) to methylene blue.

Photocatalyst	Weights (mg)		Contents (x 10^{-2} mmol)		Mole ratios		%DE
	$FeVO_4$	$Bi_7O_9I_3$	$FeVO_4$	$Bi_7O_9I_3$	$FeVO_4$:MB	$Bi_7O_9I_3$:MB	
Pure $Bi_7O_9I_3$	0.000	100.0	0.00	5.030	0.0000	1.972	39.0
3%wt–$FeVO_4$/$Bi_7O_9I_3$	3.000	97.00	1.760	4.880	0.6883	1.912	75.4
6.25%wt– $FeVO_4$/$Bi_7O_9I_3$	6.250	93.75	3.660	4.720	1.434	1.848	81.3
12.5%wt– $FeVO_4$/$Bi_7O_9I_3$	12.50	87.50	7.320	4.400	2.868	1.725	55.3
25%wt– $FeVO_4$/$Bi_7O_9I_3$	25.00	75.00	14.64	3.770	5.736	1.479	42.1
Pure $FeVO_4$	100.0	0.000	58.55	0.00	22.94	0.000	13.9

* **Photocatalysis condition:** 200 mL of methylene blue (10 mgL^{-1}; 0.0255 mmol; 0.128 mM) with 100 mg of photocatalyst

** **Molecular weights:** $FeVO_4$ = 170.78 g/mol, $Bi_7O_9I_3$ = 1987.57 g/mol, methylene blue = 391.85 g/mol

For photocatalytic degradation experiments, methylene blue (MB), rhodamine B (RhB), and methyl orange (MO) were tested as model organic dye pollutants. The photocatalyst (100 mg) was dispersed in an aqueous solution of the organic dye (200 mL, 10 mgL^{-1}). Prior to irradiation, the suspension was magnetically stirred in dark for 30 min to establish an adsorption–desorption equilibrium of the dye on the photocatalyst's surface. The suspension was then irradiated under 50W light–emitting diode (LED) lamp for 360 min. At every 30 min of irradiation, 5 mL of the suspension was sampled from the reaction suspension and the absorption intensity was measured at its maximum absorbance

wavelength using a UV–vis spectrophotometer (664 nm for MB, 554 nm for RhB, and 464 nm for MO). Photolysis of the dye was also performed under the same experimental conditions. Decolorization efficiency (%DE) was calculated using the following equation: %DE = $[(C_0-C)/C_0] \times 100$, where C_0 and C were concentrations of the dye when the adsorption–desorption equilibrium was achieved and the dye after the light irradiation, respectively. The mole ratios between the $FeVO_4$ (or the $Bi_7O_9I_3$) in the nanocomposites and the MB were summarized in Table 6.2.

Table 6.2 Weights (mg) and contents (mmol) of the $FeVO_4$ and $Bi_7O_9I_3$, and mole ratios of $FeVO_4$ (or $Bi_7O_9I_3$) to methylene blue.

Photocatalyst	**Weights (mg)**		**Contents (x 10^{-2} mmol)**		**Mole ratios**		**%DE**
	$FeVO_4$	**$Bi_7O_9I_3$**	**$FeVO_4$**	**$Bi_7O_9I_3$**	**$FeVO_4$:MB**	**$Bi_7O_9I_3$:MB**	
Pure $Bi_7O_9I_3$	0.000	100.0	0.00	5.030	0.0000	1.972	39.0
3%wt–$FeVO_4$/$Bi_7O_9I_3$	3.000	97.00	1.760	4.880	0.6883	1.912	75.4
6.25%wt– $FeVO_4$/$Bi_7O_9I_3$	6.250	93.75	3.660	4.720	1.434	1.848	81.3
12.5%wt– $FeVO_4$/$Bi_7O_9I_3$	12.50	87.50	7.320	4.400	2.868	1.725	55.3
25%wt– $FeVO_4$/$Bi_7O_9I_3$	25.00	75.00	14.64	3.770	5.736	1.479	42.1
Pure $FeVO_4$	100.0	0.000	58.55	0.00	22.94	0.000	13.9

* **Photocatalysis condition:** 200 mL of methylene blue (10 mgL^{-1}; 0.0255 mmol; 0.128 mM) with 100 mg of photocatalyst

** **Molecular weights:** $FeVO_4$ = 170.78 g/mol, $Bi_7O_9I_3$ = 1987.57 g/mol, methylene blue = 391.85 g/mol

Photoelectrochemical properties of the 6.25%wt–$FeVO_4$/$Bi_7O_9I_3$ in comparison with the pure $Bi_7O_9I_3$ were investigated by linear sweep voltammogram (LSV). PEC measurement was conducted on an electrochemical analyzer (Autolab, μAUTOLABIII) equipped with a conventional three–electrode system. The electrolyte solution was a 0.5 M Na_2SO_4 aqueous solution (pH = 6.0). A platinum (Pt) sheet was used as a counter electrode and Ag/AgCl (3.0 M KCl) served as a reference electrode. A working electrode consisted of sample film coated on a fluorine–doped tin oxide (FTO)–coated glass substrate using the 'doctor blading' technique, as follows: 50.0 mg of the sample was dispersed in a mixture of 5 mL ethanol, 0.05 mL terpineol, and 0.05 mL Triton X–100. Then, the slurry was coated on an FTO–coated glass substrate with a fixed area of 1 × 1 cm^2. After that, the substrate was heated at 250°C for 45 min to eliminate any remaining organic compounds. LSV was measured at a potential scan rate of 50 $mV.s^{-1}$, and applied voltage potential was varied from −0.9 V to 2.0 V under dark and light irradiation. The light source was a 50W LED lamp. The potentials were reported versus Ag/AgCl and reversible hydrogen electrode (RHE). Notably, the Ag/AgCl scale was converted into an RHE scale via the Nernst relation; V_{RHE} (volt) = $V_{Ag/AgCl}$ + (0.0591 × pH) + 0.210 V.

6.2 Physicochemical characterization

Figure 6.1 shows XRD spectra of all the synthesized powders. For $FeVO_4$, the main diffraction peaks located at 2*theta* of 25.01°, 27.11°, 27.68°, and 42.09° corresponded to (120), (01–2), (–220), and (–330) planes of a triclinic $FeVO_4$ structure (JCPDS No. 038–1372), respectively. The XRD spectrum of the bismuth oxyiodide sample was similar to that of tetragonal BiOI (JCPDS No. 010–0445) but the positions of all diffraction peaks slightly shifted to smaller diffraction angles. The diffraction peaks of the sample, observed at 2*theta* of 28.82°, 31.51°, 45.28°, 49.35°, and 54.71°, matched well with those of $Bi_7O_9I_3$ reported in the previous studies [10,104,105]. The position shift of the diffraction peaks could be due to the extra bismuth and oxygen in the lattice, thus causing an expansion and distortion of the

standard BiOI crystal structure [10,105,106]. No characteristic peak of any impurities was observed, suggesting that a high purity of the $FeVO_4$ and $Bi_7O_9I_3$ powders was successfully obtained by the cyclic microwave irradiation method. XRD spectrum of the 25%wt–$FeVO_4/Bi_7O_9I_3$ nanocomposite exhibited characteristic diffraction peaks of both $FeVO_4$ and $Bi_7O_9I_3$, while XRD spectra of the $FeVO_4/Bi_7O_9I_3$ nanocomposites with lower amounts of $FeVO_4$ showed diffraction peaks of the tetragonal $Bi_7O_9I_3$ structure. This could be due to the lower diffraction peak intensity of the pure $FeVO_4$. However, the existence of $FeVO_4$ in these samples was recognized from the EDX analysis, as illustrated in Figure 6.2(d).

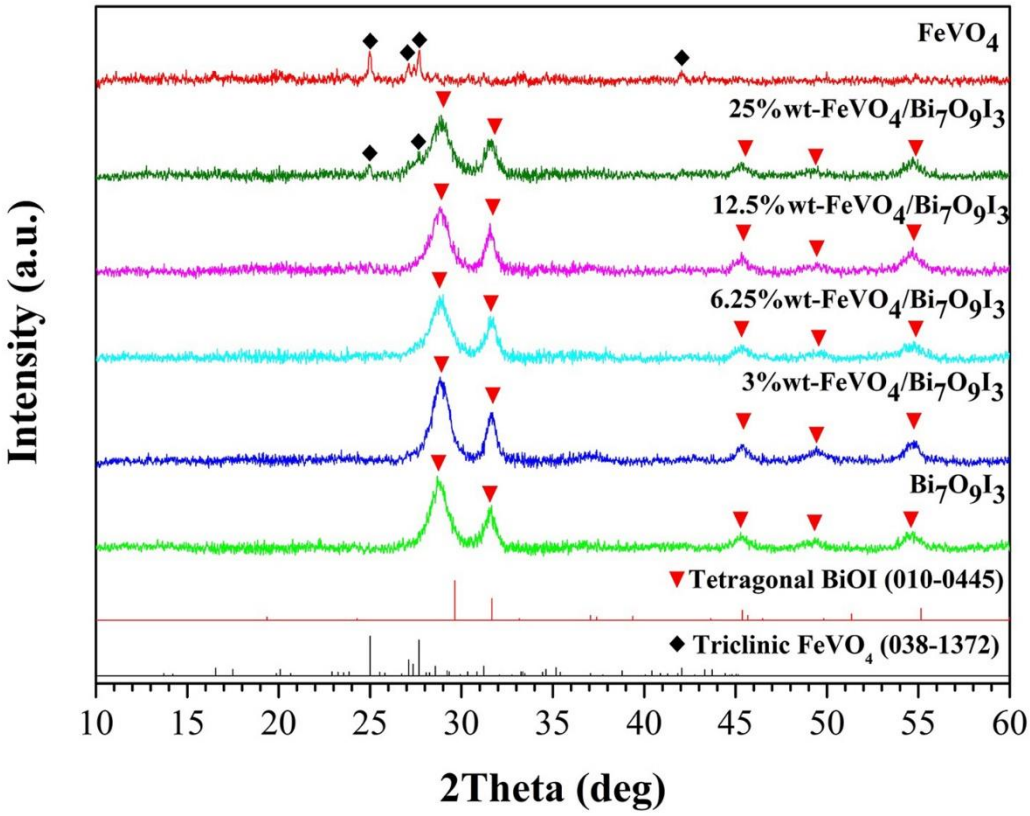

Figure 6.1 XRD patterns of the $FeVO_4$, $Bi_7O_9I_3$, and $FeVO_4/Bi_7O_9I_3$ nanocomposites with different weight percentages of $FeVO_4$.

FESEM and TEM images of the $FeVO_4$, $Bi_7O_9I_3$, and 6.25%wt $FeVO_4/Bi_7O_9I_3$ powders are shown in Figure 6.2. The $FeVO_4$ powder (Figures 6.2(a) and 6.2(e)) were composed of spherical nanoparticles with a diameter of about 100 nm. Morphology of the $Bi_7O_9I_3$ powder (Figures 6.2(b) and 2(f)) also showed spherical nanoparticles with a diameter of approximately 10 nm and with slight agglomeration. EDX spectrum of the $Bi_7O_9I_3$ (Figure 6.3) revealed the presence of Bi, O, and I elements, where the atomic ratio of Bi:O:I was 2.34:3.09:1.00, indicating a formation of the iodide–poor bismuth oxyiodide ($Bi_7O_9I_3$). The lattice spacing measured from the fringes of $FeVO_4$ (inset of Figure 6.2(e)) and $Bi_7O_9I_3$ (inset of Figure 6.2(f)) nanoparticles was 0.32 nm which corresponded to the d–spacing of the (–220) and the (102) crystal planes of triclinic $FeVO_4$ and tetragonal BiOI, respectively. The wider lattice spacing observed from $Bi_7O_9I_3$, compared to that of BiOI, could be due to the expansion of the BiOI crystal structure [19], which was consistent with the XRD result. For 6.25%wt–$FeVO_4/Bi_7O_9I_3$ (Figure 6.2(c)), mixed $FeVO_4$ and $Bi_7O_9I_3$ nanoparticles were observed. Microstructure of the $FeVO_4/Bi_7O_9I_3$ nanocomposite was similar to that of pure $FeVO_4$ and $Bi_7O_9I_3$, indicating that the wet impregnation method for the synthesized nanocomposite had a negligible effect on the microstructure. The corresponding EDX spectrum, shown in Figure 6.2(d), revealed the characteristic peaks of Fe, V, Bi, O, and I elements, confirming that the nanocomposite was indeed composed of $FeVO_4$ and $Bi_7O_9I_3$. TEM image of the 6.25%wt–$FeVO_4/Bi_7O_9I_3$ nanocomposite (Figure 6.4) also indicated that the $Bi_7O_9I_3$ nanoparticles were closely attached with the $FeVO_4$ nanoparticles. The HRTEM images (insets of Figure 6.4) revealed the crystal lattice spacings of 0.32 nm and 0.30 nm, corresponding to the (–220) and (100) planes of $FeVO_4$ and $Bi_7O_9I_3$, respectively, thus confirming that the synthesized nanocomposite apparently had a crystalline structure. EDX mapping of the nanocomposite (Figure 6.5) also showed that the Fe, V, Bi, O, and I elements were uniformly distributed throughout the nanocomposite material. These results provided reliable evidence that the $FeVO_4$ nanoparticles successfully combined with the $Bi_7O_9I_3$ nanoparticles, forming a $FeVO_4/Bi_7O_9I_3$ heterojunction. The heterojunction structure of the $FeVO_4/Bi_7O_9I_3$ played an important part in promoted the photogenerated electrons and holes transfer across the contact interface between $FeVO_4$ and $Bi_7O_9I_3$, consequently reduced the recombination of

photogenerated electron–hole pairs. Noticeably, the iodine content in the 6.25%wt–$FeVO_4/Bi_7O_9I_3$ nanocomposite was low, corresponding to the detailed chemical composition of the synthesized $Bi_7O_9I_3$ nanoparticles illustrated in the inset of Figure 6.3.

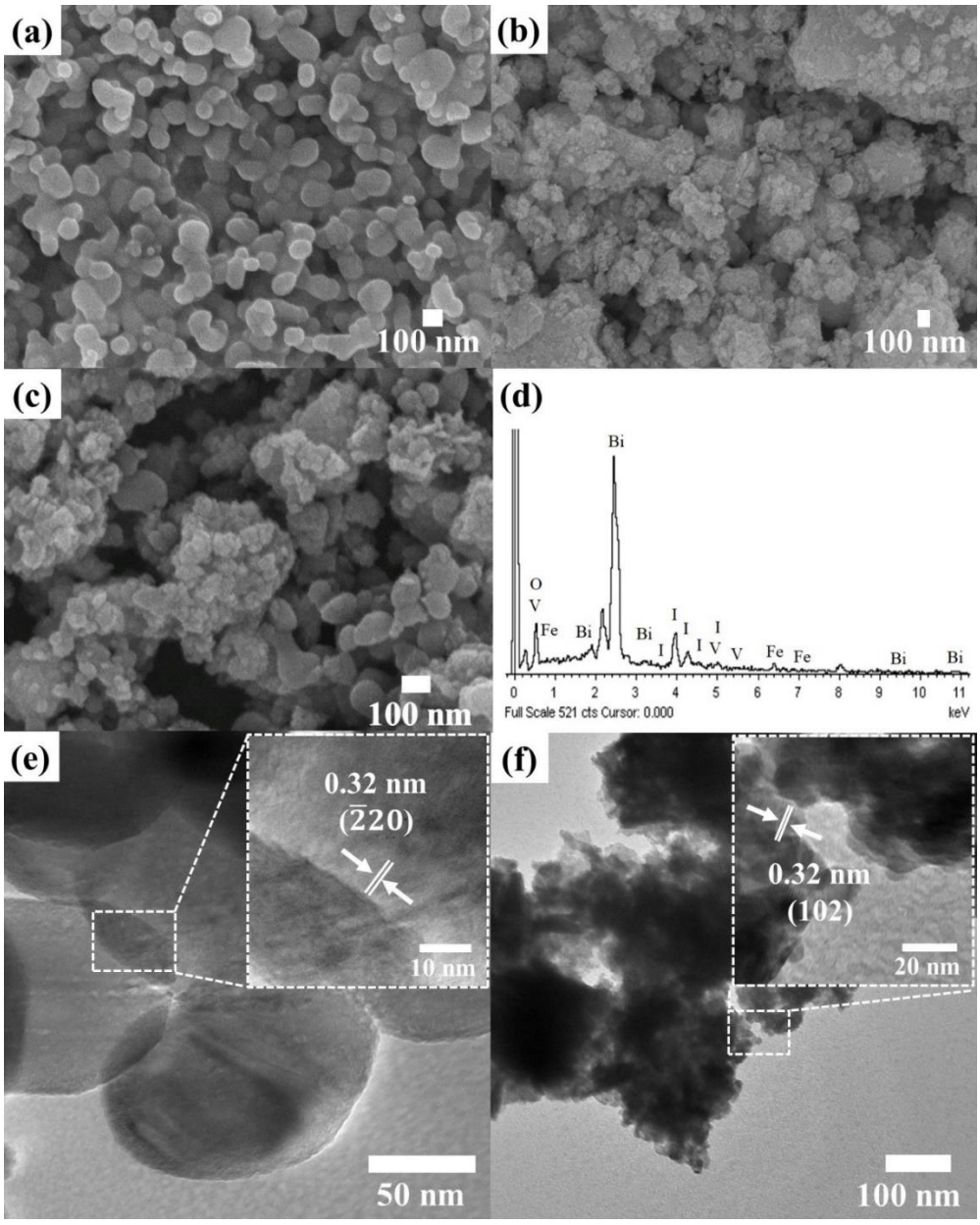

Figure 6.2 FESEM images of the (a) $FeVO_4$, (b) $Bi_7O_9I_3$, and (c) 6.25%wt-$FeVO_4/Bi_7O_9I_3$ nanocomposite. (d) EDX spectrum of the 6.25%wt-$FeVO_4/Bi_7O_9I_3$ nanocomposite. (e) and (f) TEM images of the $FeVO_4$ and the $Bi_7O_9I_3$, respectively. Insets of (e) and (f) are the corresponding HRTEM images of the $FeVO_4$ and the $Bi_7O_9I_3$.

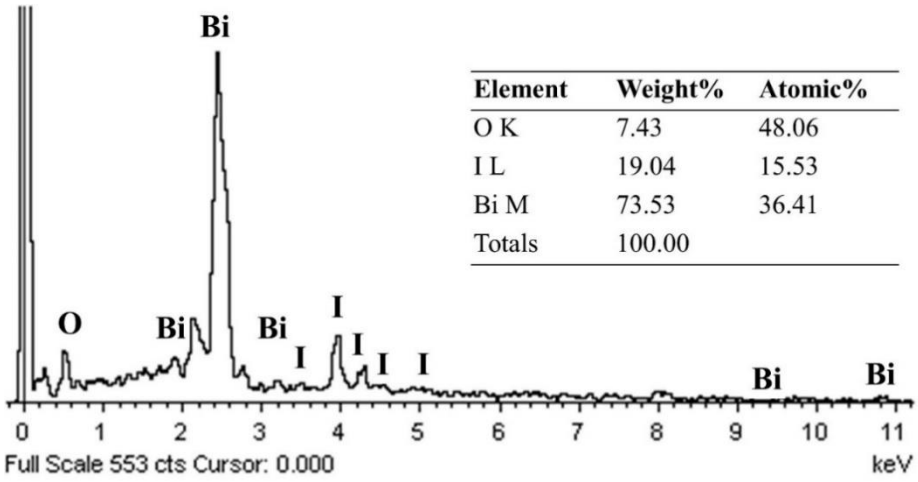

Element	Weight%	Atomic%
O K	7.43	48.06
I L	19.04	15.53
Bi M	73.53	36.41
Totals	100.00	

Figure 6.3 EDX spectrum and detailed chemical composition of the synthesized $Bi_7O_9I_3$ nanoparticles.

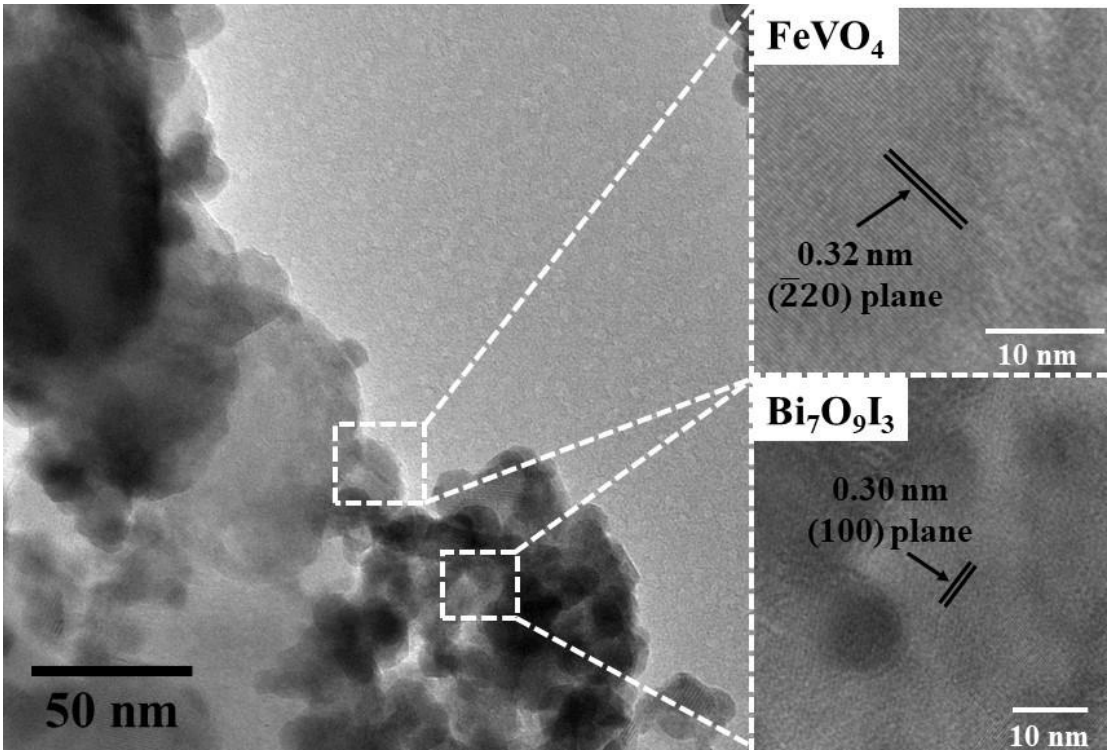

Figure 6.4 TEM image of the 6.25%wt–$FeVO_4$/$Bi_7O_9I_3$ nanocomposite. Upper and lower insets show the corresponding HRTEM images of the $FeVO_4$ and the $Bi_7O_9I_3$, respectively.

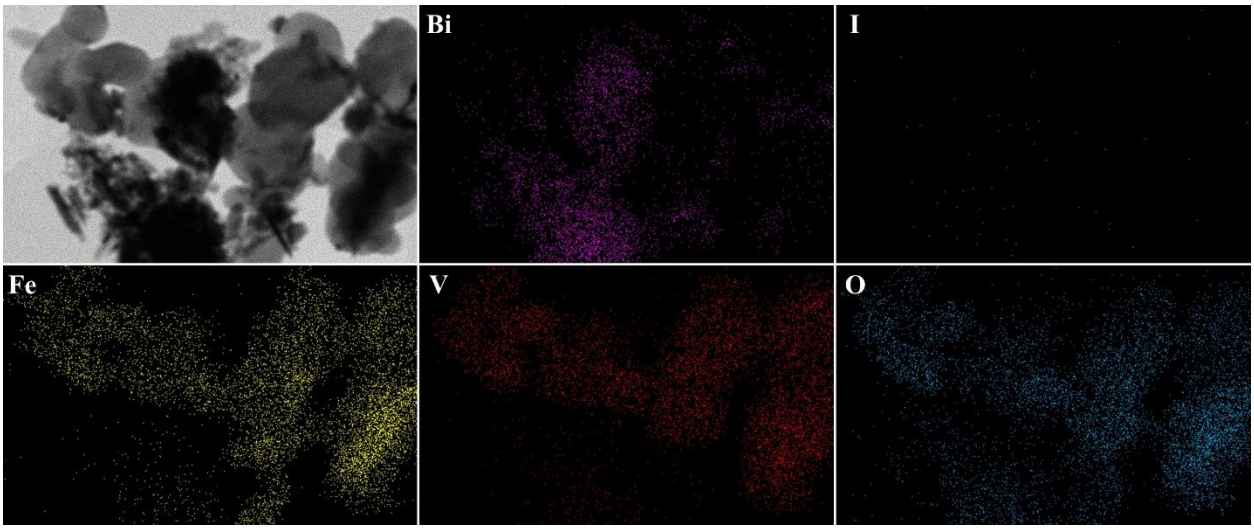

Figure 6.5 EDX mapping of the 6.25%wt–$FeVO_4$/$Bi_7O_9I_3$ nanocomposite.

UV–vis DRS spectra of the $FeVO_4$, $Bi_7O_9I_3$, and 6.25%wt–$FeVO_4$/$Bi_7O_9I_3$ powders are shown in Figure 6.6(a). The reflectance spectra were converted to the absorption coefficient $F(R)$ according to the Kubelka–Munk equation [107]: $F(R) = (1-R)^2/2R$, where R is the proportion of light reflected. Optical band gap energy (E_g) can be determined from the following equation: $E_g = 1241/\lambda_{absorbance}$, where λ is the wavelength (nm). The absorption onsets in the visible–light region of the $FeVO_4$, $Bi_7O_9I_3$, and 6.25%wt–$FeVO_4$/$Bi_7O_9I_3$ powders were 590.5, 563.6, and 579.4 nm which corresponded to 2.10 eV, 2.20 eV, and 2.14 eV, respectively. This result suggested that the introduction of $FeVO_4$ into $Bi_7O_9I_3$ resulted in an improved visible–light absorption ability. In addition, the redshift of the absorption onset of the 6.25%wt–$FeVO_4$/$Bi_7O_9I_3$ nanocomposite, compared with that of the pure $Bi_7O_9I_3$, could be due to the formation of the $FeVO_4$/$Bi_7O_9I_3$ heterojunction. PL spectrum of the 6.25%wt–$FeVO_4$/$Bi_7O_9I_3$ nanocomposite (Figure 6.6(b)) was analyzed in comparison with the pure $Bi_7O_9I_3$ to evaluate the separation efficiency of the photogenerated electron–hole pairs in the nanocomposite. As shown in Figure 6.6(b), emission peaks of the samples were observed at 494 nm and 530 nm. Emission intensity of the PL spectrum for the 6.25%wt–$FeVO_4$/$Bi_7O_9I_3$ nanocomposite was lower than that of the pure $Bi_7O_9I_3$. It

is known that a lower PL intensity indicates a more separation of electron–hole pairs and an improved photocatalytic activity. Thus, this result indicated that the formation of the $FeVO_4/Bi_7O_9I_3$ heterojunction facilitated effective separation of the electron–hole pairs.

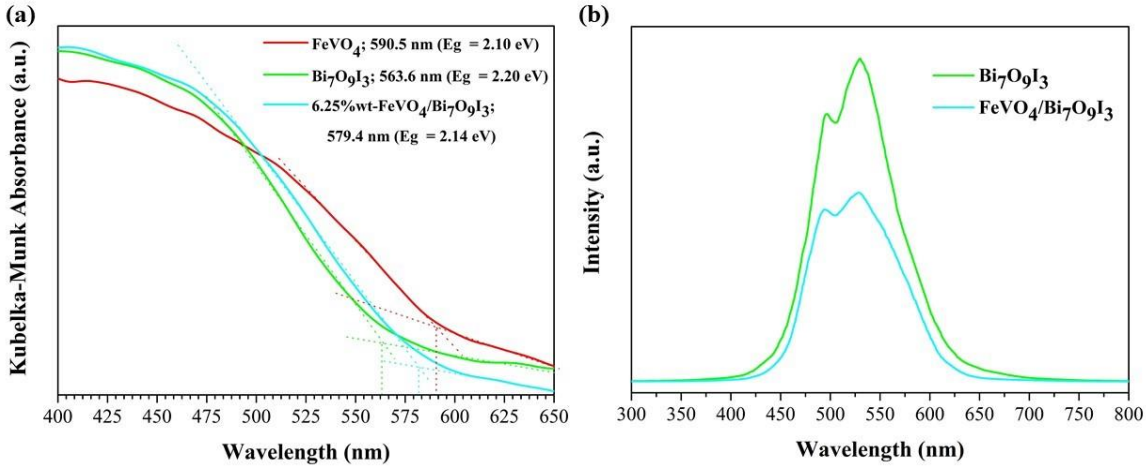

Figure 6.6 (a) UV–vis DRS of the $FeVO_4$, $Bi_7O_9I_3$, and 6.25%wt–$FeVO_4/Bi_7O_9I_3$ nanocomposites, and (b) PL spectrum of the 6.25%wt–$FeVO_4/Bi_7O_9I_3$ nanocomposite in comparison with the $Bi_7O_9I_3$.

Elemental composition and chemical state of the $FeVO_4$, $Bi_7O_9I_3$, and 6.25%wt–$FeVO_4/Bi_7O_9I_3$ powders were identified by XPS as shown in Figure 6.7. Survey XPS spectra, presented in Figure 6.7(a), showed that the $FeVO_4$ powder contained only Fe, V, and O elements, while the $Bi_7O_9I_3$ powder contained only Bi, O, and I elements, indicating high purity of these powders. The 6.25%wt–$FeVO_4/Bi_7O_9I_3$ nanocomposite was composed of Fe, V, O, Bi, and I elements, which was consistent with the earlier EDX analyses (Figures 6.2(d) and 6.5). This result confirmed the coexistence of the $FeVO_4$ and $Bi_7O_9I_3$ in the nanocomposite. Notably, the C 1s peak at 284.6 eV could originate from hydrocarbons in the XPS instrument. High–resolution XPS spectra of Bi 4f are presented in Figure 6.7(b). For pure $Bi_7O_9I_3$, the two strong peaks at the Bi region of 159.2 eV and 164.5 eV were assigned to the binding energy of Bi $4f_{7/2}$ and Bi $4f_{5/2}$, respectively, which were the characteristics of Bi^{3+} [10,19]. The peaks of Bi $4f_{7/2}$ and Bi $4f_{5/2}$ for the 6.25%wt–$FeVO_4/Bi_7O_9I_3$ nanocomposite, located at 158.9 eV and 164.2 eV,

respectively, appeared to have shifted to lower values compared to those of the pure $Bi_7O_9I_3$ [108,109]. The XPS spectra of I 3d (Figure 6.7(c)) showed that the peaks at 619.2 eV and 630.7 eV were ascribed to I $3d_{5/2}$ and I $3d_{3/2}$, respectively, confirming that the valence state of I in the sample was −1 [10]. For the 6.25%wt–$FeVO_4$/$Bi_7O_9I_3$ nanocomposite, the peaks of I $3d_{5/2}$ and I $3d_{3/2}$ were observed at 621.6 eV and 633.0 eV, respectively, which positively shifted from those of the pure $Bi_7O_9I_3$ [109]. In Figure 6.7(d), the main binding energies of Fe $2p_{3/2}$ and Fe $2p_{1/2}$ for the 6.25%wt–$FeVO_4$/$Bi_7O_9I_3$ (713.6 eV and 727.3 eV, respectively) appeared at higher energy levels than those of the pure $FeVO_4$ (710.8 eV and 724.4 eV, respectively). In addition, three sub–peaks in the Fe 2p spectra corresponded to tetrahedral structures and the satellite peak were also observed. The V 2p spectra of the 6.25%wt–$FeVO_4$/$Bi_7O_9I_3$ nanocomposite, presented in Figure 6.7(e), revealed the two main peaks of V $2p_{3/2}$ and V $2p_{1/2}$ (519.3 eV and 526.6 eV, respectively) [111,112], which were higher than those of the pure $FeVO_4$ (517.1 eV and 524.6 eV, respectively). Notably, a weak V^{4+} peak was found at a binding energy of around 516 eV because of oxygen vacancies in their crystal structures. Figure 6.7(f) shows the O 1s spectra of the $FeVO_4$, $Bi_7O_9I_3$, and 6.25%wt–$FeVO_4$/$Bi_7O_9I_3$. For $FeVO_4$, the binding energy peaks at 530.1 eV and 532.2 eV could be attributed to the two chemical bonds of O–V and O–Fe, respectively [110]. The O 1s peaks of the pure $Bi_7O_9I_3$, located at 529.9 eV and 531.2 eV, attributed to the Bi–O bonds in the $Bi_2O_2^{2+}$ layers and the hydroxyl groups of the adsorbed water molecules on the surface, respectively [106,113]. For the nanocomposite, the O 1s peaks with four sub–peaks, located at 531.3 eV, 532.3 eV, 533.4 eV, and 534.3 eV, were observed. These peaks could be attributed to the O–H bonds in the surface–adsorbed water molecules, Bi–O bonds in $Bi_7O_9I_3$, O–V bonds in $FeVO_4$, and O–Fe bonds in $FeVO_4$, respectively. Notably, the shift in the binding energies of Bi 4f and I 3d after introducing $FeVO_4$ clearly implied an interfacial chemical interaction between $FeVO_4$ and $Bi_7O_9I_3$ in the nanocomposite, instead of a physical contact between each individual material; this corresponded well with the TEM, HRTEM, and EDX analyses. Figure 6.7(g) shows the valence band XPS (VB XPS) spectra of the $FeVO_4$ and $Bi_7O_9I_3$. The positions of the valence band edges (E_{VB}) of the $FeVO_4$ and $Bi_7O_9I_3$ were determined to be 2.06 eV and 1.42 eV, respectively. The conduction band (CB) edge positions of the

pure $FeVO_4$ and $Bi_7O_9I_3$ could be calculated using the following formula: $E_{CB} = E_{VB} - E_g$, where E_g is the band gap of the $FeVO_4$ (2.10 eV) or the $Bi_7O_9I_3$ (2.20 eV). Here, the E_{CB} of the $FeVO_4$ and the $Bi_7O_9I_3$ were −0.04 eV and −0.78 eV, respectively.

6.3 Photocatalytic activity tests

Figure 6.8(a) shows %DE of methylene blue (MB) using $FeVO_4$, $Bi_7O_9I_3$, and $FeVO_4/Bi_7O_9I_3$ as the photocatalysts. Almost no change was observed when only the MB solution was exposed to the LED light, indicating that MB photolysis could be insignificant. The %DE of 13.9, 39.0, 75.4, 81.3, 55.3, and 42.1 within 360 min of the irradiation were found from $FeVO_4$, $Bi_7O_9I_3$, and the $FeVO_4/Bi_7O_9I_3$ nanocomposites having the amounts of $FeVO_4$ of 3%wt, 6.25%wt, 12.5%wt, and 25%wt, respectively. All the $FeVO_4/Bi_7O_9I_3$ nanocomposites provided greater photocatalytic degradation efficiency than that of pure $FeVO_4$ or pure $Bi_7O_9I_3$. The 6.25%wt–$FeVO_4/Bi_7O_9I_3$ nanocomposite with a mole ratio between $FeVO_4$ and $Bi_7O_9I_3$ of 0.78:1 resulted in the highest photocatalytic MB degradation (Table 6.1). In addition, the 6.25%wt–$FeVO_4/Bi_7O_9I_3$ nanocomposite showed a higher degradation activity (%DE = 81.3) than that of the physical mixture of $FeVO_4$ and $Bi_7O_9I_3$ (%DE = 46.8), indicating that the enhanced photocatalytic activity of the nanocomposite was originated by the formation of $FeVO_4/Bi_7O_9I_3$ heterojunction, which provided efficient photogenerated electron–hole transport pathway and suppressed electron–hole pairs recombination process. The plot of decolorization efficiency (%) *vs.* $FeVO_4$:MB and $Bi_7O_9I_3$:MB mole ratios presented in Figure 6.9 implied that both of the $FeVO_4$ and $Bi_7O_9I_3$ contents in the nanocomposite affected greatly to the photocatalytic efficiency. The $FeVO_4$:MB and $Bi_7O_9I_3$:MB mole ratios were 1.434:1 and 1.848:1, respectively, provided the highest decolorization efficiency. The decolorization efficiency of MB increased as the $Bi_7O_9I_3$ content in the nanocomposite decreased slightly (or the $FeVO_4$ content increased substantially). However, the photocatalytic activity of the nanocomposite decreased when increasing the excessive amount of the $FeVO_4$ (12.5%wt and 25%wt). This could be because the excess $FeVO_4$ nanoparticles covered and shaded the active surface

of the photocatalyst, as observed in the FESEM image (Figure 6.10), inhibiting light absorption and consequently decreasing the quantity of photogenerated charges [114]. These results demonstrated that the optimum loading amount of $FeVO_4$ in the $FeVO_4/Bi_7O_9I_3$ nanocomposite improved the charge separation and reduced the electron–hole recombination on $Bi_7O_9I_3$ without blocking the active sites of the photocatalyst, thus enhancing photocatalytic activity. The photocatalytic reaction kinetic of the degradation of MB was further investigated using the pseudo–first–order kinetic model, as follows: $\ln(C_0/C) = kt$, where k is the pseudo–first–order rate constant derived from the slope of a linear plot between $\ln(C_0/C)$ and irradiation time (t), as presented in Figure 6.8(b). The 6.25%wt–$FeVO_4/Bi_7O_9I_3$ photocatalyst provided the highest rate constant value (4.6×10^{-3} min^{-1}), indicating that, among others, the 6.25%wt–$FeVO_4/Bi_7O_9I_3$ was the best photocatalyst.

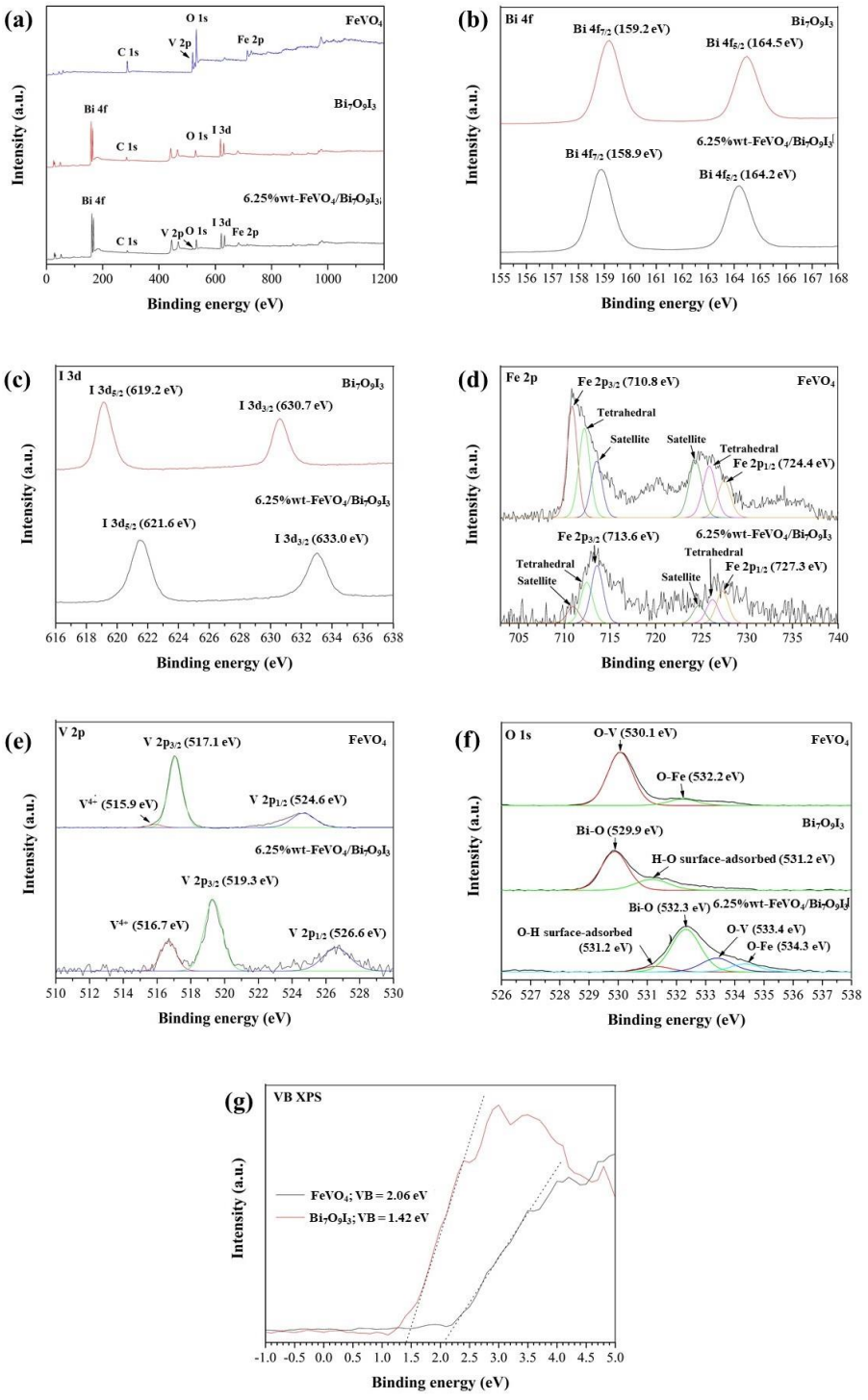

Figure 6.7 *(a)* Survey XPS spectra of the $FeVO_4$, $Bi_7O_9I_3$, and 6.25 %wt–$FeVO_4/Bi_7O_9I_3$ nanocomposite; high–resolution spectra of *(b)* Bi 4f, *(c)* I 3d, *(d)* Fe 2p, *(e)* V 2p, and *(f)* O 1s, and *(g)* valence band XPS (VB XPS) spectra of $FeVO_4$ and $Bi_7O_9I_3$.

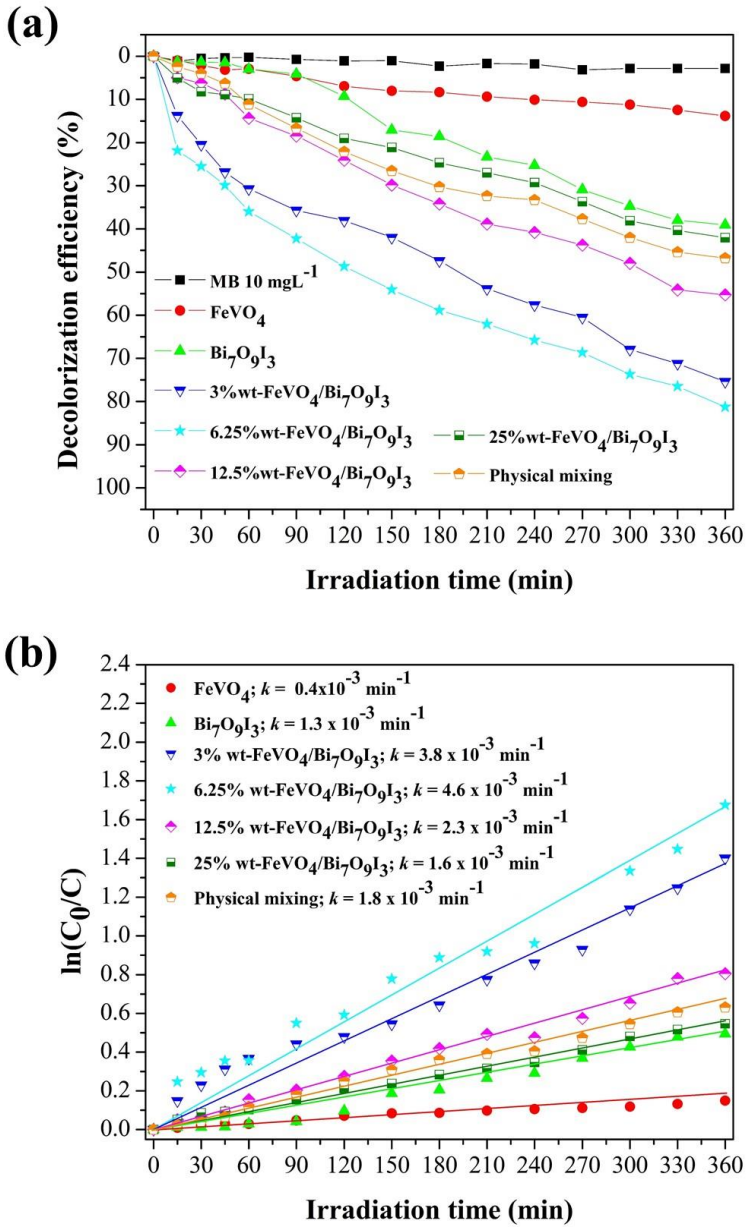

Figure 6.8 *(a)* Decolorization efficiency (%) of the MB irradiated using LED lamp and *(b)* photocatalytic reaction kinetics of the degradation of MB. Photocatalysis condition: 200 mL of methylene blue (10 mgL^{-1} or 0.0255 mmol) with 100 mg of the photocatalyst.

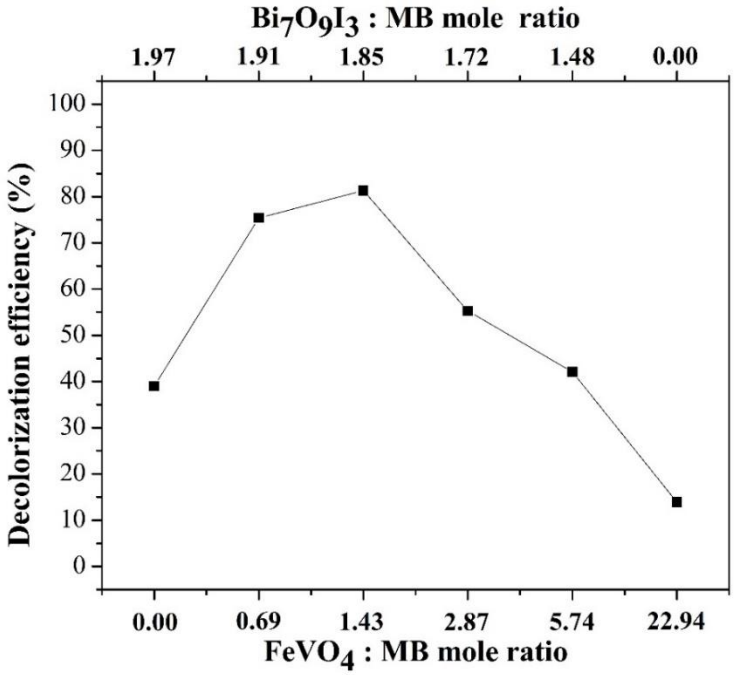

Figure 6.9 Plot of decolorization efficiency (%) vs. $FeVO_4$:MB mole ratio (and vs. $Bi_7O_9I_3$:MB mole ratio).

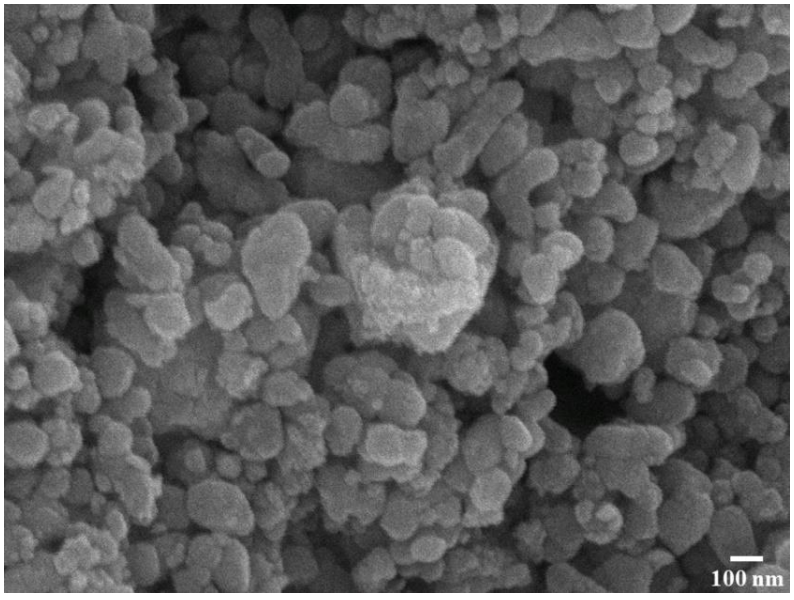

Figure 6.10 FESEM image of the 12.5%wt–$FeVO_4/Bi_7O_9I_3$ powder.

Two other dyes, rhodamine B (RhB) and methyl orange (MO), were chosen to evaluate the universality of the $FeVO_4/Bi_7O_9I_3$ photocatalyst for photodegradation of organic dyes under visible–light irradiation. The decolorization efficiencies of RhB and MO in the presence of the 6.25%wt–$FeVO_4/Bi_7O_9I_3$ photocatalyst compared to that of MB are shown in Figure 6.11(a). The %DE of RhB and MO without photocatalyst could be negligible. This photocatalyst decolorized RhB and MO with efficiencies of 98.9% and 94.9% and rate constants of 1.3×10^{-2} min^{-1}, and 8.1×10^{-3} min^{-1}, respectively (Figure 6.12(a)). The absorption spectra of MB, RhB, and MO during the photodegradation processes by the $FeVO_4/Bi_7O_9I_3$ photocatalyst are shown in Figure 6.13. The difference in %DE could be attributed to the different molecular structures of the dyes used in the present work, which resulted in different degradation mechanisms, as described in the previous literatures [115–117]. Briefly, the RhB molecules rapidly degraded due to an *N*–de–ethylation process, while the MO molecules were decomposed by a stepwise demethylation process. In addition, the azo group (–N=N–) of the MO molecule was more reactive than that of the MB molecule, and the sulfonyl group ($–S(=O)_2–$) of the MO molecule was more reactive than the sulfur involved in the $=S^+$ – aromatic ring in the MB molecule [116].

Due to the superior photodegradation of RhB, the photocatalytic degradation of the RhB experiment by the 6.25%wt–$FeVO_4/Bi_7O_9I_3$ photocatalyst was repeated under the same conditions, as shown in Figure 6.11(b). No significant loss in the photocatalytic degradation of RhB was observed during three test runs, indicating the good reusability and stability of the photocatalyst. The effect of the initial dye concentration on photocatalytic degradation was also studied by varying the RhB concentration from 10 mgL^{-1} to 30 mgL^{-1} in the presence of the 6.25%wt–$FeVO_4/Bi_7O_9I_3$ photocatalyst. Figure 6.11(c) shows the degradation of RhB with different initial concentrations under visible–light irradiation. After 360 min of irradiation, 98.9%, 94.8%, and 81.3% of 10 mgL^{-1}, 20 mgL^{-1}, and 30 mgL^{-1} of the RhB solution, respectively, were decolorized. The rate constants of the decolorization (Figure 6.12(b)) were decreased with the increasing of initial concentration of RhB, owing to the decrease in the ratio of the photocatalyst to the RhB molecule in the solution. This led to a

reduction in the light intensity, which reached the photocatalyst's surface, and a reduction in the number of active radicals, which contributed to the degradation of RhB [11,118].

Active species trapping experiments were performed to determine the main active species of the photocatalytic activity of the 6.25%wt–$FeVO_4/Bi_7O_9I_3$ photocatalyst. Different radical scavengers (1 mM) including ascorbic acid (ASC) [119], ethylenediaminetetraacetic acid disodium salt (EDTA–2Na) [119], dimethyl sulfoxide (DMSO) [120], and potassium dichromate ($K_2Cr_2O_7$) [121] were, respectively, used as scavengers for trapping superoxide radicals ($O_2^{\bullet-}$), holes (h^+), hydroxyl radicals ($HO^\bullet$), and photogenerated electrons (e^-). The corresponding results are shown in Figure 6.11(d). As illustrated, the photodegradation of RhB was dramatically quenched in the presence of ASC and EDTA–2Na, indicating that $O_2^{\bullet-}$ and h^+ were both important for the photodegradation process. The addition of DMSO and $K_2Cr_2O_7$ slightly suppressed the photodegradation of RhB, indicating that $HO^\bullet$ and e^- had only a small effect on the photodegradation process.

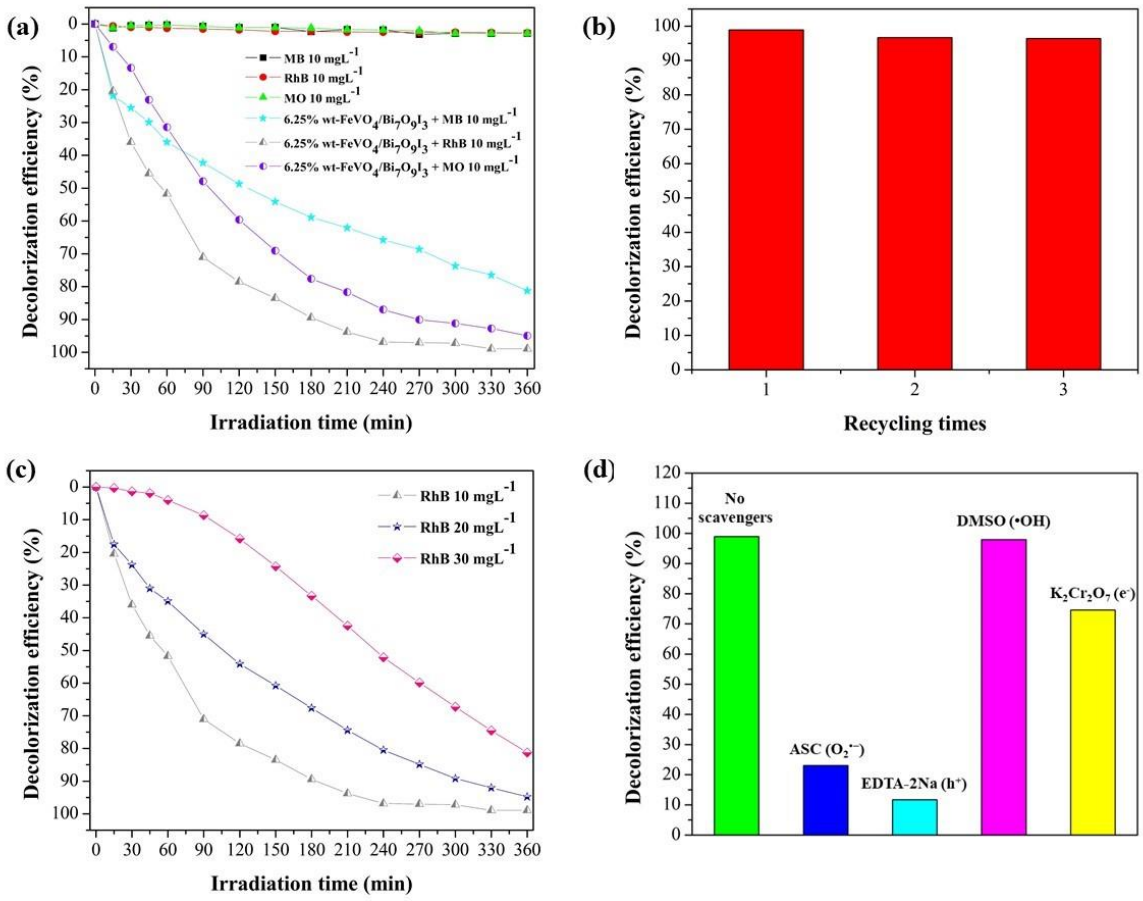

Figure 6.11 (a) Decolorization efficiency (%) of RhB and MO compared to that of MB, (b) the reusing assessment of the 6.25%wt–$FeVO_4/Bi_7O_9I_3$ photocatalyst for photocatalytic degradation of 10 mgL^{-1} of RhB, (c) the effect of initial concentration on photocatalytic degradation of RhB, and (d) the trapping experiments of active species in the photocatalytic reaction in the presence of the 6.25%wt-$FeVO_4/Bi_7O_9I_3$ photocatalyst.

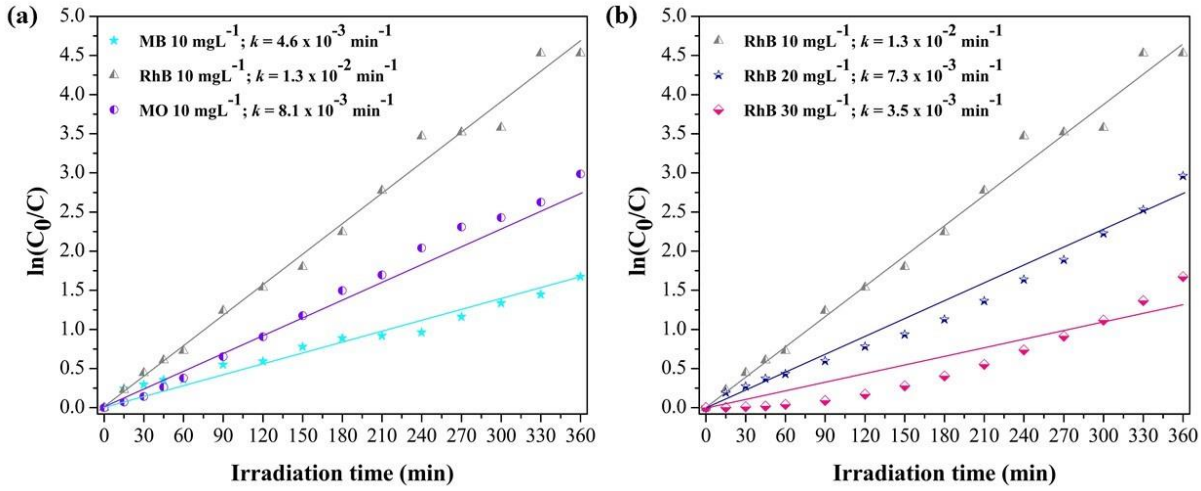

Figure 6.12 Photocatalytic reaction kinetics of the degradation of the (a) 10 mgL^{-1} of MB, RhB, and MO solutions and (b) different initial concentrations of RhB solution.

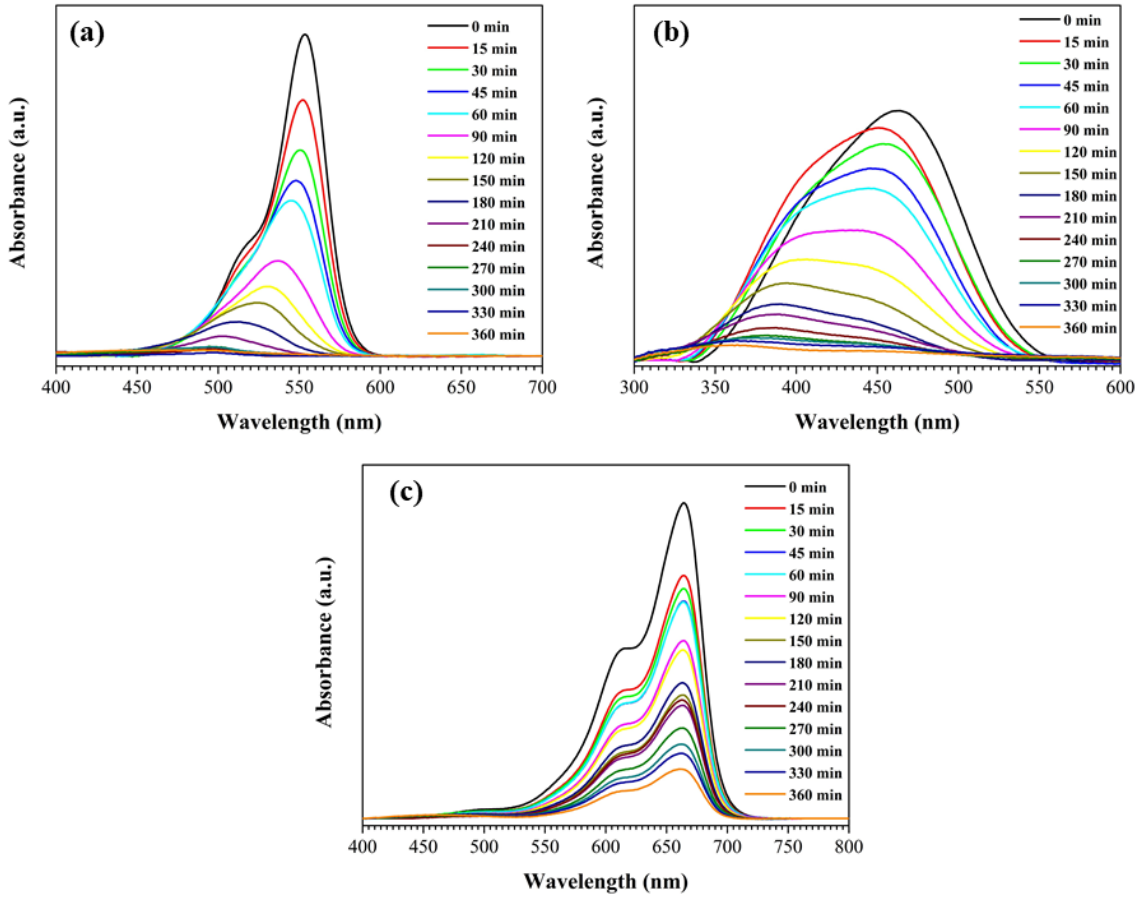

Figure 6.13 The UV–vis absorption spectra of the (a) RhB, (b) MO, and (c) MB solutions during the photodegradation processes.

Based on the aforementioned experimental results, a schematic diagram of the photocatalytic mechanism of the $FeVO_4/Bi_7O_9I_3$ nanocomposite system for the degradation of dye was proposed (Figure 6.14). Under visible–light irradiation, both $FeVO_4$ and $Bi_7O_9I_3$ were excited and subsequently generated electrons (e^-) and holes (h^+). The difference between the energy bands of $FeVO_4$ and $Bi_7O_9I_3$ allowed the efficient transfer of e^- and h^+ between them. The h^+ on the valence band (VB) of $FeVO_4$ (2.06 eV) migrated to the VB of $Bi_7O_9I_3$ (1.42 eV) due to the less positive VB edge potential of $Bi_7O_9I_3$ compared to that of $FeVO_4$. Meanwhile, the e^- on the conduction band (CB) of $Bi_7O_9I_3$ (–0.78 eV) migrated to the CB of $FeVO_4$ (–0.04 eV) due to the less negative CB edge potential of $FeVO_4$ compared to that of $Bi_7O_9I_3$. Thus, the formation of a "type II heterojunction" [13] between $FeVO_4$ and $Bi_7O_9I_3$ effectively improved the separation of the photogenerated e^- and h^+, which resulted in the enhanced photocatalytic activity of the $FeVO_4/Bi_7O_9I_3$ heterojunction structure. Then, the e^- in the CB of $FeVO_4$ was scavenged by O_2 on the surface of the photocatalyst to generate $O_2^{\bullet-}$ radicals. The h^+ in the VB of $Bi_7O_9I_3$ would attack the dye to form intermediate products. The photocatalytic degradation reaction would subsequently proceed, in which the intermediate products [19,122,123] could transform and eventually decompose to CO_2 and H_2O by both the $O_2^{\bullet-}$ radical and h^+.

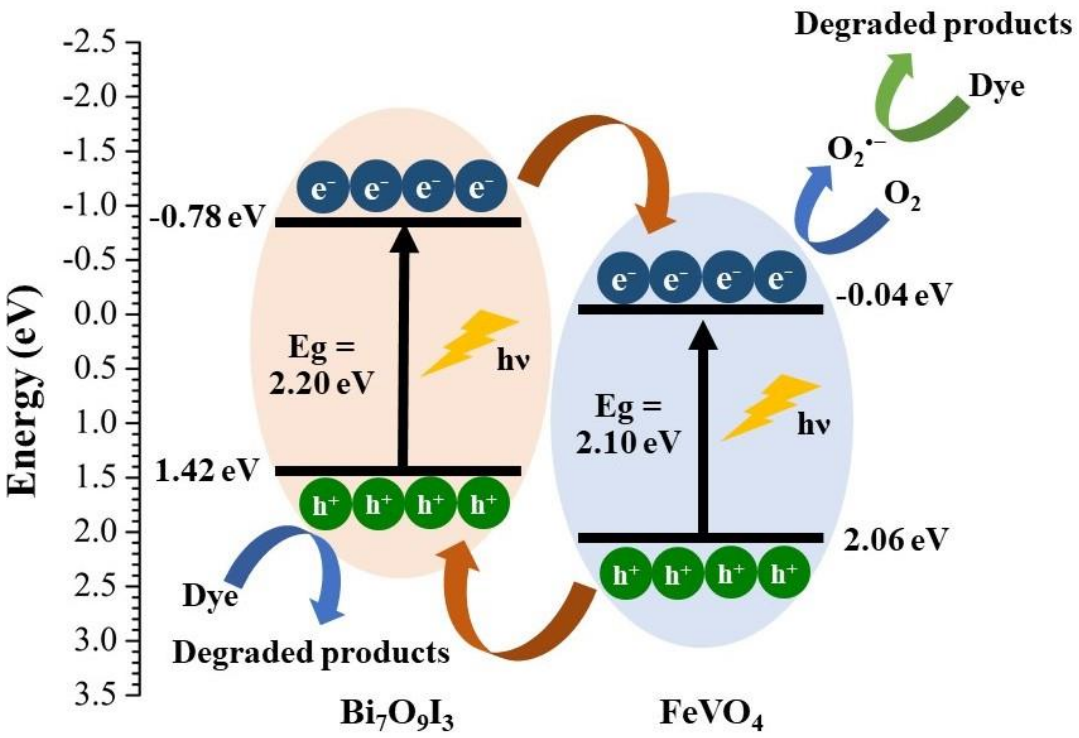

Figure 6.14 Schematic diagram of the photocatalytic mechanism of the $FeVO_4/Bi_7O_9I_3$ nanocomposite system for the degradation of dye.

6.4 Photoelectrochemical measurements

Linear sweep voltammograms of the $Bi_7O_9I_3$ and the 6.25%wt–$FeVO_4/Bi_7O_9I_3$ photoanodes operated either in dark or under visible–light irradiation are shown in Figure 6.15. Under dark condition, almost no photocurrent responses were visualized for the $Bi_7O_9I_3$ and the 6.25%wt–$FeVO_4/Bi_7O_9I_3$ photoanodes. Under visible–light irradiation, the $Bi_7O_9I_3$ photoanode illustrated a photocurrent density of 0.0078 $mA.cm^{-2}$ at an applied potential of 1.23 V (*vs.* RHE), while the 6.25%wt–$FeVO_4/Bi_7O_9I_3$ photoanode showed an enhanced photocurrent density of 0.029 $mA.cm^{-2}$ at the same applied potential. The photocurrent density of the 6.25%wt–$FeVO_4/Bi_7O_9I_3$ photoanode was ca. 3.7 times higher than that of the $Bi_7O_9I_3$ photoanode. The enhanced photocurrent density of the $FeVO_4/Bi_7O_9I_3$ nanocomposite could be explained by the fact that the generation and separation efficiency of the photogenerated charge

had significantly improved *via* the formation of the heterojunction between $FeVO_4$ and $Bi_7O_9I_3$ [124]. The onset potential value of the $Bi_7O_9I_3$ photoanode for water oxidation was 1.59 V (*vs.* RHE), while the onset potential value of the 6.25%wt–$FeVO_4/Bi_7O_9I_3$ photoanode shifted to 1.50 V (*vs.* RHE). The cathodic shift of the onset potential value demonstrated that the charge transport was more efficient and that the photocurrent density had improved [97,125].

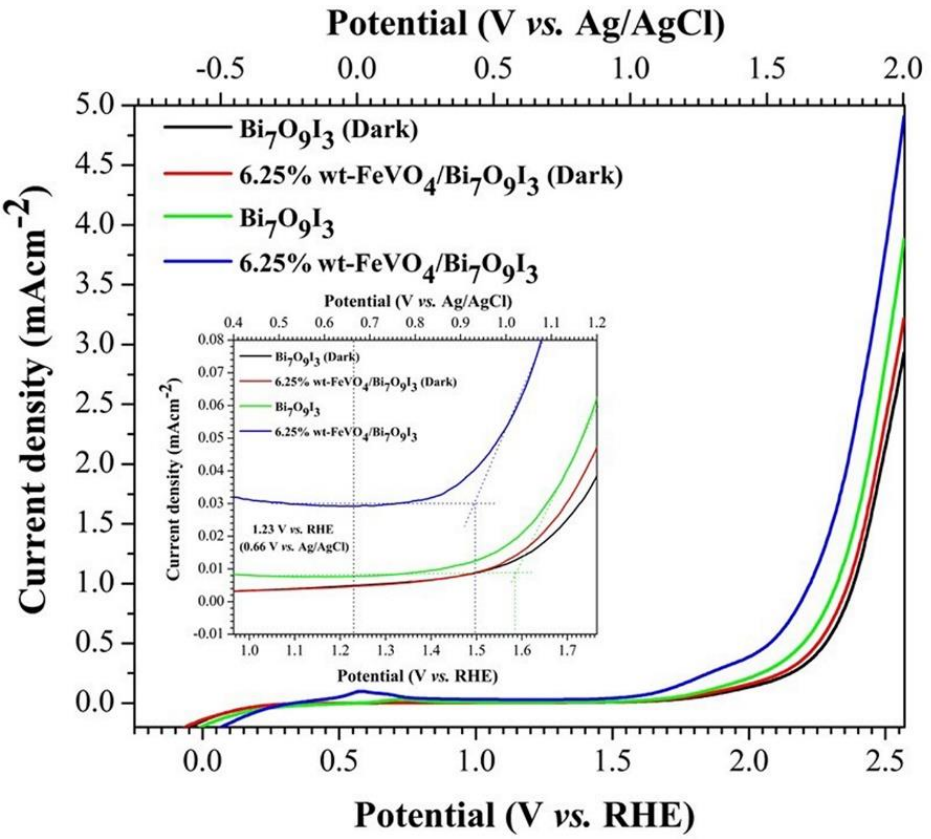

Figure 6.15 Linear sweep voltammograms of the $Bi_7O_9I_3$ and the 6.25%wt-$FeVO_4/Bi_7O_9I_3$ photoanodes in dark and under light illumination.

Chapter 7 Conclusion

$CuInS_2$ nanoparticles were synthesized by a cyclic microwave irradiation method using three different polyol solvents – ethylene glycol (EG), glycerol (Gly), and propylene glycol (PG). Different polyol solvents have different physical and chemical properties which differentially affect the microwave synthesis of nanomaterials. The characteristics of the synthesized powders were examined by XRD and FESEM techniques. In addition, the reducing capability of each solvent was determined by FTIR technique. Characterized by XRD, the powders synthesized using ethylene glycol and glycerol were pure $CuInS_2$ with tetragonal structure. However, $CuInS_2$ with the existence of CuS was obtained when using propylene glycol due to the lower resulting reaction temperature. FTIR spectra of the residual solvents after the synthesis process were determined and this revealed that ethylene glycol and glycerol were the solvents with good reducing capability. FESEM images revealed that the synthesized $CuInS_2$ powders were composed of nanoparticles with diameters in the range of 20–100 nm. The $CuInS_2$ nanoparticles synthesized using glycerol were smaller than those synthesized using ethylene glycol, due to the higher viscosity of glycerol.

In addition, hollow– microsphere $CuInS_2$ was successfully synthesized by a cyclic microwave irradiation method using L–cysteine as a sulfur source. The effect of microwave power (180–600 W) on the purity, morphology, and particle size of the synthesized powders was investigated. X–ray diffraction (XRD) analysis showed that the synthesized powders were pure $CuInS_2$ with a tetragonal structure. Transmission electron microscopy (TEM) analysis revealed that the $CuInS_2$ powder synthesized at 180 W composed of solid microspheres with a diameter of about 250 nm. Increasing the microwave power to 300 W and 450 W transformed some of the sub–microspheres into hollow sub–microspheres. At 600 W, all of the $CuInS_2$ sub–microspheres were hollow. Based on time–dependent experiment, formation mechanisms of the $CuInS_2$ solid and hollow sub–microspheres were discussed. The

photoconductivity of the $CuInS_2$ hollow sub–microspheres was greater than that of the $CuInS_2$ solid sub–microspheres, suggesting that the $CuInS_2$ hollow sub–microspheres were favorable to increase current carrier concentration and to improve electron transport. UV–Vis diffuse reflectance spectrum (UV–Vis DRS) of the $CuInS_2$ hollow sub–microspheres showed strong absorption intensity with a direct band gap energy of 1.48 eV, which is potentially useful in solar–light driven applications.

Tetragonal and monoclinic $BiVO_4$ (t–$BiVO_4$ and m–$BiVO_4$) were successfully synthesized via a cyclic microwave irradiation method at low microwave heating power. The photocatalysts were characterized by X–ray powder diffraction (XRD), field emission scanning electron microscopy (FESEM), transmission electron microscopy (TEM) and UV–Vis diffuse reflectance spectroscopy (UV–Vis DRS). The effect of different phases of $BiVO_4$ on the decolorization efficiency of methylene blue under visible light irradiation was investigated. Results clearly showed that the m–$BiVO_4$ exhibited monoclinic phase the higher decolorization efficiency than the t–$BiVO_4$ due to its larger particles surface area and narrower band gap energy tetragonal phase. The m–$BiVO_4$ catalyst degraded 60.75% of methylene blue was degraded within 360 min under visible light irradiation. The calculated reaction rate constant (k) for the methylene blue degradation was 2.5×10^{-3} min^{-1}.

Novel $CuInS_2$/m–$BiVO_4$ composites with different mass ratios were successfully synthesized by cyclic microwave radiation, followed by thermal treatment process. The $CuInS_2$/m–$BiVO_4$ composite with mass ratio of 1:3 exhibited the highest decolorization efficiency; 90.21% of MB degraded within 360 min. The difference in the decolorization efficiency of MB, RhB, and MO in the presence of the $CuInS_2$/m–$BiVO_4$ photocatalyst caused by the surface charge of the photocatalyst, types of the dyes as well as their molecular structures. The photoelectrochemical properties of the $CuInS_2$/m–$BiVO_4$ photoelectrode, including the current density and the onset potential were enhanced. The current response of the $CuInS_2$/m–$BiVO_4$ photoelectrode was 4.6 times higher than that of the pure m–$BiVO_4$. The enhancement of the photocatalytic and PEC performance was caused by the increased ability to absorb visible light, and the enhanced charge separation and transportation between the $CuInS_2$ and m–$BiVO_4$ contact

interface. The $CuInS_2$/m–$BiVO_4$ composite is a promising photocatalyst for treating organic pollutants in wastewater as well as a photoelectrode for photoelectrochemical application.

Novel $FeVO_4$/$Bi_7O_9I_3$ nanocomposites with different weight percentages (3, 6.25, 12.5, and 25%wt) of $FeVO_4$ were successfully synthesized by cyclic microwave irradiation, followed by wet impregnation. The applications for photocatalytic dye degradation and photoelectrochemical (PEC) were investigated. The 6.25%wt–$FeVO_4$/$Bi_7O_9I_3$ nanocomposite exhibited excellent photocatalytic degradation of methylene blue, rhodamine B, and methyl orange with decolorization efficiencies of 81.3%, 98.9%, and 94.9% within 360 min, respectively. Moreover, this nanocomposite possessed excellent reusability and stability during the photocatalytic degradation process. PEC performance in water oxidation of the 6.25%wt–$FeVO_4$/$Bi_7O_9I_3$ photoanode was evaluated by linear sweep voltammetry (LSV) measurement. Enhanced PEC performance with photocurrent density of 0.029 $mA.cm^{-2}$ at 1.23 V (*vs.* RHE) was observed under visible–light irradiation, which was ca. 3.7 times higher than that of the pure $Bi_7O_9I_3$. Based on the optical characterization, energy band positions, and active species trapping experiments, a possible photocatalytic mechanism of the $FeVO_4$/$Bi_7O_9I_3$ heterojunction was discussed. The enhancement in the photocatalytic and the PEC performance ascribed to synergistic effects of visible–light absorption and a favorable "type II heterojunction" structure of the $FeVO_4$/$Bi_7O_9I_3$ nanocomposite. These were the main effects that promoted the photogenerated electrons and holes transfer across the contact interface between $FeVO_4$ and $Bi_7O_9I_3$, as well as suppressed the recombination of photogenerated electron–hole pairs and facilitated charge separation and transportation.

Chapter 8 References

[1] T. Jafari, E. Moharreri, A. Amin, R. Miao, W. Song, S. Suib, Photocatalytic Water Splitting—The Untamed Dream: A Review of Recent Advances, Molecules. 21 (2016) 900. doi:10.3390/molecules21070900.

[2] S. Xia, L. Zhang, G. Pan, P. Qian, Z. Ni, Photocatalytic degradation of methylene blue with a nanocomposite system: synthesis, photocatalysis and degradation pathways, Phys.Chem.Chem.Phys. 17 (2015) 5345–5351. doi:10.1039/c4cp03877k.

[3] M. Umar, H. Abdul, Organic Pollutants – Monitoring, Risk and Treatment, in: R. M., Nageeb (Ed.), InTech, 1st ed., InTech, 2013: pp. 195–208. doi:10.5772/53699.

[4] W.S. Kuo, P.H. Ho, Solar photocatalytic decolorization of methylene blue in water, Chemosphere. 45 (2001) 77–83. doi:10.1016/S0045-6535(01)00008-X.

[5] S. Dong, J. Feng, M. Fan, Y. Pi, L. Hu, X. Han, M. Liu, J. Sun, J. Sun, Recent developments in heterogeneous photocatalytic water treatment using visible light-responsive photocatalysts: A review, RSC Adv. 5 (2015) 14610–14630. doi:10.1039/c4ra13734e.

[6] A. Hernández-Ramírez, I. Medina-Ramírez, Photocatalytic Semiconductors, Springer, Switzerland, 2015. doi:10.1007/978-3-319-10999-2.

[7] A. Malathi, J. Madhavan, M. Ashokkumar, P. Arunachalam, A review on $BiVO_4$ photocatalyst: Activity enhancement methods for solar photocatalytic applications, Appl. Catal. A Gen. 555 (2018) 47–74. doi:10.1016/j.apcata.2018.02.010.

[8] J.H. Kim, J.S. Lee, $BiVO_4$-based heterostructured photocatalysts for solar water splitting: A review, Energy Environ. Focus. 3 (2014) 339–353. doi:10.1166/eef.2014.1121.

[9] H. Zhao, F. Tian, R. Wang, R. Chen, A review on bismuth-related nanomaterials for photocatalysis, Rev. Adv. Sci. Eng. 3 (2014) 3–27. doi:10.1166/rase.2014.1050.

[10] X. Xiao, W.-D. Zhang, Hierarchical Bi7O9I3 micro/nano-architecture: facile synthesis, growth mechanism, and high visible light photocatalytic performance, RSC Adv. 1 (2011) 1099. doi:10.1039/c1ra00323b.

[11] X. Xiao, R. Hao, X. Zuo, J. Nan, L. Li, W. Zhang, Microwave-assisted synthesis of hierarchical Bi7O9I3 microsheets for efficient photocatalytic degradation of bisphenol-A under visible light

irradiation, Chem. Eng. J. 209 (2012) 293–300. doi:10.1016/j.cej.2012.07.142.

[12] Q.C. Liu, D.K. Ma, Y.Y. Hu, Y.W. Zeng, S.M. Huang, Various bismuth oxyiodide hierarchical architectures: Alcohothermal– controlled synthesis, photocatalytic activities, and adsorption capabilities for phosphate in water, Appl. Mater. Interfaces. 5 (2013) 11927–11934. doi:10.1021/am4036702.

[13] R. Marschall, Semiconductor composites: Strategies for enhancing charge carrier separation to improve photocatalytic activity, Adv. Funct. Mater. 24 (2014) 2421–2440. doi:10.1002/adfm.201303214.

[14] H. Li, W. Hong, Y. Cui, X. Hu, S. Fan, L. Zhu, Enhancement of the visible light photocatalytic activity of Cu2O/BiVO4 catalysts synthesized by ultrasonic dispersion method at room temperature, Mater. Sci. Eng. B Solid-State Mater. Adv. Technol. 181 (2014) 1–8. doi:10.1016/j.mseb.2013.11.001.

[15] Z. Xiang, Y. Wang, D. Zhang, P. Ju, BiOI/$BiVO_4$ p–n heterojunction with enhanced photocatalytic activity under visible-light irradiation, J. Ind. Eng. Chem. 40 (2016) 83–92. doi:10.1016/j.jiec.2016.06.009.

[16] Z. Xiang, Y. Wang, P. Ju, Y. Long, D. Zhang, Facile fabrication of AgI/$BiVO_4$ composites with enhanced visible photocatalytic degradation and antibacterial ability, J. Alloys Compd. 721 (2017) 622–627. doi:10.1016/j.jallcom.2017.06.030.

[17] Q. Wang, T. Niu, L. Wang, C. Yan, J. Huang, J. He, H. She, B. Su, Y. Bi, FeF_2/$BiVO_4$ heterojuction photoelectrodes and evaluation of its photoelectrochemical performance for water splitting, Chem. Eng. J. 337 (2018) 506–514. doi:10.1016/j.cej.2017.12.126.

[18] I. Tateishi, H. Katsumata, T. Suzuki, S. Kaneco, Visible-Light-Induced AgI/Bi7O9I3 Composites with Enhanced Photocatalytic Activity, Catal. Letters. 147 (2017) 1503–1509. doi:10.1007/s10562-017-2059-8.

[19] H. Liu, Y. Su, Z. Chen, Z. Jin, Y. Wang, Bi7O9I3/reduced graphene oxide composite as an efficient visible-light-driven photocatalyst for degradation of organic contaminants, J. Mol. Catal. A Chem. 391 (2014) 175–182. doi:10.1016/j.molcata.2014.04.029.

[20] D. Liu, Z. Jiang, C. Zhu, K. Qian, Z. Wu, J. Xie, Graphene-analogue BN-modified microspherical BiOI photocatalysts driven by visible light, Dalt. Trans. 45 (2016) 2505–2516.

doi:10.1039/C5DT03408F.

[21] Y. Wang, Q. Wang, X. Zhan, F. Wang, M. Safdar, J. He, Visible light driven type II heterostructures and their enhanced photocatalysis properties: a review, Nanoscale. 5 (2013) 8326. doi:10.1039/c3nr01577g.

[22] Y. Xiang, P. Ju, Y. Wang, Y. Sun, D. Zhang, J. Yu, Chemical etching preparation of the Bi2WO6/BiOI p–n heterojunction with enhanced photocatalytic antifouling activity under visible light irradiation, Chem. Eng. J. 288 (2016) 264–275. doi:10.1016/j.cej.2015.11.103.

[23] Y.J. Yuan, D.Q. Chen, Y.W. Huang, Z.T. Yu, J.S. Zhong, T.T. Chen, W.G. Tu, Z.J. Guan, D.P. Cao, Z.G. Zou, MoS_2 nanosheet–modified $CuInS_2$ photocatalyst for visible–light–driven hydrogen production from water, ChemSusChem. 9 (2016) 1003–1009. doi:10.1002/cssc.201600006.

[24] Y. Wang, J. Yang, W. Gao, R. Cong, T. Yang, Organic–free hydrothermal synthesis of chalcopyrite $CuInS_2$ and its photocatalytic activity for nitrate ions reduction, Mater. Lett. 137 (2014) 99–101. doi:10.1016/j.matlet.2014.08.144.

[25] M. Yue, R. Wang, B. Ma, R. Cong, W. Gao, T. Yang, Superior performance of $CuInS_2$ for photocatalytic water treatment: full conversion of highly stable nitrate ions into harmless N_2 under visible light, Catal. Sci. Technol. 6 (2016) 8300–8308. doi:10.1039/C6CY01858K.

[26] F. Shen, W. Que, Y. He, Y. Yuan, X. Yin, G. Wang, Enhanced photocatalytic activity of ZnO microspheres via hybridization with CuInSe2 and CuInS2 nanocrystals, ACS Appl. Mater. Interfaces. 4 (2012) 4087–92. doi:10.1021/am3008533.

[27] H. Fakhri, A.R. Mahjoub, A.H.C. Khavar, Synthesis and characterization of ZnO/$CuInS_2$ nanocomposite and investigation of their photocatalytic properties under visible light irradiation, Appl. Surf. Sci. 318 (2014) 65–73. doi:10.1016/j.apsusc.2014.01.024.

[28] F. Shen, W. Que, Y. Liao, X. Yin, Photocatalytic activity of TiO_2 nanoparticles sensitized by $CuInS_2$ quantum dots, Ind. Eng. Chem. Res. 50 (2011) 9131–9137. doi:10.1021/ie2007467.

[29] Y. Li, Z. Liu, Y. Wang, Z. Liu, J. Han, J. Ya, ZnO/$CuInS_2$ core/shell heterojunction nanoarray for photoelectrochemical water splitting, Int. J. Hydrogen Energy. 37 (2012) 15029–15037. doi:10.1016/j.ijhydene.2012.07.117.

[30] T. Li, X. Li, Q. Zhao, Y. Shi, W. Teng, Fabrication of n–type $CuInS_2$ modified TiO_2 nanotube arrays heterostructure photoelectrode with enhanced photoelectrocatalytic properties, Appl. Catal. B

Environ. 156–157 (2014) 362–370. doi:10.1016/j.apcatb.2014.03.035.

[31] C. Li, Z. Xi, W. Fang, M. Xing, J. Zhang, Enhanced photocatalytic hydrogen evolution activity of $CuInS_2$ loaded TiO_2 under solar light irradiation, J. Solid State Chem. 226 (2015) 94–100. doi:10.1016/j.jssc.2015.02.011.

[32] B. Ozturk, G.S. Pozan Soylu, Synthesis of surfactant-assisted FeVO4 nanostructure: Characterization and photocatalytic degradation of phenol, J. Mol. Catal. A Chem. 398 (2015) 65–71. doi:10.1016/j.molcata.2014.11.013.

[33] S.J. Hu, J. Yang, X.H. Liao, Highly Efficient Degradation of Methylene Blue on Microwave Synthesized FeVO4 Nanoparticles Photocatalysts under Visible-Light Irradiation, Appl. Mech. Mater. 372 (2013) 153–157. doi:10.4028/www.scientific.net/AMM.372.153.

[34] Y. Li, S. Chen, A. Xu, F. Ma, F. Chen, W. Lu, Research on the nanocrystal FeVxOycatalysts for new reaction from propane to propylene and CO, Appl. Surf. Sci. 320 (2014) 552–557. doi:10.1016/j.apsusc.2014.09.126.

[35] J. Li, W. Zhao, Y. Guo, Z. Wei, M. Han, H. He, S. Yang, C. Sun, Facile synthesis and high activity of novel BiVO4/FeVO4 heterojunction photocatalyst for degradation of metronidazole, Appl. Surf. Sci. 351 (2015) 270–279. doi:10.1016/j.apsusc.2015.05.134.

[36] X. Liu, Y. Kang, Synthesis and high visible-light activity of novel Bi2O3/FeVO4 heterojunction photocatalyst, Mater. Lett. 164 (2016) 229–231. doi:10.1016/j.matlet.2015.10.137.

[37] P. James W. Caras, Electromagnetic spectrum, (2013).

[38] G. Booth, H. Zollinger, K. McLaren, W.G. Sharples, A. Westwell, Dyes, General Survey, in: Ullmann's Encycl. Ind. Chem., Wiley-VCH Verlag GmbH & Co. KGaA, Weinheim, Germany, 2000. doi:10.1002/14356007.a09_073.

[39] M. Rochkind, S. Pasternak, Y. Paz, Using Dyes for Evaluating Photocatalytic Properties: A Critical Review, Molecules. 20 (2015) 88–110. doi:10.3390/molecules20010088.

[40] U.G. Akpan, B.H. Hameed, Parameters affecting the photocatalytic degradation of dyes using TiO2-based photocatalysts: A review, J. Hazard. Mater. 170 (2009) 520–529. doi:10.1016/j.jhazmat.2009.05.039.

[41] L.H. and V.F. Allan Clements, Colorants, (n.d.).

[42] W.Z. Tang, Z. Zhang, H. An, M.O. Quintana, D.F. Torres, TiO2/UV Photodegradation of Azo Dyes

in Aqueous Solutions, Environ. Technol. 18:1 (1997) 1–12. doi:10.1080/09593330199796184666.

[43] T. Wei, C. Wan, Heterogeneous Photocatalytic Oxidation of Phenol with Titanium Dioxide Powders, Ind. Eng. Chem. Res. 30 (1991) 1293–1300. doi:10.1021/ie00054a033.

[44] S. Kaneco, M.A. Rahman, T. Suzuki, H. Katsumata, K. Ohta, Optimization of solar photocatalytic degradation conditions of bisphenol A in water using titanium dioxide, J. Photochem. Photobiol. A Chem. 163 (2004) 419–424. doi:10.1016/j.jphotochem.2004.01.012.

[45] Sigma–aldrich, Methylene blue certified by the Biological Stain Commission | Sigma–Aldrich, (n.d.).

[46] P. Lidström, J. Tierney, B. Wathey, J. Westman, Microwave assisted organic synthesis—a review, Tetrahedron. 57 (2001) 9225–9283. doi:10.1016/S0040–4020(01)00906–1.

[47] H. Brittany, Microwave Synthesis: Chemistry at the speed of light, (2002) 1–296.

[48] Y.–J. Zhu, F. Chen, Microwave–Assisted Preparation of Inorganic Nanostructures in Liquid Phase, Chem. Rev. 114 (2014) 6462–6555. doi:10.1021/cr400366s.

[49] D. Gangrade, L. Sd, M. Al, Overview on microwave synthesis – Important tool for green Chemistry, Int J Res Pharm Sci. 5 (2015) 37–42. www.ijrpsonline.com.

[50] S. Shen, L. Zhao, Z. Zhou, L. Guo, Enhanced Photocatalytic Hydrogen Evolution over Cu–Doped ZnIn2S4 under Visible Light, J. Phys. Chem. C. 112 (2008) 16148. doi:10.1021/jp804525q.

[51] X. Gou, F. Cheng, Y. Shi, L. Zhang, S. Peng, J. Chen, P. Shen, Shape–Controlled Synthesis of Ternary Chalcogenide ZnIn2S4 and CuIn (S,Se)2 Nano–/Microstructures via Facile Solution Route, J. Am. Chem. Soc. 128 (2006) 7222–7229. doi:10.1021/ja0580845.

[52] M. Reza Gholipour, C.T. Dinh, F. Béland, T.O. Do, Nanocomposite heterojunctions as sunlight–driven photocatalysts for hydrogen production from water splitting, Nanoscale. 7 (2015) 8187–8208. doi:10.1039/c4nr07224c.

[53] J. Ye, L. Sun, S. Gao, Fabrication of hollow PbS nanospheres and application in phenol release, Springerplus. 2 (2013) 1–6. doi:10.1186/2193–1801–2–323.

[54] S. Wang, J. Zhang, J. Jiang, R. Liu, B. Zhu, M. Xu, Y. Wang, J. Cao, M. Li, Z. Yuan, S. Zhang, W. Huang, S. Wu, Porous ceria hollow microspheres: Synthesis and characterization, Microporous Mesoporous Mater. 123 (2009) 349–353. doi:10.1016/j.micromeso.2009.04.020.

[55] Y. Liu, L. Wang, W. Jin, C. Zhang, M. Zhou, W. Chen, Synthesis and photocatalytic property of

TiO_2@V_2O_5 core–shell hollow porous microspheres towards gaseous benzene, J. Alloys Compd. 690 (2017) 604–611. doi:10.1016/j.jallcom.2016.08.137.

[56] P. Cui, J. Wang, Z. Wang, J. Chen, X. Xing, L. Wang, R. Yu, Bismuth oxychloride hollow microspheres with high visible light photocatalytic activity, Nano Res. 9 (2016) 593–601. doi:10.1007/s12274–015–0939–z.

[57] H.M. Yang, S.Y. Ma, H.Y. Jiao, Q. Chen, Y. Lu, W.X. Jin, W.Q. Li, T.T. Wang, X.H. Jiang, Z. Qiang, H. Chen, Synthesis of Zn_2SnO_4 hollow spheres by a template route for high–performance acetone gas sensor, Sensors Actuators, B Chem. 245 (2017) 493–506. doi:10.1016/j.snb.2017.01.205.

[58] G. Han, M. Wang, D. Li, J. Bai, G. Diao, Novel upconversion Er, Yb–CeO_2 hollow spheres as scattering layer materials for efficient dye–sensitized solar cells, Sol. Energy Mater. Sol. Cells. 160 (2017) 54–59. doi:10.1016/j.solmat.2016.10.021.

[59] N. Yu, G. Li, Y. Gao, X. Liu, S. Ma, Stimuli–sensitive hollow spheres from chitosan–graft–β–cyclodextrin for controlled drug release, Int. J. Biol. Macromol. 93 (2016) 971–977. doi:10.1016/j.ijbiomac.2016.09.068.

[60] X. Zhu, C.Q. Wang, pH and redox–operated nanovalve for size–selective cargo delivery on hollow mesoporous silica spheres, J. Colloid Interface Sci. 480 (2016) 39–48. doi:10.1016/j.jcis.2016.06.043.

[61] J. Xu, B. Lu, W. Tang, H. Hu, Y. Yang, C. Cui, J. Zhao, L. Xu, Y. Zhang, J. Pan, TiO 2 hollow spheres as light scattering centers in TiO 2 photoanodes for dye–sensitized solar cells: the effect of sphere diameter, J. Alloys Compd. 663 (2015) 211–216. doi:10.1016/j.jallcom.2015.12.118.

[62] J. Chen, C. Li, F. Xu, Y. Zhou, W. Lei, L. Sun, Y. Zhang, Hollow SnO<inf>2</inf> microspheres for high–efficiency bilayered dye sensitized solar cell, RSC Adv. 2 (2012) 7384–7387. doi:10.1039/c2ra20909h.

[63] L. Zheng, Y. Xu, Y. Song, C. Wu, M. Zhang, Y. Xie, Nearly monodisperse CuInS2 hierarchical microarchitectures for photocatalytic H2 evolution under visible light, Inorg. Chem. 48 (2009) 4003–4009. doi:10.1021/ic802399f.

[64] C. Yu, L. Zhang, L. Tian, D. Liu, F. Chen, C. Wang, Synthesis and formation mechanism of $CuInS_2$ nanocrystals with a tunable phase, CrystEngComm. 16 (2014) 9596–9602. doi:10.1039/C4CE00893F.

[65] M. Mousavi–Kamazani, M. Salavati–Niasari, M. Sadeghinia, Facile hydrothermal synthesis, formation mechanism and solar cell application of CuInS2 nanoparticles using novel starting reagents, Mater. Lett. 142 (2015) 145–149. doi:10.1016/j.matlet.2014.12.014.

[66] S.Y. Hu, Y.C. Lee, B.J. Chen, Characterization of calcined CuInS2nanocrystals prepared by microwave–assisted synthesis, J. Alloys Compd. 690 (2017) 15–20. doi:10.1016/j.jallcom.2016.08.098.

[67] X. Geng, L. Zhai, J. Hu, L. Wang, Z. Xiong, C. Zou, L. Zhang, Y. Yang, S. Huang, The synthesis of hollow $CuInS_2$ microspheres with hierarchical structures, Mater. Chem. Phys. 149 (2015) 743–750. doi:10.1016/j.matchemphys.2014.11.039.

[68] J. Zai, H. Chen, C. Huang, J. Huang, F. Chen, M. Xu, X. Qian, The fabrication of hollow cubic–like $CuInS_2$ cages using Cu_2O crystals as sacrificing template, Mater. Chem. Phys. 143 (2013) 15–18. doi:10.1016/j.matchemphys.2013.08.056.

[69] S. Lei, C. Wang, Q. Huang, L. Liu, Y. Ge, Q. Tang, B. Cheng, Y. Xiao, L. Zhou, Fabrication of hollow–sphere films of wurtzite CuInS2on copper substrate, Mater. Chem. Phys. 143 (2013) 195–202. doi:10.1016/j.matchemphys.2013.08.051.

[70] D. Wu, J. Duan, C. Zhang, K. Guo, H. Zhu, Sacrificial template synthesis and photothermal conversion enhancements of hierarchical and hollow CuInS2 microspheres, J. Phys. Chem. C. 117 (2013) 9121–9128. doi:10.1021/jp400806k.

[71] Y. Qi, K. Tang, S. Zeng, W. Zhou, Template–free one–step fabrication of porous $CuInS_2$ hollow microspheres, Microporous Mesoporous Mater. 114 (2008) 395–400. doi:10.1016/j.micromeso.2008.01.027.

[72] A. Mirzaei, G. Neri, Microwave–assisted synthesis of metal oxide nanostructures for gas sensing application: A review, Sensors Actuators, B Chem. 237 (2016) 749–775. doi:10.1016/j.snb.2016.06.114.

[73] N. Chumha, T. Thongtem, S. Thongtem, D. Tantraviwat, S. Kittiwachana, S. Kaowphong, A single–step method for synthesis of CuInS2nanostructures using cyclic microwave irradiation, Ceram. Int. 42 (2016) 15643–15649. doi:10.1016/j.ceramint.2016.07.019.

[74] E. H. Grant, S. Gabriel, C. Gabriel, D. Michael P. Mingos, B. S. J. Halstead, Dielectric parameters relevant to microwave dielectric heating, Chem. Soc. Rev. 27 (1998) 213–224.

doi:10.1039/a827213z.

[75] G. V. Mashalkar, P.A. Chalikwar, A.C. Kumbharkhane, Temperature–dependent dielectric relaxation study of polyhydric alcohols (propane–1,3 and 1,2–diol) using a TDR technique, Phys. Chem. Liq. 53 (2015) 307–317. doi:10.1080/00319104.2014.961190.

[76] I. Boz, Influence of synthesis conditions on particle morphology of nanosized, 31 (2008) 619–624.

[77] J.C. Colmenares, R. Luque, Heterogeneous photocatalytic nanomaterials: Prospects and challenges in selective transformations of biomass–derived compounds, Chem. Soc. Rev. 43 (2014) 765–778. doi:10.1039/c3cs60262a.

[78] T. Laino, C. Tuma, P. Moor, E. Martin, S. Stolz, A. Curioni, Mechanisms of propylene glycol and triacetin pyrolysis, J. Phys. Chem. A. 116 (2012) 4602–4609. doi:10.1021/jp300997d.

[79] Y. Zhang, L. Liu, J. Ying, J. Qian, L. Liu, L. Wang, Biomolecule–assisted synthesis of ZnIn2S4 flower–like hollow microspheres, Mater. Lett. 105 (2013) 185–188. doi:10.1016/j.matlet.2013.03.117.

[80] N. Sahin, K. Servat, T. Napporn, Y. Holade, K. Kokoh, Recent Advances in Carbon Supported Metal Nanoparticles Preparation for Oxygen Reduction Reaction in Low Temperature Fuel Cells, Catalysts. 5 (2015) 310–348. doi:10.3390/catal5010310.

[81] X. Chen, X. Zhang, Z. Wang, J. Wan, Y. Qian, Biomolecule–assisted hydrothermal synthesis and one–dimensional self–assembly of copper sulfide nanocrystallites, Mater. Chem. Phys. 98 (2006) 419–421. doi:10.1016/j.matchemphys.2005.09.056.

[82] L.Y. Chen, Z. De Zhang, W.Z. Wang, Self–assembled porous 3D flowerlike β–In_2S_3 structures: Synthesis, characterization, and optical properties, J. Phys. Chem. C. 112 (2008) 4117–4123. doi:10.1021/jp710074h.

[83] F. Li, T. Kong, W. Bi, D. Li, Z. Li, X. Huang, Synthesis and optical properties of CuS nanoplate–based architectures by a solvothermal method, Appl. Surf. Sci. 255 (2009) 6285–6289. doi:10.1016/j.apsusc.2009.02.001.

[84] M. Saranya, C. Santhosh, R. Ramachandran, A. Nirmala Grace, Growth of CuS Nanostructures by Hydrothermal Route and Its Optical Properties, J. Nanotechnol. 2014 (2014) 1–8. doi:10.1155/2014/321571.

[85] M. Li, W.H. Zhou, J. Guo, Y.L. Zhou, Z.L. Hou, J. Jiao, Z.J. Zhou, Z.L. Du, S.X. Wu, Synthesis of pure metastable wurtzite CZTS nanocrystals by facile one–pot method, J. Phys. Chem. C. 116 (2012) 26507–26516. doi:10.1021/jp307346k.

[86] M. Aslam, M.K. Jangid, B. Ananthoju, N. V. Medhekar, J. Mohapatra, D. Bahadur, Cation/Anion Substitution in Cu_2ZnSnS_4 for Improved Photovoltaic Performance, Sci. Rep. 6 (2016) 1–11. doi:10.1038/srep35369.

[87] N. Yang, Z. Tang, Z. Dong, J. Zhai, L. Jiang, D. Wang, J.E. Halpert, L. Yi, X. Lai, Accurate Control of Multishelled ZnO Hollow Microspheres for Dye–Sensitized Solar Cells with High Efficiency, Adv. Mater. 24 (2012) 1046–1049. doi:10.1002/adma.201104626.

[88] H. Zhang, R. Wu, H. Xu, F. Li, S. Wang, J. Wang, T. Zhang, A simple spray reaction synthesis and characterization of hierarchically porous SnO_2 microspheres for an enhanced dye sensitized solar cell, RSC Adv. 7 (2017) 12446–12454. doi:10.1039/c6ra27235e.

[89] P.P. Sahoo, P.A. Maggard, Crystal Chemistry, Band Engineering, and Photocatalytic Activity of the LiNb 3 O 8 –CuNb 3 O 8 Solid Solution, Inorg. Chem. 52 (2013) 4443–4450. doi:10.1021/ic302649s.

[90] A. Walsh, Y. Yan, M.N. Huda, M.M. Al–Jassim, S.–H.H. Wei, Band Edge Electronic Structure of BiVO4 : Elucidating the Role of the Bi s and V d Orbitals, Chem. Mater. 21 (2009) 547–551. doi:10.1021/cm802894z.

[91] D. Benlin, X. Tu, W. Zhao, X. Wang, D.Y.C. Leung, J. Xu, A novel three–dimensional heterojunction photocatalyst for the photocatalytic oxidation of crystal violet and reduction of Cr^{6+}, Chemosphere. 211 (2018) 10–16. doi:10.1016/j.chemosphere.2018.07.131.

[92] H. Liu, H. Hao, J. Xing, J. Dong, Z. Zhang, Z. Zheng, K. Zhao, Enhanced photocatalytic capability of zinc ferrite nanotube arrays decorated with gold nanoparticles for visible light–driven photodegradation of rhodamine B, J. Mater. Sci. 51 (2016) 5872–5879. doi:10.1007/s10853–016–9888–5.

[93] Q. Liu, H. Lu, Z. Shi, F. Wu, J. Guo, K. Deng, L. Li, 2D $ZnIn_2S_4$ nanosheet/1D TiO_2 nanorod heterostructure arrays for improved photoelectrochemical water splitting, ACS Appl. Mater. Interfaces. 6 (2014) 17200–17207. doi:10.1021/am505015j.

[94] Q. Wang, J. He, Y. Shi, S. Zhang, T. Niu, H. She, Y. Bi, Z. Lei, Synthesis of MFe_2O_4 (M = Ni,

Co)/$BiVO_4$ film for photolectrochemical hydrogen production activity, Appl. Catal. B Environ. 214 (2017) 158–167. doi:10.1016/j.apcatb.2017.05.044.

[95] Z. Wu, X. Yan, H. Shen, J. Li, W. Shi, Enhanced visible–light–driven photocatalytic activity of Bi12O15Cl6/Bi2WO6 Z–scheme heterojunction photocatalysts for tetracycline degradation, Mater. Sci. Eng. B Solid–State Mater. Adv. Technol. 231 (2018) 86–92. doi:10.1016/j.mseb.2018.10.003.

[96] L. Xia, J. Bai, J. Li, Q. Zeng, L. Li, B. Zhou, High–performance $BiVO_4$ photoanodes cocatalyzed with an ultrathin α–Fe_2O_3 layer for photoelectrochemical application, Appl. Catal. B Environ. 204 (2017) 127–133. doi:10.1016/j.apcatb.2016.11.015.

[97] Y.X. Yu, W.X. Ouyang, W.D. Zhang, Photoelectrochemical property of the BiOBr–BiOI/ZnO heterostructures with tunable bandgap, J. Solid State Electrochem. 18 (2014) 1743–1750. doi:10.1007/s10008–014–2402–6.

[98] M.M. Khan, S.A. Ansari, M.E. Khan, M.O. Ansari, B.K. Min, M.H. Cho, Visible light–induced enhanced photoelectrochemical and photocatalytic studies of gold decorated SnO<inf>2</inf> nanostructures, New J. Chem. 39 (2015) 2758–2766. doi:10.1039/c4nj02245a.

[99] Z. Zhang, M. Wang, W. Cui, H. Sui, Synthesis and characterization of a core–shell $BiVO_4$@g–C_3N_4 photo–catalyst with enhanced photocatalytic activity under visible light irradiation, RSC Adv. 7 (2017) 8167–8177. doi:10.1039/C6RA27766G.

[100] Y. He, L. Li, W. Fan, C. Zhang, M.K.H. Leung, A novel and facile solvothermal–and–hydrothermal method for synthesis of uniform $BiVO_4$ film with high photoelectrochemical performance, J. Alloys Compd. 732 (2018) 593–602. doi:10.1016/j.jallcom.2017.10.153.

[101] V. Renuga, C. Neela Mohan, A. Manikandan, Influence of Mn^{2+} ions on Both Core/Shell of $CuInS_2$/ZnS Nanocrystals, Mater. Res. Bull. 98 (2017) 265–274. doi:10.1016/j.materresbull.2017.09.067.

[102] M. Mousavi, A. Habibi–Yangjeh, Magnetically separable ternary g–C_3N_4/Fe_3O_4/BiOI nanocomposites: Novel visible–light–driven photocatalysts based on graphitic carbon nitride, J. Colloid Interface Sci. 465 (2016) 83–92. doi:10.1016/j.jcis.2015.11.057.

[103] X. Li, J. Xia, W. Zhu, J. Di, B. Wang, S. Yin, Z. Chen, H. Li, Facile synthesis of few–layered MoS_2 modified BiOI with enhanced visible–light photocatalytic activity, Colloids Surfaces A

Physicochem. Eng. Asp. 511 (2016) 1–7. doi:10.1016/j.colsurfa.2016.09.033.

[104] M. Long, P. Hu, H. Wu, Y. Chen, B. Tan, W. Cai, Understanding the composition and electronic structure dependent photocatalytic performance of bismuth oxyiodides, J. Mater. Chem. A. 3 (2015) 5592–5598. doi:10.1039/C4TA06134A.

[105] G. Wu, Y. Zhao, Y. Li, H. Ma, J. Zhao, pH-dependent synthesis of iodine-deficient bismuth oxyiodide microstructures: Visible-light photocatalytic activity, J. Colloid Interface Sci. 510 (2018) 228–236. doi:10.1016/j.jcis.2017.09.053.

[106] C. Liao, Z. Ma, X. Chen, X. He, J. Qiu, Controlled synthesis of bismuth oxyiodide toward optimization of photocatalytic performance, Appl. Surf. Sci. 387 (2016) 1247–1256. doi:10.1016/j.apsusc.2016.06.140.

[107] C.D. Morton, I.J. Slipper, M.J.K. Thomas, B.D. Alexander, Synthesis and characterisation of Fe-V-O thin film photoanodes, J. Photochem. Photobiol. A Chem. 216 (2010) 209–214. doi:10.1016/j.jphotochem.2010.08.010.

[108] H. Li, Y. Cui, W. Hong, B. Xu, Enhanced photocatalytic activities of BiOI/ZnSn(OH)6 composites towards the degradation of phenol and photocatalytic H2 production, Chem. Eng. J. 228 (2013) 1110–1120. doi:10.1016/j.cej.2013.05.086.

[109] Y. Huang, H. Li, W. Fan, F. Zhao, W. Qiu, H. Ji, Y. Tong, Defect Engineering of Bismuth Oxyiodide by IO3-Doping for Increasing Charge Transport in Photocatalysis, ACS Appl. Mater. Interfaces. 8 (2016) 27859–27867. doi:10.1021/acsami.6b10653.

[110] X. She, Z. Zhang, M. Baek, K. Yong, Elevated photoelectrochemical activity of FeVO 4 /ZnFe 2 O 4 /ZnO branch-structures via slag assisted-synthesis, RSC Adv. 7 (2017) 16787–16794. doi:10.1039/C7RA00812K.

[111] S. Samanta, R. Srivastava, Thermal catalysis vs. photocatalysis: A case study with FeVO4/g-C3N4 nanocomposites for the efficient activation of aromatic and benzylic C–H bonds to oxygenated products, Appl. Catal. B Environ. 218 (2017) 621–636. doi:10.1016/j.apcatb.2017.06.043.

[112] Q. Nong, M. Cui, H. Lin, L. Zhao, Y. He, Fabrication, characterization and photocatalytic activity of g-C3N4 coupled with FeVO4 nanorod, RSC Adv. 5 (2015) 27933–27939. doi:10.1039/C5RA01484K.

[113] X.J. Wang, F.T. Li, D.Y. Li, R.H. Liu, S.J. Liu, Facile synthesis of flower–like BiOI hierarchical spheres at room temperature with high visible–light photocatalytic activity, Mater. Sci. Eng. B. 193 (2015) 112–120. doi:10.1016/j.mseb.2014.12.013.

[114] Z. Cui, M. Si, Z. Zheng, L. Mi, W. Fa, H. Jia, Preparation and characterization of Ag3PO4/BiOI composites with enhanced visible light driven photocatalytic performance, Catal. Commun. 42 (2013) 121–124. doi:10.1016/j.catcom.2013.08.011.

[115] Y. Lei, G. Wang, S. Song, W. Fan, M. Pang, Room temperature, template–free synthesis of BiOI hierarchical structures : Visible–light photocatalytic and electrochemical hydrogen storage properties, Dalt. Trans. 39 (2010) 3273–3278. doi:10.1039/b922126c.

[116] H. Lachheb, E. Puzenat, A. Houas, M. Ksibi, E. Elaloui, C. Guillard, J.M. Herrmann, Photocatalytic degradation of various types of dyes (Alizarin S, Crocein Orange G, Methyl Red, Congo Red, Methylene Blue) in water by UV–irradiated titania, Appl. Catal. B Environ. 39 (2002) 75–90. doi:10.1016/S0926–3373(02)00078–4.

[117] Y. Liu, J. Xu, L. Wang, H. Zhang, P. Xu, X. Duan, H. Sun, S. Wang, Three–dimensional BiOI/BiOX (X = Cl or Br) nanohybrids for enhanced visible–light photocatalytic activity, Nanomaterials. 7 (2017). doi:10.3390/nano7030064.

[118] S.M. Aghdam, M. Haghighi, S. Allahyari, L. Yosefi, Precipitation dispersion of various ratios of BiOI/BiOCl nanocomposite over g–C3N4 for promoted visible light nanophotocatalyst used in removal of acid orange 7 from water, J. Photochem. Photobiol. A Chem. 338 (2017) 201–212. doi:10.1016/j.jphotochem.2017.02.013.

[119] J. Lv, Q. Hu, C. Cao, Y. Zhao, Modulation of valence band maximum edge and photocatalytic activity of BiOX by incorporation of halides, Chemosphere. 191 (2018) 427–437. doi:10.1016/j.chemosphere.2017.09.149.

[120] J. Xu, L. Li, C. Guo, Y. Zhang, S. Wang, Removal of benzotriazole from solution by BiOBr photocatalysis under simulated solar irradiation, Chem. Eng. J. 221 (2013) 230–237. doi:10.1016/j.cej.2013.01.081.

[121] X. Li, C. Niu, D. Huang, X. Wang, X. Zhang, G. Zeng, Q. Niu, Preparation of magnetically separable Fe3O4/BiOI nanocomposites and its visible photocatalytic activity, Appl. Surf. Sci. 286 (2013) 40–46. doi:10.1016/j.apsusc.2013.08.139.

[122] J. Cao, C. Zhou, H. Lin, B. Xu, S. Chen, Surface modification of m-BiVO4 with wide band-gap semiconductor BiOCl to largely improve the visible light induced photocatalytic activity, Appl. Surf. Sci. 284 (2013) 263–269. doi:10.1016/j.apsusc.2013.07.092.

[123] H. Huang, K. Xiao, Y. He, T. Zhang, F. Dong, X. Du, Y. Zhang, In situ assembly of BiOI@Bi12O17Cl2p-n junction: Charge induced unique front-lateral surfaces coupling heterostructure with high exposure of BiOI {001} active facets for robust and nonselective photocatalysis, Appl. Catal. B Environ. 199 (2016) 75–86. doi:10.1016/j.apcatb.2016.06.020.

[124] L. Wang, W.A. Daoud, BiOI/TiO2-nanorod array heterojunction solar cell: Growth, charge transport kinetics and photoelectrochemical properties, Appl. Surf. Sci. 324 (2015) 532–537. doi:10.1016/j.apsusc.2014.10.110.

[125] L. Xia, J. Bai, J. Li, Q. Zeng, L. Li, B. Zhou, High-performance BiVO4 photoanodes cocatalyzed with an ultrathin α-Fe2O3 layer for photoelectrochemical application, Appl. Catal. B Environ. 204 (2017) 127–133. doi:10.1016/j.apcatb.2016.11.015.

Outputs

ผลงานตีพิมพ์ในวารสารวิชาการนานาชาติ

1. Nawapong Chumha, Titipun Thongtem, Somchai Thongtem, Sila Kittiwachana, Sulawan Kaowphong*, Effect of different polyol solvents on the synthesis of $CuInS_2$ nanoparticles by cyclic microwave irradiation, Journal of Ceramic Processing Research, 18(12) (2017) 871–874.

2. Nawapong Chumha, Titipun Thongtem, Somchai Thongtem, Sila Kittiwachana, Sulawan Kaowphong*, Cyclic microwave radiation synthesis, photoconductivity, and optical properties of $CuInS_2$ hollow sub–microspheres, Applied Surface Science 447 (2018) 292–299.

3. Auttaphon Chachvalvutikul, Jaroon Jakmunee, Somchai Thongtem, Sila Kittiwachana, Sulawan Kaowphong*, Novel $FeVO_4/Bi_7O_9I_3$ nanocomposite with enhanced photocatalytic dye degradation and photoelectrochemical properties, Applied Surface Science 475 (2019) 175–184.

การนำผลงานวิจัยไปใช้ประโยชน์ ในเชิงวิชาการ

1. ผู้วิจัยสามารถสังเคราะห์วัสดุชนิดใหม่ที่มีประสิทธิภาพสูงในการเป็นตัวเร่งปฏิกิริยาด้วยแสงวิซิเบิล ด้วยเทคนิคไมโครเวฟแบบรอบ ซึ่งเป็นเทคนิคที่ถูกพัฒนาขึ้นในกลุ่มวิจัยโดยมี ศ. เกียรติคุณ ดร. สมชาย ทองเต็ม เป็นอาจารย์ที่ปรึกษาโครงการ ซึ่งเป็นการลดต้นทุนในการผลิต และลดการนำเข้าของเครื่องมือสังเคราะห์จากต่างประเทศ
2. องค์ความรู้จากผลงานวิจัยนี้สามารถตีพิมพ์ในวารสารระดับนานาชาติ
3. ประโยชน์ต่อการเรียนการสอนโดยเป็นกรณีศึกษาในกระบวนวิชา 203719 เคมีของวัสดุอนินทรีย์ (Chemistry of Inorganic Materials) ให้แก่นักศึกษาในระดับบัณฑิตศึกษา
4. การนำผลงานวิจัยไปวิจัยต่อยอดโดยการทดลองนำวัสดุที่พัฒนาขึ้นไปประยุกต์ใช้เป็นตัวรับแสง (solar absorber) ใน solar cell
5. สามารถผลิตบัณฑิตที่มีคุณภาพ (ระดับปริญญาเอก 1 คน ระดับปริญญาโท 2 คน)

Appendices

Journal of Ceramic Processing Research. Vol. 18, No. 12, pp. 871~874 (2017)

J O U R N A L O F
Ceramic Processing Research

Effect of different polyol solvents on the synthesis of $CuInS_2$ nanoparticles by cyclic microwave irradiation

Nawapong Chumha[a], Titipun Thongtem[a], Somchai Thongtem[b], Sila Kittiwachana[a,c,d] and Sulawan Kaowphong[a,c,d,*]

[a]*Department of Chemistry, Faculty of Science, Chiang Mai University, Chiang Mai 50200, Thailand*
[b]*Department of Physics and Materials Science, Faculty of Science, Chiang Mai University, Chiang Mai 50200, Thailand*
[c]*Center of Excellence in Materials Science and Technology, Chiang Mai University, Chiang Mai 50200, Thailand*
[d]*Center of Excellence for Innovation in Chemistry, Faculty of Science, Chiang Mai University, Chiang Mai 50200, Thailand*

$CuInS_2$ nanoparticles were synthesized by a cyclic microwave irradiation method at 600 W for 75 cycles. The effect of different polyol solvents (ethylene glycol, glycerol, and propylene glycol) on the synthesis of the $CuInS_2$ nanoparticles was investigated. Characterized by XRD, the powders synthesized using ethylene glycol and glycerol were pure $CuInS_2$ with tetragonal structure. However, $CuInS_2$ with the existence of CuS was obtained when using propylene glycol due to the lower resulting reaction temperature. FTIR spectra of the residual solvents after the synthesis process were determined and this revealed that ethylene glycol and glycerol were the solvents with good reducing capability. FESEM images revealed that the synthesized $CuInS_2$ powders were composed of nanoparticles with diameters in the range of 20-100 nm. The $CuInS_2$ nanoparticles synthesized using glycerol were smaller than those synthesized using ethylene glycol, due to the higher viscosity of glycerol.

Key words: $CuInS_2$, Microwave radiation, Semiconductors, Nanocrystalline materials.

Introduction

$CuInS_2$ has been extensively used as an absorber material for photovoltaic applications due to its direct band gap of 1.5 eV [1, 2]. Several synthesis methods, such as colloidal [1], hydrothermal [2] and microwave [3], have been recently used to prepare $CuInS_2$ nanostructures. Of these, microwave synthesis has attracted considerable attention because it is an efficient, energy saving and environmentally benign method for synthesizing nanocrystalline metal oxides and sulfides with various sizes and morphologies [4, 5]. In microwave synthesis, the microwave radiation interacts with polar molecules or conducting ions in solution to create rapid volumetric heating, resulting in shorter reaction time and higher reaction rate [5]. Polyol or polyalcohol is usually employed as a solvent for microwave synthesis to prepare inorganic nanomaterials due to its high boiling point, high dielectric loss constant, and good reducing capability [6-8].

Different polyol solvents have different physical and chemical properties which differentially affect the microwave synthesis of nanomaterials. This study synthesized $CuInS_2$ nanoparticles by a cyclic microwave irradiation method using three different polyol solvents- ethylene glycol (EG), glycerol (Gly), and propylene glycol (PG) -to investigate their effects on the characteristics of the synthesized powders. The characteristics of the synthesized powders were examined by XRD and FESEM techniques. In addition, the reducing capability of each solvent was determined by FTIR technique.

*Corresponding author:
Tel : +66-53-943341
Fax: +66-53-892277
E-mail: sulawan.k@cmu.ac.th, sulawank@gmail.com

Experimental Procedure

In a typical procedure, $CuCl_2 \cdot 2H_2O$ (2 mmol), $InCl_3 \cdot 4H_2O$ (2 mmol), and CH_3CSNH_3 (4 mmol) were separately dissolved in 10.0 mL of the polyol solvent. The solutions were mixed together for 30 min, and then the mixed solution was irradiated using 2.45 GHz microwave radiation at 600 W for 75 cycles. For each cycle, the microwave power was turned on for 30 s of every 60 s (50% power). The resulting powder was collected and washed with deionized water and then ethanol. Finally, the powder was dried at 80 °C overnight and then characterized using XRD, FTIR, and FESEM techniques.

The purity, crystallinity, and crystal structure of the synthesized powders were characterized by XRD (Rigaku MiniFlex II) with a Cu$K\alpha$ radiation (1.5406 Å). Vibration modes of the powders were investigated by FTIR (Bruker TENSOR27) using the KBr pellet technique. Particle size and morphology of the powders were determined by FESEM (JEOL JSM-6335F), operated at 15 kV of accelerating voltage. UV-Vis

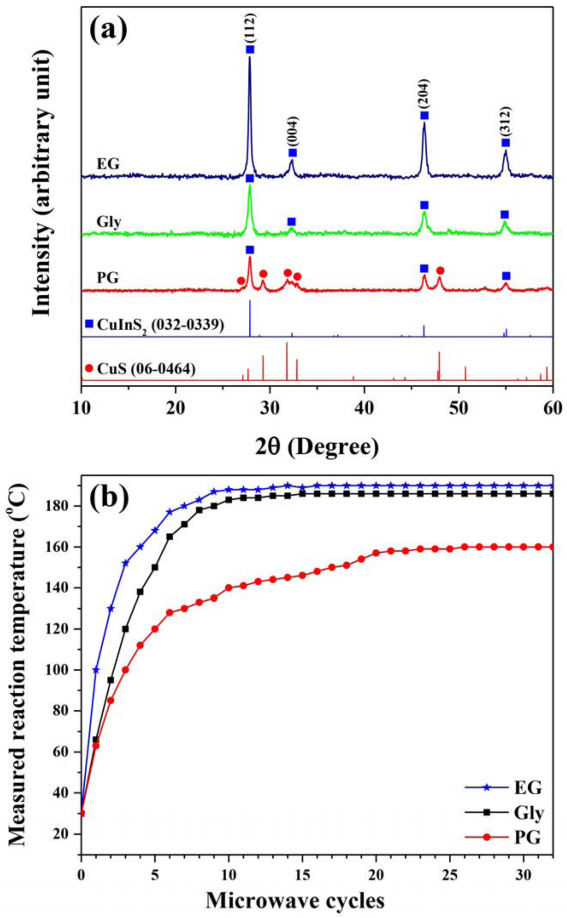

Fig. 1. (a) XRD pattern of the powders synthesized using different solvents and (b) measured reaction temperatures of the different solvents irradiated at 600 W with the prolonged reaction time.

diffuse reflectance spectra (DRS) were recorded on the samples diluted in BaSO4 by a UV-Vis-NIR spectrophotometer (UV-3101PC, Shimadzu) equipped with an ISR-3100 integrating sphere attachment.

Results and Discussion

The XRD spectra of the powders synthesized using different solvents are shown in Fig. 1(a). In all powders, the diffraction peaks at 2θ of 27.86 °, 32.24 °, 46.32 °, and 54.87 ° were indexed to the (112), (004), (204), and (312) planes of a tetragonal $CuInS_2$ structure (JCPDS no. 032-0339). However, in the XRD spectrum of the powder synthesized using PG, the diffraction peaks of a hexagonal CuS structure (JCPDS no. 06-0464) were also found, implying that pure $CuInS_2$ did not completely form at the given microwave heating power. In addition, the intensity of the diffraction peaks of the $CuInS_2$ powder synthesized using EG were higher than those synthesized using Gly and PG, suggesting higher crystallinity. These results could be explained by the reaction temperature of the solvents. The ability of a conductive media to convert electromagnetic energy into heat at a given frequency and microwave power is

Table 1. Some properties of the solvents used [5, 10-12].

Solvents	Ethylene glycol	Glycerol	Propylene glycol
Structure	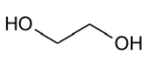	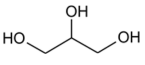	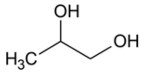
Boiling point (°C)	197	290	187
Dielectric loss tangent (at 2.45 GHz)	1.35 (at 20 °C)	0.54 (at 20 °C)	~ 0.23 (at 25 °C)
Viscosity (mPa·s at 25 °C)	16.2	934	11.3

determined by the dielectric loss tangent (tan $\delta = \delta''/\delta'$), where δ'' is the dielectric loss and δ' is the dielectric constant [5-7]. A solvent with high tan δ more effectively convert microwave energy to thermal energy; as a result, high reaction temperature can be achieved. The tan δ of the solvents used in this research are shown in Table 1. In Fig. 1(b), the measured reaction temperatures of EG, Gly and PG irradiated at 600 W were 190 °C, 186 °C, and 157 °C, respectively. The higher crystallinity of the $CuInS_2$ powder synthesized using EG could be due to the higher reaction temperature of the solution, relating to its higher tan δ [5]. On the other hand, the lowest tan δ of PG corresponded to the lowest reaction temperature of the solution. This could be the reason that the CuS phase still remained in the $CuInS_2$ powder synthesized using PG at given microwave power. This result was consistent with the previous study reporting the remaining of CuS when the temperature was lower than 160 °C [9].

The formation of $CuInS_2$ nanostructures was related to the reduction of Cu^{2+} to Cu^{+} in solvent under microwave radiation [13]. After the reduction, the H_2S released from CH_3CSNH_3 reacted with Cu^{+} and In^{3+} to yield $CuInS_2$. Since each polyol solvent possesses different oxidation potentials, a solvent with stronger reducing capability is a more effective reducing agent. During the synthesis process, the hydroxyl groups in polyol solvent can be oxidized by the metallic precursor. To investigate the reducing capability of the polyol solvents, pure solvents, residual solvents after the synthesis, and pure solvents irradiated at 600 W for 75 cycles were further analyzed by FTIR (Fig. 2). Vibration peaks of the pure solvents (EG, Gly and PG) exhibited at 3384-3385 cm^{-1}, 2933-2946 cm^{-1}, 2879-2883 cm^{-1}, 1652-1654 cm^{-1}, 1414-1457 cm^{-1}, and 1079-1110 cm^{-1} are attributed to O-H stretching, C-H asymmetric stretching, C-H symmetric stretching, O-H bending, C–H bending, and C-O stretching, respectively [14].

The FTIR spectrum of the residual EG after the synthesis showed a strong vibration peak of C = O stretching at 1758 cm^{-1}, contributed to the ketone

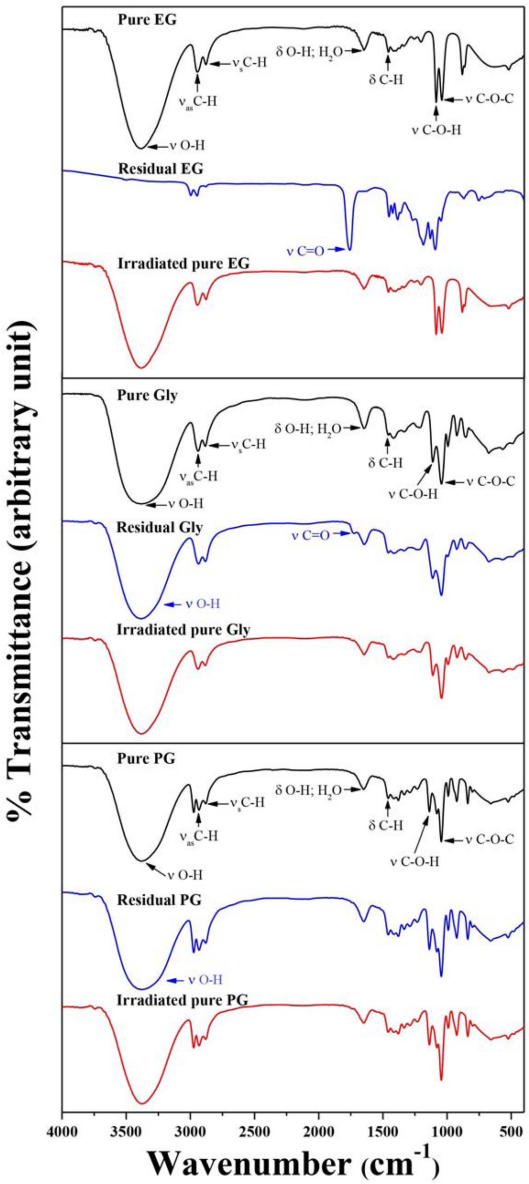

Fig. 2. FTIR spectra of pure solvents, residual solvents after the synthesis process and pure solvents irradiated at 600 W for 75 cycles.

carbonyl group of diacetyl [15]. In addition, the O-H stretching band of the hydroxyl group was disappeared, implying that EG was completely oxidized to diacetyl during the microwave reaction. The FTIR spectrum of the residual Gly showed a weak vibration peak of C=O stretching at 1725 cm^{-1}, contributed to the aldehyde group of glyceraldehyde or ketone carbonyl group of dihydroxyacetone, and the remaining of the O–H stretching band could be the hydroxyl groups of the oxidation products [16]. Generally, PG can also reduce the metallic precursor resulting in acetone, propanal, and allyl alcohol [17]. But, these product compounds can evaporate and/or decompose during the microwave synthesis, due to their relatively low boiling points (56 ºC, 48 ºC, and 97 ºC for acetone, propanal, and allyl

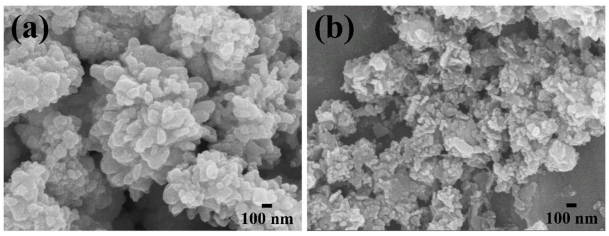

Fig. 3. FESEM images of the $CuInS_2$ nanoparticles synthesized using (a) EG and (b) Gly.

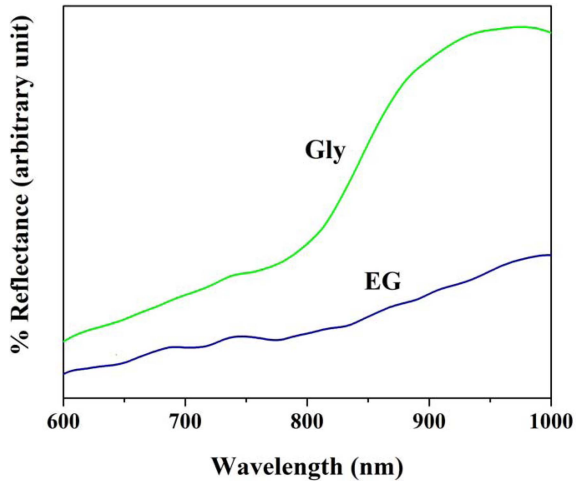

Fig. 4. UV-Vis diffuse reflectance spectrum of the $CuInS_2$ nanoparticles.

alcohol, respectively [18]). For this reason, the vibration peaks of the C = O stretching of these products were not observed in the FTIR spectrum of the residual PG. However, the remaining of O-H stretching band implied that PG was not completely reduced Cu^{2+} ions during the microwave synthesis in according to the XRD result (Fig. 1(a). It is noted that the FTIR spectra of the EG, Gly, and PG irradiated at 600 W for 75 cycles (Fig. 2) were the same as the respective pure solvents, confirming that the microwave irradiation did not decompose the pure solvents. These results suggested that microwave radiation enhanced the reducing capability of EG and Gly. As a result, the CuS was not found in the $CuInS_2$ powders synthesized using EG and Gly as revealed in their XRD spectra (Fig. 1(a)). Based on the XRD and the FTIR results, EG was the most favorable solvent for the microwave synthesis where the $CuInS_2$ powder synthesized using EG had the highest crystallinity.

FESEM images (Fig. 3) of the $CuInS_2$ powders synthesized using EG and Gly were composed of $CuInS_2$ nanoparticles with diameters in the range of 20-100 nm. The nanoparticles synthesized using Gly were smaller than those synthesized using EG. This difference could be due to the different solvent viscosities (Table 1). The viscosity of Gly is significantly higher than EG; the solubility and diffusion rate of ions in the Gly solution is, therefore, lower. This suppresses crystalline growth, resulting in the smaller size of the synthesized $CuInS_2$

nanoparticles. The optical properties of the $CuInS_2$ powders synthesized using EG and Gly were investigated by UV-Vis diffuse reflectance spectrum (Fig. 4). The spectrum exhibited light absorption in the visible light region, extending into the near-infrared region. The $CuInS_2$ nanoparticles synthesized using Gly exhibited stronger absorption compared to those synthesized using EG. The $CuInS_2$ nanoparticles with smaller in size have a greater ability to reflect and scatter light. Thus, we obtained different results of light absorption ability.

Conclusions

In summary, we reported the effect of different polyol solvents (ethylene glycol, glycerol, and propylene glycol) on the cyclic microwave irradiation synthesis of the $CuInS_2$ nanoparticles. The purity and crystallinity of the $CuInS_2$ nanoparticles depended on the resulting reaction temperature and the reducing capability of the polyol solvents used. The size of the $CuInS_2$ nanoparticles was also influenced by the viscosity of the polyol solvents. In addition, the size affected the light absorption ability. The results of this research could be useful in the microwave irradiation synthesis of other related inorganic nanomaterials.

Acknowledgements

This research was financially supported by the Thailand Research Fund (TRF) and the Office of the Higher Education Commission (Grant number MRG 6080270), the Energy Policy and Planning Office (EPPO) Thailand, the Center of Excellent (CoE) in Materials Science and Technology, and the Chiang Mai University (CMU) Junior Research Fellowship Program, and the Center of Excellence for Innovation in Chemistry (PERCH-CIC), Office of the Higher Education Commission, Ministry of Education, Thailand. Nawapong Chumha would like to thank the Science Achievement Scholarship of Thailand and the Graduate School of Chiang Mai University.

References

1. Z. Hao, Y. Cui, and G. Wang, Mater. Lett. 146 (2015) 77-80.
2. Y. Wang, J. Yang, W. Gao, R. Cong, and T. Yang, Mater. Lett. 137 (2014) 99-101.
3. S.M. Hosseinpour-Mashkani, M. Salavati-Niasari, F. Mohandes, and K. Venkateswara-Rao, Mater. Sci. Semicond. Proc. 16 (2013) 390-402.
4. A. Mirzaei, and G. Neri, Sens. Actuators B 237 (2016) 749-775.
5. Y. Zhu and F. Chen, Chem. Rev. 114 (2014) 6462-6555.
6. B.L. Hayes, Microwave Synthesis: Chemistry at the Speed of Light, CEM Publishing, New York, 2002.
7. M.B. Gawande, S.N. Shelke, R. Zboril, and R.S. Varma, Acc. Chem. Res. 47 (2014) 1338-1348.
8. H. Grisaru, O. Palchik, and A. Gedanken, Inorg.Chem. 42[22] (2003) 7148-7155.
9. Y. Qi, K. Tang, S. Zeng, and W. Zhou, Micropor. Mesopor. Mater. 114 (2008) 395-400.
10. C. Gabriel, S. Gabriel, E.H. Grant, E.H. Grant, B.S.J. Halstead, and D.M.P. Mingos, Chem. Soc. Rev. 27 (1998) 213-224.
11. G.V. Mashalkar, P.A. Chalikwar, and A.C. Kumbharkhane, Phys. Chem. Liq. 53 (2015) 307-317.
12. J.G. Speight, Lange's Handbook of Chemistry, 16 ed., McGraw-Hill Book, 2005.
13. N. Chumha, T. Thongtem, S. Thongtem, D. Tantraviwat, S. Kittiwachana, and S. Kaowphong, Ceram. Int. 42 (2016) 15643-15649.
14. B. Stuart, Infrared spectroscopy: Fundamentals and applicationsChichester, J. Wiley, New Jersey, 2004.
15. T. Gürkaynak Altinçekiç, and I. Boz, Bull. Mater. Sci. 31[4] (2008) 619-624.
16. J.C. Colmenares, and R. Luque, Chem. Soc. Rev. 43 (2014) 765-778.
17. T. Laino, C. Tuma, P. Moor, E. Martin, S. Stolz, and A. Curioni, J. Phys. Chem. A 116 (2012) 4602-4609.
18. D. Mackay, W. Shiu, K. Ma, and S. Lee, Handbook of physical-chemical properties and environmental fate for organic chemicals, CRC Press, Boca Raton, 2006.

Applied Surface Science 447 (2018) 292–299

Contents lists available at ScienceDirect

Applied Surface Science

journal homepage: www.elsevier.com/locate/apsusc

Full Length Article

Cyclic microwave radiation synthesis, photoconductivity, and optical properties of $CuInS_2$ hollow sub-microspheres

Nawapong Chumha [a], Titipun Thongtem [a,b], Somchai Thongtem [b,c], Sila Kittiwachana [a,d,e], Sulawan Kaowphong [a,d,e,*]

[a] Department of Chemistry, Faculty of Science, Chiang Mai University, Chiang Mai 50200, Thailand
[b] Materials Science Research Center, Faculty of Science, Chiang Mai University, Chiang Mai 50200, Thailand
[c] Department of Physics and Materials Science, Faculty of Science, Chiang Mai University, Chiang Mai 50200, Thailand
[d] Center of Excellence in Materials Science and Technology, Chiang Mai University, Chiang Mai 50200, Thailand
[e] Center of Excellence for Innovation in Chemistry, Faculty of Science, Chiang Mai University, Chiang Mai 50200, Thailand

ARTICLE INFO

Article history:
Received 7 September 2017
Revised 21 March 2018
Accepted 26 March 2018
Available online 27 March 2018

Keywords:
$CuInS_2$
Microwave synthesis
Electron microscopy
Photoconductivity
Optical properties

ABSTRACT

$CuInS_2$ powder was synthesized by a cyclic microwave irradiation method using L-cysteine as a sulfur source. The effect of microwave power (180–600 W) on the purity, morphology, and particle size of the synthesized powders was investigated. X-ray diffraction (XRD) analysis showed that the synthesized powders were pure $CuInS_2$ with a tetragonal structure. Transmission electron microscopy (TEM) analysis revealed that the $CuInS_2$ powder synthesized at 180 W composed of solid microspheres with a diameter of about 250 nm. Increasing the microwave power to 300 W and 450 W transformed some of the sub-microspheres into hollow sub-microspheres. At 600 W, all of the $CuInS_2$ sub-microspheres were hollow. Based on time-dependent experiment, formation mechanisms of the $CuInS_2$ solid and hollow sub-microspheres were discussed. The photoconductivity of the $CuInS_2$ hollow sub-microspheres was greater than that of the $CuInS_2$ solid sub-microspheres, suggesting that the $CuInS_2$ hollow sub-microspheres were favorable to increase current carrier concentration and to improve electron transport. UV–vis diffuse reflectance spectrum (UV–vis DRS) of the $CuInS_2$ hollow sub-microspheres showed strong absorption intensity with a direct band gap energy of 1.48 eV, which is potentially useful in solar-light driven applications.

1. Introduction

Recently, hollow nano/microstructure materials have attracted extensive attention because of their unique structures that enable useful physical properties, such as large specific surface area, low density, and good surface permeability [1,2]. Studies have demonstrated that their large surface areas are favorable for improving photocatalytic efficiency [3,4], performance of gas sensors [5], and dye loading capacity of dye-sensitized solar cells [6]. The cavities inside hollow microspheres are also useful in drug delivery and chemical storage applications [7,8]. In addition, the multiple reflection and scattering of light within their structures enhance the solar energy conversion efficiency of solar cells, due to the longer optical path length and greater light absorption than other morphologies [6,9,10].

$CuInS_2$ powder has been considered as an attractive semiconductor photocatalyst for H_2 evolution reaction [11,12], organic dye degradation [13], and nitrate ions removal [14,15]. Moreover, $CuInS_2$ is an efficient light-absorbing material for application in solar cells due to its direct band gap of 1.5 eV that matches the solar spectrum with a large absorption coefficient [16,17]. $CuInS_2$ hollow nano/microspheres have been synthesized through sacrificial templates, such as Cu_2O nanospheres [18], cubic Cu_2O crystals [19], $Cu(OH)_2$ films [20], and CuS hollow microspheres [21], but these require multistep synthetic procedures and expensive materials. Although a previous study used a solvothermal method to synthesize $CuInS_2$ hollow microspheres without using any templates [22], it required complicated equipment and considerable time. In addition, these studies did not report on the potential use of hollow nano/microspheres for solar energy conversion applications. Microwave heating has been used for the synthesis of nanocrystalline materials with various morphologies and sizes [23,24]. It is a low-cost, energy-saving, and highly efficient method for fabricating nanomaterials with high purity, small particle sizes,

* Corresponding author at: Department of Chemistry, Faculty of Science, Chiang Mai University, Chiang Mai 50200, Thailand.
E-mail address: sulawank@gmail.com (S. Kaowphong).

https://doi.org/10.1016/j.apsusc.2018.03.210
0169-4332/

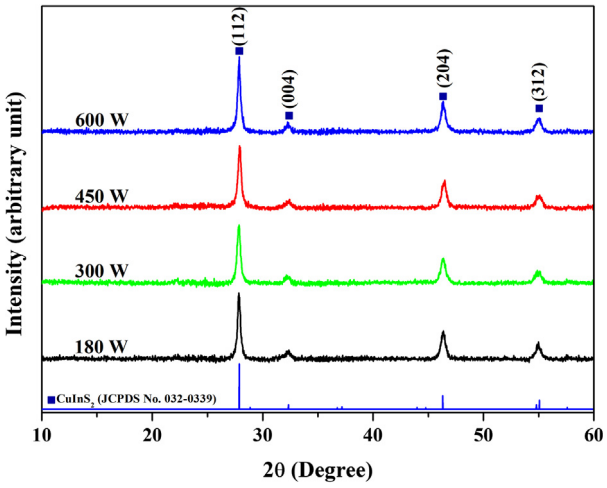

Fig. 1. XRD pattern of the $CuInS_2$ powders synthesized using different microwave powers.

and narrow size distribution. The microwave radiation interacts with polar molecules and conducting ions to provide rapid volumetric heating and results in a shorter reaction time and faster reaction rate comparing to conventional heating methods [24]. Our previous study [25] successfully synthesized $CuInS_2$ nanoparticles via cyclic microwave irradiation method using thioacetamide as a sulfur source. The $CuInS_2$ nanoparticles in microclusters were purified at 450 W and 600 W of the microwave powers. Although, the broken $CuInS_2$ hollow microsphere was found at 180 W, the CuS was still co-existed and morphological inhomogeneity was obtained.

In this study, the uniform $CuInS_2$ hollow sub-microspheres were synthesized by a cyclic microwave radiation method without using any templates or surfactants. L-cysteine, an inexpensive, simple, and environmentally friendly thiol-containing amino acid, was chosen as a sulfur source. It has a strong affinity to metal ions, forming metal-ligand complexes that can serve as a precursor for the preparation of inorganic materials [26]. Ethylene glycol was used as a solvent due to its high boiling point and high dipole moment, which was suitable for microwave heating synthesis [27]. In addition, microwave irradiation enhances the reducing power of ethylene glycol [28]. We then investigated the effect of different microwave powers on the purity, particle size, and morphology of the synthesized $CuInS_2$ powders. We also conducted time-dependent experiment to study possible formation mechanisms of the $CuInS_2$ hollow and solid sub-microspheres. Finally, photoconductivities and optical properties of the $CuInS_2$ hollow and solid sub-microspheres were compared and discussed in this research.

2. Experimental procedure

2.1. Synthesis of $CuInS_2$ powder

$CuCl_2{\cdot}2H_2O$ (2 mmol) (BDH Chemicals, Ltd.; 98%), $InCl_3{\cdot}4H_2O$ (2 mmol) (Sigma–Aldrich, Co.; 99.9%), and $C_3H_7NO_2S$ (4 mmol) (Sigma–Aldrich, Co.; 97.0%) were separately dissolved in 10.0 mL of ethylene glycol. The solutions were mixed together at room temperature for 30 min. Subsequently, the mixed solution was irradiated using 2.45 GHz microwave radiation at different microwave powers (180–600 W) for 75 cycles. Each cycle was 30 s on for every 60 s interval. Black powder was collected and washed with deionized water and ethanol, respectively. Finally, the powder was dried overnight at 80 °C for further characterization using different techniques.

2.2. Characterizations

Purity, structure, and crystallinity of the powders were characterized by X-ray diffraction spectroscopy (XRD, Rigaku Miniflex II) with CuK_α radiation (λ = 1.5406 Å). Particle size and morphology of the powders were determined by a transmission electron microscope (TEM, JEOL JEM–2010) operating at 200 kV. UV–vis diffuse reflectance spectra were recorded by a UV–vis–NIR spectrophotometer (UV-3101PC, Shimadzu), equipped with an ISR-3100 integrating sphere attachment. Twenty-five mg of each sample was well mixed with 0.5 g of $BaSO_4$ and spread onto the sampling plate prior to the measurement.

2.3. Current-voltage measurement

Simple photovoltaic devices were fabricated as follows: 0.05 g of $CuInS_2$ powder was dispersed in the mixture of 5 mL of ethanol, 0.05 mL of terpineol, and 0.05 mL of Triton X–100. Then, the $CuInS_2$ slurry was coated on a fluorine doped tin oxide (FTO)-coated glass substrate using a spin coater at 500 rpm for 30 s. The substrate was heated at 250 °C for 30 min to eliminate the remaining organic compounds. Finally, the substrate was coated by radio frequency (RF) sputtering of the Au electrode. Current-voltage curves of the devices were measured by a Keithley 2611A source meter under illumination using a solar simulator (AM1.5, 100 mW/cm^2). Light flux density was calibrated with a second class pyranometer (Hukseflux, LP02).

3. Results and discussion

The XRD patterns of the powders synthesized using different microwave powers are shown in Fig. 1. All of the diffraction peaks were well matched to the JCPDS database no. 032-0339, which corresponded to a tetragonal $CuInS_2$ structure. No diffraction peaks from possible impurities, such as CuS, Cu_2S, and In_2S_3, were detected, indicating the purity of the synthesized $CuInS_2$ powders. Using L-cysteine as a sulfur source, a complete formation of $CuInS_2$ was attained at a lower microwave power, and the crystallite size of the $CuInS_2$ nanoparticles was relatively larger than that of our previous study [25], indicating that the difference in sulfur sources affected the purity and the size of the $CuInS_2$ crystals. XRD patterns of the powders, synthesized at 180 W for 75 cycles using different sulfur sources, are shown in Fig. S1. XRD diffraction angle, FWHM, and the estimated crystallite size of the $CuInS_2$ powders synthesized using different sulfur sources are summarized in Table S1. Using L-cysteine, the width of the diffraction peak was relatively narrower, revealing that the crystallite size of the $CuInS_2$ crystals was larger than that of those synthesized using thioacetamide. These results could be explained by the rate of the sulfur released during the synthesis process. During the synthesis process using L-cysteine, a transparent solution was obtained after the reactants were mixed, suggesting that L-cysteine coordinated with the metal ions in the reaction system to form complexes [29,30]. After heating, the complexes decomposed and slowly released S^{2-} to generate $CuInS_2$ nuclei. The slow formation rate of $CuInS_2$ led to the powder with higher purity as well as better growth of the $CuInS_2$ nanocrystals. As a result, pure $CuInS_2$ nanocrystals with larger crystallite size were obtained. The formation mechanism of the $CuInS_2$ prepared using L-cysteine was further discussed with the results from time-dependent experiment.

Upon the use of thioacetamide as a sulfur source, a dark-brown solution formed immediately when the reactants were mixed

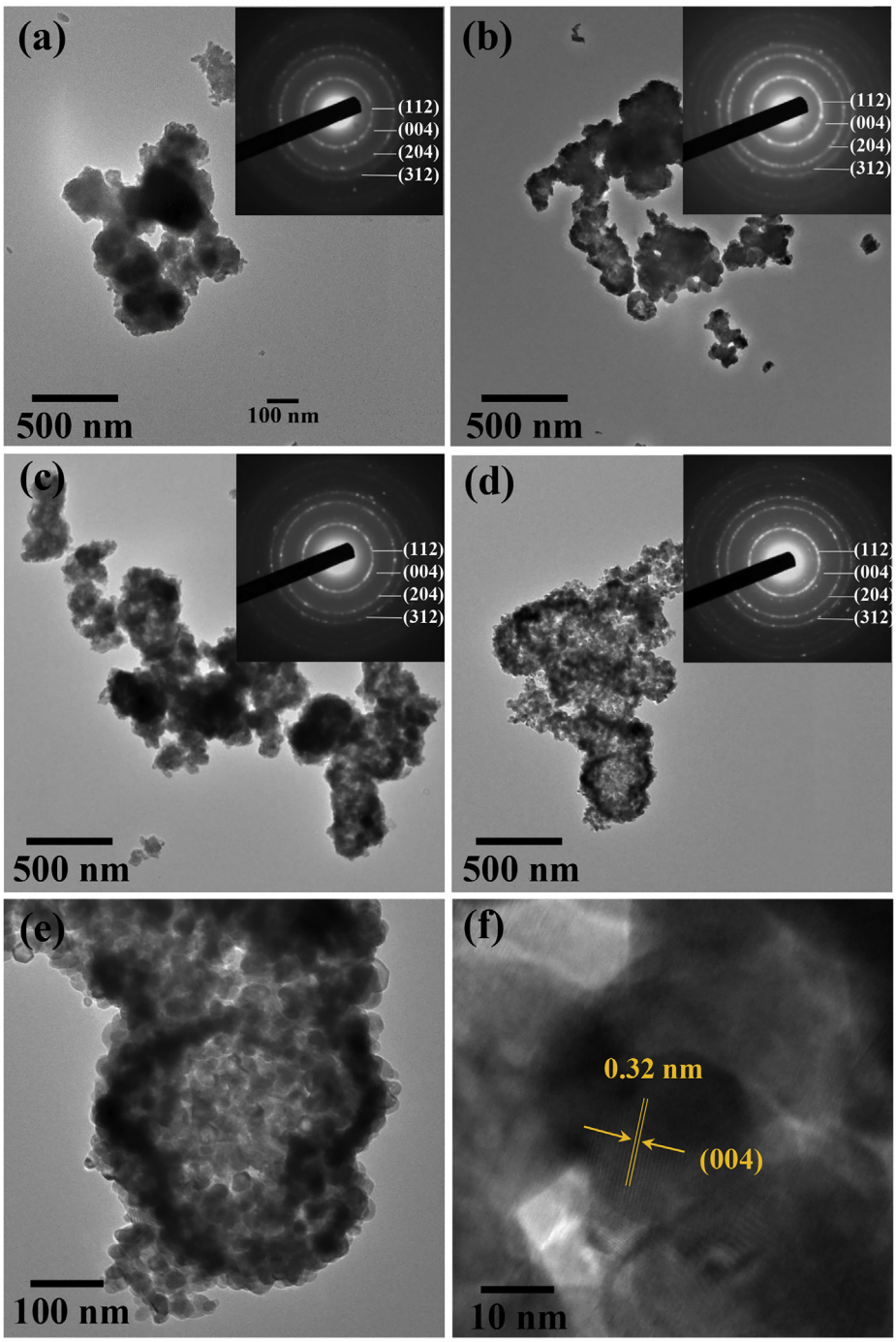

Fig. 2. TEM images and SAED patterns of the $CuInS_2$ powders synthesized using (a) 180 W, (b) 300 W, (c) 450 W and (d) 600 W. (e) Higher magnified TEM and (f) high resolution TEM images of the $CuInS_2$ powders synthesized using 600 W for 75 processing cycles.

together. This suggested that thioacetamide was easily hydrolyzed resulting in the rapidly generated H_2S. Then, H_2S molecules reacted directly with Cu^{2+} ions to form CuS particles quickly, which were subsequently reduced to Cu^+ by ethylene glycol. Finally, Cu^+ reacted with In^{3+} and H_2S to form $CuInS_2$ nanoparticles [25]. The CuS could not be completely reduced to Cu^+ at the given microwave power. Thus, the CuS phase still remained in the $CuInS_2$ sample. In addition, the fast formation rate resulted in a large number of the $CuInS_2$ nanocrystals with relatively small crystallite size mixed with the CuS particles.

The TEM images of the $CuInS_2$ powders synthesized using different microwave powers are shown in Fig. 2. The powder synthesized at 180 W composed of microspheres with a diameter of about 250 nm. The dark center of the sub-microspheres suggested that the $CuInS_2$ powder was solid sub-microspheres (Fig. 2(a)). Increasing the microwave power to 300 W (Fig. 2(b)) and 450 W (Fig. 2(c)) transformed some of the solid sub-microspheres to hollow sub-microspheres with a diameter of about 200 nm and wall thicknesses in the range of 80–100 nm. At 600 W, hollow sub-microspheres with a diameter of about 300 nm and wall thicknesses in the range of 40–60 nm were clearly observed (Fig. 2(d) and (e)). All of the hollow sub-microspheres had a uniform morphology. All of the corresponding SAED patterns showed bright $CuInS_2$ concentric rings corresponding to the (1 1 2), (0 0 4), (2 0 4), and (3 1 2) diffraction planes. These

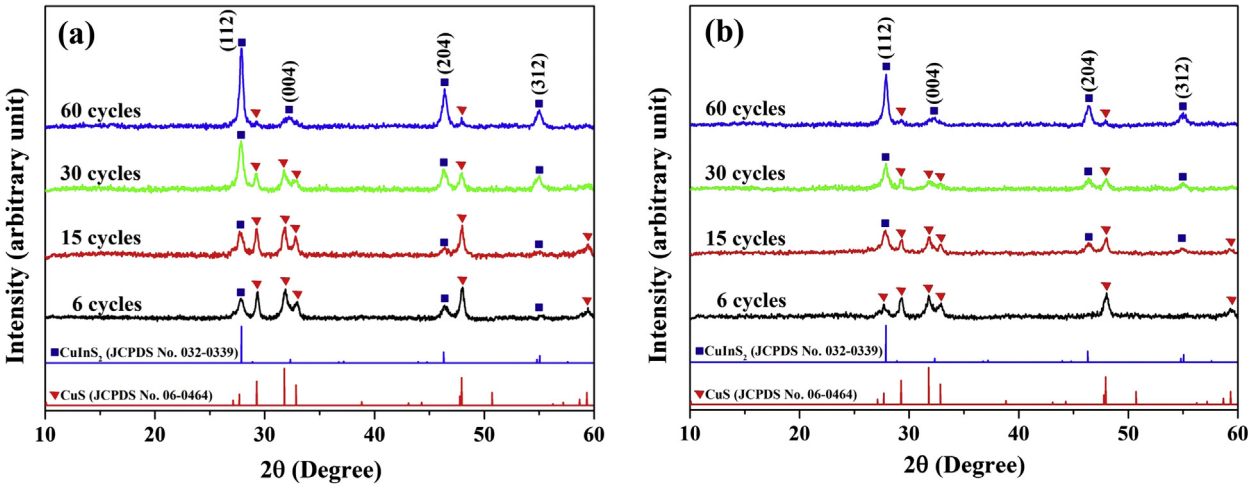

Fig. 3. XRD patterns of the $CuInS_2$ powders synthesized using (a) 180 W and (b) 600 W with different processing cycles.

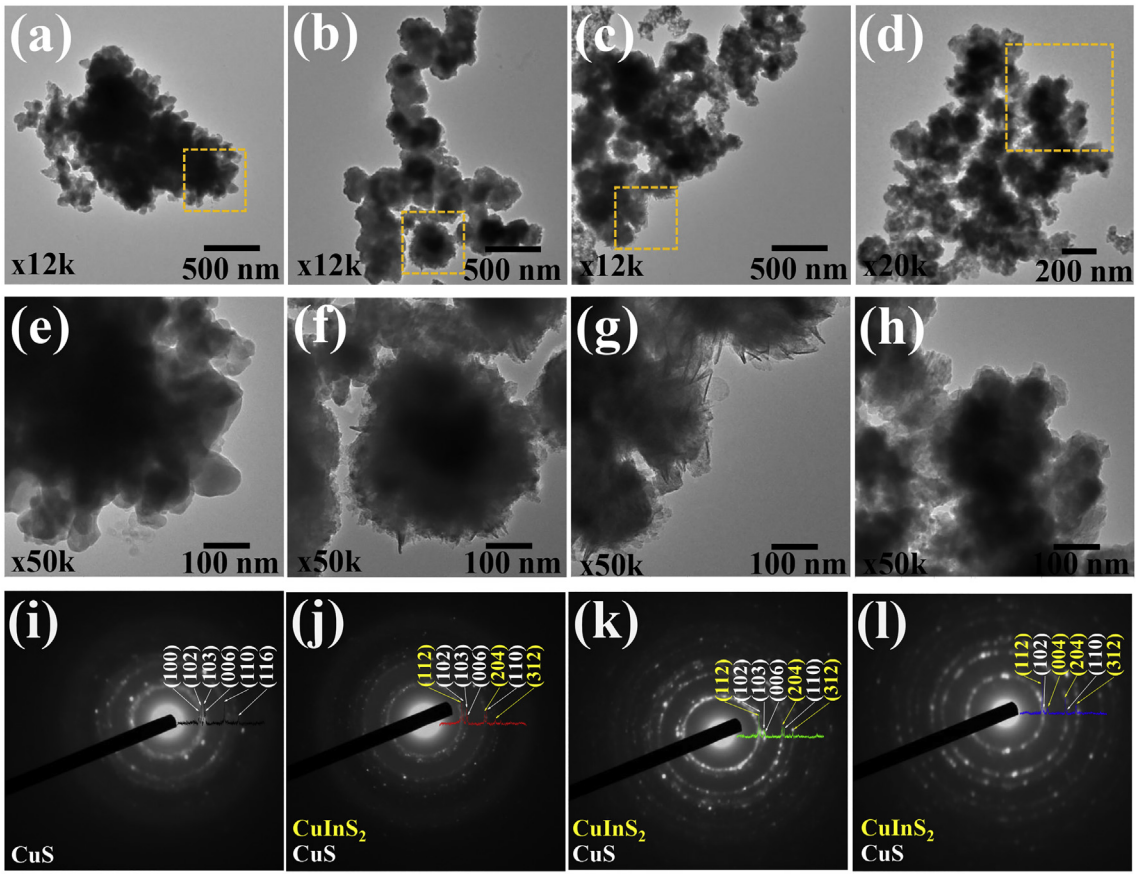

Fig. 4. (a–d) TEM images, (e–h) high magnification TEM images, and (i–l) SAED patterns of the powders synthesized at 600 W for 6, 15, 30, and 60 cycles, respectively.

results confirmed that all of the $CuInS_2$ powders were crystallized with a tetragonal structure in accordance with the above XRD analysis. High resolution TEM (HRTEM) image of the hollow sub-microspheres (Fig. 2(f)) indicated that the $CuInS_2$ hollow sub-microspheres was an apparent crystalline structure. The crystal lattice fringe of the 0.32 nm planar spaces corresponded well with the (0 0 4) plane of tetragonal $CuInS_2$.

To investigate the formation mechanisms of the $CuInS_2$ solid and hollow sub-microspheres, the powders were synthesized at 180 W and 600 W with different processing cycles. Then, XRD and TEM analyses were performed on these synthesized powders. It should be noted that this time-dependent study was performed by irradiating each of the solutions with different processing cycles. For example, one solution was prepared for 15 cycles and another solution was for 30 cycles. The XRD patterns of the powders synthesized at 180 W with different processing cycles are shown in Fig. 3(a). All of the XRD spectra showed that the synthesized powders contained a tetragonal $CuInS_2$ phase mixed with a hexagonal CuS phase. The XRD patterns of the powders synthesized at 600 W with different processing cycles are shown

in Fig. 3(b). The XRD spectrum of the powder synthesized at 600 W for 6 cycles can be indexed to a hexagonal CuS structure. At 15, 30, and 60 cycles, the additional diffraction peaks at 2θ of 27.76°, 32.35°, 46.39°, and 54.92° indexed to the (1 1 2), (0 0 4), (2 0 4), and (3 1 2) planes of the tetragonal $CuInS_2$ structure, respectively, indicating the existence of the $CuInS_2$ phase. When the irradiation times were lengthened, the diffraction peak intensities of the $CuInS_2$ phase gradually stronger, while those of the CuS phase decreased, demonstrating the increased purity and crystallinity of the $CuInS_2$ powders.

The TEM images and SAED patterns of the powders synthesized at 600 W with different processing cycles are shown in Fig. 4. At 6 cycles, the powder composed of agglomerated nanoparticles with diameters in the range of 50–100 nm (Fig. 4(a) and (e)). The corresponding SAED pattern (Fig. 4(i)) showed concentric rings corresponding to the (1 0 0), (1 0 2), (1 0 3), (0 0 6), (1 1 0), and (1 1 6) diffraction planes of the hexagonal CuS structure. When the irradiation times were prolonged to 15 cycles (Fig. 4(b) and (f)), and 30 cycles (Fig. 4(c) and (g)), the nanoparticles were transformed into microspheres with 200–400 nm diameter composed of several nanoflakes. The corresponding SAED patterns (Fig. 4(j) and (k)) showed bright concentric rings of the hexagonal CuS and tetragonal $CuInS_2$ structures, which were consistent with the JCPDS databases. At 60 cycles, the nanoflake-assembled sub-microspheres transformed into sub-microspheres made up of nanoparticles (Fig. 4(d) and (h)). The diffraction planes of CuS were still observed in the corresponding SAED pattern (Fig. 4(l)). Notably, the bright concentric rings of $CuInS_2$ became sharpened when the processing time was increased to 75 cycles, as shown in Fig. 2(d), implying that the recrystallization process was simultaneously proceeding. TEM images and SAED patterns of the powders synthesized at 180 W with 6 and 30 cycles are shown in Fig. 5. At 6 cycles, the powder appeared to contain spherical nanoparticles with diameters in a range of 20–30 nm (Fig. 5(a) and (c)). The corresponding SAED pattern (Fig. 5(e)) showed concentric rings of the hexagonal CuS and tetragonal $CuInS_2$ structures. At 30 cycles, the spherical nanoparticles tended to form agglomerates (Fig. 5(b) and (d)) with the corresponding SAED pattern (Fig. 5(f)) showed concentric rings of the hexagonal CuS and tetragonal $CuInS_2$ structures.

Based on the time-dependent study, the formation mechanisms of the $CuInS_2$ hollow and solid sub-microspheres were discussed. During the experiment, when $CuCl_2$, $InCl_3$, and L-cysteine were mixed in ethylene glycol, a transparent solution was obtained after the reactants were mixed, suggesting that the Cu^{2+} and In^{3+} ions coordinated with L-cysteine to form $Cu(L\text{-cysteine})_n^{2+}$ and $In(L\text{-cysteine})_n^{3+}$ complexes through thiol chains [29,30], due to the strong nucleophilicity of the thiol group of L-cysteine. Under heating, the coordination bond between the thiol group and Cu^{2+} weakened the S—H bond in the L-cysteine. Then, the C—S bond in the $Cu(L\text{-cysteine})_n^{2+}$ complex was gradually broken. The released S^{2-} combined with Cu^{2+} to form tiny CuS particles. Notably, unstable In_2S_3 was not found according to the hard soft acid base (HSAB) concept [31]; which has been used in chemistry to predict the stability of various compounds. Using 600 W of the microwave power, the reaction rate rose rapidly during the microwave heating process. As a result, the CuS nanoparticles quickly aggregated together to form CuS sub-microspheres to minimize their surface energy and the total energy of the system. This led to the formation of poorly crystallized CuS nanoparticles that were comprised of a primary core of CuS sub-microspheres. Then, well-crystallized CuS nanoflakes formed on the surface of the primary CuS sub-microspheres due to the intrinsic anisotropic characteristics of the hexagonal CuS structure [32,33]. When the number of processing cycles increased, the reaction temperature increased and the CuS nanoflakes coated on the surface of the primary CuS sub-microspheres were then reduced to Cu_2S by ethylene glycol. The produced Cu_2S subsequently reacted with In^{3+} and S^{2-} ions in the solution to form $CuInS_2$ nanoparticles covering the surface of the primary CuS sub-microspheres. Simultaneously, the primary CuS core dissolved, producing a cavity inside the sub-microspheres. The dissolved CuS was also reduced to Cu_2S by ethylene glycol, and then reacted with In^{3+} and S^{2-} to form $CuInS_2$ nuclei. Finally, the secondary $CuInS_2$ nuclei crystallized and grew on the external surface of the sub-microspheres, consistent with the previous study [22]. Using a lower microwave power of 180 W, the reaction proceeded more slowly. Consequently, formation of the $CuInS_2$ nanoparticles was slower than that of the reaction at 600 W of microwave power. The $CuInS_2$ nanoparticles were gradually agglomerated to reduce their surface energy. When the reaction temperature was increased by extending the irradiation time, the agglomerated nanoparticles became more compact to form the solid sub-microspheres.

In order to investigate the potential use of the synthesized $CuInS_2$ powders as an active layer in solar cell applications, the photoconductivity of the $CuInS_2$ photoelectrode was studied. Current-voltage (I-V) curves of the $CuInS_2$ thin films were measured under illumination using a solar simulator (AM1.5, 100 mW/cm^2). Fig. 6 shows the current-voltage curves of the fabricated devices operated in the dark (black line) and under illumination (red line). The current linearly increased with the applied voltage, implying the ohmic nature of the contacts. At all bias voltages, the conductivity of the device under illumination was higher than that under dark condition because electrons in valence band of $CuInS_2$ were excited to conduction band under illumination [34]. The cur-

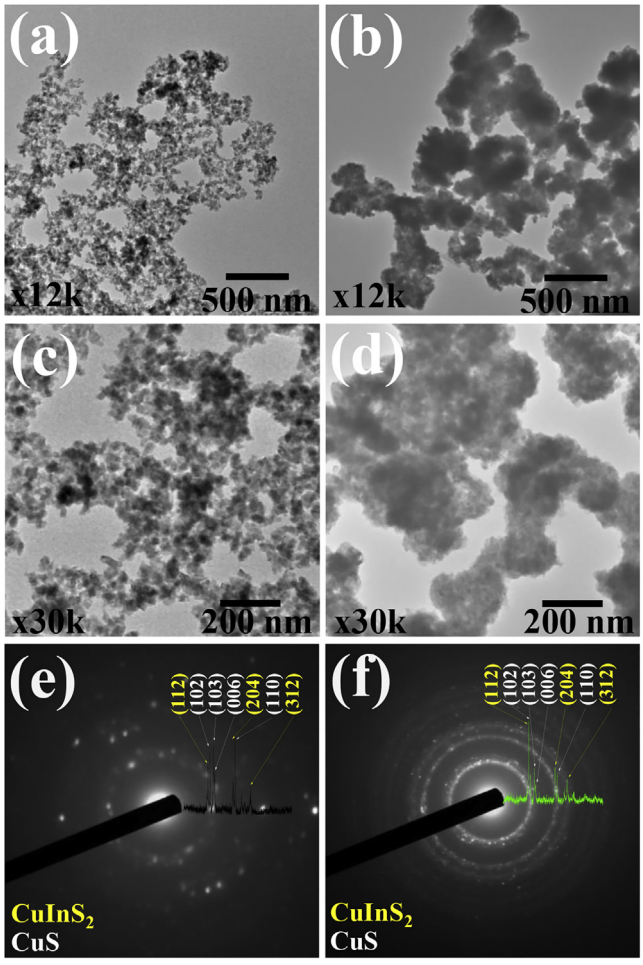

Fig. 5. (a–b) TEM images, (c–d) high magnification TEM images, and (e–f) SAED patterns of the powders synthesized at 180 W for 6 and 30 cycles, respectively.

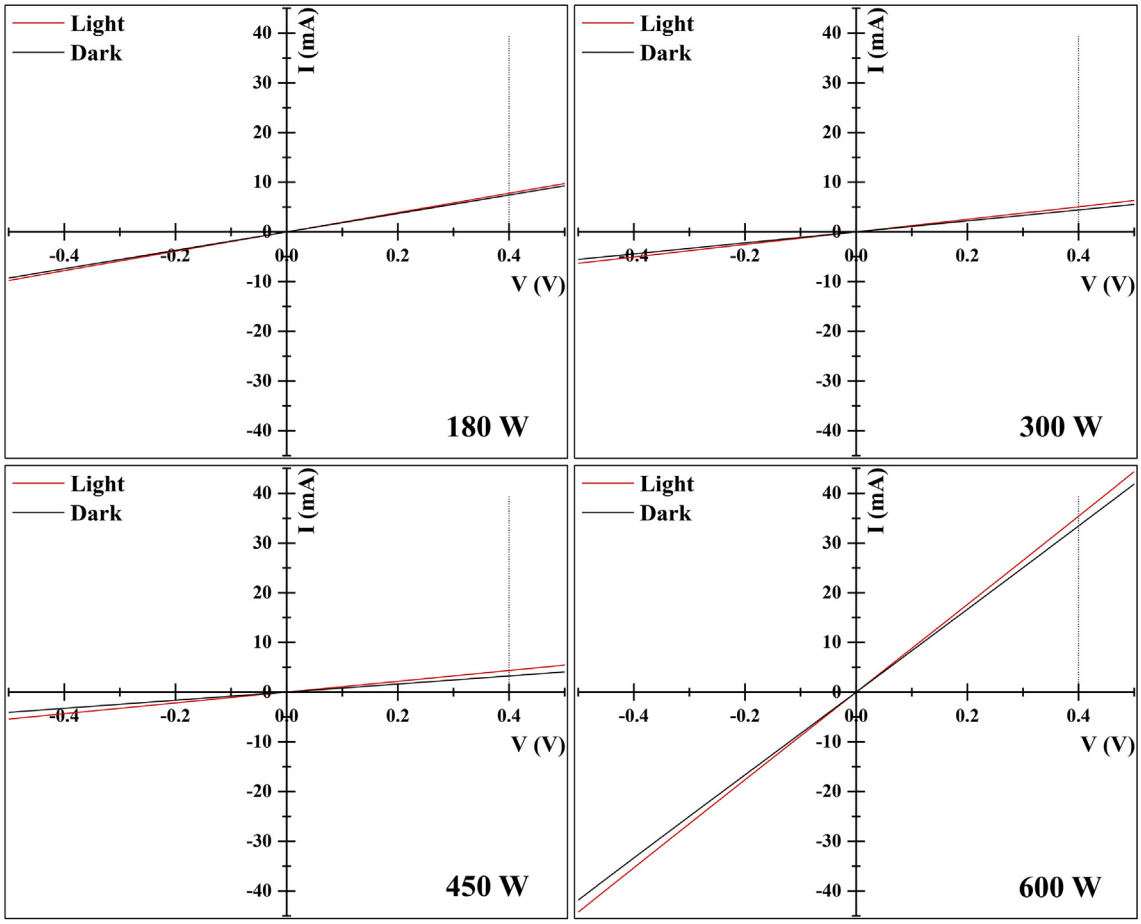

Fig. 6. Current-voltage curves of the $CuInS_2$ powders synthesized at different microwave powers operated in the dark (black line) and under illumination (red line). (For interpretation of the references to colour in this figure legend, the reader is referred to the web version of this article.)

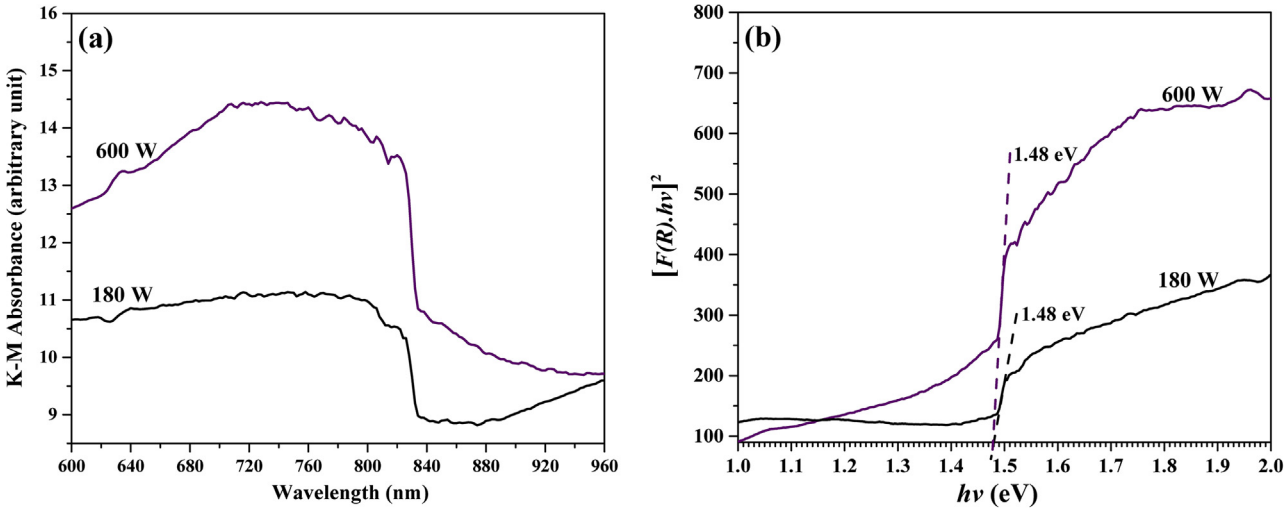

Fig. 7. (a) UV–vis diffuse reflectance spectra of the $CuInS_2$ powders synthesized using different microwave powers. (b) Plot of $(F(R)h\nu)^2$ versus $h\nu$ for estimating the band gap energy.

rent difference between the dark and illuminated (ΔI) conditions of the $CuInS_2$ films at a given bias voltage were measured to determine their photoconductivities. At a bias voltage of 0.4 V, the photoconductivities of the devices fabricated using the $CuInS_2$ powders synthesized at 180, 300, 450, and 600 W were 0.37, 0.63, 1.10, and 1.98 mA, respectively. The device fabricated using the $CuInS_2$ hollow sub-microspheres exhibited the improved photoconductivity with lower resistance, suggesting that the $CuInS_2$ hollow sub-microspheres were favorable to increase current carrier concentration and to improve electron transport [34–37].

To confirm the enhancement of photoconductivity of the $CuInS_2$ hollow sub-microspheres, optical properties of the $CuInS_2$ powders

synthesized at 180 W and 600 W of microwave powers were investigated by analyzing UV–vis diffuse reflectance spectra (Fig. 7). The reflectance spectra were converted into an absorption coefficient $F(R)$, according to the Kubelka-Munk equation: $F(R) = (1\text{-}R)^2/2R$, where R is the proportion of light reflected. The Kubelka-Munk (K-M) absorption spectra (Fig. 7(a)) exhibited light absorption in the region of visible light, extending into the near-infrared region. Among the most basic requirements for a high performance in solar cell, it can be seen that the $CuInS_2$ powder synthesized at 600 W showed a stronger absorption intensity [35]. This feature might be caused by the unique $CuInS_2$ hollow structure, which enhanced the ability of the light reflecting and scattering in their structure. This promotes current carrier concentration and electron transport and, hence, leads to the improved photoconductivity [34,35]. In addition, the apparent crystalline structure, as revealed by the HRTEM (Fig. 2(f)) analysis, improved the conversion efficiency, resulting in the enhancement of photoconductivity [36]. The band gap energy of the $CuInS_2$ powders were estimated by a plot of $(F(R)\cdot h\nu)^2$ versus $h\nu$, and by extrapolating the linear portion of the curve to intersect the $h\nu$ axis (Fig. 7(b)). The estimated band gap energy was 1.48 eV, which was close to the values observed in other studies [21,22]. Together, these results indicated that the $CuInS_2$ hollow microspheres could become highly useful in solar-light driven applications.

4. Conclusions

This study successfully synthesized $CuInS_2$ hollow sub-microspheres by a cyclic microwave radiation method at 600 W for 75 cycles. Based on time-dependent experiments, it appeared that the $CuInS_2$ hollow sub-microspheres formed by metal-ligand complexation and recrystallization. Owing to the improved photoconductivity and absorption ability of the $CuInS_2$ hollow sub-microspheres, the synthesized $CuInS_2$ hollow sub-microspheres are a potential candidate for applications in solar energy conversion and optoelectronic devices. The synthetic method developed in this study provided a simple, one-step, and rapid process for fabricating highly pure $CuInS_2$ that could also be extended to synthesizing other hollow ternary chalcogenide materials.

Acknowledgements

This research was financially supported by the Thailand Research Fund (TRF) and the Office of the Higher Education Commission (Grant number MRG6080270), the Energy Policy and Planning Office (EPPO) Thailand, the Center of Excellence (CoE) in Materials Science and Technology, Chiang Mai University under the admistration of Materials Science Research Center, Faculty of Science, Chiang Mai University, the Chiang Mai University (CMU) Junior Research Fellowship Program, and the Center of Excellence for Innovation in Chemistry (PERCH-CIC), Office of the Higher Education Commission, Ministry of Education (OHEC), Thailand.

Appendix A. Supplementary material

Supplementary data associated with this article can be found, in the online version, at https://doi.org/10.1016/j.apsusc.2018.03.210.

References

[1] J. Ye, L. Sun, S. Gao, Fabrication of hollow PbS nanospheres and application in phenol release, Springer Plus 2 (2013) 323.
[2] S. Wang, J. Zhang, J. Jiang, R. Liu, B. Zhu, M. Xu, Y. Wang, J. Cao, M. Li, Z. Yuan, S. Zhang, W. Huang, S. Wu, Porous ceria hollow microspheres: synthesis and characterization, Micropor. Mesopor. Mater. 123 (2009) 349–353.
[3] Y. Liu, L. Wang, W. Jin, C. Zhang, M. Zhou, W. Chen, Synthesis and photocatalytic property of TiO_2@V_2O_5 core-shell hollow porous microspheres towards gaseous benzene, J. Alloys Compd. 690 (2017) 604–611.
[4] P. Cui, J. Wang, Z. Wang, J. Chen, X. Xing, L. Wang, R. Yu, Bismuth oxychloride hollow microspheres with high visible light photocatalytic activity, Nano Res. 9 (3) (2016) 593–601.
[5] H.M. Yang, S.Y. Ma, H.Y. Jiao, Q. Chen, Y. Lu, W.X. Jin, W.Q. Li, T.T. Wang, X.H. Jiang, Z. Qiang, H. Chen, Synthesis of Zn_2SnO_4 hollow spheres by a template route for high-performance acetone gas sensor, Sens. Actuat. B Chem. 245 (2017) 493–506.
[6] G. Han, M. Wang, D. Li, J. Bai, G. Diao, Novel upconversion Er, Yb-CeO_2 hollow spheres as scattering layer materials for efficient dye-sensitized solar cells, Sol. Energy Mater. Sol. C 160 (2017) 54–59.
[7] N. Yu, G. Li, Y. Gao, X. Liu, S. Ma, Stimuli-sensitive hollow spheres from chitosan-graft-β-cyclodextrin for controlled drug release, Int. J. Biol. Macromol. 93 (2016) 971–977.
[8] X. Zhu, C.Q. Wang, pH and redox-operated nanovalve for size-selective cargo delivery on hollow mesoporous silica spheres, J. Colloid Interface Sci. 480 (2016) 39–48.
[9] J. Zhao, Y. Yang, C. Cui, H. Hu, Y. Zhang, J. Xu, B. Lu, L. Xu, J. Pan, W. Tang, TiO_2 hollow spheres as light scattering centers in TiO_2 photoanodes for dye-sensitized solar cells: the effect of sphere diameter, J. Alloys Compd. 663 (2016) 211–216.
[10] J. Chen, C. Li, F. Xu, Y. Zhou, W. Lei, L. Sun, Y. Zhang, Hollow SnO_2 microspheres for high-efficiency bilayered dye sensitized solar cell, RSC Adv. 2 (2012) 7384–7387.
[11] L. Zheng, Y. Xu, Y. Song, C.Z. Wu, M. Zhang, Y. Xie, Nearly monodisperse $CuInS_2$ hierarchical microarchitectures for photocatalytic H_2 evolution under visible light, Inorg. Chem. 48 (9) (2009) 4003–4009.
[12] Y. Yuan, D. Chen, Y. Huang, Z. Yu, J. Zhong, T. Chen, W. Tu, Z. Guan, D. Cao, Z. Zou, MoS_2 nanosheet-modified $CuInS_2$ photocatalyst for visible-light-driven hydrogen production from water, Chem. Sus. Chem. 9 (2016) 1003–1009.
[13] C. Yu, L. Zhang, L. Tian, D. Liu, F. Chen, C. Wang, Synthesis and formation mechanism of $CuInS_2$ nanocrystals with a tunable phase, Cryst. Eng. Commun. 16 (2014) 9596–9602.
[14] Y. Wang, J. Yang, W. Gao, R. Cong, T. Yang, Organic-free hydrothermal synthesis of chalcopyrite $CuInS_2$ and its photocatalytic activity for nitrate ions reduction, Mater. Lett. 137 (2014) 99–101.
[15] M. Yue, R. Wang, B. Ma, R. Cong, W. Gao, T. Yang, Superior performance of $CuInS_2$ for photocatalytic water treatment: full conversion of highly stable nitrate ions into harmless N_2 under visible light, Catal. Sci. Technol. 6 (2016) 8300–8308.
[16] M. Mousavi-Kamazani, M. Salavati-Niasari, M. Sadeghinia, Facile hydrothermal synthesis, formation mechanism and solar cell application of $CuInS_2$ nanoparticles using novel starting reagents, Mater. Lett. 142 (2015) 145–149.
[17] S. Hu, Y. Lee, B. Chen, Characterization of calcined $CuInS_2$ nanocrystals prepared by microwave-assisted synthesis, J. Alloys Compd. 690 (2017) 15–20.
[18] X. Geng, L. Zhai, J. Hu, L. Wang, Z. Xiong, C. Zou, L. Zhang, Y. Yang, S. Huang, The synthesis of hollow $CuInS_2$ microspheres with hierarchical structures, Mater. Chem. Phys. 149–150 (2015) 743–750.
[19] J. Zai, H. Chen, C. Huang, J. Huang, F. Chen, M. Xu, X. Qian, The fabrication of hollow cubic-like $CuInS_2$ cages using Cu_2O crystals as sacrificing template, Mater. Chem. Phys. 143 (2013) 15–18.
[20] S. Lei, C. Wang, Q. Huang, L. Liu, Y. Ge, Q. Tang, B. Cheng, Y. Xiao, L. Zhou, Fabrication of hollow-sphere films of wurtzite $CuInS_2$ on copper substrate, Mater. Chem. Phys. 143 (2013) 195–202.
[21] D. Wu, J. Duan, C. Zhang, K. Guo, H. Zhu, Sacrificial template synthesis and photothermal conversion enhancements of hierarchical and hollow $CuInS_2$ microspheres, J. Phys. Chem. C 117 (2013) 9121–9128.
[22] Y. Qi, K. Tang, S. Zeng, W. Zhou, Template-free one-step fabrication of porous $CuInS_2$ hollow microspheres, Micropor. Mesopor. Mater. 114 (2008) 395–400.
[23] A. Mirzaei, G. Neri, Microwave-assisted synthesis of metal oxide nanostructures for gas sensing application: a review, Sens. Actuators B 237 (2016) 749–775.
[24] Y. Zhu, F. Chen, Microwave-assisted preparation of inorganic nanostructures in liquid phase, Chem. Rev. 114 (2014) 6462–6555.
[25] N. Chumha, T. Thongtem, S. Thongtem, D. Tantraviwat, S. Kittiwachana, S. Kaowphong, A single-step method for synthesis of $CuInS_2$ nanostructures using cyclic microwave irradiation, Ceram. Int. 42 (14) (2016) 15643–15649.
[26] Y. Zhang, L. Liu, J. Ying, J. Qian, L. Liu, L. Wang, Biomolecule-assisted synthesis of $ZnIn_2S_4$ flower-like hollow microspheres, Mater. Lett. 105 (2013) 185–188.
[27] Y. Holade, N. Sahin, K. Servat, T. Napporn, K. Kokoh, Recent advances in carbon supported metal nanoparticles preparation for oxygen reduction reaction in low temperature fuel cells, Catalysts 5 (2015) 310–348.
[28] J. Zhu, H. Wang, Synthesis of metal chalcogenide nanoparticles, in: H.S. Nalwa (Ed.), Encyclopedia of Nanoscience and Nanotechnology, vol. 10, American Scientific Publishers, 2004, pp. 347–367.
[29] X. Chen, X. Zhang, Z. Wang, J. Wan, Y. Qian, Biomolecule-assisted hydrothermal synthesis and one-dimensional self-assembly of copper sulfide nanocrystallites, Mater. Chem. Phys. 98 (2006) 419–421.
[30] L. Chen, Z. Zhang, W. Wang, Self-assembled porous 3D flowerlike β-In_2S_3 structures: synthesis, characterization, and optical properties, J. Phys. Chem. C 112 (2008) 4117–4123.
[31] J.E. Huheey, E.A. Keiter, R.L. Keiter, Inorganic Chemistry: Principles of Structure and Reactivity, fourth ed., HarperCollins College Publishers, New York, 1993.

[32] F. Li, T. Kong, W. Bi, D. Li, Z. Li, X. Huang, Synthesis and optical properties of CuS nanoplate-based architectures by a solvothermal method, Appl. Surf. Sci. 255 (2009) 6285–6289.
[33] M. Saranya, C. Santhosh, R. Ramachandran, A. Nirmala Grace, Growth of CuS nanostructures by hydrothermal route and its optical properties, J. Nanotechnol. 2014 (2014) 1–8.
[34] M. Li, W. Zhou, J. Guo, Y. Zhou, Z. Hou, J. Jiao, Z. Zhou, Z. Du, S. Wu, Synthesis of pure metastable wurtzite CZTS nanocrystals by facile one-pot method, J. Phys. Chem. C 116 (2012) 26507–26516.
[35] B. Ananthoju, J. Mohapatra, M.K. Jangid, D. Bahadur, N.V. Medhekar, M. Aslam, Cation/anion substitution in Cu_2ZnSnS_4 for improved photovoltaic performance, Sci. Rep. 6 (2016) 35369.
[36] Z. Dong, X. Lai, J.E. Halpert, N. Yang, L. Yi, J. Zhai, D. Wang, Z. Tang, L. Jiang, Accurate control of multishelled ZnO hollow microspheres for dye-sensitized solar cells with high efficiency, Adv. Mater. 24 (2012) 1046–1049.
[37] H. Zhang, R. Wu, H. Xu, F. Li, S. Wang, J. Wang, T. Zhang, A simple spray reaction synthesis and characterization of hierarchically porous SnO_2 microspheres for an enhanced dye sensitized solar cell, RSC Adv. 7 (2017) 12446–12454.

Applied Surface Science 475 (2019) 175–184

Contents lists available at ScienceDirect

Applied Surface Science

journal homepage: www.elsevier.com/locate/apsusc

Full Length Article

Novel $FeVO_4/Bi_7O_9I_3$ nanocomposite with enhanced photocatalytic dye degradation and photoelectrochemical properties

Auttaphon Chachvalvutikul[a,b], Jaroon Jakmunee[b,c,d], Somchai Thongtem[c], Sila Kittiwachana[b,c,d], Sulawan Kaowphong[b,c,d,*]

[a] Master's Degree Program in Chemistry, Faculty of Science, Chiang Mai University, Chiang Mai 50200, Thailand
[b] Department of Chemistry, Faculty of Science, Chiang Mai University, Chiang Mai 50200, Thailand
[c] Center of Excellence in Materials Science and Technology, Chiang Mai University, Chiang Mai 50200, Thailand
[d] Center of Excellence for Innovation in Chemistry, Faculty of Science, Chiang Mai University, Chiang Mai 50200, Thailand

ARTICLE INFO

Keywords:
$FeVO_4/Bi_7O_9I_3$
Nanocomposite
Photocatalytic activity
Photoelectrochemical
Visible light

ABSTRACT

Novel $FeVO_4/Bi_7O_9I_3$ nanocomposites with different weight percentages (3, 6.25, 12.5, and 25%wt) of $FeVO_4$ were successfully synthesized by cyclic microwave irradiation, followed by wet impregnation. The applications for photocatalytic dye degradation and photoelectrochemical (PEC) were investigated. The 6.25%wt-$FeVO_4/Bi_7O_9I_3$ nanocomposite exhibited excellent photocatalytic degradation of methylene blue, rhodamine B, and methyl orange with decolorization efficiencies of 81.3%, 98.9%, and 94.9% within 360 min, respectively. Moreover, this nanocomposite possessed excellent reusability and stability during the photocatalytic degradation process. PEC performance in water oxidation of the 6.25%wt-$FeVO_4/Bi_7O_9I_3$ photoanode was evaluated by linear sweep voltammetry (LSV) measurement. Enhanced PEC performance with photocurrent density of 0.029 mA cm^{-2} at 1.23 V (*vs.* RHE) was observed under visible-light irradiation, which was ca. 3.7 times higher than that of the pure $Bi_7O_9I_3$. Based on the optical characterization, energy band positions, and active species trapping experiments, a possible photocatalytic mechanism of the $FeVO_4/Bi_7O_9I_3$ heterojunction was discussed. The enhancement in the photocatalytic and the PEC performance ascribed to synergistic effects of visible-light absorption and a favorable "type II heterojunction" structure of the $FeVO_4/Bi_7O_9I_3$ nanocomposite. These were the main effects that promoted the photogenerated electrons and holes transfer across the contact interface between $FeVO_4$ and $Bi_7O_9I_3$, as well as suppressed the recombination of photogenerated electron-hole pairs and facilitated charge separation and transportation.

1. Introduction

Semiconductor photocatalytic technology has been considered as a promising approach to solve environmental contamination and to conserve energy such as removal of organic pollutants from wastewater, production of O_2 and H_2 gases from water splitting, and reduction of CO_2 gas under solar light [1–3]. Transition metal oxides with wide band gaps, such as TiO_2 and ZnO, have been regarded as well-known photocatalysts due to their excellent photocatalytic activity, high chemical stability, non-toxicity, and low cost. However, they are capable of utilizing only UV light (accounted for 4% of all solar energy), thus limiting their photocatalytic performance. To harness solar radiation more efficiently, many visible-light responsive photocatalysts have been developed [4,5]. Among them, bismuth oxyhalides (BiOX, X = Cl, Br, I) have shown excellent visible-light photocatalytic activity due to their small band gaps (1.7–3.2 eV) [6] and unique structure [7–9]. Particularly, iodide-deficient bismuth oxyiodide ($Bi_7O_9I_3$) has attracted considerable interest in recent years as it has exhibited excellent visible-light photocatalytic activity for degradation of organic compounds such as colorless bisphenol-A, phenol, and rhodamine B under visible-light irradiation [7,8,10]. Nevertheless, the photocatalytic efficiency of $Bi_7O_9I_3$ remains far from suitable for practical applications because the quantum yield of $Bi_7O_9I_3$ is rather poor due to the rapid recombination of photogenerated electron–hole pairs and slow rate of photogenerated charge transfer [11,12]. Therefore, it is necessary to develop a strategy that effectively facilitates the separation of photogenerated charge. Coupling of two semiconductors to form a heterojunction is considered as an effective strategy toward extending the visible-light spectral responsive range, thus improving the efficiency of photogenerated charge separation and enhancing the photocatalytic

* Corresponding author at: Department of Chemistry, Faculty of Science, Chiang Mai University, Chiang Mai 50200, Thailand.
E-mail address: sulawank@gmail.com (S. Kaowphong).

https://doi.org/10.1016/j.apsusc.2018.12.214
Received 15 August 2018; Received in revised form 5 December 2018; Accepted 23 December 2018
Available online 24 December 2018
0169-4332/

activity [13–16].

Nanocrystalline $FeVO_4$ with a band gap energy of 2.0 eV is a highly stable and preferred catalyst for photocatalytic degradation of organic pollutants under a natural solar light irradiation [17,18] and a catalytic oxidation [19]. It can be used as a potential visible-light photocatalyst through a combination with other semiconductors to form heterojunctions such as $BiVO_4/FeVO_4$ [20] and $Bi_2O_3/FeVO_4$ [21]. These heterojunctions can facilitate an efficient charge separation and suppress the recombination of photogenerated electron–hole pairs, thereby leading to enhanced photocatalytic performance. Additionally, the enhancement of the photocatalytic performance can be triggered by an increase in the visible-light absorption ability, which enables the heterojunctions to absorb more visible light and produce more electron–hole pairs [12,20,21]. Hence, coupling $Bi_7O_9I_3$ with $FeVO_4$ containing matched band potentials to form a $FeVO_4/Bi_7O_9I_3$ heterojunction is a promising way to enhance photocatalytic performance.

In this work, synthesis, photocatalytic dye degradation, and photoelectrochemical activity of a novel $FeVO_4/Bi_7O_9I_3$ nanocomposite was reported for the first time. The $FeVO_4$ and the $Bi_7O_9I_3$ powders were prepared separately using a cyclic microwave irradiation method, which was a simple, rapid, economical, and environmentally friendly technique [22,23]. The two components were then mixed together to form a heterojunction via a wet impregnation method [24]. Photocatalytic degradation of methylene blue, rhodamine B, and methyl orange by the $FeVO_4/Bi_7O_9I_3$ nanocomposite was examined. Potential use of the $FeVO_4/Bi_7O_9I_3$ nanocomposite as a photoanode for photoelectrochemical (PEC) water oxidation was also investigated. A possible photocatalytic mechanism of the $FeVO_4/Bi_7O_9I_3$ heterojunction was proposed based on the optical characterization, energy band positions, and active species trapping experiments.

2. Experimental procedure

2.1. Preparation of $Bi_7O_9I_3$

$Bi(NO_3)_3{\cdot}5H_2O$ (1 mmol) and KI (1 mmol) were separately dissolved in 20.0 mL of ethylene glycol. The solutions were mixed together for 30 min. The mixed solution was then irradiated using 2.45 GHz microwave radiation operated at 600 W for 60 cycles. Each irradiation cycle lasted 30 s with a 90 s interval. The orange-yellow powder obtained was filtered, washed with deionized water, and dried overnight in an oven at 70 °C.

2.2. Preparation of $FeVO_4$

$Fe(NO_3)_3{\cdot}9H_2O$ (2 mmol) and NH_4VO_3 (2 mmol) were separately dissolved in 20.0 mL of deionized water. The solutions were mixed together for 30 min. Then, the pH of the mixed solution was adjusted to 4 by slowly adding 2.0 M of NH_4OH solution. Subsequently, the solution was irradiated using 2.45 GHz microwave radiation operated at 600 W for 30 cycles. Each cycle was lasted 30 s with a 90 s interval. The brown powder obtained was then filtered, washed with deionized water, and dried overnight in an oven at 70 °C. Finally, the powder was calcined in air at 600 °C for 5 h to yield $FeVO_4$ powder.

2.3. Preparation of $FeVO_4/Bi_7O_9I_3$ nanocomposites

First, the $Bi_7O_9I_3$ powder was sonochemically dispersed in 50.0 mL of methanol for 30 min. The required amount of the $FeVO_4$ powder was then mixed with the $Bi_7O_9I_3$ suspension and stirred at room temperature until methanol was completely volatized. Finally, the $FeVO_4/Bi_7O_9I_3$ powder was dried at 70 °C for 24 h and subsequently heated at 200 °C for 30 min. The amounts of $FeVO_4$ in the $FeVO_4/Bi_7O_9I_3$ nanocomposites were 3%, 6.25%, 12.5%, and 25% by weight, and the resulted $FeVO_4/Bi_7O_9I_3$ nanocomposites were denoted as x%wt-$FeVO_4/Bi_7O_9I_3$, where x = 3, 6.25, 12.5, and 25. Mole ratios between $FeVO_4$ and $Bi_7O_9I_3$ in the nanocomposites were presented in Table S1. The $FeVO_4/Bi_7O_9I_3$ powder were also synthesized by a physical grinding for comparison.

2.4. Characterizations

Purity, structure, and crystallinity of the powders were characterized by X-ray diffraction spectroscopy (XRD, Rigaku Miniflex II) with CuK_α radiation (λ = 1.5406 Å). Morphology and particle size of the powders were examined by field emission scanning electron microscopy (FESEM, JEOL JSM-6335F) and transmission electron microscopy (TEM, JEOL JEM-2010) with energy dispersive X-ray (EDX) spectrometry. Optical properties were also studied by UV–vis diffuse reflectance spectroscopy (UV–vis DRS, UV-1800 Shimadzu) using an instrument equipped with a specular reflectance attachment. Elemental composition and chemical state were measured by X-ray photoelectron spectroscopy (XPS, AXIS Ultra DLD, Kratos Analytical Ltd.) using an Al K_α X-ray source at 1.4 keV radiation. Binding energy of adventitious carbon (C 1s) peak at 284.6 eV was used for energy referencing. Photoluminescence spectra were recorded by a photoluminescence spectrometer (PL, Avantes AvaSpec-2048TEC-USB2) with an excitation wavelength of 345 nm.

2.5. Photocatalytic degradation experiments

For photocatalytic degradation experiments, methylene blue (MB), rhodamine B (RhB), and methyl orange (MO) were tested as model organic dye pollutants. The photocatalyst (100 mg) was dispersed in an aqueous solution of the organic dye (200 mL, 10 mg L^{-1}). Prior to irradiation, the suspension was magnetically stirred in dark for 30 min to establish an adsorption–desorption equilibrium of the dye on the photocatalyst's surface. The suspension was then irradiated under 50 W light-emitting diode (LED) lamp for 360 min. At every 30 min of irradiation, 5 mL of the suspension was sampled from the reaction suspension and the absorption intensity was measured at its maximum absorbance wavelength using a UV–vis spectrophotometer (664 nm for MB, 554 nm for RhB, and 464 nm for MO). Photolysis of the dye was also performed under the same experimental conditions. Decolorization efficiency (%DE) was calculated using the following equation: $\%DE = [(C_0 - C)/C_0] \times 100$, where C_0 and C were concentrations of the dye when the adsorption–desorption equilibrium was achieved and the dye after the light irradiation, respectively. The mole ratios between the $FeVO_4$ (or the $Bi_7O_9I_3$) in the nanocomposites and the MB were summarized in Table S1.

2.6. Photoelectrochemical (PEC) measurement

PEC properties of the 6.25%wt-$FeVO_4/Bi_7O_9I_3$ in comparison with the pure $Bi_7O_9I_3$ were investigated by linear sweep voltammogram (LSV). PEC measurement was conducted on an electrochemical analyzer (Autolab, μAUTOLABIII) equipped with a conventional three-electrode system. The electrolyte solution was a 0.5 M Na_2SO_4 aqueous solution (pH = 6.0). A platinum (Pt) sheet was used as a counter electrode and Ag/AgCl (3.0 M KCl) served as a reference electrode. A working electrode consisted of sample film coated on a fluorine-doped tin oxide (FTO)-coated glass substrate using the 'doctor blading' technique, as follows: 50.0 mg of the sample was dispersed in a mixture of 5 mL ethanol, 0.05 mL terpineol, and 0.05 mL Triton X-100. Then, the slurry was coated on an FTO-coated glass substrate with a fixed area of 1 × 1 cm^2. After that, the substrate was heated at 250 °C for 45 min to eliminate any remaining organic compounds. LSV was measured at a potential scan rate of 50 mV s^{-1}, and applied voltage potential was varied from −0.9 V to 2.0 V under dark and light irradiation. The light source was a 50 W LED lamp. The potentials were reported versus Ag/

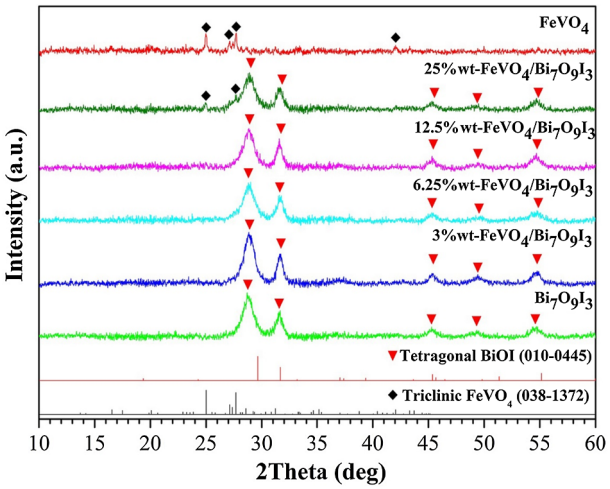

Fig. 1. XRD patterns of the $FeVO_4$, $Bi_7O_9I_3$, and $FeVO_4/Bi_7O_9I_3$ nanocomposites with different weight percentages of $FeVO_4$.

AgCl and reversible hydrogen electrode (RHE). Notably, the Ag/AgCl scale was converted into an RHE scale via the Nernst relation; V_{RHE} (volt) = $V_{Ag/AgCl}$ + (0.0591 × pH) + 0.210 V.

3. Results and discussion

3.1. Structural and morphological studies

3.1.1. XRD analysis

Fig. 1 shows XRD spectra of all the synthesized powders. For $FeVO_4$, the main diffraction peaks located at 2θ of 25.01°, 27.11°, 27.68°, and 42.09° corresponded to (1 2 0), (0 1 −2), (−2 2 0), and (−3 3 0) planes of a triclinic $FeVO_4$ structure (JCPDS No. 038-1372), respectively. The XRD spectrum of the bismuth oxyiodide sample was similar to that of tetragonal BiOI (JCPDS No. 010-0445) but the positions of all diffraction peaks slightly shifted to smaller diffraction angles. The diffraction peaks of the sample, observed at 2θ of 28.82°, 31.51°, 45.28°, 49.35°, and 54.71°, matched well with those of $Bi_7O_9I_3$ reported in the previous studies [10,25,26]. The position shift of the diffraction peaks could be due to the extra bismuth and oxygen in the lattice, thus causing an expansion and distortion of the standard BiOI crystal structure [10,26,27]. No characteristic peak of any impurities was observed, suggesting that a high purity of the $FeVO_4$ and $Bi_7O_9I_3$ powders was successfully obtained by the cyclic microwave irradiation method. XRD spectrum of the 25%wt-$FeVO_4/Bi_7O_9I_3$ nanocomposite exhibited characteristic diffraction peaks of both $FeVO_4$ and $Bi_7O_9I_3$, while XRD spectra of the $FeVO_4/Bi_7O_9I_3$ nanocomposites with lower amounts of $FeVO_4$ showed diffraction peaks of the tetragonal $Bi_7O_9I_3$ structure. This could be due to the lower diffraction peak intensity of the pure $FeVO_4$. However, the existence of $FeVO_4$ in these samples was recognized from the EDX analysis, as illustrated in Fig. 2(d).

3.1.2. FESEM, TEM, and EDX analyses

FESEM and TEM images of the $FeVO_4$, $Bi_7O_9I_3$, and 6.25%wt $FeVO_4/Bi_7O_9I_3$ powders are shown in Fig. 2. The $FeVO_4$ powder (Fig. 2(a) and (e)) were composed of spherical nanoparticles with a diameter of about 100 nm. Morphology of the $Bi_7O_9I_3$ powder (Fig. 2(b) and (f)) also showed spherical nanoparticles with a diameter of approximately 10 nm and with slight agglomeration. EDX spectrum of the $Bi_7O_9I_3$ (Fig. S1) revealed the presence of Bi, O, and I elements, where the atomic ratio of Bi:O:I was 2.34:3.09:1.00, indicating a formation of the iodide-poor bismuth oxyiodide ($Bi_7O_9I_3$). The lattice spacing measured from the fringes of $FeVO_4$ (inset of Fig. 2(e)) and $Bi_7O_9I_3$ (inset of Fig. 2(f)) nanoparticles was 0.32 nm which corresponded to the d-spacing of the (−2 2 0) and the (1 0 2) crystal planes of triclinic $FeVO_4$ and tetragonal BiOI, respectively. The wider lattice spacing observed from $Bi_7O_9I_3$, compared to that of BiOI, could be due to the expansion of the BiOI crystal structure [12], which was consistent with the XRD result. For 6.25%wt-$FeVO_4/Bi_7O_9I_3$ (Fig. 2(c)), mixed $FeVO_4$ and $Bi_7O_9I_3$ nanoparticles were observed. Microstructure of the $FeVO_4/Bi_7O_9I_3$ nanocomposite was similar to that of pure $FeVO_4$ and $Bi_7O_9I_3$, indicating that the wet impregnation method for the synthesized nanocomposite had a negligible effect on the microstructure. The corresponding EDX spectrum, shown in Fig. 2(d), revealed the characteristic peaks of Fe, V, Bi, O, and I elements, confirming that the nanocomposite was indeed composed of $FeVO_4$ and $Bi_7O_9I_3$. TEM image of the 6.25%wt-$FeVO_4/Bi_7O_9I_3$ nanocomposite (Fig. 3) also indicated that the $Bi_7O_9I_3$ nanoparticles were closely attached with the $FeVO_4$ nanoparticles. The HRTEM images (insets of Fig. 3) revealed the crystal lattice spacings of 0.32 nm and 0.30 nm, corresponding to the (−2 2 0) and (1 0 0) planes of $FeVO_4$ and $Bi_7O_9I_3$, respectively, thus confirming that the synthesized nanocomposite apparently had a crystalline structure. EDX mapping of the nanocomposite (Fig. S2) also showed that the Fe, V, Bi, O, and I elements were uniformly distributed throughout the nanocomposite material. These results provided reliable evidence that the $FeVO_4$ nanoparticles successfully combined with the $Bi_7O_9I_3$ nanoparticles, forming a $FeVO_4/Bi_7O_9I_3$ heterojunction. The heterojunction structure of the $FeVO_4/Bi_7O_9I_3$ played an important part in promoted the photogenerated electrons and holes transfer across the contact interface between $FeVO_4$ and $Bi_7O_9I_3$, consequently reduced the recombination of photogenerated electron-hole pairs. Noticeably, the iodine content in the 6.25%wt-$FeVO_4/Bi_7O_9I_3$ nanocomposite was low, corresponding to the detailed chemical composition of the synthesized $Bi_7O_9I_3$ nanoparticles illustrated in the inset of Fig. S1.

3.1.3. Optical properties

UV–vis DRS spectra of the $FeVO_4$, $Bi_7O_9I_3$, and 6.25%wt-$FeVO_4/Bi_7O_9I_3$ powders are shown in Fig. 4(a). The reflectance spectra were converted to the absorption coefficient $F(R)$ according to the Kubelka–Munk equation [28]: $F(R) = (1 - R)^2/2R$, where R is the proportion of light reflected. Optical band gap energy (E_g) can be determined from the following equation: $E_g = 1241/\lambda_{absorbance}$, where λ is the wavelength (nm). The absorption onsets in the visible-light region of the $FeVO_4$, $Bi_7O_9I_3$, and 6.25%wt-$FeVO_4/Bi_7O_9I_3$ powders were 590.5, 563.6, and 579.4 nm which corresponded to 2.10 eV, 2.20 eV, and 2.14 eV, respectively. This result suggested that the introduction of $FeVO_4$ into $Bi_7O_9I_3$ resulted in an improved visible-light absorption ability. In addition, the redshift of the absorption onset of the 6.25%wt-$FeVO_4/Bi_7O_9I_3$ nanocomposite, compared with that of the pure $Bi_7O_9I_3$, could be due to the formation of the $FeVO_4/Bi_7O_9I_3$ heterojunction. PL spectrum of the 6.25%wt-$FeVO_4/Bi_7O_9I_3$ nanocomposite (Fig. 4(b)) was analyzed in comparison with the pure $Bi_7O_9I_3$ to evaluate the separation efficiency of the photogenerated electron–hole pairs in the nanocomposite. As shown in Fig. 4(b), emission peaks of the samples were observed at 494 nm and 530 nm. Emission intensity of the PL spectrum for the 6.25%wt-$FeVO_4/Bi_7O_9I_3$ nanocomposite was lower than that of the pure $Bi_7O_9I_3$. It is known that a lower PL intensity indicates a more separation of electron–hole pairs and an improved photocatalytic activity. Thus, this result indicated that the formation of the $FeVO_4/Bi_7O_9I_3$ heterojunction facilitated effective separation of the electron–hole pairs.

3.1.4. XPS analysis

Elemental composition and chemical state of the $FeVO_4$, $Bi_7O_9I_3$, and 6.25%wt-$FeVO_4/Bi_7O_9I_3$ powders were identified by XPS as shown in Fig. 5. Survey XPS spectra, presented in Fig. 5(a), showed that the $FeVO_4$ powder contained only Fe, V, and O elements, while the $Bi_7O_9I_3$ powder contained only Bi, O, and I elements, indicating high purity of

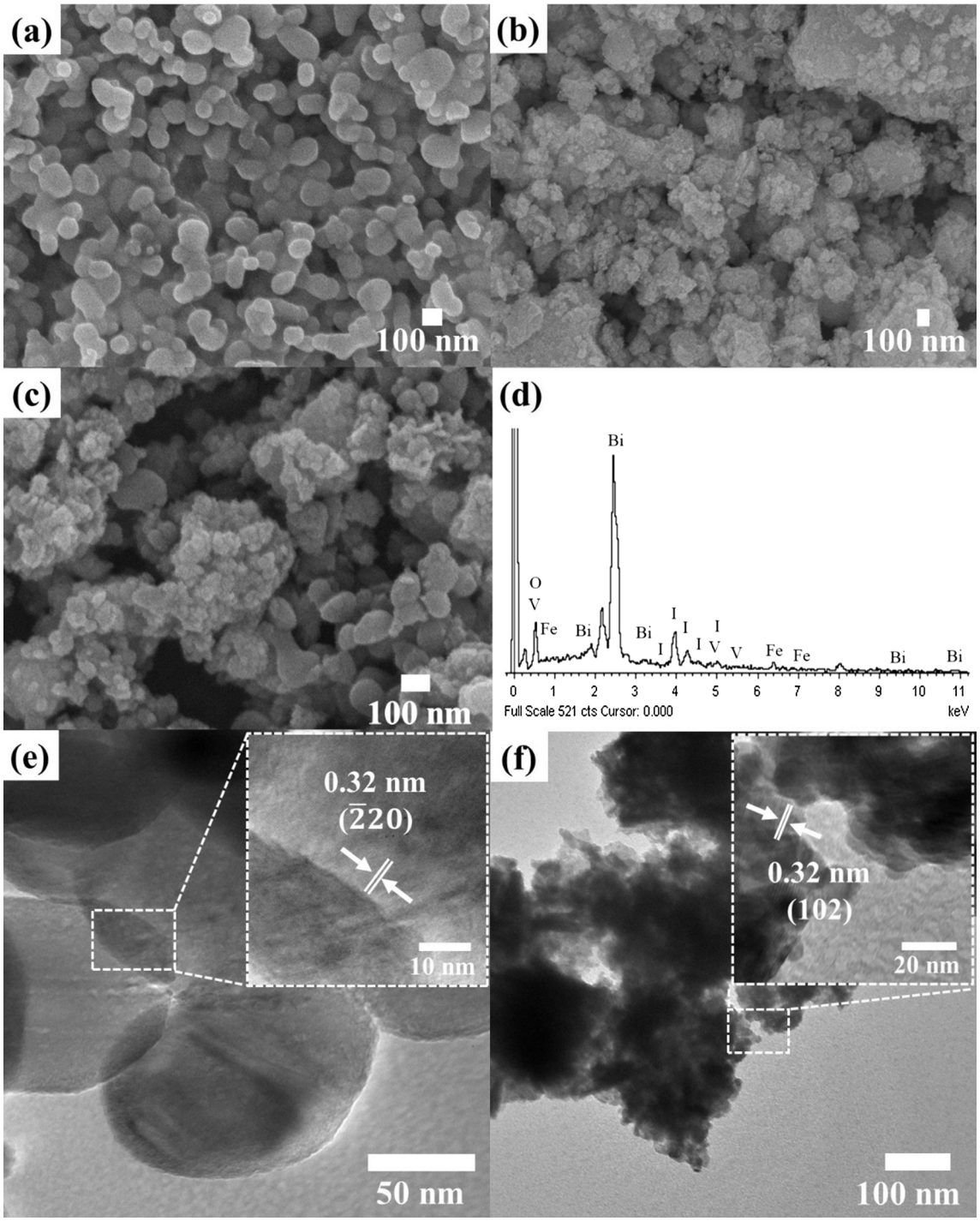

Fig. 2. FESEM images of the (a) $FeVO_4$, (b) $Bi_7O_9I_3$, and (c) 6.25%wt-$FeVO_4$/$Bi_7O_9I_3$ nanocomposite. (d) EDX spectrum of the 6.25%wt-$FeVO_4$/$Bi_7O_9I_3$ nanocomposite. (e) and (f) TEM images of the $FeVO_4$ and the $Bi_7O_9I_3$, respectively. Insets of (e) and (f) are the corresponding HRTEM images of the $FeVO_4$ and the $Bi_7O_9I_3$.

these powders. The 6.25%wt-$FeVO_4$/$Bi_7O_9I_3$ nanocomposite was composed of Fe, V, O, Bi, and I elements, which was consistent with the earlier EDX analyses (Figs. 2(d) and S2). This result confirmed the co-existence of the $FeVO_4$ and $Bi_7O_9I_3$ in the nanocomposite. Notably, the C 1s peak at 284.6 eV could originate from hydrocarbons in the XPS instrument. High-resolution XPS spectra of Bi 4f are presented in Fig. 5(b). For pure $Bi_7O_9I_3$, the two strong peaks at the Bi region of 159.2 eV and 164.5 eV were assigned to the binding energy of Bi $4f_{7/2}$ and Bi $4f_{5/2}$, respectively, which were the characteristics of Bi^{3+} [10,12]. The peaks of Bi $4f_{7/2}$ and Bi $4f_{5/2}$ for the 6.25%wt-$FeVO_4$/$Bi_7O_9I_3$ nanocomposite, located at 158.9 eV and 164.2 eV, respectively, appeared to have shifted to lower values compared to those of the pure $Bi_7O_9I_3$ [29,30]. The XPS spectra of I 3d (Fig. 5(c)) showed that the peaks at 619.2 eV and 630.7 eV were ascribed to I $3d_{5/2}$ and I $3d_{3/2}$, respectively, confirming that the valence state of I in the sample was −1 [10]. For the 6.25%wt-$FeVO_4$/$Bi_7O_9I_3$ nanocomposite, the peaks of I $3d_{5/2}$ and I $3d_{3/2}$ were observed at 621.6 eV and 633.0 eV, respectively, which positively shifted from those of the pure $Bi_7O_9I_3$ [30]. In Fig. 5(d), the main binding energies of Fe $2p_{3/2}$ and Fe $2p_{1/2}$ for the 6.25%wt-$FeVO_4$/$Bi_7O_9I_3$ (713.6 eV and 727.3 eV, respectively) appeared at higher energy levels than those of the pure $FeVO_4$ (710.8 eV and 724.4 eV, respectively). In addition, three sub-peaks in the Fe 2p

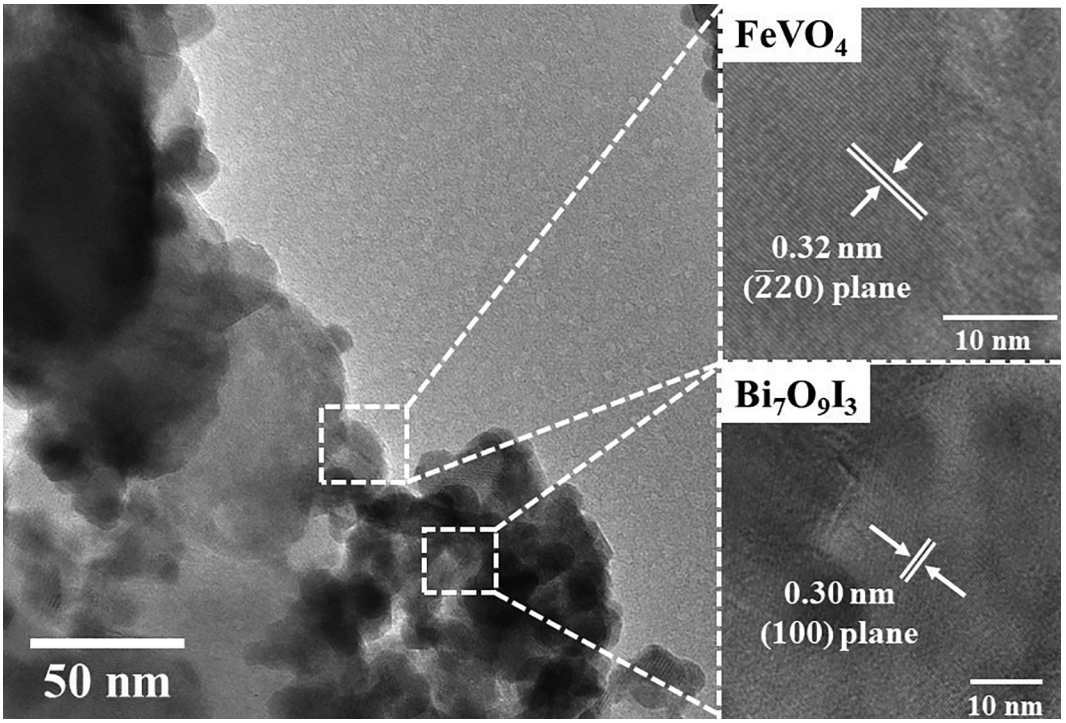

Fig. 3. TEM image of the 6.25%wt-$FeVO_4$/$Bi_7O_9I_3$ nanocomposite. Upper and lower insets show the corresponding HRTEM images of the $FeVO_4$ and the $Bi_7O_9I_3$, respectively.

spectra corresponded to tetrahedral structures and the satellite peak were also observed [31]. The V 2p spectra of the 6.25%wt-$FeVO_4$/$Bi_7O_9I_3$ nanocomposite, presented in Fig. 5(e), revealed the two main peaks of V $2p_{3/2}$ and V $2p_{1/2}$ (519.3 eV and 526.6 eV, respectively) [32,33], which were higher than those of the pure $FeVO_4$ (517.1 eV and 524.6 eV, respectively). Notably, a weak V^{4+} peak was found at a binding energy of around 516 eV because of oxygen vacancies in their crystal structures [31]. Fig. 5(f) shows the O 1s spectra of the $FeVO_4$, $Bi_7O_9I_3$, and 6.25%wt-$FeVO_4$/$Bi_7O_9I_3$. For $FeVO_4$, the binding energy peaks at 530.1 eV and 532.2 eV could be attributed to the two chemical bonds of O—V and O—Fe, respectively [31]. The O 1s peaks of the pure $Bi_7O_9I_3$, located at 529.9 eV and 531.2 eV, attributed to the Bi—O bonds in the $Bi_2O_2^{2+}$ layers and the hydroxyl groups of the adsorbed water molecules on the surface, respectively [27,34]. For the nanocomposite, the O 1s peaks with four sub-peaks, located at 531.3 eV, 532.3 eV, 533.4 eV, and 534.3 eV, were observed. These peaks could be attributed to the O—H bonds in the surface-adsorbed water molecules, Bi—O bonds in $Bi_7O_9I_3$, O—V bonds in $FeVO_4$, and O—Fe bonds in $FeVO_4$, respectively. Notably, the shift in the binding energies of Bi 4f and I 3d after introducing $FeVO_4$ clearly implied an interfacial chemical interaction between $FeVO_4$ and $Bi_7O_9I_3$ in the nanocomposite, instead of a physical contact between each individual material; this corresponded well with the TEM, HRTEM, and EDX analyses. Fig. 5(g) shows the valence band XPS (VB XPS) spectra of the $FeVO_4$ and $Bi_7O_9I_3$. The positions of the valence band edges (E_{VB}) of the $FeVO_4$ and $Bi_7O_9I_3$ were determined to be 2.06 eV and 1.42 eV, respectively. The conduction band (CB) edge positions of the pure $FeVO_4$ and $Bi_7O_9I_3$ could be calculated using the following formula: $E_{CB} = E_{VB} - E_g$, where E_g is the band gap of the $FeVO_4$ (2.10 eV) or the $Bi_7O_9I_3$ (2.20 eV). Here, the E_{CB} of the $FeVO_4$ and the $Bi_7O_9I_3$ were −0.04 eV and −0.78 eV (*vs.* NHE), respectively.

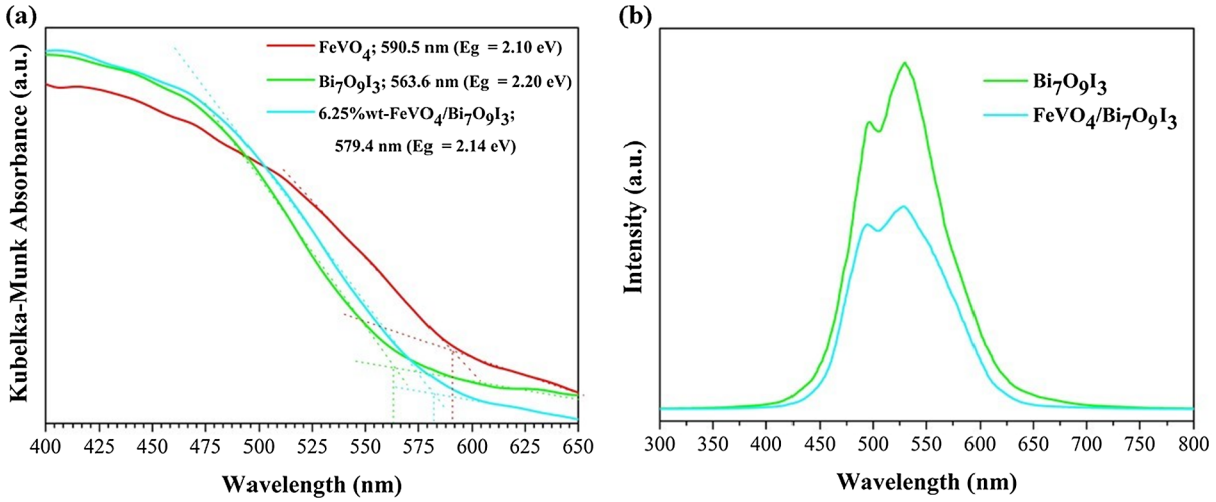

Fig. 4. (a) UV–vis DRS of the $FeVO_4$, $Bi_7O_9I_3$, and 6.25%wt-$FeVO_4$/$Bi_7O_9I_3$ nanocomposites, and (b) PL spectrum of the 6.25%wt-$FeVO_4$/$Bi_7O_9I_3$ nanocomposite in comparison with the $Bi_7O_9I_3$.

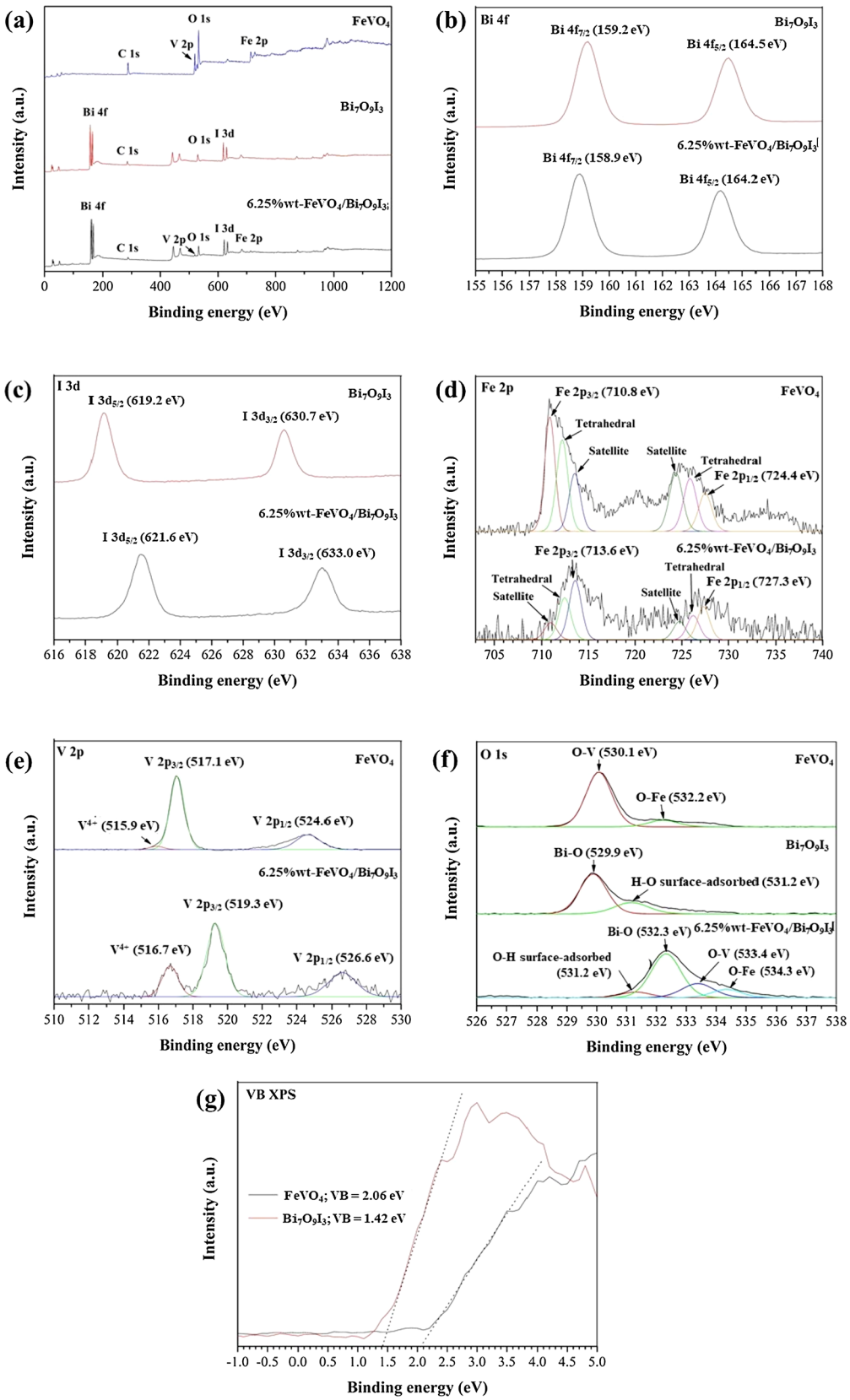

Fig. 5. (a) Survey XPS spectra of the $FeVO_4$, $Bi_7O_9I_3$, and 6.25%wt-$FeVO_4$/$Bi_7O_9I_3$ nanocomposite; high-resolution spectra of (b) Bi 4f, (c) I 3d, (d) Fe 2p, (e) V 2p, and (f) O 1s, and (g) valence band XPS (VB XPS) spectra of $FeVO_4$ and $Bi_7O_9I_3$.

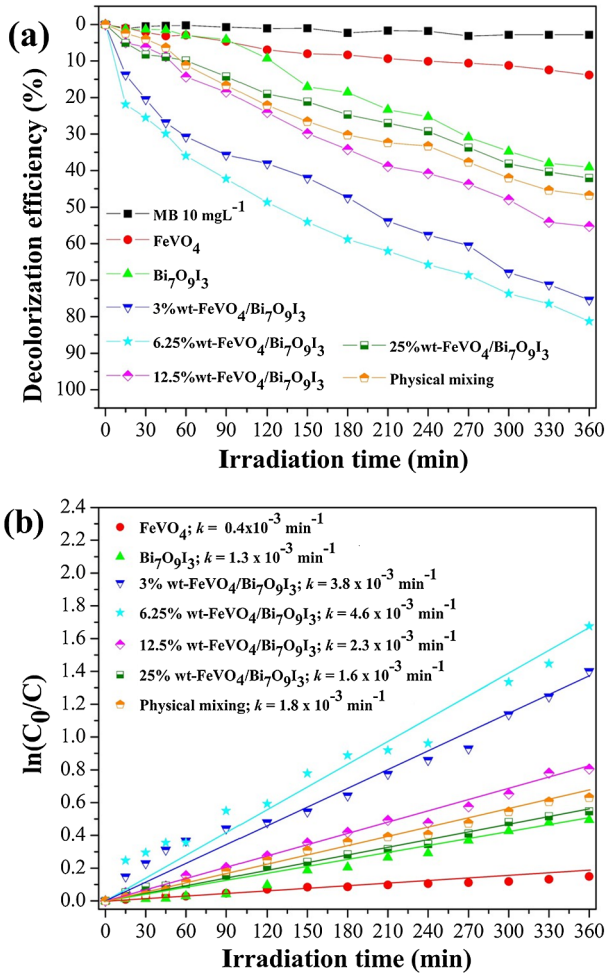

Fig. 6. (a) Decolorization efficiency (%) of the MB irradiated using LED lamp and (b) photocatalytic reaction kinetics of the degradation of MB. Photocatalysis condition: 200 mL of methylene blue (10 mgL^{-1} or 0.0255 mmol) with 100 mg of the photocatalyst.

3.2. Photocatalytic activity

3.2.1. Photocatalytic degradation

Fig. 6(a) shows %DE of methylene blue (MB) using $FeVO_4$, $Bi_7O_9I_3$, and $FeVO_4/Bi_7O_9I_3$ as the photocatalysts. Almost no change was observed when only the MB solution was exposed to the LED light, indicating that MB photolysis could be insignificant. The %DE of 13.9, 39.0, 75.4, 81.3, 55.3, and 42.1 within 360 min of the irradiation were found from $FeVO_4$, $Bi_7O_9I_3$, and the $FeVO_4/Bi_7O_9I_3$ nanocomposites having the amounts of $FeVO_4$ of 3%wt, 6.25%wt, 12.5%wt, and 25%wt, respectively. All the $FeVO_4/Bi_7O_9I_3$ nanocomposites provided greater photocatalytic degradation efficiency than that of pure $FeVO_4$ or pure $Bi_7O_9I_3$. The 6.25%wt-$FeVO_4/Bi_7O_9I_3$ nanocomposite with a mole ratio between $FeVO_4$ and $Bi_7O_9I_3$ of 0.78:1 resulted in the highest photocatalytic MB degradation (Table S1). In addition, the 6.25%wt-$FeVO_4/Bi_7O_9I_3$ nanocomposite showed a higher degradation activity (%DE = 81.3) than that of the physical mixture of $FeVO_4$ and $Bi_7O_9I_3$ (%DE = 46.8), indicating that the enhanced photocatalytic activity of the nanocomposite was originated by the formation of $FeVO_4/Bi_7O_9I_3$ heterojunction, which provided efficient photogenerated electron-hole transport pathway and suppressed electron-hole pairs recombination process. The plot of decolorization efficiency (%) *vs.* $FeVO_4$:MB and $Bi_7O_9I_3$:MB mole ratios presented in Fig. S3 implied that both of the $FeVO_4$ and $Bi_7O_9I_3$ contents in the nanocomposite affected greatly to the photocatalytic efficiency. The $FeVO_4$:MB and $Bi_7O_9I_3$:MB mole ratios were 1.434:1 and 1.848:1, respectively, provided the highest decolorization efficiency. The decolorization efficiency of MB increased as the $Bi_7O_9I_3$ content in the nanocomposite decreased slightly (or the $FeVO_4$ content increased substantially). However, the photocatalytic activity of the nanocomposite decreased when increasing the excessive amount of the $FeVO_4$ (12.5%wt and 25%wt). This could be because the excess $FeVO_4$ nanoparticles covered and shaded the active surface of the photocatalyst, as observed in the FESEM image (Fig. S4), inhibiting light absorption and consequently decreasing the quantity of photogenerated charges [35]. These results demonstrated that the optimum loading amount of $FeVO_4$ in the $FeVO_4/Bi_7O_9I_3$ nanocomposite improved the charge separation and reduced the electron–hole recombination on $Bi_7O_9I_3$ without blocking the active sites of the photocatalyst, thus enhancing photocatalytic activity. The photocatalytic reaction kinetic of the degradation of MB was further investigated using the pseudo-first-order kinetic model, as follows: $\ln(C_0/C) = kt$, where k is the pseudo-first-order rate constant derived from the slope of a linear plot between $\ln(C_0/C)$ and irradiation time (t), as presented in Fig. 6(b). The 6.25%wt-$FeVO_4/Bi_7O_9I_3$ photocatalyst provided the highest rate constant value ($4.6 \times 10^{-3}\,min^{-1}$), indicating that, among others, the 6.25%wt-$FeVO_4/Bi_7O_9I_3$ was the best photocatalyst.

Two other dyes, rhodamine B (RhB) and methyl orange (MO), were chosen to evaluate the universality of the $FeVO_4/Bi_7O_9I_3$ photocatalyst for photodegradation of organic dyes under visible-light irradiation. The decolorization efficiencies of RhB and MO in the presence of the 6.25% wt-$FeVO_4/Bi_7O_9I_3$ photocatalyst compared to that of MB are shown in Fig. 7(a). The %DE of RhB and MO without photocatalyst could be negligible. This photocatalyst decolorized RhB and MO with efficiencies of 98.9% and 94.9% and rate constants of $1.3 \times 10^{-2}\,min^{-1}$, and $8.1 \times 10^{-3}\,min^{-1}$, respectively (Fig. S5(a)). The absorption spectra of MB, RhB, and MO during the photodegradation processes by the $FeVO_4/Bi_7O_9I_3$ photocatalyst are shown in Fig. S6. The difference in %DE could be attributed to the different molecular structures of the dyes used in the present work, which resulted in different degradation mechanisms, as described in the previous literatures [36–38]. Briefly, the RhB molecules rapidly degraded due to an *N*-de-ethylation process, while the MO molecules were decomposed by a stepwise demethylation process. In addition, the azo group (−N═N−) of the MO molecule was more reactive than that of the MB molecule, and the sulfonyl group (−S(═O)$_2$−) of the MO molecule was more reactive than the sulfur involved in the $=S^+-$ aromatic ring in the MB molecule [37].

Due to the superior photodegradation of RhB, the photocatalytic degradation of the RhB experiment by the 6.25%wt-$FeVO_4/Bi_7O_9I_3$ photocatalyst was repeated under the same conditions, as shown in Fig. 7(b). No significant loss in the photocatalytic degradation of RhB was observed during three test runs, indicating the good reusability and stability of the photocatalyst. The effect of the initial dye concentration on photocatalytic degradation was also studied by varying the RhB concentration from 10 mg L^{-1} to 30 mg L^{-1} in the presence of the 6.25% wt-$FeVO_4/Bi_7O_9I_3$ photocatalyst. Fig. 7(c) shows the degradation of RhB with different initial concentrations under visible-light irradiation. After 360 min of irradiation, 98.9%, 94.8%, and 81.3% of 10 mg L^{-1}, 20 mg L^{-1}, and 30 mg L^{-1} of the RhB solution, respectively, were decolorized. The rate constants of the decolorization (Fig. S5(b)) were decreased with the increasing of initial concentration of RhB, owing to the decrease in the ratio of the photocatalyst to the RhB molecule in the solution. This led to a reduction in the light intensity, which reached the photocatalyst's surface, and a reduction in the number of active radicals, which contributed to the degradation of RhB [7,39].

Active species trapping experiments were performed to determine the main active species of the photocatalytic activity of the 6.25%wt-$FeVO_4/Bi_7O_9I_3$ photocatalyst. Different scavengers (1 mM) including ascorbic acid (ASC) [40], ethylenediaminetetraacetic acid disodium salt (EDTA-2Na) [40], dimethyl sulfoxide (DMSO) [41], and potassium dichromate ($K_2Cr_2O_7$) [42] were, respectively, used as scavengers for trapping superoxide radicals ($O_2^{\cdot -}$), holes (h^+), hydroxyl radicals ($HO^{\cdot}$), and photogenerated electrons (e^-). The corresponding results are shown in Fig. 7(d). As illustrated, the photodegradation of RhB was dramatically

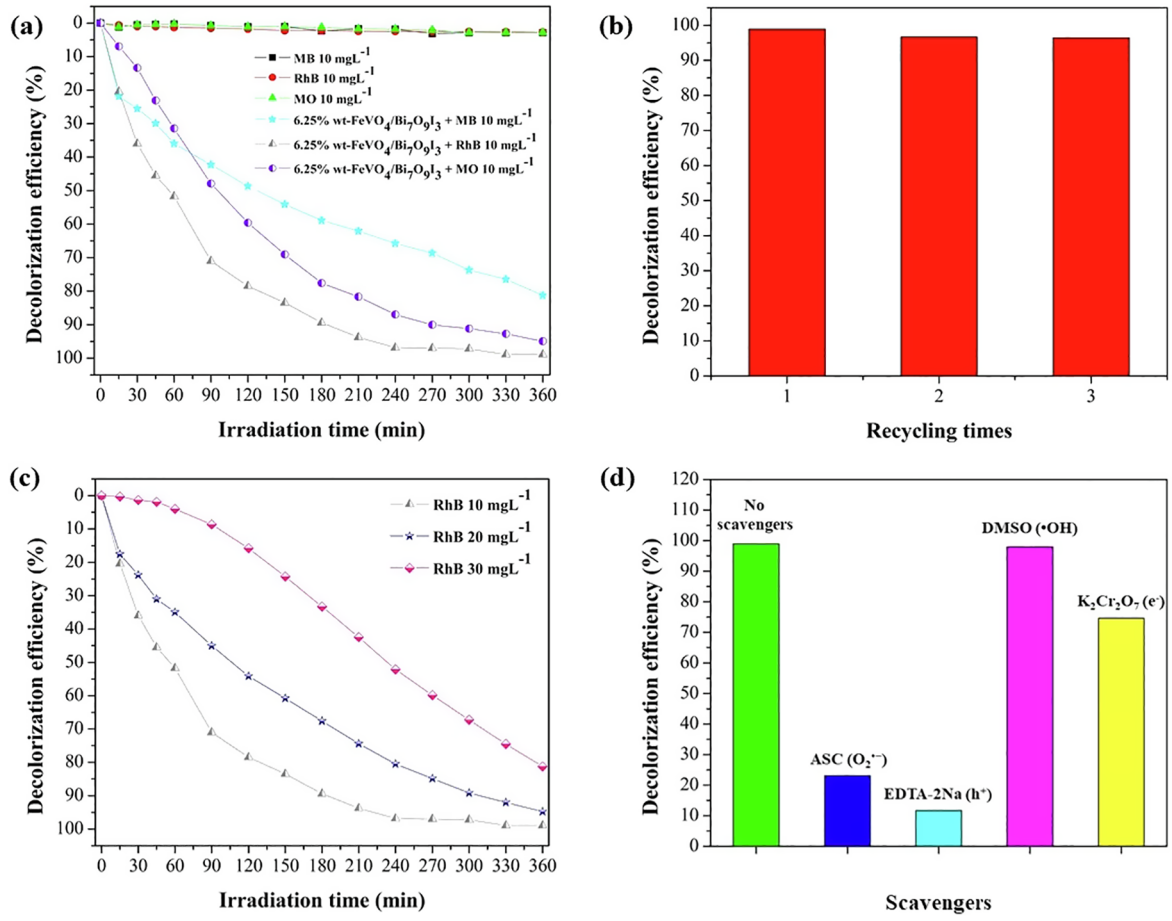

Fig. 7. (a) Decolorization efficiency (%) of RhB and MO compared to that of MB, (b) the reusing assessment of the 6.25%wt-$FeVO_4/Bi_7O_9I_3$ photocatalyst for photocatalytic degradation of 10 mgL^{-1} of RhB, (c) the effect of initial concentration on photocatalytic degradation of RhB, and (d) the trapping experiments of active species in the photocatalytic reaction with 360 min visible-light irradiation in the presence of the 6.25%wt-$FeVO_4/Bi_7O_9I_3$ photocatalyst.

quenched in the presence of ASC and EDTA-2Na, indicating that $O_2^{\cdot -}$ and h^+ were both important for the photodegradation process. The addition of DMSO and $K_2Cr_2O_7$ slightly suppressed the photodegradation of RhB, indicating that $HO^{\cdot}$ and e^- had only a small effect on the photodegradation process.

3.2.2. Photoelectrochemical property

Linear sweep voltammograms of the $Bi_7O_9I_3$ and the 6.25%wt-$FeVO_4/Bi_7O_9I_3$ photoanodes operated either in dark or under visible-light irradiation are shown in Fig. 8. Under dark condition, almost no photocurrent responses were visualized for the $Bi_7O_9I_3$ and the 6.25% wt-$FeVO_4/Bi_7O_9I_3$ photoanodes. Under visible-light irradiation, the $Bi_7O_9I_3$ photoanode illustrated a photocurrent density of 0.0078 mA cm^{-2} at an applied potential of 1.23 V (*vs.* RHE), while the 6.25%wt-$FeVO_4/Bi_7O_9I_3$ photoanode showed an enhanced photocurrent density of 0.029 mA cm^{-2} at the same applied potential. The photocurrent density of the 6.25%wt-$FeVO_4/Bi_7O_9I_3$ photoanode was ca. 3.7 times higher than that of the $Bi_7O_9I_3$ photoanode. The enhanced photocurrent density of the $FeVO_4/Bi_7O_9I_3$ nanocomposite could be explained by the fact that the generation and separation efficiency of the photogenerated charge had significantly improved *via* the formation of the heterojunction between $FeVO_4$ and $Bi_7O_9I_3$ [43]. The onset potential value of the $Bi_7O_9I_3$ photoanode for water oxidation was 1.59 V (*vs.* RHE), while the onset potential value of the 6.25%wt-$FeVO_4/Bi_7O_9I_3$ photoanode shifted to 1.50 V (*vs.* RHE). The cathodic shift of the onset potential value demonstrated that the charge transport was more efficient and that the photocurrent density had improved [44,45].

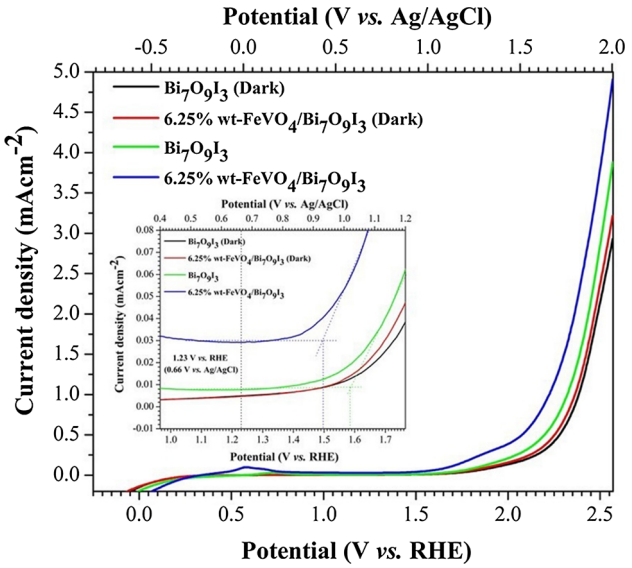

Fig. 8. Linear sweep voltammograms of the $Bi_7O_9I_3$ and the 6.25%wt-$FeVO_4/Bi_7O_9I_3$ photoanodes in dark and under light irradiation.

3.2.3. Photocatalytic mechanism

Based on the aforementioned experimental results, a schematic diagram of the photocatalytic mechanism of the $FeVO_4/Bi_7O_9I_3$ nanocomposite system for the degradation of dye was proposed (Fig. 9). Under

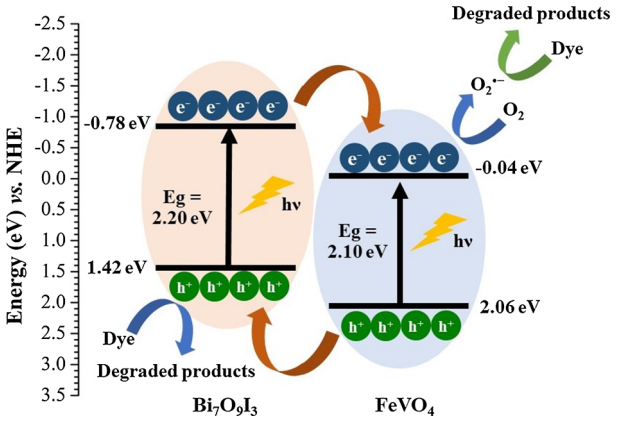

Fig. 9. Schematic diagram of the photocatalytic mechanism of the $FeVO_4$/$Bi_7O_9I_3$ nanocomposite system for the degradation of dye.

visible-light irradiation, both $FeVO_4$ and $Bi_7O_9I_3$ were excited and subsequently generated electrons (e^-) and holes (h^+). The difference between the energy bands of $FeVO_4$ and $Bi_7O_9I_3$ allowed the efficient transfer of e^- and h^+ between them. The h^+ on the valence band (VB) of $FeVO_4$ (2.06 eV *vs.* NHE) migrated to the VB of $Bi_7O_9I_3$ (1.42 eV *vs.* NHE) due to the less positive VB edge potential of $Bi_7O_9I_3$ compared to that of $FeVO_4$. Meanwhile, the e^- on the conduction band (CB) of $Bi_7O_9I_3$ (−0.78 eV *vs.* NHE) migrated to the CB of $FeVO_4$ (−0.04 eV *vs.* NHE) due to the less negative CB edge potential of $FeVO_4$ compared to that of $Bi_7O_9I_3$. Thus, the formation of a "type II heterojunction" [16] between $FeVO_4$ and $Bi_7O_9I_3$ effectively improved the separation of the photogenerated e^- and h^+, which resulted in the enhanced photocatalytic activity of the $FeVO_4$/$Bi_7O_9I_3$ heterojunction structure. Then, the e^- in the CB of $FeVO_4$ was scavenged by O_2 on the surface of the photocatalyst to generate $O_2^{\cdot-}$ radicals. The h^+ in the VB of $Bi_7O_9I_3$ would attack the dye to form intermediate products. The photocatalytic degradation reaction would subsequently proceed, in which the intermediate products [12,46,47] could transform and eventually decompose to CO_2 and H_2O by both the $O_2^{\cdot-}$ radical and h^+.

4. Conclusions

Novel $FeVO_4$/$Bi_7O_9I_3$ nanocomposites with different weight percentages of $FeVO_4$ were reported. The $FeVO_4$ and $Bi_7O_9I_3$ contents played an important role in the photocatalytic activity of the nanocomposite. The 6.25%wt-$FeVO_4$/$Bi_7O_9I_3$ photocatalyst exhibited excellent photocatalytic efficiency for the degradation of different organic dyes under visible light irradiation. In addition, it was effective in the reuse, and exhibited good stability after three times of usage. The $O_2^{\cdot-}$ and h^+ were found to contribute as the main active species in the trapping experiments for the decomposition of RhB under visible-light irradiation. The photocurrent response of the 6.25%wt-$FeVO_4$/$Bi_7O_9I_3$ photoanode was ca. 3.7 times higher than that of the pure $Bi_7O_9I_3$. The improved photogenerated charge separation in the $FeVO_4$/$Bi_7O_9I_3$ nanocomposite was mainly responsible for the enhanced photocatalytic activity, which was supported by photoluminescence spectra. Owing to notable enhancements in the photocatalytic dye degradation and the photoelectrochemical property of the $FeVO_4$/$Bi_7O_9I_3$ heterojunction, it is potentially applicable to the field of environmental remediation as well as solar water splitting.

Acknowledgments

This research was financially supported by the Thailand Research Fund (TRF) and the Office of the Higher Education Commission (Grant number MRG6080270), the Center of Excellence (CoE) in Materials Science and Technology under the administration of Materials Science Research Center, Faculty of Science, Chiang Mai University, and the Center of Excellence for Innovation in Chemistry (PERCH-CIC), Office of the Higher Education Commission, Ministry of Education (OHEC), Thailand. Auttaphon Chachvalvutikul would like to thank the Institute for the Promotion of Teaching Science and Technology (IPST), Thailand.

Appendix A. Supplementary material

Supplementary data to this article can be found online at https://doi.org/10.1016/j.apsusc.2018.12.214.

References

[1] S. Xia, L. Zhang, G. Pan, P. Qian, Z. Ni, Photocatalytic degradation of methylene blue with a nanocomposite system: synthesis, photocatalysis and degradation pathways, Phys. Chem. Chem. Phys. 17 (2015) 5345–5351, https://doi.org/10.1039/C4CP03877K.

[2] A.O. Ibhadon, P. Fitzpatrick, M. Sciences, C. Road, C. Innovation, C.T. Park, Heterogeneous photocatalysis: recent advances and applications, Catalysts 3 (2013) 1–29, https://doi.org/10.3390/catal30x000x.

[3] S. Gao, C. Guo, J. Lv, Q. Wang, Y. Zhang, S. Hou, J. Gao, J. Xu, A novel 3D hollow magnetic Fe_3O_4/BiOI heterojunction with enhanced photocatalytic performance for bisphenol A degradation, Chem. Eng. J. 307 (2017) 1055–1065, https://doi.org/10.1016/j.cej.2016.09.032.

[4] S. Dong, J. Feng, M. Fan, Y. Pi, L. Hu, X. Han, M. Liu, J. Sun, J. Sun, Recent developments in heterogeneous photocatalytic water treatment using visible light-responsive photocatalysts: a review, RSC Adv. 5 (2015) 14610–14630, https://doi.org/10.1039/c4ra13734e.

[5] A. Hernández-Ramírez, I. Medina-Ramírez, Photocatalytic semiconductors, Springer, Switzerland; 2015. doi:10.1007/978-3-319-10999-2.

[6] H. Cheng, B. Huang, Y. Dai, Engineering BiOX (X = Cl, Br, I) nanostructures for highly efficient photocatalytic applications, Nanoscale 6 (2014) 2009–2026, https://doi.org/10.1039/c3nr05529a.

[7] X. Xiao, R. Hao, X. Zuo, J. Nan, L. Li, W. Zhang, Microwave-assisted synthesis of hierarchical $Bi_7O_9I_3$ microsheets for efficient photocatalytic degradation of bisphenol-A under visible light irradiation, Chem. Eng. J. 209 (2012) 293–300, https://doi.org/10.1016/j.cej.2012.07.142.

[8] Q.C. Liu, D.K. Ma, Y.Y. Hu, Y.W. Zeng, S.M. Huang, Various bismuth oxyiodide hierarchical architectures: alcohothermal-controlled synthesis, photocatalytic activities, and adsorption capabilities for phosphate in water, Appl. Mater. Interface 5 (2013) 11927–11934, https://doi.org/10.1021/am4036702.

[9] O. Mehraj, B.M. Pirzada, N.A. Mir, M.Z. Khan, S. Sabir, A highly efficient visible-light-driven novel p-n junction Fe_2O_3/BiOI photocatalyst: surface decoration of BiOI nanosheets with Fe_2O_3 nanoparticles, Appl. Surf. Sci. 387 (2016) 642–651, https://doi.org/10.1016/j.apsusc.2016.06.166.

[10] X. Xiao, W.-D. Zhang, Hierarchical $Bi_7O_9I_3$ micro/nano-architecture: facile synthesis, growth mechanism, and high visible light photocatalytic performance, RSC Adv. 1 (2011) 1099, https://doi.org/10.1039/c1ra00323b.

[11] I. Tateishi, H. Katsumata, T. Suzuki, S. Kaneco, Visible-light-induced AgI/$Bi_7O_9I_3$ composites with enhanced photocatalytic activity, Catal. Lett. 147 (2017) 1503–1509, https://doi.org/10.1007/s10562-017-2059-8.

[12] H. Liu, Y. Su, Z. Chen, Z. Jin, Y. Wang, $Bi_7O_9I_3$/reduced graphene oxide composite as an efficient visible-light-driven photocatalyst for degradation of organic contaminants, J. Mol. Catal. A Chem. 391 (2014) 175–182, https://doi.org/10.1016/j.molcata.2014.04.029.

[13] D. Liu, Z. Jiang, C. Zhu, K. Qian, Z. Wu, J. Xie, Graphene-analogue BN-modified microspherical BiOI photocatalysts driven by visible light, Dalt. Trans. 45 (2016) 2505–2516, https://doi.org/10.1039/C5DT03408F.

[14] Y. Wang, Q. Wang, X. Zhan, F. Wang, M. Safdar, J. He, Visible light driven type II heterostructures and their enhanced photocatalysis properties: a review, Nanoscale 5 (2013) 8326, https://doi.org/10.1039/c3nr01577g.

[15] Y. Xiang, P. Ju, Y. Wang, Y. Sun, D. Zhang, J. Yu, Chemical etching preparation of the Bi_2WO_6/BiOI p-n heterojunction with enhanced photocatalytic antifouling activity under visible light irradiation, Chem. Eng. J. 288 (2016) 264–275, https://doi.org/10.1016/j.cej.2015.11.103.

[16] R. Marschall, Semiconductor composites: strategies for enhancing charge carrier separation to improve photocatalytic activity, Adv. Funct. Mater. 24 (2014) 2421–2440, https://doi.org/10.1002/adfm.201303214.

[17] B. Ozturk, G.S. Pozan Soylu, Synthesis of surfactant-assisted $FeVO_4$ nanostructure: characterization and photocatalytic degradation of phenol, J. Mol. Catal. A Chem. 398 (2015) 65–71, https://doi.org/10.1016/j.molcata.2014.11.013.

[18] S.J. Hu, J. Yang, X.H. Liao, Highly efficient degradation of methylene blue on microwave synthesized $FeVO_4$ nanoparticles photocatalysts under visible-light irradiation, Appl. Mech. Mater. 372 (2013) 153–157, https://doi.org/10.4028/www.scientific.net/AMM.372.153.

[19] Y. Li, S. Chen, A. Xu, F. Ma, F. Chen, W. Lu, Research on the nanocrystal FeV_xO_y catalysts for new reaction from propane to propylene and CO, Appl. Surf. Sci. 320 (2014) 552–557, https://doi.org/10.1016/j.apsusc.2014.09.126.

[20] J. Li, W. Zhao, Y. Guo, Z. Wei, M. Han, H. He, S. Yang, C. Sun, Facile synthesis and high activity of novel $BiVO_4$/$FeVO_4$ heterojunction photocatalyst for degradation of

metronidazole, Appl. Surf. Sci. 351 (2015) 270–279, https://doi.org/10.1016/j.apsusc.2015.05.134.
[21] X. Liu, Y. Kang, Synthesis and high visible-light activity of novel Bi_2O_3/$FeVO_4$ heterojunction photocatalyst, Mater. Lett. 164 (2016) 229–231, https://doi.org/10.1016/j.matlet.2015.10.137.
[22] N. Chumha, T. Thongtem, S. Thongtem, S. Kittiwachana, S. Kaowphong, Cyclic microwave radiation synthesis, photoconductivity, and optical properties of $CuInS_2$ hollow sub-microspheres, Appl. Surf. Sci. 447 (2018) 292–299, https://doi.org/10.1016/j.apsusc.2018.03.210.
[23] N. Chumha, T. Thongtem, S. Thongtem, D. Tantraviwat, A single-step method for synthesis of $CuInS_2$ nanostructures using cyclic microwave irradiation, Ceram. Int. 42 (2016) 15643–15649, https://doi.org/10.1016/j.ceramint.2016.07.019.
[24] W.-K. Jo, J.Y. Lee, T.S. Natarajan, Fabrication of hierarchically structured novel redox-mediator-free $ZnIn_2S_4$ marigold flower/Bi_2WO_6 flower-like direct Z-scheme nanocomposite photocatalysts with superior visible light photocatalytic efficiency, Phys. Chem. Chem. Phys. 18 (2016) 1000–1016, https://doi.org/10.1039/c5cp06176h.
[25] M. Long, P. Hu, H. Wu, Y. Chen, B. Tan, W. Cai, Understanding the composition and electronic structure dependent photocatalytic performance of bismuth oxyiodides, J. Mater. Chem. A 3 (2015) 5592–5598, https://doi.org/10.1039/C4TA06134A.
[26] G. Wu, Y. Zhao, Y. Li, H. Ma, J. Zhao, pH-dependent synthesis of iodine-deficient bismuth oxyiodide microstructures: visible-light photocatalytic activity, J. Colloid Interface Sci. 510 (2018) 228–236, https://doi.org/10.1016/j.jcis.2017.09.053.
[27] C. Liao, Z. Ma, X. Chen, X. He, J. Qiu, Controlled synthesis of bismuth oxyiodide toward optimization of photocatalytic performance, Appl. Surf. Sci. 387 (2016) 1247–1256, https://doi.org/10.1016/j.apsusc.2016.06.140.
[28] C.D. Morton, I.J. Slipper, M.J.K. Thomas, B.D. Alexander, Synthesis and characterisation of Fe-V-O thin film photoanodes, J. Photochem. Photobiol. A Chem. 216 (2010) 209–214, https://doi.org/10.1016/j.jphotochem.2010.08.010.
[29] H. Li, Y. Cui, W. Hong, B. Xu, Enhanced photocatalytic activities of BiOI/$ZnSn(OH)_6$ composites towards the degradation of phenol and photocatalytic H_2 production, Chem. Eng. J. 228 (2013) 1110–1120, https://doi.org/10.1016/j.cej.2013.05.086.
[30] Y. Huang, H. Li, W. Fan, F. Zhao, W. Qiu, H. Ji, Y. Tong, Defect engineering of bismuth oxyiodide by IO_3-doping for increasing charge transport in photocatalysis, ACS Appl. Mater. Interface 8 (2016) 27859–27867, https://doi.org/10.1021/acsami.6b10653.
[31] X. She, Z. Zhang, M. Baek, K. Yong, Elevated photoelectrochemical activity of $FeVO_4$/$ZnFe_2O_4$/ZnO branch-structures via slag assisted-synthesis, RSC Adv. 7 (2017) 16787–16794, https://doi.org/10.1039/C7RA00812K.
[32] S. Samanta, R. Srivastava, Thermal catalysis vs. photocatalysis: A case study with $FeVO_4$/g-C_3N_4 nanocomposites for the efficient activation of aromatic and benzylic C-H bonds to oxygenated products, Appl. Catal. B Environ. 218 (2017) 621–636, https://doi.org/10.1016/j.apcatb.2017.06.043.
[33] Q. Nong, M. Cui, H. Lin, L. Zhao, Y. He, Fabrication, characterization and photocatalytic activity of g-C_3N_4 coupled with $FeVO_4$ nanorod, RSC Adv. 5 (2015) 27933–27939, https://doi.org/10.1039/C5RA01484K.
[34] X.J. Wang, F.T. Li, D.Y. Li, R.H. Liu, S.J. Liu, Facile synthesis of flower-like BiOI hierarchical spheres at room temperature with high visible-light photocatalytic activity, Mater. Sci. Eng. B. 193 (2015) 112–120, https://doi.org/10.1016/j.mseb.2014.12.013.
[35] Z. Cui, M. Si, Z. Zheng, L. Mi, W. Fa, H. Jia, Preparation and characterization of Ag_3PO_4/BiOI composites with enhanced visible light driven photocatalytic performance, Catal. Commun. 42 (2013) 121–124, https://doi.org/10.1016/j.catcom.2013.08.011.
[36] Y. Lei, G. Wang, S. Song, W. Fan, M. Pang, Room temperature, template-free synthesis of BiOI hierarchical structures: visible-light photocatalytic and electrochemical hydrogen storage properties, Dalt. Trans. 39 (2010) 3273–3278, https://doi.org/10.1039/b922126c.
[37] H. Lachheb, E. Puzenat, A. Houas, M. Ksibi, E. Elaloui, C. Guillard, J.M. Herrmann, Photocatalytic degradation of various types of dyes (alizarin S, crocein orange G, methyl red, congo red, methylene blue) in water by UV-irradiated titania, Appl. Catal. B Environ. 39 (2002) 75–90, https://doi.org/10.1016/S0926-3373(02)00078-4.
[38] Y. Liu, J. Xu, L. Wang, H. Zhang, P. Xu, X. Duan, H. Sun, S. Wang, Three-dimensional BiOI/BiOX (X = Cl or Br) nanohybrids for enhanced visible-light photocatalytic activity, Nanomaterials 7 (2017), https://doi.org/10.3390/nano7030064.
[39] S.M. Aghdam, M. Haghighi, S. Allahyari, L. Yosefi, Precipitation dispersion of various ratios of BiOI/BiOCl nanocomposite over g-C_3N_4 for promoted visible light nanophotocatalyst used in removal of acid orange 7 from water, J. Photochem. Photobiol. A Chem. 338 (2017) 201–212, https://doi.org/10.1016/j.jphotochem.2017.02.013.
[40] J. Lv, Q. Hu, C. Cao, Y. Zhao, Modulation of valence band maximum edge and photocatalytic activity of BiOX by incorporation of halides, Chemosphere 191 (2018) 427–437, https://doi.org/10.1016/j.chemosphere.2017.09.149.
[41] J. Xu, L. Li, C. Guo, Y. Zhang, S. Wang, Removal of benzotriazole from solution by BiOBr photocatalysis under simulated solar irradiation, Chem. Eng. J. 221 (2013) 230–237, https://doi.org/10.1016/j.cej.2013.01.081.
[42] X. Li, C. Niu, D. Huang, X. Wang, X. Zhang, G. Zeng, Q. Niu, Preparation of magnetically separable Fe_3O_4/BiOI nanocomposites and its visible photocatalytic activity, Appl. Surf. Sci. 286 (2013) 40–46, https://doi.org/10.1016/j.apsusc.2013.08.139.
[43] L. Wang, W.A. Daoud, BiOI/TiO_2-nanorod array heterojunction solar cell: growth, charge transport kinetics and photoelectrochemical properties, Appl. Surf. Sci. 324 (2015) 532–537, https://doi.org/10.1016/j.apsusc.2014.10.110.
[44] Y.X. Yu, W.X. Ouyang, W. De Zhang, Photoelectrochemical property of the BiOBr-BiOI/ZnO heterostructures with tunable bandgap, J. Solid State Electrochem. 18 (2014) 1743–1750, https://doi.org/10.1007/s10008-014-2402-6.
[45] L. Xia, J. Bai, J. Li, Q. Zeng, L. Li, B. Zhou, High-performance $BiVO_4$ photoanodes cocatalyzed with an ultrathin α-Fe_2O_3 layer for photoelectrochemical application, Appl. Catal. B Environ. 204 (2017) 127–133, https://doi.org/10.1016/j.apcatb.2016.11.015.
[46] J. Cao, C. Zhou, H. Lin, B. Xu, S. Chen, Surface modification of m-$BiVO_4$ with wide band-gap semiconductor BiOCl to largely improve the visible light induced photocatalytic activity, Appl. Surf. Sci. 284 (2013) 263–269, https://doi.org/10.1016/j.apsusc.2013.07.092.
[47] H. Huang, K. Xiao, Y. He, T. Zhang, F. Dong, X. Du, Y. Zhang, In situ assembly of BiOI@$Bi_{12}O_{17}Cl_2$ p-n junction: Charge induced unique front-lateral surfaces coupling heterostructure with high exposure of BiOI 001 active facets for robust and nonselective photocatalysis, Appl. Catal. B Environ. 199 (2016) 75–86, https://doi.org/10.1016/j.apcatb.2016.06.020.